THE APPLICATION OF NANOENGINEERING IN ADVANCED DRUG DELIVERY AND TRANSLATIONAL RESEARCH

EDITED BY: Gan Liu, Junqing Wang, Kai Han and Jingxiao Chen

PUBLISHED IN: Frontiers in Bioengineering and Biotechnology

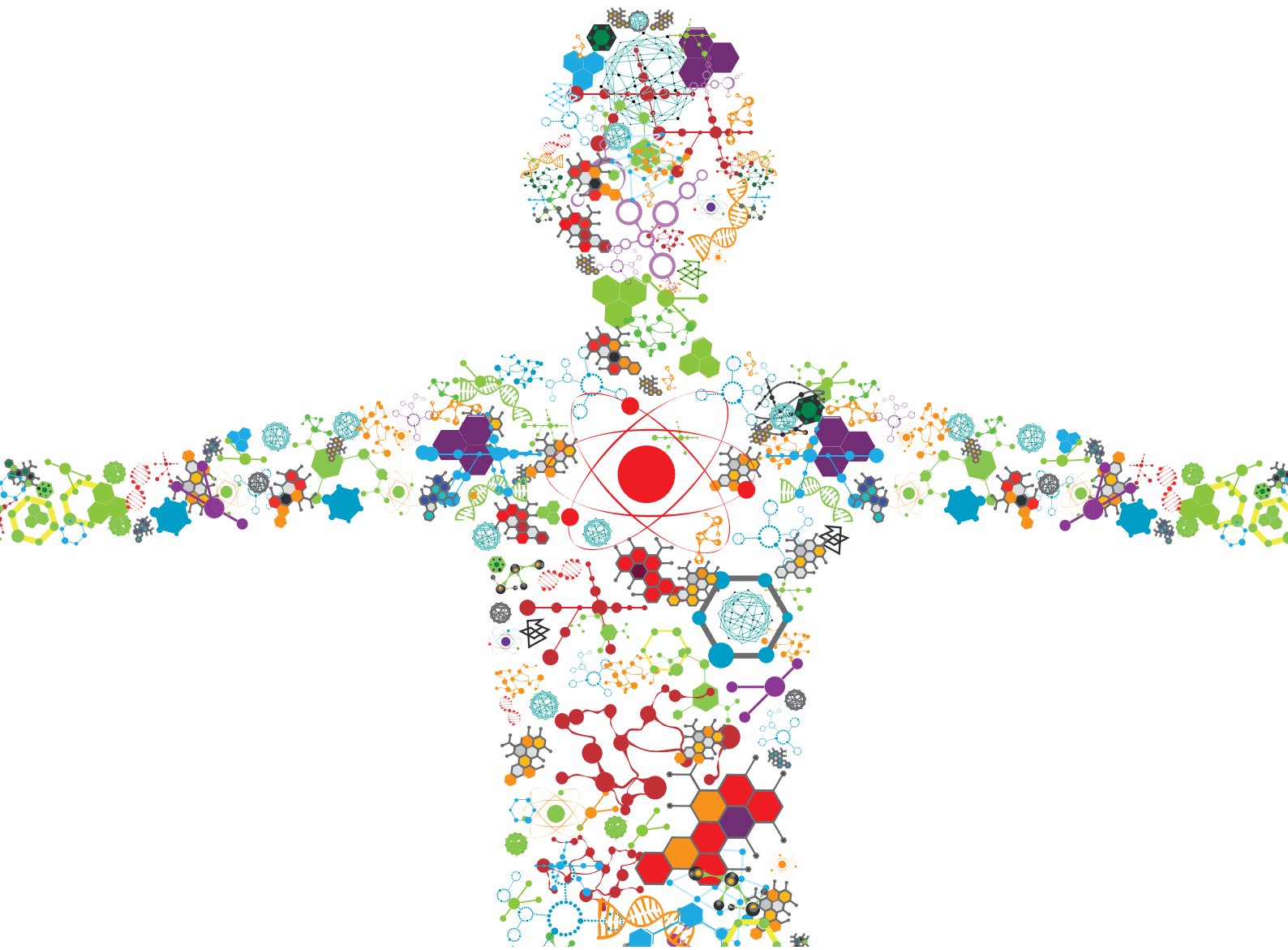

frontiers Research Topics

frontiers

Frontiers eBook Copyright Statement

The copyright in the text of individual articles in this eBook is the property of their respective authors or their respective institutions or funders. The copyright in graphics and images within each article may be subject to copyright of other parties. In both cases this is subject to a license granted to Frontiers.

The compilation of articles constituting this eBook is the property of Frontiers.

Each article within this eBook, and the eBook itself, are published under the most recent version of the Creative Commons CC-BY licence. The version current at the date of publication of this eBook is CC-BY 4.0. If the CC-BY licence is updated, the licence granted by Frontiers is automatically updated to the new version.

When exercising any right under the CC-BY licence, Frontiers must be attributed as the original publisher of the article or eBook, as applicable.

Authors have the responsibility of ensuring that any graphics or other materials which are the property of others may be included in the CC-BY licence, but this should be checked before relying on the CC-BY licence to reproduce those materials. Any copyright notices relating to those materials must be complied with.

Copyright and source acknowledgement notices may not be removed and must be displayed in any copy, derivative work or partial copy which includes the elements in question.

All copyright, and all rights therein, are protected by national and international copyright laws. The above represents a summary only. For further information please read Frontiers' Conditions for Website Use and Copyright Statement, and the applicable CC-BY licence.

ISSN 1664-8714
ISBN 978-2-88974-930-0
DOI 10.3389/978-2-88974-930-0

About Frontiers

Frontiers is more than just an open-access publisher of scholarly articles: it is a pioneering approach to the world of academia, radically improving the way scholarly research is managed. The grand vision of Frontiers is a world where all people have an equal opportunity to seek, share and generate knowledge. Frontiers provides immediate and permanent online open access to all its publications, but this alone is not enough to realize our grand goals.

Frontiers Journal Series

The Frontiers Journal Series is a multi-tier and interdisciplinary set of open-access, online journals, promising a paradigm shift from the current review, selection and dissemination processes in academic publishing. All Frontiers journals are driven by researchers for researchers; therefore, they constitute a service to the scholarly community. At the same time, the Frontiers Journal Series operates on a revolutionary invention, the tiered publishing system, initially addressing specific communities of scholars, and gradually climbing up to broader public understanding, thus serving the interests of the lay society, too.

Dedication to Quality

Each Frontiers article is a landmark of the highest quality, thanks to genuinely collaborative interactions between authors and review editors, who include some of the world's best academicians. Research must be certified by peers before entering a stream of knowledge that may eventually reach the public - and shape society; therefore, Frontiers only applies the most rigorous and unbiased reviews.
Frontiers revolutionizes research publishing by freely delivering the most outstanding research, evaluated with no bias from both the academic and social point of view. By applying the most advanced information technologies, Frontiers is catapulting scholarly publishing into a new generation.

What are Frontiers Research Topics?

Frontiers Research Topics are very popular trademarks of the Frontiers Journals Series: they are collections of at least ten articles, all centered on a particular subject. With their unique mix of varied contributions from Original Research to Review Articles, Frontiers Research Topics unify the most influential researchers, the latest key findings and historical advances in a hot research area! Find out more on how to host your own Frontiers Research Topic or contribute to one as an author by contacting the Frontiers Editorial Office: frontiersin.org/about/contact

THE APPLICATION OF NANOENGINEERING IN ADVANCED DRUG DELIVERY AND TRANSLATIONAL RESEARCH

Topic Editors:
Gan Liu, Sun Yat-sen University, China
Junqing Wang, Sun Yat-sen University, China
Kai Han, University of Michigan, United States
Jingxiao Chen, Jiangnan University, China

Citation: Liu, G., Wang, J., Han, K., Chen, J., eds. (2022). The Application of Nanoengineering in Advanced Drug Delivery and Translational Research. Lausanne: Frontiers Media SA. doi: 10.3389/978-2-88974-930-0

Table of Contents

frontiers in Bioengineering and Biotechnology

EDITORIAL
published: 24 March 2022
doi: 10.3389/fbioe.2022.886109

Editorial: The Application of Nanoengineering in Advanced Drug Delivery and Translational Research

Zhidong Chen[1], Xu Chen[1], Gan Liu[1], Kai Han[2]*, Jingxiao Chen[3]* and Junqing Wang[1]**

[1]School of Pharmaceutical Sciences (Shenzhen), Sun Yat-sen University, Shenzhen, China, [2]Department of Pharmaceutical Sciences, University of Michigan, Ann Arbor, MI, United States, [3]Key Laboratory of Carbohydrate Chemistry and Biotechnology, Ministry of Education, School of Life Sciences and Health Engineering, Jiangnan University, Wuxi, China

Keywords: nanoengineering, drug delivery, cancer, immunotherapy, exosomes, osteogenesis

Editorial on the Research Topic

The Application of Nanoengineering in Advanced Drug Delivery and Translational Research

In recent years, nanoengineering has been playing a significant role in drug delivery and translational research as it has the potential of resolving the translational challenges of traditional therapeutic agents, such as poor solubility, side effects, limited blood-circulation time, etc. Lots of research are focusing on developing novel drug delivery systems for translation with nanoengineering, including many types like micelles (Ghosh and Biswas, 2021), liposomes (Crommelin et al., 2020), lipid nanoparticles (Wang et al., 2020), nanodiscs (Kuai et al., 2017; Xu et al., 2022), hydrogel (Daly et al., 2020), and exosomes (Kalluri and LeBleu, 2020). Some results from clinical trials have shown the efficiency of nanoengineering (Martin et al., 2020). However, many problems remain to be solved, such as immune-related adverse events (Martins et al., 2019), nanotoxicity, and poor reproducibility. Therefore, designing advanced drug delivery systems for translation needs some novel and practical approaches with chemistry, biology, and materials science, which is also the theme of this Research Topic.

This Research Topic is provided through ten articles, including eight original research articles and two review articles. The original research articles involved multiple delivery systems with nanoengineering: exosomes, nanoparticles, black phosphorus nanosheets, and hydrogels. These nanosystems were rationally designed, showing improvement and intriguing effects compared with traditional therapeutic agents in different diseases.

There are two review articles on this Research Topic. In a review article, Zhang et al. mainly discussed the crucial role and related biological mechanisms of oxidative stress in diabetic wound healing. They summarized the progress in antioxidant therapy and related bioengineering technology. The authors initially highlighted the importance of oxidative stress in the pathology of diabetic ulcers from the four overlapping stages of wound healing, showing the oxidative stress induced by hyperglycemia will largely hinder the recovery of wound healing by widely impairing the majority of cells. Then, in consideration of the significance of oxidative stress, they summarized the recent progress of antioxidant therapy for diabetic wound healing. They pointed out the key pathways in oxidative stress and corresponding therapy and introduced several therapeutic agents, including endogenous molecules like vitamins, antioxidant enzymes, hormones, and medicinal plants. The authors also summarized the biological materials used in diabetic wound healing. Most of them can load the antioxidant agents to promote their efficiency. In another review article, Cui et al. emphasized the state-of-the-art hydrogels applied in cancer immunotherapy. As one of the most biocompatible and versatile biomaterials, hydrogels can be endowed with unique and useful properties by novel design, making a difference in cancer immunotherapy. They first introduced

OPEN ACCESS

Edited and reviewed by:
Hasan Uludag,
University of Alberta, Canada

****Correspondence:***
Gan Liu
liugan5@mail.sysu.edu.cn
Kai Han
hanka@med.umich.edu
Jingxiao Chen
tomchenjx@jiangnan.edu.cn
Junqing Wang
wangjunqing@mail.sysu.edu.cn

Specialty section:
This article was submitted to Biomaterials, a section of the journal Frontiers in Bioengineering and Biotechnology

Received: *28 February 2022*
Accepted: *07 March 2022*
Published: *24 March 2022*

Citation:
Chen Z, Chen X, Liu G, Han K, Chen J and Wang J (2022) Editorial: The Application of Nanoengineering in Advanced Drug Delivery and Translational Research. Front. Bioeng. Biotechnol. 10:886109. doi: 10.3389/fbioe.2022.886109

the characteristics and design principles of hydrogels as delivery systems from five respects, including load ability, implantability, injectability, degradability, and stimulus-responsibility. Then, the applications of hydrogels in cancer immunotherapy classified by the carrying cargos were discussed. In the end, the authors discussed the challenges, clinical application potential of hydrogels, and some Research Topic that need to be considered from the clinical aspect.

In an original study, Zhao et al. developed an exosomes-based nanoplatform prepared by adding dexamethasone (DEX) in exosomes(exos) secreted from mesenchymal stem cells (MSCs), which can be thought of as a promising drug delivery system of autoimmune hepatitis (AIH). Lots of research have shown that exosomes will typically accumulate in the liver, and those secreted from MSCs have the ability of liver regeneration. Taking the positive effects of exosomes on the liver and the delivery efficiency of exosomes into account, this research attempted to combine the therapeutic features of exosomes with the potent anti-inflammation drug DEX for a synergistic treatment toward AIH. The presence of exosomes will also relieve the side effect of DEX resulting from its accumulation in the liver. *In vivo* and *ex vivo* experiments in this article proved the accumulation of this system in the liver parenchyma, and with the *in vivo* treatment of the Con A-induced AIH mouse model, the efficiency of this system compared to free drugs was certified.

Escharotomy and infection sometimes could be severe clinical challenges. Wang et al. designed a sequential therapeutic hydrogel. Through the cross-linked by modified polyvinyl alcohol (PVA-SH/ε-PL) and benzaldehyde-terminated F127 triblock copolymers (PF127-CHO), this hydrogel is endowed with excellent properties which are beneficial for deep burn wounds, such as excellent mechanical and satisfactory wound cleaning properties. The authors also loaded bromelain and EGF into the same hydrogel in stages for wound cleaning and healing. All of the intriguing properties of these novel hydrogels were confirmed by *in vitro* and *in vivo* assays, making this kind of hydrogels an excellent candidate for deep burn injuries, especially for irregular-shaped deep burn wounds in poor medical conditions.

Chen et al. developed a novel peptide design strategy with artificial neural networks. An unnatural amino acids library was introduced to generate peptides targeting the GPR40 receptor. This strategy provides a new approach for peptide drug design and an opportunity to improve clinical translation efficiency. The screening strategy designed by the authors was based on AI and unnatural amino acids to overcome the limited diversity in traditional peptide design. Site-directed mutagenesis approach and molecular dynamics simulation were applied to optimize the interaction between the candidate peptides and GPR40 and verify the stability of the peptide-protein complex. This strategy can efficiently discover peptide drugs and improve clinical translation efficiency with a small computing resource.

Nanoengineering has been one of the most effective tools in cancer medicine, nanoengineering-based approaches can modulate the systemic biodistribution and targeted accumulation of the therapeutic agents (Nam et al., 2019). In this research topic, Bao et al. designed a novel nanoparticle coated with polypyrrole for photothermal/magnetothermal therapy against cancer. The main purpose of this study was to solve the deficiency of photothermal or magnetothermal-based hyperthermia cancer therapy by combining them with nanotechnology. The poor penetration ability of the photothermal and the deficient heating efficiency of the magnetothermal was improved by the combination of polypyrrole and Fe_3O_4, which also enables this system with excellent hyperthermia effects and antitumor effects under the alternating magnetic field and near-infrared at the same time. After proving the photothermal and magnetic thermal properties of this system, the cytotoxicity of this combination therapy was certified to be more efficient through *in vitro* cell experiments. The authors also did the *in vivo* test with magnetic resonance imaging (MRI) and photoacoustic imaging (PAI), showing the intriguing efficiency in anticancer and proving the safety of the AMF plus NIR-triggered dual-enhanced hyperthermia.

In another work, Cao et al. focused on cancer therapy with nanoengineering. They fabricated a biomimetic tumor-targeted black phosphorus (BP) nanoplatform to inhibit tumor cell growth. They found that the addition of oxaliplatin (1,2-diaminocyclohexane) platinum (II) (DACHPt) complexions would promote the efficiency of antitumor by photothermal effect and chemotoxicity. The mesenchymal stem cell (MSC)–derived membranes-based approach was introduced to circumvent the limitations of BP, including poor stability, dispersibility, low delivery sufficiency to the tumor site. By studying the cytotoxicity and antitumor efficacy of different nanoformulations under several conditions, this nanoplatform showed excellent tumor-targeted photothermal-chemo efficacy in cell tests. Nevertheless, *in vivo* study is encouraged to explore their antitumor potential further.

Xiong et al. reported another original research for cancer therapy with nanoengineering. They constructed novel star-shaped block polymers nanoparticles (NPs) containing Dacarbazine (DTIC), showing intriguing results against malignant melanoma (MM), which is one of the most life-threatening cancer. The introduction of these NPs brings the increased drug loading capacity of DTIC and also enables this DTIC with control release property. For the active targeted therapy of MM, the authors made further modifications with the nucleic acid aptamer AS1411. For validating the stability of this drug delivery system, the drug release profiles of DTIC, and the cell viability of NPs, they did several experiments *in vitro*. The results showed the great potential of this novel system. The antitumor efficacy and side effects of the constructed nanocarriers were evaluated by *In vivo* experiments, which demonstrated an intriguing effect to treat MM with virtually no side effects.

Nanoengineering also demonstrated potential in the area of bone-related diseases. In one original research article, a bilayer coating with double-crosslinked hydrogels containing bone morphogenic protein (BMP)-2 (alginate-GelMA/hydroxyapatite (HA)/BMP-2) was designed by Ma et al., showing intriguing potential in inducing osteogenesis of bone mesenchymal stem cells with the combination of alginate, GelMA, and BMP-2. The authors tested the biocompatibility,

release of BMP-2, expression of the gene, and osteogenesis ability of this system with human bone mesenchymal stem cells (hBMSCs), finding the best ratios between GelMA and alginate for the applications in biology, like promoting the osteogenesis of the bone defect.

In this Research Topic, another application based on nanoengineering in bone-related diseases was explored for treating and preventing post-operative infections and bone loss. Yao et al. fabricated a nanosystem based on enoxacin (Eno)-loaded mesoporous silica nanoparticles (MSN). The eight repeating sequences of aspartate (D-Asp8) and polyethylene glycol were added to this nanosystem. The purpose of designing this system was to promote the translational practice of enoxacin in limiting post-operative infection and preventing bone loss by addressing the poor specificity, limited penetration into bone tissue, and adverse effects of enoxacin. Through *in vitro* and *in vivo* experiments, the biocompatibility, drug release performance, antibacterial properties, bone-targeting properties of this system were tested, which proved the potential in post-operative infections and bone loss.

In conclusion, the current Research Topic reports the novel design and nanoengineering of all kinds of drug delivery systems with various methods based on chemistry, biology, and materials science, providing new chances for developing advanced drug delivery systems towards clinical translation. The articles in this Research Topic will be a helpful reference, promoting the development of innovative nanoengineering approaches and accelerating the translation of related technology to clinical uses.

AUTHOR CONTRIBUTIONS

All authors listed have made a substantial, direct, and intellectual contribution to the work and approved it for publication.

FUNDING

This work was supported by the National Natural Science Foundation of China (82001887, 51973084) in part by the Science and Technology Innovation Committee of Shenzhen Municipality (JCYJ20210324115003009), and the Guangdong Basic and Applied Basic Research Foundation (2019A1515110326).

ACKNOWLEDGMENTS

We thank the support of the National Natural Science Foundation of China.

REFERENCES

Crommelin, D. J. A., van Hoogevest, P., and Storm, G. (2020). The Role of Liposomes in Clinical Nanomedicine Development. What Now? Now what? *J. Controlled Release* 318, 256–263. doi:10.1016/j.jconrel.2019.12.023

Daly, A. C., Riley, L., Segura, T., and Burdick, J. A. (2020). Hydrogel Microparticles for Biomedical Applications. *Nat. Rev. Mater.* 5 (1), 20–43. doi:10.1038/s41578-019-0148-6

Ghosh, B., and Biswas, S. (2021). Polymeric Micelles in Cancer Therapy: State of the Art. *J. Controlled Release* 332, 127–147. doi:10.1016/j.jconrel.2021.02.016

Kalluri, R., and LeBleu, V. S. (2020). The Biology , Function , and Biomedical Applications of Exosomes. *Science* 367 (6478). doi:10.1126/science.aau6977

Kuai, R., Ochyl, L. J., Bahjat, K. S., Schwendeman, A., and Moon, J. J. (2017). Designer Vaccine Nanodiscs for Personalized Cancer Immunotherapy. *Nat. Mater* 16 (4), 489–496. doi:10.1038/nmat4822

Martin, J. D., Cabral, H., Stylianopoulos, T., and Jain, R. K. (2020). Improving Cancer Immunotherapy Using Nanomedicines: Progress, Opportunities and Challenges. *Nat. Rev. Clin. Oncol.* 17 (4), 251–266. doi:10.1038/s41571-019-0308-z

Martins, F., Sofiya, L., Sykiotis, G. P., Lamine, F., Maillard, M., Fraga, M., et al. (2019). Adverse Effects of Immune-Checkpoint Inhibitors: Epidemiology, Management and Surveillance. *Nat. Rev. Clin. Oncol.* 16 (9), 563–580. doi:10.1038/s41571-019-0218-0

Nam, J., Son, S., Park, K. S., Zou, W., Shea, L. D., and Moon, J. J. (2019). Cancer Nanomedicine for Combination Cancer Immunotherapy. *Nat. Rev. Mater.* 4 (6), 398–414. doi:10.1038/s41578-019-0108-1

Wang, J., Zope, H., Islam, M. A., Rice, J., Dodman, S., Lipert, K., et al. (2020). Lipidation Approaches Potentiate Adjuvant-Pulsed Immune Surveillance: A Design Rationale for Cancer Nanovaccine. *Front. Bioeng. Biotechnol.* 8, 787. doi:10.3389/fbioe.2020.00787

Xu, D., Chen, X., Chen, Z., Lv, Y., Li, Y., Li, S., et al. (2022). An In Silico Approach to Reveal the Nanodisc Formulation of Doxorubicin. *Front. Bioeng. Biotechnol.* 10. doi:10.3389/fbioe.2022.859255

Conflict of Interest: The authors declare that the research was conducted in the absence of any commercial or financial relationships that could be construed as a potential conflict of interest.

Publisher's Note: All claims expressed in this article are solely those of the authors and do not necessarily represent those of their affiliated organizations, or those of the publisher, the editors and the reviewers. Any product that may be evaluated in this article, or claim that may be made by its manufacturer, is not guaranteed or endorsed by the publisher.

Copyright © 2022 Chen, Chen, Liu, Han, Chen and Wang. This is an open-access article distributed under the terms of the Creative Commons Attribution License (CC BY). The use, distribution or reproduction in other forums is permitted, provided the original author(s) and the copyright owner(s) are credited and that the original publication in this journal is cited, in accordance with accepted academic practice. No use, distribution or reproduction is permitted which does not comply with these terms.

frontiers in Bioengineering and Biotechnology

ORIGINAL RESEARCH
published: 30 March 2021
doi: 10.3389/fbioe.2021.650376

Mesenchymal Stem Cells-Derived Exosomes as Dexamethasone Delivery Vehicles for Autoimmune Hepatitis Therapy

Jiawei Zhao[1,2†], Yue Li[1,3†], Rongrong Jia[1], Jinghui Wang[1], Min Shi[1] and Yugang Wang[1]**

[1] Department of Gastroenterology, Tongren Hospital, Shanghai Jiao Tong University School of Medicine, Shanghai, China, [2] School of Medicine, Jiangsu University, Zhenjiang, China, [3] School of Medicine, Shanghai Jiao Tong University, Shanghai, China

OPEN ACCESS

Edited by:
Junqing Wang,
Sun Yat-sen University, China

Reviewed by:
Bobin Mi,
Huazhong University of Science and Technology, China
Chen Xu,
Shanghai Changzheng Hospital, China
Yongmin Yan,
Jiangsu University, China

***Correspondence:**
Min Shi
SM1790@shtrhospital.com
Yugang Wang
WYG0061@shtrhospital.com

†These authors have contributed equally to this work and share first authorship

Specialty section:
This article was submitted to Biomaterials, a section of the journal Frontiers in Bioengineering and Biotechnology

Received: 07 January 2021
Accepted: 01 March 2021
Published: 30 March 2021

Citation:
Zhao J, Li Y, Jia R, Wang J, Shi M and Wang Y (2021) Mesenchymal Stem Cells-Derived Exosomes as Dexamethasone Delivery Vehicles for Autoimmune Hepatitis Therapy. Front. Bioeng. Biotechnol. 9:650376. doi: 10.3389/fbioe.2021.650376

Exosomes (Exos) are nanosized vesicles (around 100 nm) that recently serve as a promising drug carrier with high biocompatibility and low immunogenicity. Previous studies showed that Exos secreted from mesenchymal stem cells (MSCs) provide protection for concanavalin A (Con A)-induced liver injury. In this study, the protective effect of Exos is confirmed, and dexamethasone (DEX)-incorporated Exos named Exo@DEX are prepared. It is then investigated whether Exo@DEX can function more efficiently compared to free drugs and naive Exos in a Con A-induced autoimmune hepatitis (AIH) mouse model. The results show that Exo@DEX efficiently improves the accumulation of DEX in AIH in the liver. These data suggest that Exo@DEX is a promising drug carrier for AIH and could have applications in other diseases.

Keywords: mesenchymal stem cells, exosomes, dexamethasone, autoimmune hepatitis, delivery

INTRODUCTION

Autoimmune hepatitis (AIH) is characterized by a mild increase in serum transaminase concurrent with increased immunoglobulin G and circulating autoantibodies (Strassburg, 2010). Currently, the first-line therapy for AIH is prednisone combined with azathioprine. However, high doses of steroids could easily spread into the whole body and contribute to AIH patients abandoning such treatment due to drug complications (such as Cushing's syndrome, hypertension, peptic ulcer, infection, and neurological symptoms) (Violatto et al., 2019). Furthermore, AIH could easily be exacerbated into liver fibrosis or even cirrhosis of the liver if the disease is badly controlled and that is when liver transplantation becomes a necessity. An alternative could be the drug "navigating" destination, the injured liver, and the systematic side effects could be extensively reduced (Carbone and Neuberger, 2013). Nowadays, tissue-targeted therapies are achieved through several drug delivery systems, including nanosphere (Liang et al., 2018), liposomes (Bartneck et al., 2015), mesoporous silicon (Chen et al., 2019), or gel (Wang et al., 2019), which are engineered to concentrate the drug at a specific tissue site. However, some artificially synthetic nanoparticles are still facing some problems, such as poor biocompatibility and biotoxicity.

Exosomes (Exos) are bilayer lipid vesicles naturally secreted by cells with a diameter of around 100 nm. At first, Exos were thought to be cell excretions and have no function, but several years later, they were found to be important materials for cell-to-cell communication (Bobrie et al., 2012; Tkach and Thery, 2016). In the last few decades, Exos have begun to hold great promise as a drug delivery vehicle for small-molecule drugs, nucleic acids, and specific proteins due to their high biocompatibility, low toxicity, and various biofunctions according to their parental cells. It

was worth noting that, reportedly, Exos would normally accumulate in the liver because of the preferential liver uptake, which is extremely beneficial for the treatment of liver diseases (Borrelli et al., 2018; Gudbergsson et al., 2019). All these unique characteristics make Exos a promising drug delivery vehicle for AIH treatment.

Mesenchymal stem cells (MSCs) have gained much attention in recent years due to their therapeutic effects in various diseases. These cells are called pluripotent stem cells that can differentiate into all kinds of functional cells under certain stimulation or conditions (Borrelli et al., 2018). It has been reported that resveratrol-treated MSCs can secret platelet (PLT)-derived growth factor-DD, which activates the signal-regulated kinase pathway in renal tubular cells and promotes angiogenesis in endothelial cells to repair the cisplatin-induced kidney injury (Zhang et al., 2018). When it comes to liver diseases, MSCs exert a multifunctional effect on liver regeneration by inhibiting hepatocyte apoptosis, reversing liver fibrosis, and reducing inflammation (Alfaifi et al., 2018). Furthermore, Exos derived from MSCs can inherit their therapeutic functions. For example, Exos derived from placenta MSCs could increase utrophin expression and decrease inflammation and fibrosis in Duchenne muscular dystrophy (Bier et al., 2018). Moreover, Exos from MSCs can suppress concanavalin A (Con A)-induced liver injury (Tamura et al., 2016) and accelerate the recovery of hindlimb ischemia by activating VEGF receptors (Gangadaran et al., 2017).

Based on the above, we developed a liver-targeting Exo@DEX delivery system by loading dexamethasone (DEX) into MSC-derived Exos for the treatment of Con A-induced AIH (Bartneck et al., 2015). Our expectation is to combine the therapeutic features of MSC-Exos with the potent anti-inflammation drug DEX to achieve a synergistic treatment toward AIH, hopefully along with other liver diseases. More than that, our work also implies the application of Exos as a promising drug carrier.

MATERIALS AND METHODS

Cell Culture

Mesenchymal stem cells were extracted and purified from mouse bone marrow-derived all-nucleated cells. Non-adherent cells were removed after 72 h, and attached cells were maintained for 16 days in α-Minimum Essential Media (α-MEM, Gibco) supplemented with 2 mM L-glutamine and 55 μM 2-mercaptoethanol. The human liver cell line L02 was cultured in Roswell Park Memorial Institute 1640 media (RPMI1640, Gibco), and the murine macrophage cell line RAW264.7 was cultured in Dulbecco's modified Eagle's medium (DMEM, Gibco). All cells were cultured in media containing 10% fetal bovine serum (FBS, Gibco), (1%, v/v) penicillin, and (1%, v/v) streptomycin. Cell cultures were incubated in a 5% CO_2 incubator at 37°C.

Isolation and Purification of MSC-Exos

Mesenchymal stem cell-Exos were purified from a cell culture supernatant by ultracentrifugation as reported before (Théry et al., 2006). Briefly, MSC culture medium was collected when the cells were 80–90% confluent. The supernatant was centrifugated at 300 × *g* and 2,000 × *g* for 10 min to remove cells and dead cells, respectively. The supernatant was then centrifugated at 10,000 × *g* for 30 min to eliminate cell debris. The final supernatant is then ultracentrifuged at 100,000 × *g* for 1 h twice to pellet the Exos. The pellet was resuspended in a convenient volume of phosphate-buffered saline (PBS). Isolated Exos were either kept at 4°C for up to a week or stored at −80°C for further use.

Characterization of MSC-Exos

The expressions of CD47, HSP70, CD81, and TSG101 (Abcam) were evaluated by ProteinSimple Wes^{TM} Capillary Western Blot analyzer (PS-MK15, ProteinSimple). Antibodies were diluted in an antibody diluent with a 1:50 or 1:100 dilution (ProteinSimple kit). The morphology of Exos was identified by transmission electron microscopy (TEM) (Hitachi HT7700, Tokyo, Japan). The size distribution and zeta potential of Exos were determined by dynamic light scattering (DLS) and nanoparticle tracking analysis (NTA). Total protein of Exos was quantified using the bicinchoninic acid (BCA) assay kit (Thermo Fisher).

Drug Encapsulation

Dexamethasone was encapsuled in Exos using a sonication method reported before (Wan et al., 2017). Briefly, 50 μg of DEX was mixed with 50 μg of Exos at a 10 mL total volume at room temperature for 30 min followed by sonication in a water bath sonicator (KQ-300DE) with the following settings: 40% amplitude, 3 cycles of 15 s on/off for 1.5 min with a 2-min cooling period between each cycle. After sonication, the mixture was incubated at 37°C for 1 h and further ultra-filtrated three times to remove excess free drugs.

For the analysis of the amount of DEX incorporated in Exos, high-performance liquid chromatography (HPLC) was carried out (Agilent 1200). Separation was performed with a C18 column (150 × 4.6 mm, Phenomenex, United States). The elution solvents were water containing 0.05% acetic acid (phase A) and acetonitrile (phase B). The absorbance wavelength was set at 240 nm.

Internalization of MSC-Exos *in vitro*

Exosomes were labeled with 1,1'-dioctadecyl-3,3,3',3'-tetramethylindodicarbocyanine perchlorate (DiD, Fanbo Biochemicals) according to the manufacturer's instructions, and the excess free dye was removed with Exosome Spin Columns (Thermo Fisher). L02 and RAW264.7 cells were incubated with labeled Exos for 1, 2, or 4 h. For fluorescence microscopy, the cells were fixed with 4% paraformaldehyde at room temperature for 30 min. The cell membrane was stained with Alexa Fluor 488 phalloidin (Thermo Fisher), and the cell nucleus was stained with 4',6-diamidino-2-phenylindole (DAPI, Solarbio). Fluorescence microscopy images were obtained by confocal laser scanning microscopy (CLSM, Nikon A1R). For flow cytometry, the cells were trypsinized, washed three times, and further resuspended in PBS. The fluorescence intensity of 10,000 cells was recorded by CytoFLEX LX (Backman, United States) and analyzed by FlowJo.

Cell Proliferation Assay

L02 cells and RAW264.7 cells were seeded into a 96-well cell culture plate at a density of 10,000 cells per well for 24 h before any treatment. Afterward, the cell culture media were replaced with fresh ones containing DEX or Exo@DEX with an equivalent DEX dose at different concentrations (1, 5, and 10 μg/mL). After 24 h of incubation, the cell culture media were replaced with CCK-8 (Solarbio) solutions, and the cells were incubated for another 1 h in an incubator. The absorbance of each well was measured by a microplate reader (Infinite M200, Tecan) at 450 nm. The viability of L02 and RAW264.7 cells was then calculated according to the instructions.

For cell apoptosis experiments, L02 cells and RAW264.7 cells were seeded into a 24-well cell culture plate at a density of 25,000 cells per well for 24 h before any treatment. Afterward, the cell culture media were changed with Exo-free media or media containing DEX or Exo@DEX with an equivalent DEX dose at 10 μg/mL. After 24 h of incubation, cells were trypsinized and washed three times. Finally, the cells were resuspended in 1 mL binding buffer and stained in the dark by 5 μL annexin V–fluorescein isothiocyanate (FITC) and propidium iodide (PI) for 10 and 5 min, respectively, according to the manufacturers' instructions. Cell apoptosis was immediately examined by flow cytometry.

Supernatant Cytokine Detection

RAW264.7 cells were stimulated by lipopolysaccharide (LPS) (100 ng/mL) for 24 h to obtain pro-inflammatory macrophages and subsequently underwent thorough washing to remove LPS. Then, fresh media containing DEX (10 μg/mL), Exo (100 μg/mL), or Exo@DEX (100 μg/mL) were added. After 24 h of incubation, the cell supernatant was collected, and the cytokines (TNF-α, IFN-γ, and IL-1β) of the supernatant were detected by enzyme-linked immunosorbent assay (ELISA) kits.

Animal Models

Six- to 8-week-old BALB/c mice were purchased from Beijing Vital River Laboratory Animal Technology Co., Ltd. Mice were acclimated for 7 days before any treatment. For the construction of an AIH mice model, Con A (Solarbio) was intravenously injected via the tail vein at a dose of 20 mg/kg of body weight. Exo (5 mg/kg), DEX (0.5 mg/kg), Exo@DEX (5 mg/kg), and control solutions were injected intravenously in a total volume of 100 μL right after Con A injection.

In vivo and *ex vivo* Distribution of MSC-Exos

Exosomes were labeled with 1,1'-dioctadecyl-3,3,3',3'-tetra methylindotricarbocyanine iodide (DiR, Fanbo Biochemicals) according to the manufacturer's instructions, and the excess free dye was removed with Exosome Spin Columns. BALB/c mice (n = 3) were injected with 100 μL of DiR-labeled Exos through the tail vein. The fluorescence images of the mouse body were recorded by the KODAK *in vivo* imaging system FX Pro (KODAK, United States) at different time points.

For *ex vivo* imaging, mice were treated with DiD (Fanbo Biochemicals)-labeled Exos and were sacrificed at 2 h after the injection. The liver, kidneys, spleen, lung, and heart were collected and scanned for *ex vivo* imaging. Particularly, the livers were either grinded into single-cell suspension and filtered using a 60-μm mesh for flow cytometry or fixed with 4% paraformaldehyde for frozen sections. Frozen liver tissues were cut into 10-μm sections and further incubated with F4/80 antibody (Abcam). F4/80-positive cells were stained with FITC, and cell nuclei were stained with DAPI. Fluorescence images were obtained by CLSM.

For the analysis of the amount of DEX delivered to the liver, HPLC was carried out. All samples were treated as reported before (Violatto et al., 2019). Briefly, livers were collected and homogenized with methanol and acetonitrile, stirred for 30 min. Then water was added, and homogenization was repeated. Samples were further centrifuged at 10,000 × g for 10 min at 4°C. The supernatant was further cleaned up with solid-phase extraction using Sep-Pak C18 1-cc Vac cartridges, conditioned before use with 1 mL of methanol.

Liver Enzyme and Histology

Blood was collected 8 h after the injection to detect serum alanine aminotransferase (ALT) and aspartate aminotransferase (AST) levels. Livers were also collected, fixed in 4% paraformaldehyde, and embedded in paraffin for histological analysis.

Liver Tissue Cytokine Measurement

Obtained liver tissues were cut into pieces and homogenated on ice with an ultrasonic probe in radioimmunoprecipitation (RIPA) buffer (Solarbio) with 1 mM protein inhibitor. Protein concentrations were measured using a BCA assay kit. Lysates were centrifugated at 10,000 × g for 5 min at 4°C according to the instructions, and the suspension was collected and stored in −80°C for further use. Before tests, a pre-experiment was conducted to optimize the concentration. ELISAs were conducted to measure the following cytokines according to the instructions (mouse TNF-α ELISA kit, mouse IFN-γ ELISA kit, mouse IL-1β ELISA kit, mouse IL-6 ELISA kit, mouse IL-12 ELISA kit, and mouse myeloperoxidase ELISA kit, Solarbio).

Macrophage Apoptosis in the Liver

Obtained liver tissues were cut into pieces and grinded into single-cell suspension. Cells were primarily treated with red blood cell (RBC) lysing regents to remove RBCs. Then, the cells were labeled with F4/80 for gating of macrophages. Finally, the cells were resuspended in 1 mL of binding buffer and stained in the dark by 5 μL annexin V–FITC and PI for 10 and 5 min, respectively, according to the manufacturers' instructions. Cell apoptosis was immediately examined by flow cytometry.

Toxicity Assessment

Exo@DEX (5 mg/kg) or PBS was intravenously injected into AIH mice. Blood samples and organs were collected from the two groups 24 h after treatment. Hematoxylin-and-eosin (H&E) staining of each organ was conducted to observe the

histological effects on the heart, liver, spleen, lungs, and kidneys of mice. Anticoagulant blood was used to perform a routine blood test. Untreated blood was put on a stand for 2 h and centrifugated at 4°C for 10 min to obtain the serum. The obtained serum was used to detect blood parameters using an automatic biochemical analyzer.

RESULTS

Fabrication and Characterization of Exo@DEX

Exosomes were purified from cell culture supernatants of MSCs and were further loaded with DEX by water bath sonication. The morphology of both Exos and Exo@DEX was observed by TEM (**Figures 1A,B**). The size distribution and zeta potential of Exos and Exo@DEX were detected by both DLS and NTA. Naive Exos and DEX-loaded Exos both had a uniform size distribution, with a mean diameter of 120 and 150 nm, respectively (**Figure 1C**). The zeta potential of the two nanoparticles changed from around −10 to −6 mV due to the successful loading of DEX (**Figure 1D**). NTA showed a scattered distribution of the two nanoparticles during the detection progress. Movies and screenshots recording the movement of nanoparticles were provided (**Figure 1E** and **Supplementary Movies 1, 2**). The size distribution and zeta potential of both Exos were exhibited as scatter plots (**Figure 1F**). The size distribution was similar to that of DLS, while the zeta potential was more negative compared to the results of DLS, which may contribute to the different detection modes of the two equipment. However, the change of zeta potential was consistent with DLS. The Exo@DEX was then stored at −80°C for further use. The size and zeta potential did not have an obvious change (**Supplementary Figure 1**). Next, immunoblotting further verified that Exos and Exo@DEX expressed Exo markers (CD47, HSP70, CD81, and TSG101). It was shown that the drug loading did not alter the surface proteins of Exos (**Figure 1G** and **Supplementary Figure 2**). Importantly, we investigated the characteristics of the tenth-generation MSCs via flow cytometry. In brief, the expression of CD29, Sca-1, and CD44, positive markers of MSCs, was detected to be higher than 95%. On the other hand, the expression of the negative surface markers, CD31 and CD117, was determined by flow cytometry to be lower than 5% (**Figure 1H** and **Supplementary Figure 3**). The amount of DEX incorporated into Exos was measured by HPLC with the calculated DEX incorporation rate to be around 10% (**Supplementary Figure 4**).

Cellular Internalization of Exo@DEX and Its Effect on Macrophage *in vitro*

The liver plays an essential role in human life. It is mostly composed of hepatocytes, around 80%, and other non-parenchymal cells, including hepatic stellate cells, Kupffer cells, and sinusoidal endothelial cells. Kupffer cells originate from macrophages and are involved in phagocytosis. In addition, Kupffer cells are fundamental in the process of innate immune and inflammatory responses. They can secrete several cytokines during the occurrence of inflammation and may even contribute to the acceleration of diseases. Thus, inhibition of macrophages could be considered as an underlying possibility to ameliorate the symptoms of inflammation activity. Steroids are the currently widely used therapy for the treatment of AIH in clinical settings. However, most patients may not be able to endure the severe side effects that steroid drugs bring. As a result, novel methods need to be explored to improve the targeting ability of drugs toward livers.

We used CLSM to test the effects of co-culturing Exo@DEX with two different types of cells *in vitro* and whether Exos can be internalized into these cells. We co-cultured Exo@DEX with macrophage cell line RAW264.7 cells and liver cell line L02 cells. After 0, 1, 2, and 4 h of co-incubation, a large number of Exo@DEX emitting red fluorescence were internalized into RAW264.7 macrophages, while L02 liver cells only took up fewer Exo@DEX than macrophages (**Figure 2A** and **Supplementary Figure 5**). Cellular internalization was also measured via a flow cytometry. Fluorescence intensity of RAW 264.7 cells increased obviously in a time-dependent way and had a higher level for Exo@DEX than the uptake level by L02 cells (**Figure 2B**).

Furthermore, to test the drug effect on the two cell lines, cells were treated with both free DEX and the Exo@DEX in a dose-dependent way (0–10 μg/mL) for 24 h. A CCK-8 cell proliferation assay was performed to examine the cell viability of the two cell types. After 24 h of co-incubation, the cell viability of RAW 264.7 macrophages was suppressed at a concentration of 10 μg/mL of Exo@DEX, while that of L02 cells was barely influenced at any concentration (**Figure 2C**). Once DEX gets inside the cell and further combines with corticosteroid receptors in the cytoplasm and nucleus, a variety of inflammatory genes and cytokines would be dramatically suppressed. To explore the mechanism of cell death induced by DEX, an annexin V-and-PI staining was performed to detect the cell apoptosis level of both cells after 24 h of co-incubation through a flow cytometry. In accordance with the cell viability test, the Exo@DEX group showed higher early and late apoptosis levels than the free drug in an equivalent dose of DEX, while L02 cells were not apparently affected (**Figure 2D**), possibly due to a lower internalization amount. We also measured the production of inflammatory cytokines, including TNF-α, IFN-γ, and IL-1β in the culture supernatants. Treatments containing DEX, Exo, and Exo@DEX efficiently reduced the production of TNF-α, IFN-γ, and IL-1β (**Supplementary Figure 6**).

Exo@DEX Concentrate in the Liver Parenchyma

One of the main purposes for the construction of Exo@DEX is to increase the accumulation of the small-molecule drug DEX in liver tissues. The biodistribution of Exo and Exo@DEX after intravenous (i.v.) administration was examined *in vivo* to detect their targeting ability. Exo and Exo@DEX were both labeled with DiR to allow tracking at different time points by an *in vivo* imaging system. The signal related to the DiR-labeled Exo and Exo@DEX was clearly observed through the imaging system and remained at a high level for 24 h (**Figure 3A**). Both Exo and

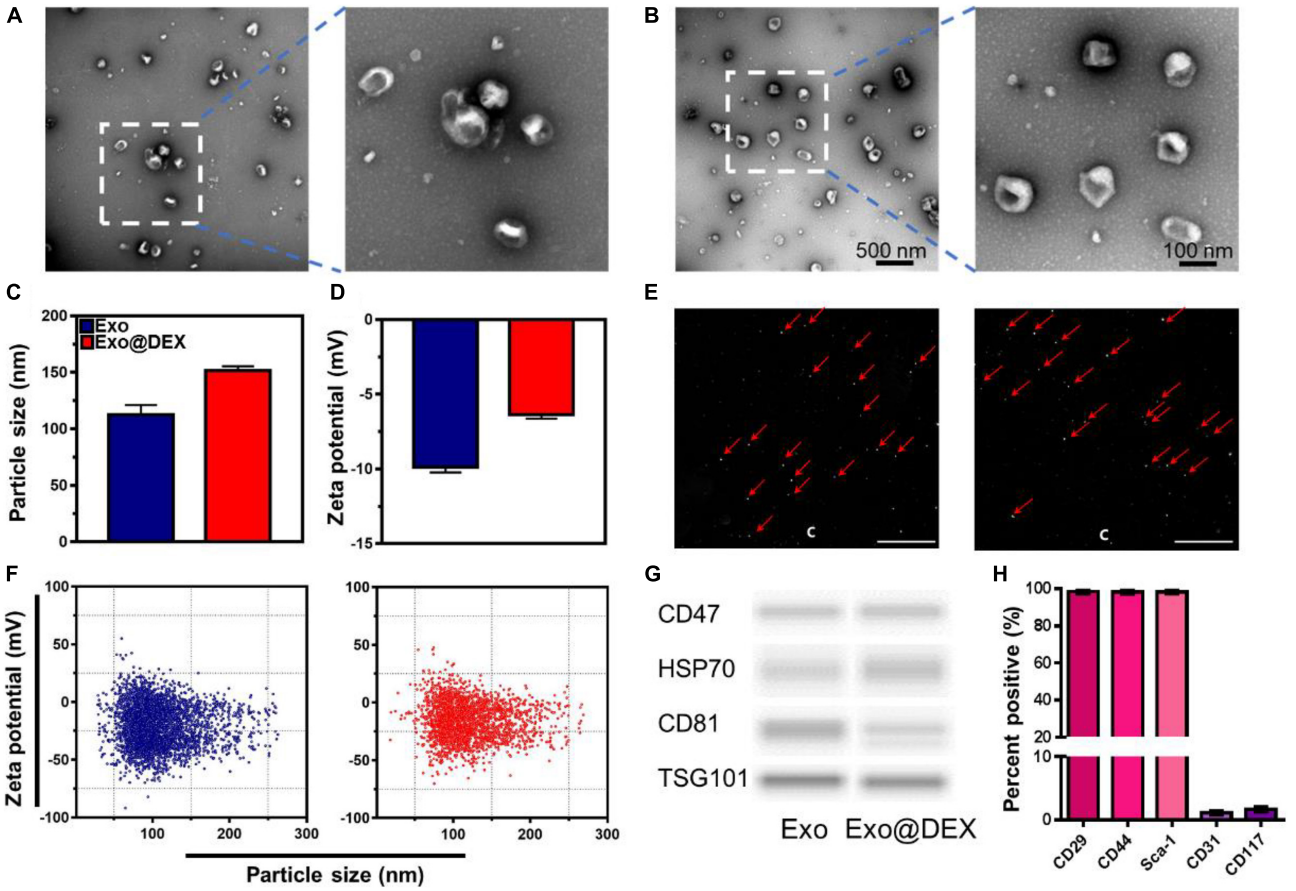

FIGURE 1 | Characterization of Exo and Exo@DEX. **(A)** TEM imaging of Exos and **(B)** DEX-loaded Exos stained with uranyl acetate. **(C)** The size distribution of Exos and Exo@DEX by DLS. **(D)** The zeta potential of Exos and Exo@DEX by DLS. **(E)** Screenshots of Exo and Exo@DEX detection by NTA. **(F)** The size distribution and zeta potential of Exos and Exo@DEX by NTA. **(G)** Western blot analysis of Exos and Exo@DEX. CD47, HSP70, CD81, and TSG101 are markers for Exos. **(H)** Quantitative analysis of MSC markers of CD29, CD44, Sca-1, CD31, and CD117.

Exo@DEX had a similar performance during a 24 h observation, indicating that the encapsulation did not affect the targeting ability of Exos. The fluorescence peak appeared at 2 h after i.v. administration (**Figure 3B**). *Ex vivo* imaging was performed 2 h after i.v. administration, and the fluorescence signal was detected in all collected organs (**Figure 3C**). The fluorescence signal was mainly discovered in the liver and spleen and was about three times higher than that in the heart, lung, and kidney (**Figure 3D**).

In addition, flow cytometry and frozen sections were used to further observe the distribution of Exos and Exo@DEX in livers. In these cases, DiR was replaced with DiD for a better imaging performance. Livers after i.v. administration were extracted and grinded into cell suspension for flow cytometry. As shown in **Figure 3E**, livers with DiD-labeled Exo and Exo@DEX treatment exhibited high fluorescence signals compared to Exos without any dye label. At the same time, collected liver tissues were preserved in 4% paraformaldehyde for a frozen section. DAPI staining was used to observe the nuclei, and a red signal represented the DiD-labeled Exo and Exo@DEX in liver tissues (**Figure 3F**). Furthermore, when hepatic macrophages were visualized by immunofluorescence staining of F4/80, most DiD-labeled Exo@DEX were localized with F4/80-positive cells (**Supplementary Figure 7**). For higher resolution, livers were extracted to analyze the amount of DEX delivered to them. Compared to free DEX, Exo@DEX was able to deliver about 2.6 times as much DEX to the liver (**Supplementary Figure 8**).

The data above were extremely important in terms of distribution because the drug-loaded Exos enable the accumulation of DEX in liver tissues and reduce free drugs in blood circulation. The underlying side effects of free DEX on unwanted organs therefore may not occur in the body of treated subjects.

Exo@DEX Therapy Protects Liver Functions in Con A-Induced Liver Injury

Hematoxylin-and-eosin tissue sections demonstrated that Exo@DEX therapy protected the structural integrity of the liver tissue. A healthy group with or without treatment showed no abnormality on the hepatic lobule and portal area, while obvious tissue structure disorders and severe cell necrosis could be seen in the PBS group, which was indicated by a yellow dashed line.

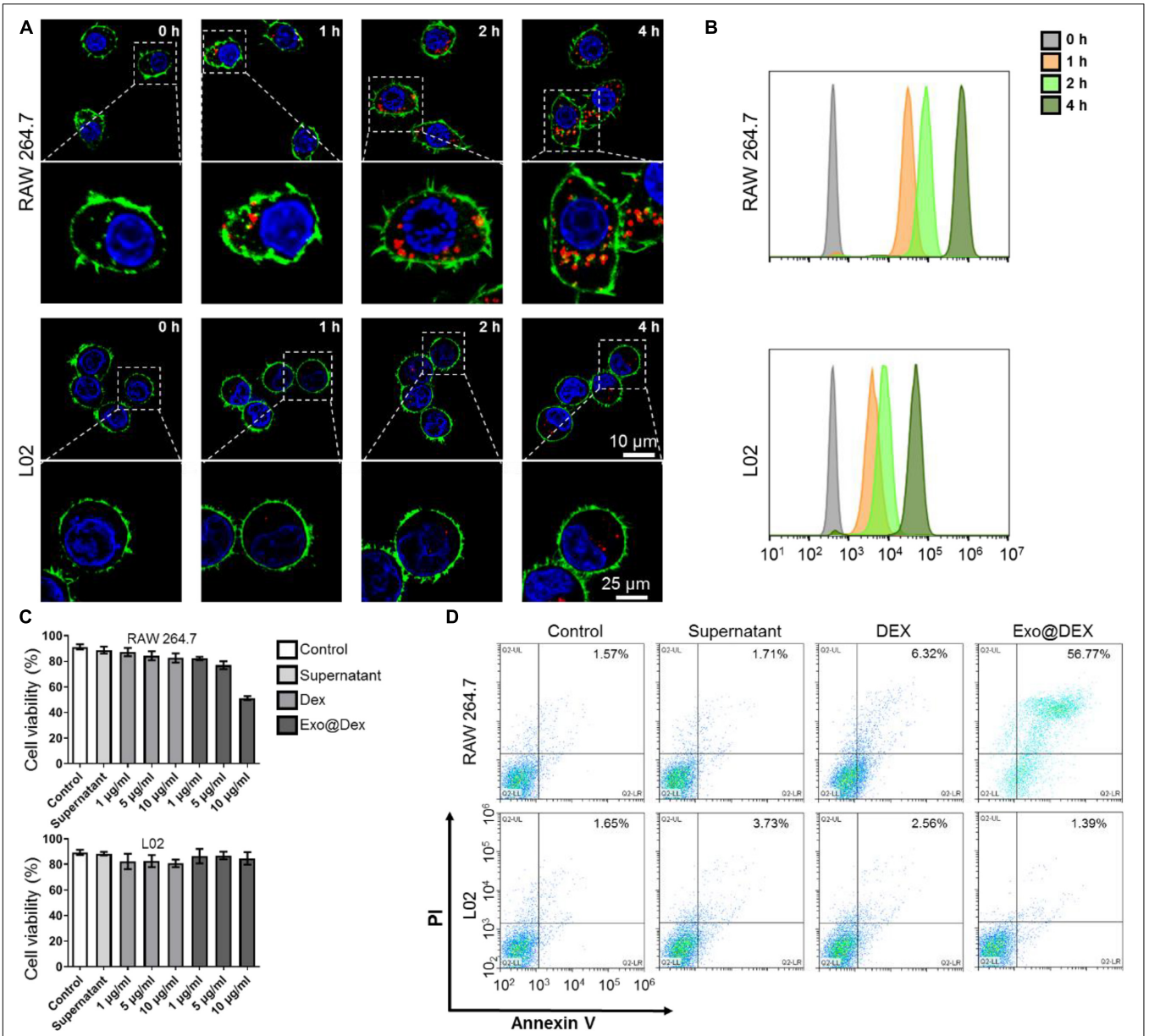

FIGURE 2 | Cellular internalization of Exo@DEX and its effect on macrophage *in vitro*. **(A)** Representative fluorescence images of Exo uptake by RAW264.7 macrophages and L02 liver cells *in vitro* in a time-dependent way (images were enlarged, indicated by a white dotted box). Nuclei were stained with DAPI (blue), the cell membrane was stained with phalloidin (green), and Exo@DEX was stained with DiD (red). **(B)** Flow cytometry assay of RAW264.7 and L02 cells incubated with DiD-labeled Exo@DEX. **(C)** CCK-8 analysis of RAW264.7 and L02 cells. Cells were incubated with Exo-free supernatant (Supernatant), non-exosomal DEX, or exosomal DEX (Exo@DEX) for 24 h. **(D)** Flow cytometry analysis of annexin V-and-PI staining of RAW264.7 and L02 cells incubated with Supernatant, DEX, or Exo@DEX.

Yellow and black arrows showed steatosis and inflammatory cell infiltration, respectively. DEX or Exo administration contributed to a certain extent to the protection of the liver structure and cell viability where mild damage indicated by steatosis could be seen. Exo@DEX treatment contributed to the recovery of tissue structure integrity, and few inflammation cells and little steatosis could be seen in this case (**Figure 4A**).

Alanine aminotransferase and AST are the two most used biomarkers for the analysis of liver functions. For the Con A-induced liver injury, the PBS group exhibited high ALT and AST levels. Compared to the PBS group, administration of DEX or Exo contributed to a certain degree to liver function protection. More importantly, injection of Exo@DEX resulted in a better therapeutic effect than the DEX or Exo group, mainly due to the targeting ability to the liver, suggesting the anti-inflammation role that Exo@DEX plays in Con A-induced liver injury (**Figures 4B,C**).

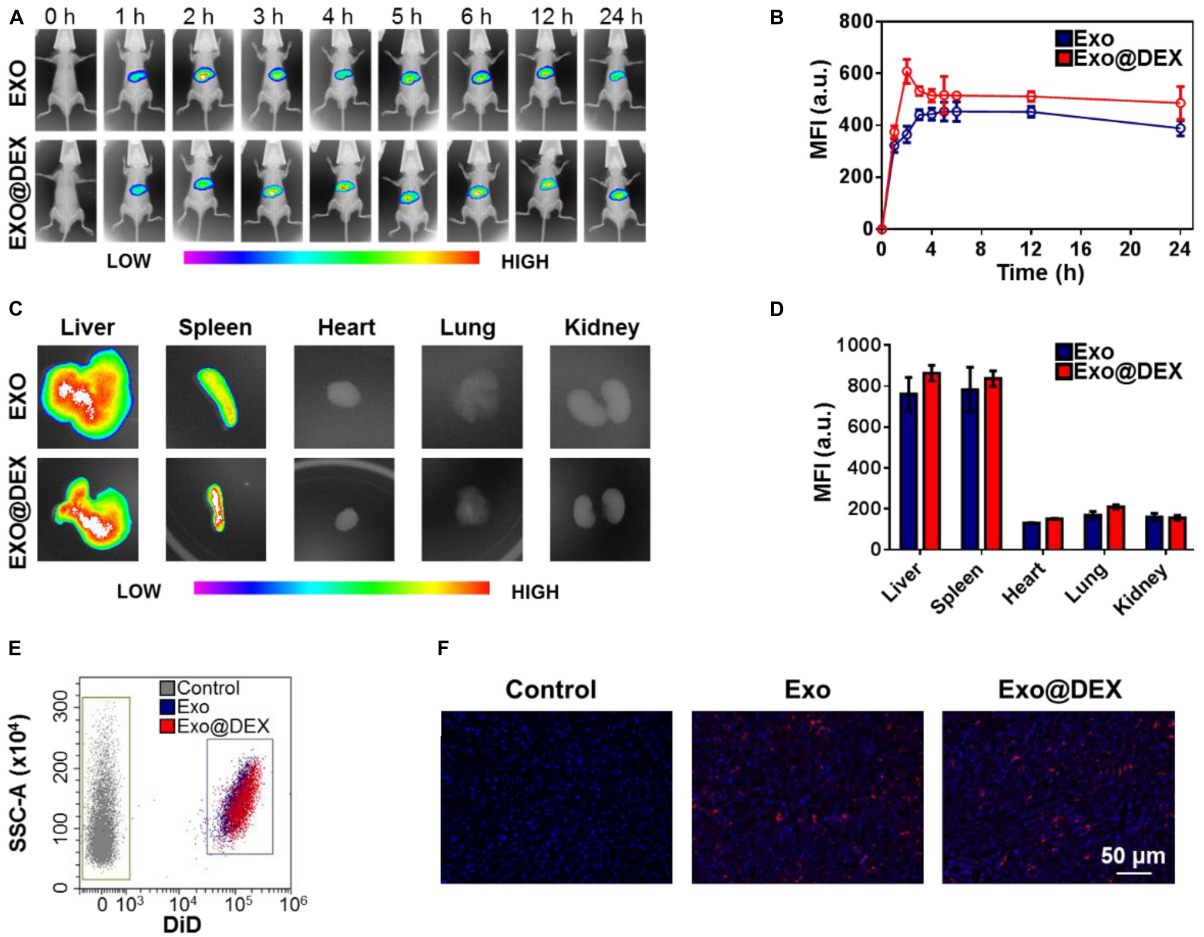

FIGURE 3 | Biodistribution of Exo@DEX *in vivo* and *ex vivo*. **(A)** *In vivo* fluorescence signal of mice treated intravenously with DiR-labeled Exo or Exo@DEX and imaged 1, 2, 3, 4, 5, 6, 12, and 24 h after the treatment. **(B)** Quantitative analysis of *in vivo* imaging. **(C)** *Ex vivo* fluorescence signal of collected organs from mice sacrificed 2 h after treatment. **(D)** Quantitative analysis of *ex vivo* imaging. **(E)** Flow cytometry analysis of homogenated liver tissues after DiD-labeled Exo or Exo@DEX treatment. **(F)** Liver tissues excised 2 h after treatment with DiD-labeled Exo@DEX or PBS, stained with DAPI, and visualized by confocal microscopy.

Importantly, we grinded liver tissues into single-cell suspension and evaluated the apoptosis of macrophages. Macrophages from mice treated with Exo@DEX showed a higher apoptotic level than free drugs (**Supplementary Figure 9**). To further demonstrate the therapeutic effects of Exo@DEX, we detected several inflammatory cytokines in liver tissues from each group, including TNF-α, INF-γ, IL-1β, IL-6, IL-12, and MPO. As shown in **Figure 5**, the cytokine levels of Exo@DEX were dramatically decreased compared to the elevated cytokine levels of the PBS group (**Figures 5A–F**).

Toxicity Study

In order to test the systematic toxicity that our treatment might have, healthy mice were given PBS or Exo@DEX to rule out potential side effects. All treatment did not contribute to any apparent signs of systematic toxicity. According to the H&E staining, no obvious tissue damage could be observed in the major organs (**Figure 6A**). We also confirmed that the above treatment did not cause any apparent hematologic abnormality because the levels of white blood cell (WBC), hemoglobin (Hb), RBC, and PLT were all within the normal range (**Figure 6B**). Meanwhile, levels of serum urea nitrogen (BUN) and ALT, AST, lactate dehydrogenase (LDH), and alkaline phosphatase (ALP), which are typical biomarkers for liver and kidney functions, were also examined, and no abnormality was observed (**Figure 6C**).

DISCUSSION

In this study, we constructed a drug-carrying Exo called Exo@DEX by loading the potent anti-inflammation drug DEX into MSC-Exos. The Exo@DEX exhibited effective protection against Con A-induced acute liver injury. There are advantages of the constructed nanoparticles. First, the size of Exo@DEX, around 100 nm, is bound to lead to long liver retention after tail vein injection. Second, the MSC-secreted Exos have preferable repair effects for injured tissues or organs. Third, the MSC-Exos possess great biocompatibility and low immunogenicity, making

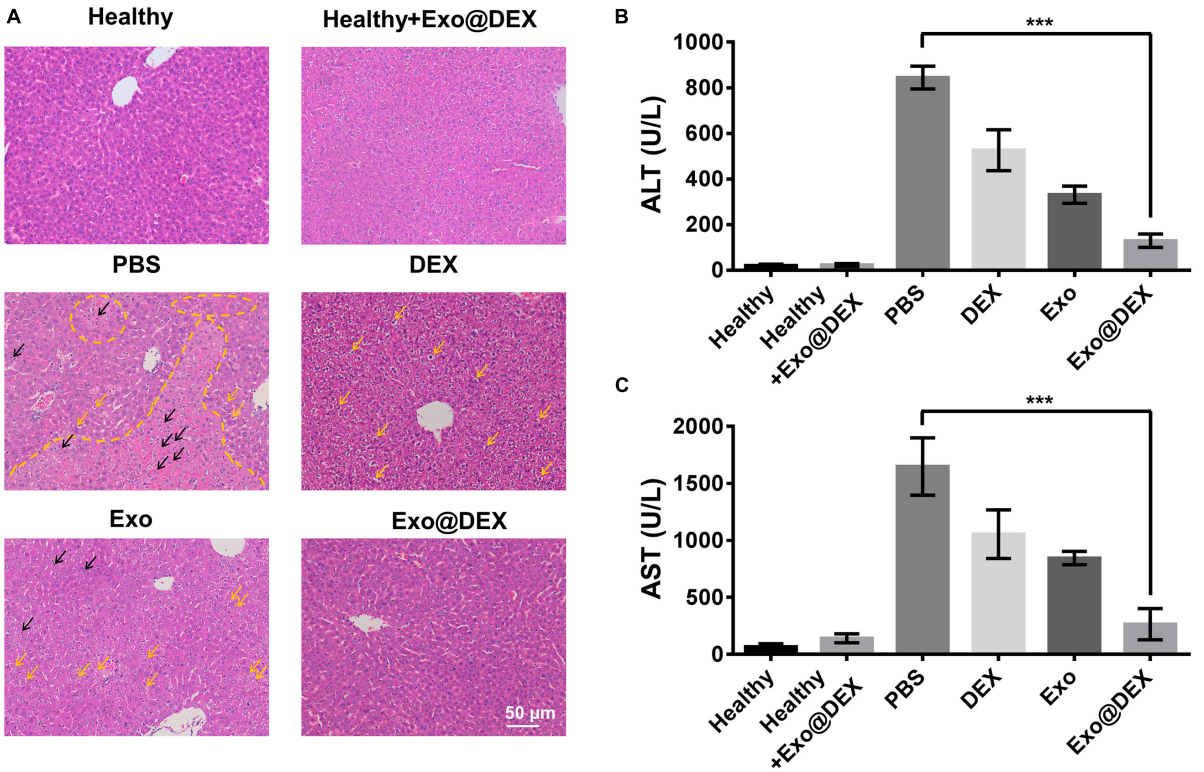

FIGURE 4 | *In vivo* treatment of the Con A-induced AIH mouse model. **(A)** H&E staining of liver sections from different groups 8 h after Con A injection and treatment. Black arrows indicate inflammatory cells. Yellow arrows indicate steatosis, suggesting mild damage to livers. The yellow line indicates large hemorrhage, suggesting severe damage. **(B,C)** Serum levels of ALT and AST were measured 8 h after Con A injection and treatment ($n = 5$ for each group). Data in **B** and **C** are presented as the mean ± SD and were assessed via one-way ANOVA (***$P < 0.001$).

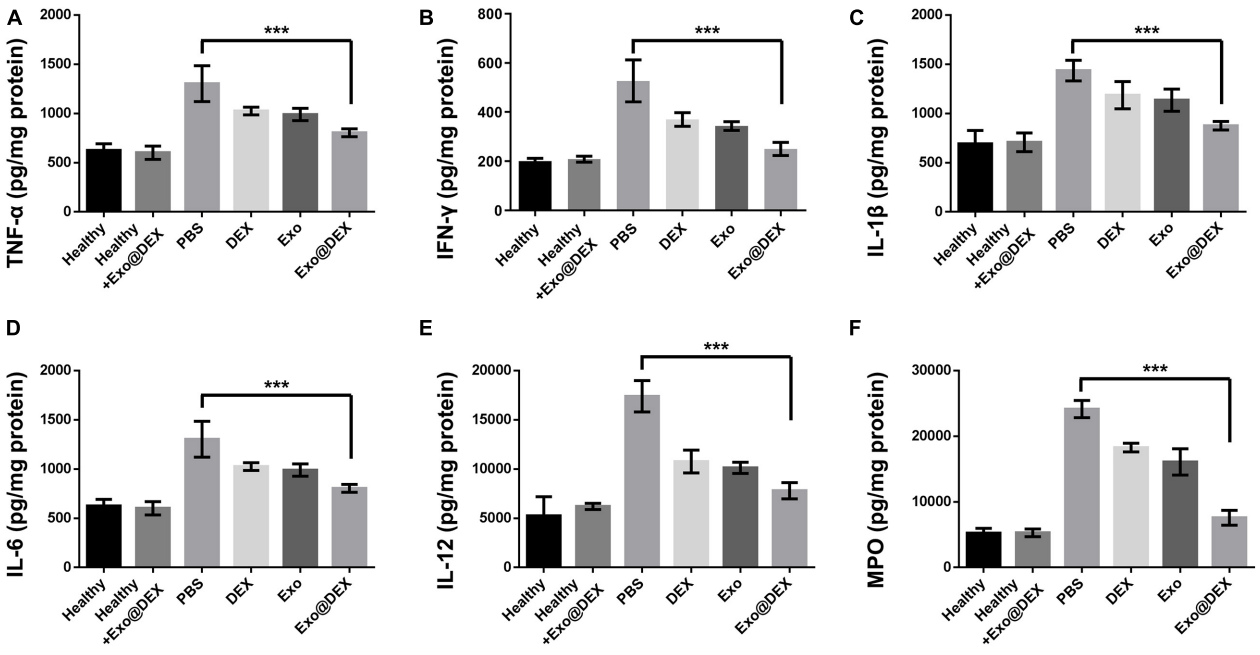

FIGURE 5 | Detection of cytokines in liver tissues. Cytokines of TNF-α **(A)**, INF-γ **(B)**, IL-1β **(C)**, IL-6 **(D)**, IL-12 **(E)**, and MPO **(F)** were measured in liver homogenates form each group ($n = 5$ for each group). Data are presented as the mean ± SD and were assessed via one-way ANOVA (***$P < 0.001$).

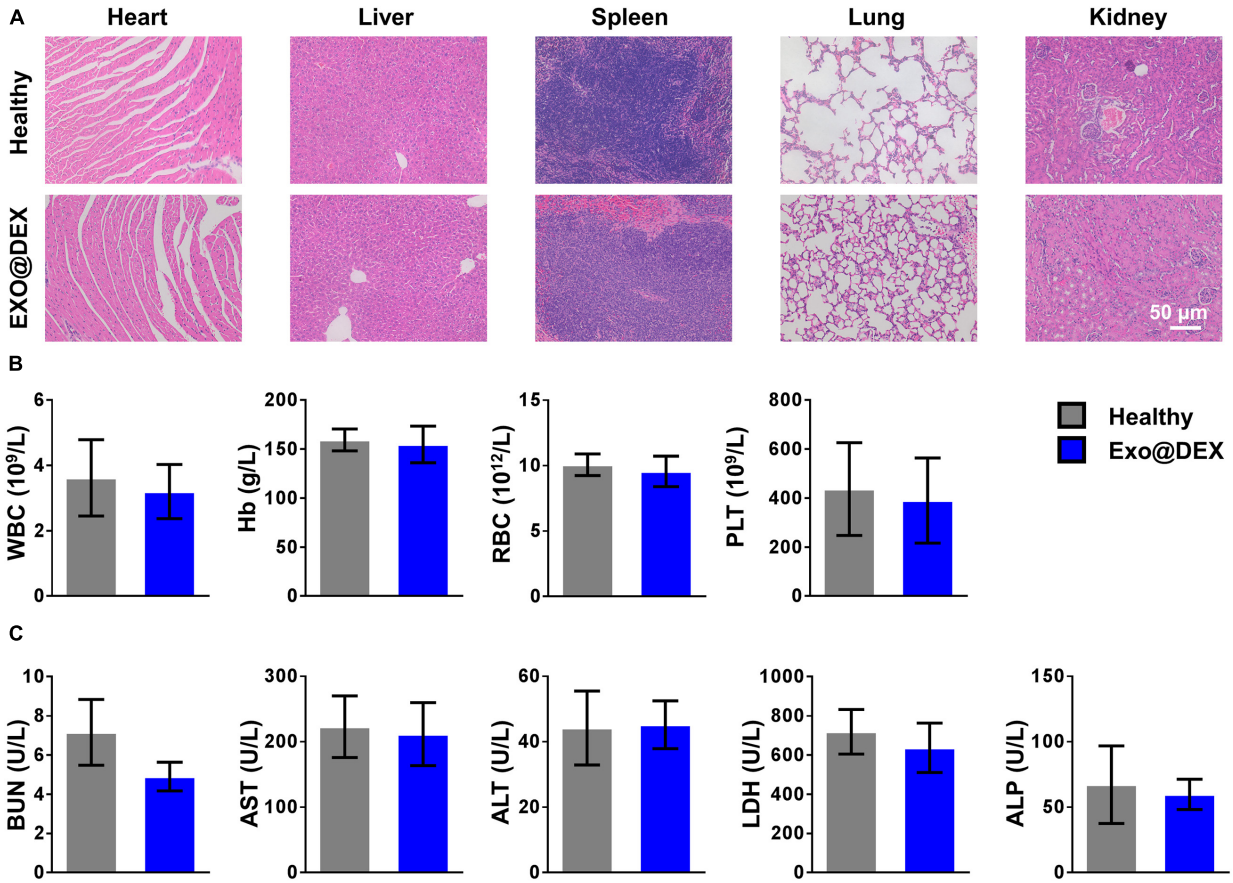

FIGURE 6 | *In vivo* toxicity assessment of Exo@DEX. **(A)** H&E staining of major organs (heart, liver, spleen, lungs, and kidneys). **(B)** Routine blood test of whole-blood parameters in mice treated with PBS or Exo@DEX. **(C)** Serum levels of liver and kidney function parameters in mice treated with PBS or Exo@DEX.

them good candidates as drug carriers. Fourth, DEX-loaded Exos can reduce the systemic bad effects on unwanted organs.

Exosome is a promising drug carrier with different properties according to its parental cells. As a vehicle, Exo has already been widely used in the treatment of cancers (Li and Nabet, 2019), including glioblastoma (Zhu et al., 2019), pancreatic cancer (Li et al., 2020), and breast cancer with lung metastasis (Xiong et al., 2019). All treatments exhibited effective inhibition in tumor volume and curative effect on the survival time of tumor-bearing mice. However, in the case of treatment for inflammatory diseases, limited research works have been done to explore the possibility for Exos to encapsulate other drugs other than chemotherapeutic drugs for cancer therapy. Our current study provides direct evidence that DEX-loaded Exos accumulate largely in the liver. Importantly, the Exo@DEX can be efficiently internalized into macrophages and have a prominent inhibition on macrophages. Among the inflammation-related cells, macrophages play a dominant role in the trigger and process of AIH, which therefore provided valid evidence for the possibility of our study (Wang et al., 2018; Violatto et al., 2019). However, more specific and deeper interactions between macrophages, liver, and DEX-loaded Exos should be explored to further explain the mechanism of how it works.

Data from the above studies suggested that Exo@DEX administration has a higher therapeutic effect over conventional DEX therapy. Furthermore, Exo@DEX may have a broader application in liver other than Con A-induced AIH. Hopefully, Exo@DEX could be used in other immune-related diseases including uveitis by intravitreous injection. In conclusion, our study provides strong evidence for the possibility of Exos as a drug vehicle in the treatment of AIH and, hopefully, a wider range of other diseases.

DATA AVAILABILITY STATEMENT

The original contributions presented in the study are included in the article/**Supplementary Material**, further inquiries can be directed to the corresponding author/s.

ETHICS STATEMENT

The Balb/c mice's experiments were approved by the Institutional Animal Care and Use Committees at the Institute of Process Engineering, Chinese Academy of Sciences. The Balb/c mice were

purchased from Vital River Laboratories (Beijing, China). The animals were maintained in accordance with the guidelines of Laboratory Animal Care. All the animals were acclimatized to the laboratory for at least 7 days before experiments.

AUTHOR CONTRIBUTIONS

YW and MS conceived the study. JZ, YL, and RJ collected and analyzed the data. JZ and YL wrote the manuscript. All authors revised the final manuscript.

FUNDING

This work was supported by grants from the National Natural Science Foundation of China (Grant Nos. 81871912 and 81970530) and Shanghai Municipal Health Bureau Key Disciplines Grant (Grant No. ZK2019C012).

SUPPLEMENTARY MATERIAL

The Supplementary Material for this article can be found online at: https://www.frontiersin.org/articles/10.3389/fbioe.2021.650376/full#supplementary-material

Supplementary Figure 1 | The size distribution and zeta potential of Exo@DEX. Size distribution and zeta potential of Exo@DEX measured by NTA before and after freezing at −80°C.

Supplementary Figure 2 | The original data of **Figure 1G**. Western blotting analysis of Exo and Exo@DEX by ProteinSimple Wes™ capillary western blot analyzer.

Supplementary Figure 3 | Characterization of MSCs. Flow cytometry analysis of MSC markers.

Supplementary Figure 4 | HPLC analysis of DEX. HPLC analysis of the incorporation of DEX into Exos.

Supplementary Figure 5 | Cellular internalization of Exo@DEX. Representative fluorescence images of Exo uptake by RAW264.7 macrophages and L02 liver cells *in vitro* (images were enlarged, indicated by a white dotted box). Cells were incubated with Exo-free supernatant (Supernatant) or DiD-labeled Exo@DEX (Exo@DEX).

Supplementary Figure 6 | Measurement of cytokines in supernatants. ELISA-based measurement of TNF-α, IFN-γ, and, IL-1β (pg/mL) in supernatants prepared from the culture medium after each different treatment ($n = 5$ for each group). Data are presented as the mean ± SD and were assessed via one-way ANOVA (****$P < 0.0001$).

Supplementary Figure 7 | Location of *in vivo* EXO@DEX in macrophages. Presence of Exo@DEX in the liver specimen and their localization in FITC-labeled F4/80-positive macrophages after the injection of DiD-labeled Exo@DEX (white arrow) (red: DiD-labeled Exo@DEX, green: FITC-labeled F4/80 macrophages, and blue: DAPI-labeled cell nuclei).

Supplementary Figure 8 | Levels of DEX measured in the liver. Mice were sacrificed 2 h after administration of DEX (0.5 mg/kg) or Exo@DEX (5 mg/kg). Levels of DEX in the liver were measured by HPLC. Data are presented as the mean ± SD and were assessed via two-tailed unpaired Student's *t*-test (***$P < 0.001$).

Supplementary Figure 9 | Flow cytometry analysis of macrophage apoptosis in the liver. **(A)** Gating of F4/80-positive cells. **(B)** Flow cytometry analysis of annexin V-and-PI staining of F4/80-positive cells from single-cell suspension of the liver.

REFERENCES

Alfaifi, M., Eom, Y. W., Newsome, P. N., and Baik, S. K. (2018). Mesenchymal stromal cell therapy for liver diseases. *J. Hepatol.* 68, 1272–1285. doi: 10.1016/j.jhep.2018.01.030

Bartneck, M., Scheyda, K. M., Warzecha, K. T., Rizzo, L. Y., Hittatiya, K., Luedde, T., et al. (2015). Fluorescent cell-traceable dexamethasone-loaded liposomes for the treatment of inflammatory liver diseases. *Biomaterials* 37, 367–382. doi: 10.1016/j.biomaterials.2014.10.030

Bier, A., Berenstein, P., Kronfeld, N., Morgoulis, D., Ziv-Av, A., Goldstein, H., et al. (2018). Placenta-derived mesenchymal stromal cells and their exosomes exert therapeutic effects in duchenne muscular dystrophy. *Biomaterials* 174, 67–78. doi: 10.1016/j.biomaterials.2018.04.055

Bobrie, A., Colombo, M., Krumeich, S., Raposo, G., and Thery, C. (2012). Diverse subpopulations of vesicles secreted by different intracellular mechanisms are present in exosome preparations obtained by differential ultracentrifugation. *J. Extracell Vesicles* 1:18397. doi: 10.3402/jev.v1i0.18397

Borrelli, D. A., Yankson, K., Shukla, N., Vilanilam, G., Ticer, T., and Wolfram, J. (2018). Extracellular vesicle therapeutics for liver disease. *J. Control Release* 273, 86–98. doi: 10.1016/j.jconrel.2018.01.022

Carbone, M., and Neuberger, J. M. (2013). Autoimmune liver disease, autoimmunity and liver transplantation. *J. Hepatol.* 60, 210–223. doi: 10.1016/j.jhep.2013.09.020

Chen, L., Zhou, L. L., Wang, C. H., Han, Y., Lu, Y. L., Liu, J., et al. (2019). Tumor-targeted drug and cpg delivery system for phototherapy and docetaxel-enhanced immunotherapy with polarization toward m1-type macrophages on triple negative breast cancers. *Adv. Mater.* 31:e1904997. doi: 10.1002/adma.201904997

Gangadaran, P., Rajendran, R. L., Lee, H. W., Kalimuthu, S., Hong, C. M., Jeong, S. Y., et al. (2017). Extracellular vesicles from mesenchymal stem cells activates vegf receptors and accelerates recovery of hindlimb ischemia. *J. Control Release* 264, 112–126. doi: 10.1016/j.jconrel.2017.08.022

Gudbergsson, J. M., Jnsson, K., Simonsen, J. B., and Johnsen, K. B. (2019). Systematic review of targeted extracellular vesicles for drug delivery-considerations on methodological and biological heterogeneity. *J. Control Release* 306, 108–120. doi: 10.1016/j.jconrel.2019.06.006

Li, I., and Nabet, B. Y. (2019). Exosomes in the tumor microenvironment as mediators of cancer therapy resistance. *Mol. Cancer* 18:32. doi: 10.1186/s12943-019-0975-5

Li, Y. J., Wu, J. Y., Wang, J. M., Hu, X. B., Cai, J. X., and Xiang, D. X. (2020). Gemcitabine loaded autologous exosomes for effective and safe chemotherapy of pancreatic cancer. *Acta Biomater.* 101, 519–530. doi: 10.1016/j.actbio.2019.10.022

Liang, H. X., Huang, K., Su, T., Li, Z. H., Hu, S. Q., Dinh, P. U., et al. (2018). Mesenchymal stem cell/red blood cell-inspired nanoparticle therapy in mice with carbon tetrachloride-induced acute liver failure. *ACS Nano* 12, 6536–6544. doi: 10.1021/acsnano.8b00553

Strassburg, C. P. (2010). Autoimmune hepatitis. *Best Pract. Res. Clin. Gastroenterol.* 24, 667–682. doi: 10.1016/j.bpg.2010.07.011

Tamura, R., Uemoto, S., and Tabata, Y. (2016). Immunosuppressive effect of mesenchymal stem cell-derived exosomes on a concanavalin a-induced liver injury model. *Inflamm. Regen.* 36:26. doi: 10.1186/s41232-016-0030-5

Théry, C., Amigorena, S., Raposo, G., and Clayton, A. (2006). Isolation and characterization of exosomes from cell culture supernatants and biological fluids. *Curr. Protoc. Cell Biol.* 30, 3.22.1–3.22.29. doi: 10.1002/0471143030.cb0322s30

Tkach, M., and Thery, C. (2016). Communication by extracellular vesicles: where we are and where we need to go. *Cell* 164, 1226–1232. doi: 10.1016/j.cell.2016.01.043

Violatto, M. B., Casarin, E., Talamini, L., Russo, L., Baldan, S., Tondello, C., et al. (2019). Dexamethasone conjugation to biodegradable avidin-nucleic-acid-nano-assemblies promotes selective liver targeting and improves therapeutic efficacy in an autoimmune hepatitis murine model. *ACS Nano* 13, 4410–4423. doi: 10.1021/acsnano.8b09655

Wan, Y., Wang, L., Zhu, C., Zheng, Q., Wang, G., Tong, J., et al. (2017). Aptamer-conjugated extracellular nanovesicles for targeted drug delivery. *Cancer Res*. 78, 798–808. doi: 10.1158/0008-5472.CAN-17-2880

Wang, L., Zhang, X. H., Yang, K., Fu, Y. V., Xu, T. S., Li, S. L., et al. (2019). A novel double-crosslinking-double-network design for injectable hydrogels with enhanced tissue adhesion and antibacterial capability for wound treatment. *Adv. Funct. Mater*. 30:1904156. doi: 10.1002/adfm.201904156

Wang, W., Chen, K., Xia, Y., Mo, W., and Niu, P. (2018). The hepatoprotection by oleanolic acid preconditioning: focusing on pparalpha activation. *PPAR Res*. 2, 1–14. doi: 10.1155/2018/3180396

Xiong, F., Ling, X., Chen, X., Chen, J., and Wu, J. (2019). Pursuing specific chemotherapy of orthotopic breast cancer with lung metastasis from docking nanoparticles driven by bioinspired exosomes. *Nano Lett*. 19, 3256–3266. doi: 10.1021/acs.nanolett.9b00824

Zhang, R. X., Yin, L., Zhang, B., Shi, H., Sun, Y., Ji, C., et al. (2018). Resveratrol improves human umbilical cord-derived mesenchymal stem cells repair for cisplatin-induced acute kidney injury. *Cell Death Dis*. 9:965. doi: 10.1038/s41419-018-0959-1

Zhu, Q., Ling, X., Yang, Y., Zhang, J., Li, Q., Niu, X., et al. (2019). Embryonic stem cells-derived exosomes endowed with targeting properties as chemotherapeutics delivery vehicles for glioblastoma therapy. *Adv. Sci*. 6:1801899. doi: 10.1002/advs.201801899

Conflict of Interest: The authors declare that the research was conducted in the absence of any commercial or financial relationships that could be construed as a potential conflict of interest.

The reviewer YY declared a shared affiliation, with no collaboration, with one of the authors, JZ, to the handling editor at the time of the review.

Copyright © 2021 Zhao, Li, Jia, Wang, Shi and Wang. This is an open-access article distributed under the terms of the Creative Commons Attribution License (CC BY). The use, distribution or reproduction in other forums is permitted, provided the original author(s) and the copyright owner(s) are credited and that the original publication in this journal is cited, in accordance with accepted academic practice. No use, distribution or reproduction is permitted which does not comply with these terms.

frontiers in Bioengineering and Biotechnology

ORIGINAL RESEARCH
published: 14 June 2021
doi: 10.3389/fbioe.2021.694100

De novo Design of G Protein-Coupled Receptor 40 Peptide Agonists for Type 2 Diabetes Mellitus Based on Artificial Intelligence and Site-Directed Mutagenesis

Xu Chen[1,2†], Zhidong Chen[1,2†], Daiyun Xu[2], Yonghui Lyu[2], Yongxiao Li[2], Shengbin Li[2], Junqing Wang[2] and Zhe Wang[1]**

[1] Department of Pathology, The Eighth Affiliated Hospital, Sun Yat-sen University, Shenzhen, China, [2] School of Pharmaceutical Sciences (Shenzhen), Sun Yat-sen University, Shenzhen, China*

G protein-coupled receptor 40 (GPR40), one of the G protein-coupled receptors that are available to sense glucose metabolism, is an attractive target for the treatment of type 2 diabetes mellitus (T2DM). Despite many efforts having been made to discover small-molecule agonists, there is limited research focus on developing peptides acting as GPR40 agonists to treat T2DM. Here, we propose a novel strategy for peptide design to generate and determine potential peptide agonists against GPR40 efficiently. A molecular fingerprint similarity (MFS) model combined with a deep neural network (DNN) and convolutional neural network was applied to predict the activity of peptides constructed by unnatural amino acids (UAAs). Site-directed mutagenesis (SDM) further optimized the peptides to form specific favorable interactions, and subsequent flexible docking showed the details of the binding mechanism between peptides and GPR40. Molecular dynamics (MD) simulations further verified the stability of the peptide–protein complex. The R-square of the machine learning model on the training set and the test set reached 0.87 and 0.75, respectively; and the three candidate peptides showed excellent performance. The strategy based on machine learning and SDM successfully searched for an optimal design with desirable activity comparable with the model agonist in phase III clinical trials.

Keywords: T2DM, GPR40, artificial intelligence, oligopeptides, molecular fingerprint, site-directed mutagenesis

OPEN ACCESS

Edited by:
Jianxun Ding,
Changchun Institute of Applied Chemistry, Chinese Academy of Sciences, China

Reviewed by:
Wei Tao,
Harvard Medical School, United States
Wenliang Li,
Jilin Medical University, China
Qingqing Xiong,
Tianjin Medical University Cancer Institute and Hospital, China
Bobin Mi,
Huazhong University of Science and Technology, China

****Correspondence:***
Junqing Wang
wangjunqing@mail.sysu.edu.cn
Zhe Wang
Wangzh379@mail.sysu.edu.cn

† These authors have contributed equally to this work

Specialty section:
This article was submitted to Biomaterials, a section of the journal Frontiers in Bioengineering and Biotechnology

Received: *12 April 2021*
Accepted: *07 May 2021*
Published: *14 June 2021*

Citation:
Chen X, Chen Z, Xu D, Lyu Y, Li Y, Li S, Wang J and Wang Z (2021) De novo Design of G Protein-Coupled Receptor 40 Peptide Agonists for Type 2 Diabetes Mellitus Based on Artificial Intelligence and Site-Directed Mutagenesis. Front. Bioeng. Biotechnol. 9:694100. doi: 10.3389/fbioe.2021.694100

INTRODUCTION

Type 2 diabetes mellitus (T2DM) is a degenerative disease caused by impairment in insulin action and pancreatic β-cell function, characterized by the inability to maintain glucose homeostasis. During the past two decades, T2DM has emerged as one of the most severe global healthcare concerns (Zheng et al., 2018). The general objective of all therapeutic modalities for T2DM is to decrease the circulating blood glucose levels. Currently, there are various types of drugs that play important roles in glycemic control. The mechanisms of action involve (i) insulin receptor ligands (insulin analogs), (ii) reduction of insulin resistance (biguanides and thiazolidinediones),

(iii) stimulation of β-cells by insulin secretagogues (sulfonylureas and meglitinides), (iv) lowering postprandial blood glucose level via alpha-glucosidase inhibitors (acarbose and miglitol), and (v) blocking renal glucose reabsorption via a sodium-glucose cotransporter-2 (SGLT2) inhibitor (dapagliflozin) (Chatterjee et al., 2017). Although most treatments can manage glucose levels in T2DM patients, the progressive decline in β-cell function leads to inevitable dependence on exogenous insulin supply. Therefore, the novel mechanism and potent candidates should draw our attention in the treatment of T2DM (Chen et al., 2016).

G protein-coupled receptors (GPCRs) are among the most attractive membrane targets for many drugs (Sriram and Insel, 2018). In recent years, a growing number of GPCRs are being discovered with a wide variety of ligands, including free fatty acids, sucrose, acetate, lactate, and ketone bodies; and they are implicated in many pathophysiological functions (Blad et al., 2012). G protein-coupled receptor 40 (GPR40), also known as free fatty acid receptor 1 (FFAR1), is a member of the long-chain fatty acid GPCR family. Current studies proved that GPR40 plays a pivotal role in the potentiation of glucose-dependent insulin secretion from pancreatic β-cells, and it also regulates glucagon-like peptide 1 (GLP-1) and gastric inhibitory peptide (GIP) secretion (Li et al., 2020). The view that the agonists of GPR40 may be beneficial for treating T2DM is substantially studied (Nutan et al., 2017). Clinical candidates targeting GPR40 to enhance insulin secretion have been reported in the literature (Naik et al., 2013). Moreover, GPR40 agonists have been described as having superior effects, including cardioprotection, suppressing glucagon levels, and weight loss, than other hypoglycemic drugs (Mancini and Poitout, 2015).

The current development of GPR40 agonists primarily focuses on small molecules, whose limitations, such as low selectivity, high toxicity, and low efficiency, can contribute to failures in clinical trials (Naik et al., 2012; Kim et al., 2018). Therefore, new entities should draw our attention to the development of GPR40 agonists. In this regard, peptides show high bioactivity associated with high specificity, and low toxicity has made them attractive therapeutic agents. Thus, the development of synthetic peptides is an attractive modality to active GPR40. However, little is known on the process of discovery in peptides for targeting GPR40, partly because the core binding pocket is inaccessible to the natural peptides. To this end, peptidomimetic composed of unnatural amino acids (UAAs) can significantly increase its structural diversity and improve binding affinity and selectivity toward GPR40. Besides, the blood circulation time is important for the duration of action. In this context, peptide drugs can provide tunable circulation times through extended sequence engineering or drug delivery systems (Zorzi et al., 2017; Wang et al., 2018, 2020). In the case of membrane protein, the binding site of GPR40 was located in the extracellular part, so peptides targeting GPR40 can act without membrane penetration.

In response to the rapidly growing demand for binding, functional, and ADMET (absorption, distribution, metabolism, and excretion) information of many drug-like bioactive compounds, various public databases (e.g., DrugBank, PubChem, ChEMBL, and Zinc) have been developed for drug discovery. Quantitative structure–activity relationships (QSAR) modeling can largely increase drug design efficiency (Krishna and Anuradha, 2020), but how to build QSAR models for GPR40 remains elusive. Recently, the artificial intelligence (AI) method, deep neural network (DNN) algorithm, has been well represented as a novel approach to build QSAR models (Hessler and Baringhaus, 2018). The use of deep learning in chemical discovery has received considerable attention in recent years. For example, DNN predicted cell permeability based on the chemical structure of organic fluorescent (Soliman et al., 2021), and the convolution neural network (CNN) was used to find the relationship between the chemical structure of odor molecules and their related odors (Sharma et al., 2021). The graph convolutional neural network (GCN) successfully predicted the reverse synthesis reaction (Ishida et al., 2019), and the transformer neural network directly designed potential ligand molecules based on the sequence of the protein target (Grechishnikova, 2021). DNN had achieved many successes in molecular descriptor-based tasks and had the advantage of being easy to construct (Li et al., 2018; Cai et al., 2019). The commonly used two-dimensional (2D) CNN had made brilliant achievements in computer vision, and the derived one-dimensional (1D) CNN was suitable for sequence data, such as gene sequence and natural language processing (Esteva et al., 2021; Sun et al., 2021; Zhang et al., 2021). Molecular descriptors could be used as input of DNN to construct QSAR models, and quantified molecular descriptors could be regarded as a unique sequence for 1D CNN to use. Nevertheless, there was no perfect AI model, and performance comparison between models on a specific task can help obtain more accurate results (Yang et al., 2019).

Here, we describe a novel AI combining mutation scanning approach to design new promising oligopeptide agonists for GPR40 (**Figure 1**). Initially, the ChEMBL database (version 28) was used to extract 528 compounds with known bioactivity and structural profiles. A QSAR model was constructed based on DNN. The molecular fingerprint search method was employed to screen active chemical entities among the oligopeptides generated from the library of natural amino acids (AAs)/UAAs. The obtained candidate oligopeptides were then evaluated for the binding affinity to GPR40 through flexible docking procedures. The initial lead oligopeptides were further processed by the site-directed mutagenesis (SDM) optimization to achieve potential hits toward GPR40. The peptides were further analyzed in molecular dynamics (MD) simulations and showed good stability. These top candidates might be up-and-coming for the treatment of T2DM.

MATERIALS AND METHODS

Data Set

A total of 2,084 GPR40 agonists with EC50 measurements have been extracted from the ChEMBL database (Mendez et al., 2018). The unit of measurement for EC50 is nmol. Fasiglifam (TAK-875), a potent GPR40 selective agonist withdrawn from phase III clinical trials due to drug-induced hepatotoxicity (Yabuki et al., 2013), was used as a positive control to evaluate the

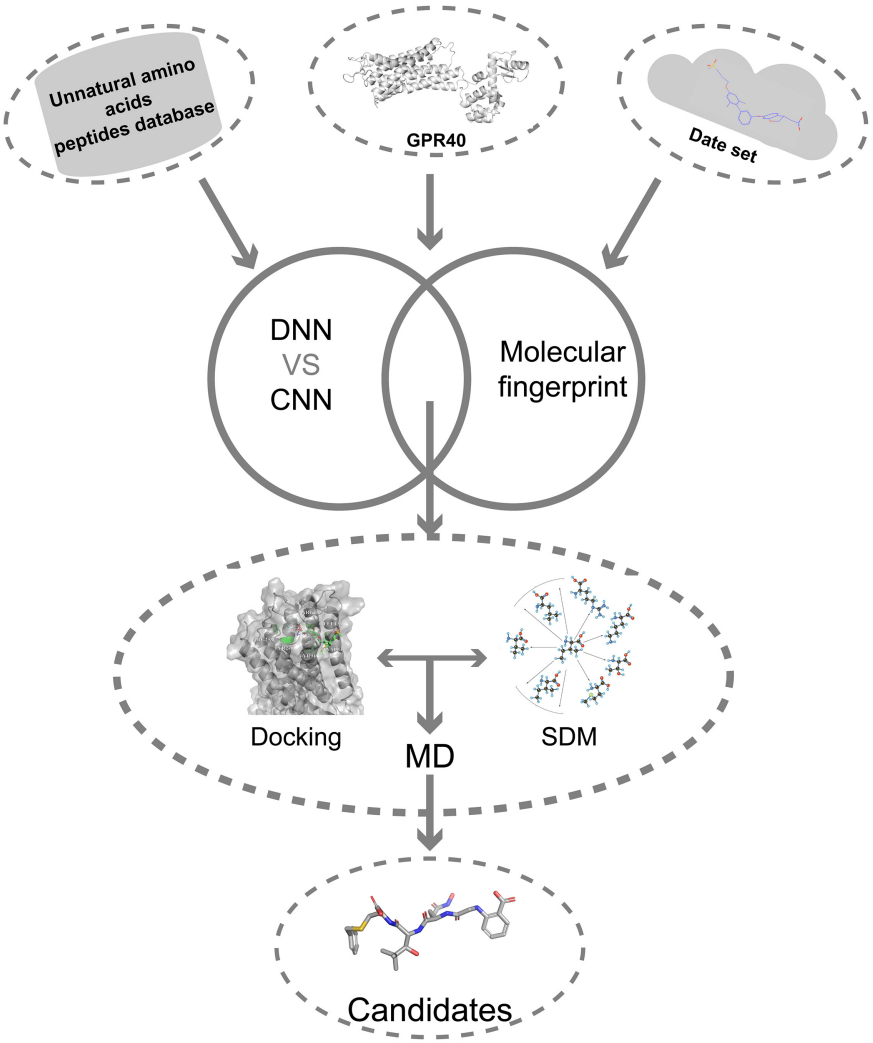

FIGURE 1 | The overall flowchart.

efficacy profile of the obtained TAK-875 analogs. In this study, only the compounds that interact with the same region in the TAK-875 binding site were kept, and all duplicate entries were removed. The final data set that consisted of 528 molecules is listed in **Supplementary Table 1**. All molecular structures were constructed in molecular operating environment (MOE) version 2019.0102 and imported into the database (Vilar et al., 2008). Structure preparation was performed on all molecules to repair structural errors and add hydrogen atoms. Protonate3D was used to protonate all molecules. The temperature of Protonate3D was set to 300K, the pH was set to 7, and the ion concentration was set to 0.1 mol/L. Energy minimization was performed for each molecule to obtain the optimal configuration. The root mean square gradient of energy minimization was set to 0.1 kcal/mol/A.

Feature Calculation

A total of 153 2D molecular descriptors were calculated in MOE. The names of all molecular descriptors and their specific meanings are listed in **Supplementary Table 2**. The EC50 value of each molecule is logarithmically processed to pEC50 (Eq. 1).

$$pEC_{50} = -\log EC_{50} + 9 \quad (1)$$

To improve the model accuracy, Morgan fingerprints with a length of 1,024-bit strings were calculated by the RDKit toolkit to compare the performance with the MOE 2D descriptors Landrum (2016). All quantitative features were standardized. The pEC50 of 528 molecules in the data set is typically in the range between 4 and 9, and the molecular weight is roughly between 200 and 600 (**Figure 2A**).

The UAA Library and the Oligopeptide Database

The AA database used in this study contains 20 natural AAs and 850 UAAs derived from 20 canonical AAs. All UAA category information is in **Supplementary Table 3**. The number of peptide residues is limited to 3–5. The molecular weight of the peptide

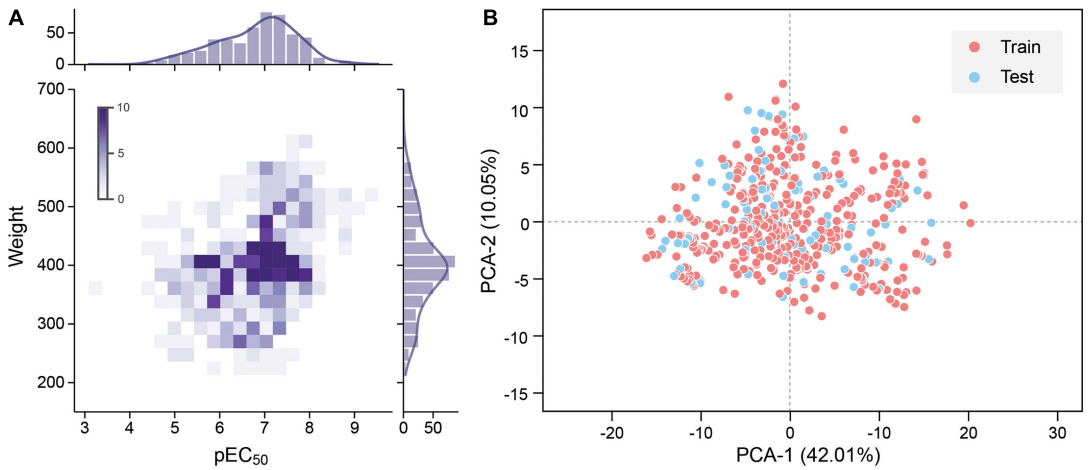

FIGURE 2 | (A) Molecular weight and pEC50 distribution of the data set. Frequency increases with the color from light to dark. **(B)** 2D principal component analysis (PCA) results of the data set. The red dot is the training set, and the blue dot is the test set.

is similar to the data set molecule, which helps to improve the accuracy of peptide activity prediction and facilitates the peptide's entry into the GPR40 binding site. Three random-constructed virtual peptides (tripeptides, tetrapeptides, and pentapeptides) libraries were generated, where each peptide library consists of 100,000 peptide entries. The generation and preservation of peptide structures were done by MOE's SVL script.

Model Training

Convolution neural network is a feedforward neural network that includes convolution calculations (LeCun et al., 2015). It can learn features from data and generalize them to specific data. CNN has achieved great success in speech recognition, image recognition, and other fields. The molecular features calculated based on MOE can be expressed as a 1×153 vector form; hence 1D CNN can be well adapted to the task of predicting the activity of oligopeptides based on molecular features. In contrast, the DNN is a fully connected neural network, which is more prone to overfitting than CNN. The hyperparameters of the neural network are important for the training and accuracy of the model. We repeatedly adjusted and confirmed the best hyperparameters in the training process. A CNN with seven convolutional layers, three max-pooling layers, and one Flatten layer is built (**Figure 3**). The size of the local receptive field was 1×3; and the number of feature maps of the convolutional layer was 16, 16, 64, 64, 128, 128, and 64 in order. The filter size of the pooling layer was 3. The Flatten layer was used to expand the output of the pooling layer and connect to the final dense layer. The batch size was set to 10.

Here, DNN contains three hidden layers (**Figure 3**). The number of units contained in each hidden layer is 150, 30, and 10 in order. The first and second hidden layers applied Dropout to prevent overfitting, and the Dropout Rate was defined as 0.9.

The rectified linear unit was used as the activation function of CNN and DNN, mean square error (MSE) (Eq. 2) was defined as the loss function, and the Adam optimizer was used to minimize the loss function (Nair and Hinton, 2010; Kingma and Ba, 2014). The initial learning rate of the Adam optimizer was set to 0.001 and 0.0008 in CNN and DNN, respectively.

$$\text{Mean Square Error} = \frac{1}{m}\sum_{i=1}^{m}(y_i - \widehat{y_i})^2 \tag{2}$$

where m is the sample size, y_i is the actual value of the sample's pEC50, and $\widehat{y_i}$ is the predicted value of the sample by the model. The data set was divided into a training set and a test set according to the ratio of 4:1. Principal component analysis (PCA) was performed with all the features as input, and the features were mapped to two principal components with 42.01 and 10.05% variances. The data set shows high chemical diversity. 2D PCA shows that the training set and the test set are located in the same chemical space (**Figure 2B**). All input features in CNN and DNN had undergone maximum and minimum standardization processing. The last layer of CNN and DNN did not use the activation function and outputs pEC50. R-square was used to evaluate the accuracy of model fitting (Eq. 3).

$$R - \text{square} = 1 - \frac{\sum_i (\widehat{y_i} - \overline{y_i})^2}{\sum_i (y_i - \overline{y_i})^2} \tag{3}$$

where $\widehat{y_i}$ is the predicted value of the sample by the model, y_i is the actual pEC50 value, and $\overline{y_i}$ is the mean pEC50.

Principal Component Analysis and LASSO Feature Selection

To improve the accuracy of the model, speed up model training, and reduce overfitting, PCA and LASSO feature selection were applied to reduce redundant features (Tibshirani, 2011). The data set was reduced in dimensionality by solving the covariance matrix. The variance accumulation threshold of PCA was set to 0.99 to remove low variance features. LASSO regression can compress the coefficients of the regression variables to 0 and make the parameters become sparse because it has

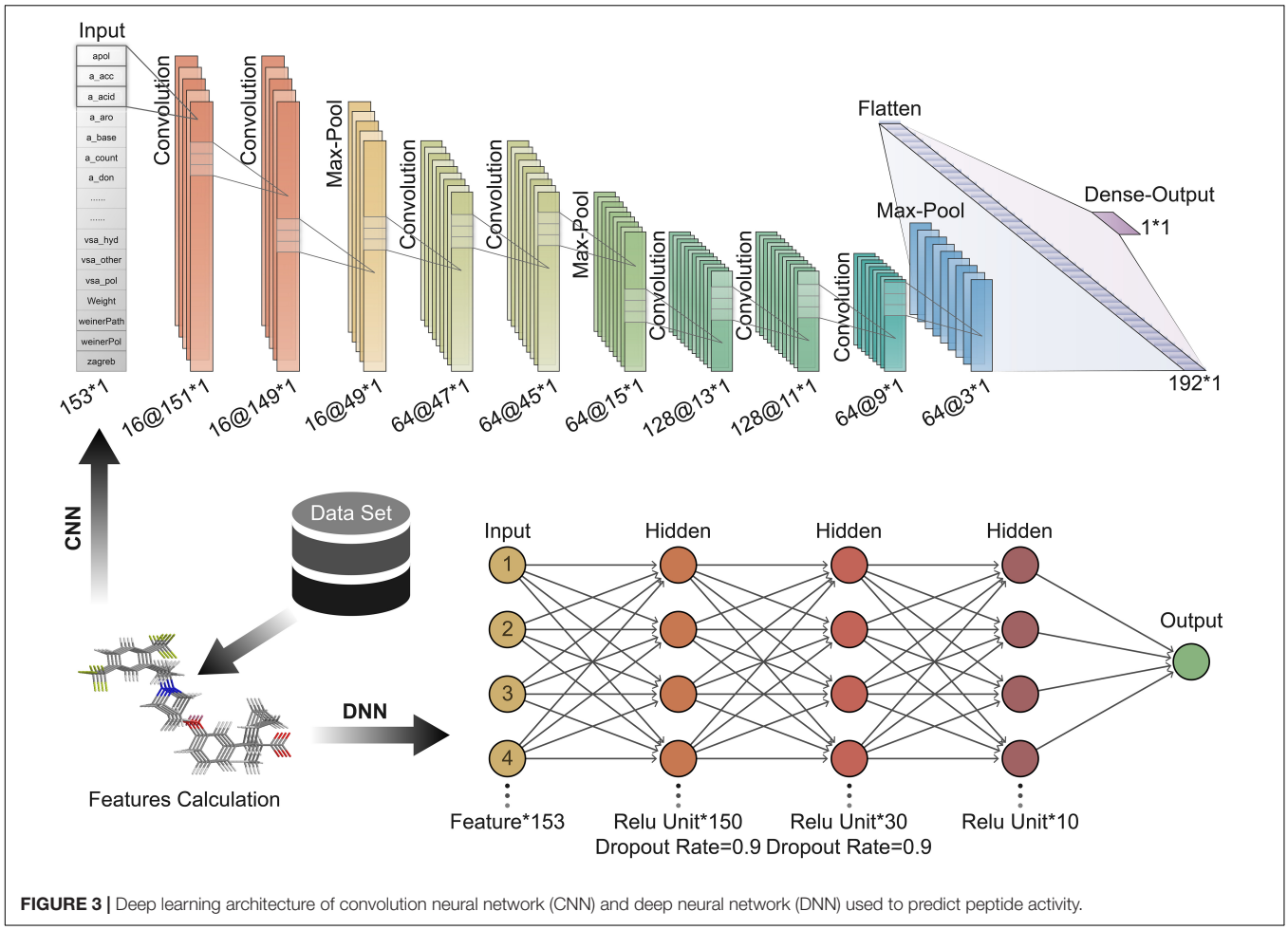

FIGURE 3 | Deep learning architecture of convolution neural network (CNN) and deep neural network (DNN) used to predict peptide activity.

L1 regularization terms. Here, the alpha value of the LASSO regression estimator was set to 0.001 to limit the L1 regular term, and the maximum number of iterations was set to 8,000 to fit all features.

Molecular Similarity Search

The fundamental assumption in drug discovery is that structurally similar molecules exhibit similar biological activities (Muegge and Mukherjee, 2016). Hence, the molecular fingerprint method allows for ligand-based virtual screening and predicts bioactivity or other properties of candidates that have not been tested with the fingerprint model built from the database of the active template. In simple terms, fingerprint models transfer the structure of active templates and candidates simultaneously into numbers or matrices and compare them with mathematical methods, for example, the Tanimoto coefficient (Cereto-Massagué et al., 2015). According to the design principle of the fingerprint system, different fingerprint schemes bring out different molecular attributes. For instance, the description of GpiDAPH3 is "3-point pharmacophore-based fingerprint calculated from the 2D molecular graph. Each atom is given one of 8 atom types computed from 3 atomic properties: "in pi system," "is donor," "is acceptor." Anions and cations are not represented. Then, all triplets of atoms are coded as features using the three graph distances and three atom types of each triangle. The resulting fingerprint is represented as a sparse feature list."

Nearly all common fingerprint types, like BIT_MACCS, MACCS, TAD, TAT, and GpiDAPH3, are available in MOE, so the most proper type should be designed first. It has been proved that there is no generally superior fingerprint to be used (Muegge and Mukherjee, 2016), Thus, in this study, we initially used the GpiDAPH3 fingerprint model to determine which score function (Must match, Maximum, Minimum, and Average and Distance) is suitable for this condition. With the most suitable score function, fingerprint types were then tested for the superior fingerprint type in our database. Having a certain score function and fingerprint type, we trained our fingerprint model to predict the bioactivity of candidates. The data set of molecular fingerprint model consisted of 528 molecules, which were as identical as DNN and CNN models.

Structure Preparation and Molecular Docking

The crystal structure of the human GPR40-TAK-875 complex (PDB:4PHU) was obtained from Protein Data Bank to perform

the docking study (Berman et al., 2000; Srivastava et al., 2014). The structure preparation, Protonate3D, and energy minimization were carried out by MOE. The structure preparation repaired the gap in the protein structure. Protonate3D added hydrogen atoms to the structure and completed the protonation in the default ionization state. The terminal amide, sulfonamide, and imidazole groups were able to flip to optimize the hydrogen bond network. All water molecules were removed. The atomic restraint strength was set to 10, and the extent of the flat bottom of the flat-bottom restraint was set to 0.25 to prevent excessive positional deviation of the atoms. The energy minimization with a root mean square gradient of 0.1 kcal/mol/A was performed to optimize protein conformation. The binding site of GPR40 was created according to the TAK-875 (partial agonist) in crystal complexes.

The molecular docking was performed by the MOE. The same energy minimization protocol as the protein structure was performed on the peptides. Peptides were placed at the binding site by the method of Triangle Matcher. The 30 postures generated by the placement method for each peptide would be refined in the Amber10:EHT force field using the Induced Fit method (Gerber and Müller, 1995; Case et al., 2008). Generalized Born/volume integral/weighted surface area (GBVI/WSA) dG Scoring is used to evaluate the binding free energy of the docking result (Eq. 4).

$$\triangle G \approx c+\alpha\left[\frac{2}{3}\left(\triangle E_{Coul}+\triangle E_{sol}\right)+\triangle E_{vdW}+\beta\triangle SA_{weighted}\right] \quad (4)$$

where c is the average gain and loss of rotation and translation entropy, α; β is the constant determined during the function training process; E_{Coul} is the Coulomb electrostatic term; E_{sol} is the solvation electrostatic term calculated by GB/VI solvation model; E_{vdW} is van der Waals contribution; and SA_{weighted} is surface area weighted by exposure.

Site-Directed Mutagenesis and Re-Dock

Amino acid single-point mutations were applied in candidate oligopeptides to improve their affinity and stability by attempting to form the salt bridge equivalent to TAK-875. The selected UAAs were sequentially substituted to the designated positions following the reassessment of the interaction between the updated peptide and GPR40. New peptides were isolated from the complex structure created by the mutation. The peptide conformation was preserved, and re-docking to GPR40 for refinement and for further rescoring the GPR40–peptide interactions was performed.

Molecular Dynamics Simulations

Further analysis of stability about the GPR40–candidate peptides complexes was conducted by MD simulations with GROMACS 2020.5 software on Manjaro platform after flexible docking (Abraham et al., 2015). The topology files of candidate peptides, an indispensable component in MD, were obtained from the Swissparam webserver (Zoete et al., 2011). The GPR40–peptides complexes were firstly placed in a periodic cubic box (1.2-nm edge), and then the TIP3P water molecules and 0.145 M of NaCl ions were added. The steepest descent minimization algorithm with 5,000 steps at most was conducted to avoid excessive local stress. Before the formal simulation, 1-ns NVT pre-equilibrium and 1-ns NPT pre-equilibrium were done to stabilize the temperature (310K) and pressure (1 bar). Formal simulation lasted 10 ns, and the CHARMM27 was applied (Brooks et al., 2009). The analysis of the dynamics simulations consisted of root mean square deviation (RMSD), mean square displacement (MSD), root mean square fluctuation (RMSF), solvent-accessible surface areas (SASAs), radius of gyration (gyrate), and system energy.

RESULTS AND DISCUSSION

Comparison of CNN and DNN

To obtain high-precision activity prediction results, CNN and DNN were constructed to compare their fitness with the task. Both neural networks were trained based on all molecules in the data set. All molecular features were normalized with Min–Max scaling before input into the neural network to improve training efficiency. The CNN was trained for 100 epochs with a batch size of 10. In the ninth epoch, the MSE of the training set and the test set was reduced to 0.0084 and 0.0090, respectively. Then the MSE begins to fluctuate slightly, the MSE of the training set continues to decline, and the MSE of the test set fluctuates within a certain range (**Supplementary Figure 1**). When training to the last 10 epochs, the MSE of the training set dropped from 0.0020 to 0.0010, and the MSE of the test set fluctuated between 0.0089 and 0.0110. DNN traverses all samples in each step, and 1,000 steps of training were executed. At the 270th step, the MSE on the training set and the test set was reduced to 0.0018 and 0.0051, respectively. The training set MSE had been declining throughout the training process. The MSE of the test set begin to rise slowly after the 270th step, and it becomes stable at the end of training (**Supplementary Figure 2**). During the last 100 steps, the MSE of the training set fluctuates slightly around 0.0004, and the MSE of the test set fluctuates around 0.0083. When compared with DNN, CNN has a greater loss function oscillation, and the ability to reduce the loss function is worse than DNN. Yet on the test set, the highest R-square of DNN reaches 0.750 (**Figure 4A**), while that of CNN is only 0.620 (**Figure 4B**). DNN was shown to outperform CNN on the task of activity prediction. Nevertheless, both neural networks exhibit slight overfitting; thus, the early stopping strategy was applied to DNN.

Performance of Features

Both MOE 2D features and Morgan fingerprints features were input to DNN for training. To ensure that the model converges, DNN trained 2000 steps on the Morgan fingerprint data set. At the 1,250th step, the MSE of the training set and the test set both drop to 0.02 and stabilized thereafter (**Supplementary Figure 3**). The DNN based on Morgan fingerprint training exhibits a more gradual decline in MSE than the DNN based

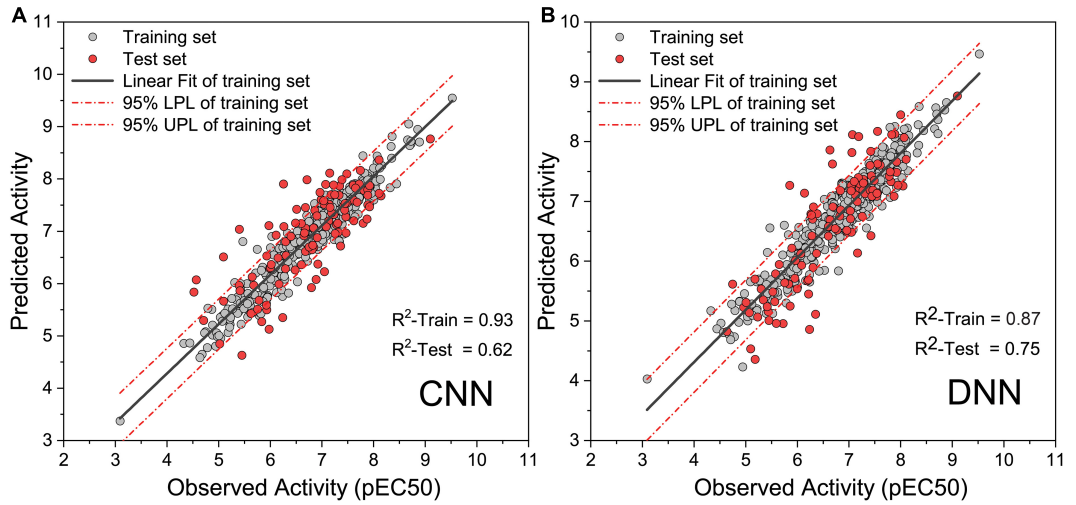

FIGURE 4 | Observed activity and predicted activity of training set and test set using **(A)** The deep neural network (DNN) and **(B)** The convolution neural network (CNN).

on MOE 2D feature training. The test set MSE of the Morgan fingerprint model was stable at 0.02, which was much higher than the MSE of MOE 2D feature model, and the Morgan fingerprint model did not achieve good accuracy. Subsequently, based on the MOE 2D features, we attempted to optimize the features through PCA and LASSO feature selection to improve the accuracy of the model. Z-score standardization was performed on the data set, the cumulative variance threshold was set to 0.99, and the 153-dimensional features had been reduced by PCA to generate 43 new features. The variance of the top 10 new features is shown in **Figure 5A**. The fitting accuracy of the LASSO regression estimator reaches 0.71, and there are 83 features whose coefficients are not 0 after fitting (**Supplementary Table 4**). The new features obtained by the two methods were input to DNN for 100 pieces of training, and each training contains 1,000 steps. The R-square of the model training set and the test set would be checked every 10 steps, and the largest R-square that satisfied the difference between the training set R-square and the test set R-square less than 0.2 in 1,000 steps would be recorded. The R-square frequency distribution curves of the training set and test set obtained by 100 trainings on the original feature data set, PCA dimensionality reduction feature data set, and LASSO feature selection data set are shown in **Figures 5C,D**. The performance of new features obtained by PCA dimensionality reduction was relatively poor and produced more low-precision models. After the removal of low-importance features via LASSO feature selection, the model still showed good accuracy. Still, the overall trend of model accuracy has a slight decrease as compared with the original data (**Figures 5B–D**). LASSO feature selection improved the model training speed and only sacrificed a little model accuracy. This method could effectively improve training efficiency when training on an extensive data set. To obtain the highest precision model, we still used raw data for training regardless of training speed. Finally, the DNN model with R-squares of 0.87 and 0.75 for the training set and test set obtained through the early stopping strategy was retained.

Molecular Fingerprint Similarity

All the fingerprint models were built in MOE. For the most accurate and suitable fingerprint model in this situation, the score function and type of fingerprint model must be tested. To evaluate different fingerprint models better, the training set and the testing set were carefully designed. All the training set in fingerprint models consisted of active entities (low EC50 in ChEMBL) since the purpose of the fingerprint model is to exploit novel potential active entities in other databases. As for the testing set, the active entities (low EC50 in ChEMBL) were encoded index1-50, and on the contrary, the inactive entities (high EC50 in ChEMBL) were encoded index51-100. Since all of the fingerprint models were built from active entities, a higher similarity score represents more possibilities of being an active entity. Therefore, an ideal model should be available to distinguish active entities from inactive entities. To this end, the entities index1-50 should be with a high similarity score, and index51-100 should be with a low similarity score. Furthermore, the k, slope of the regression line, which is the relationship between similarity score and index, can reflect the quality of the model in some distance. When the absolute value of k is high, it means that there is a tendency of the decrease in similarity score with the increase of index, which also matches with an ideal model.

GpiDAPH, a common and gorgeous fingerprint model, was chosen to evaluate which score function (Average, Distance, Maximum, Minimum, and Must match) is the most appropriate one. The predicted similarity score and index of testing data are shown in **Supplementary Figure 4**, and the values of k are shown in **Figure 6A**. Comparing the value of k and the distribution of the similarity score, the score function of maximum is chosen as the best score function in this research (**Supplementary Figure 4C**).

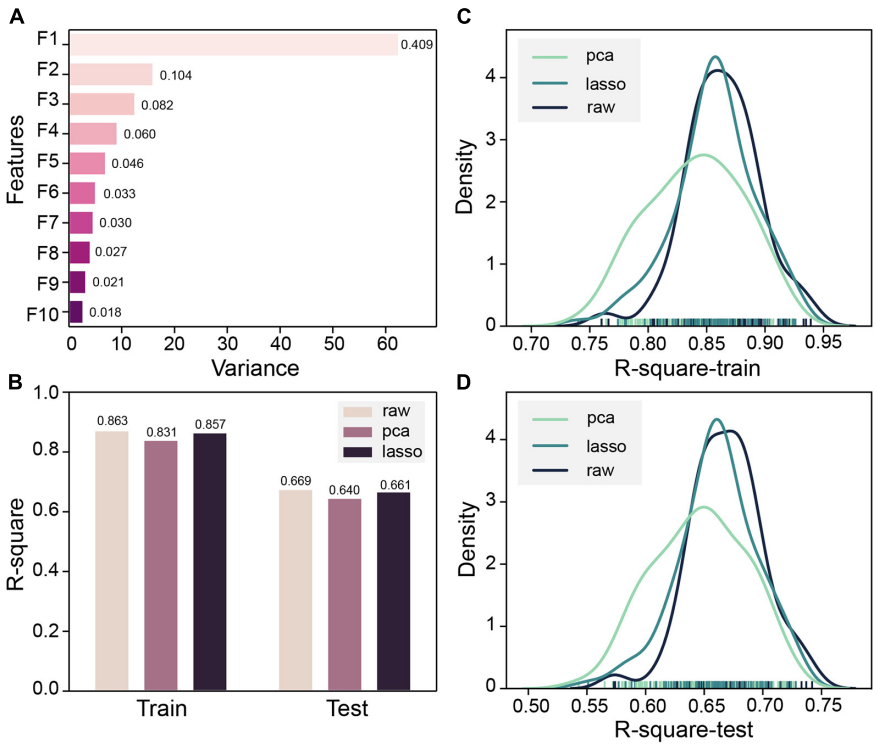

FIGURE 5 | (A) Top 10 principal component analysis (PCA) features and their variance ratios. **(B)** R-square average of 100 trainings of deep neural network (DNN) based on PCA, LASSO, and original features on the training set and test set. **(C)** Train set R-square distribution of DNN based on PCA, LASSO, and original features in 100 trainings. **(D)** The test set R-square distribution of DNN based on PCA, LASSO, and original features in 100 trainings.

The types of fingerprint models were then evaluated with the same method. The result is shown in **Figure 6B** and **Supplementary Figure 5**. The value of k shows little difference among Bit_MACCS, GpiDAPH, and MACCS, so the suitable type cannot be designed yet. Therefore, the entities with higher bioactivity (EC50) were chosen to consist new training set, and the testing set was accordingly adjusted. The new training set and testing set are constructed to evaluate these three fingerprint types further, and the result is shown in **Figure 6C** and **Supplementary Figure 6**. The GpiDAPH fingerprint model shows the best performance in distinguishing between active and inactive molecules and is thus the chosen type in this study (**Figure 6D** and **Supplementary Figure 6B**). Unlike other molecular fingerprint models, in **Figure 6D**, the similarity values of active entities (index1-50) are mainly located in the upper left corner, while the inactive entities (index51-100) are in the bottom right corner.

Activity Prediction of Peptides and AA Preferences

Deep neural network model and molecular fingerprint similarity (MFS) were used to evaluate the performance of oligopeptides. All peptides were sorted by evaluation scores via two models. The output results of the model were divided into six groups according to the model and peptide length, namely, DNN-Tripeptide, DNN-Tetrapeptide, DNN-Pentapeptide, MFS-Tripeptide, MFS-Tetrapeptide, and MFS-Pentapeptide. The top-ranked 50 oligopeptides in each group were selected as samples for AA frequency statistics to observe the AA preference of high-scoring peptides. AAs were classified according to the backbone for frequency statistics, and the AA frequency (*aaf*) of each sample was calculated according to Eq. (5).

$$aaf = \frac{CA}{TA} \tag{5}$$

where *CA* is the frequency of a type of AA that appears in a sample and *TA* is the total number of AAs contained in a sample. The top 5 types of AAs ranked by *aaf* in each sample were selected and integrated. The favorable AAs determined by the DNN model were cysteine and methionine derivatives (CM), phenylalanine derivatives (F), proline derivatives, alicyclic AAs (P), alanine derivatives (A), α-methyl AAs (AM), and lysine and arginine derivatives (RK). The favorable AAs determined by MFS were P, A, F, nitro, and dinitrophenyl AAs (NI), glycine derivatives (G), and *N*-methyl AAs (NM). The most frequently occurring AAs among the nine preferred AAs show the backbone of this type of AA (**Figure 7B**). DNN's most preferred AA is CM, and CM had *aaf* of 0.273 in the DNN-Tripeptide sample (**Figure 7A**). Similarly, CM also achieved higher *aaf* (0.210 and 0.172, respectively) in DNN-Tetrapeptide and DNN-Pentapeptide. The most preferred AA class of MFS was P. The

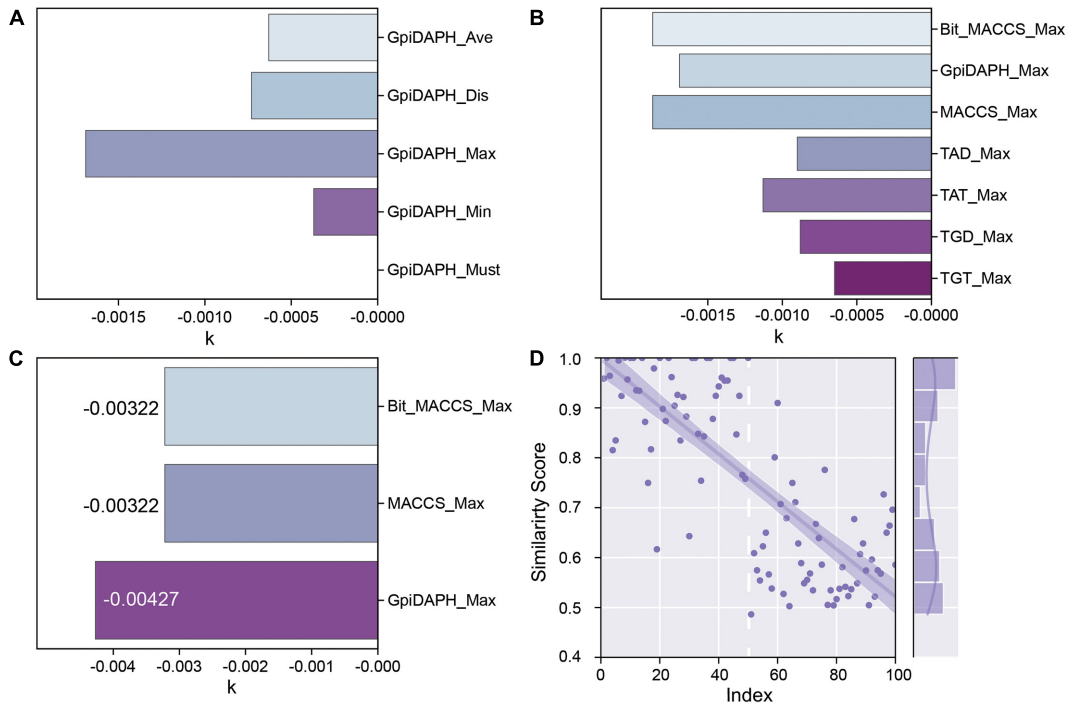

FIGURE 6 | (A) The *k* values of the fingerprint model when using different score functions. **(B)** The *k* values of each type of fingerprint model when using the Maximum scoring function. **(C)** The *k* values of Bit_MACCS, MACCS, and GpiDAPH on the new training set. **(D)** Similarity scores by GpiDAPH fingerprint model of active (index1-50) and inactive (index51-100) molecules.

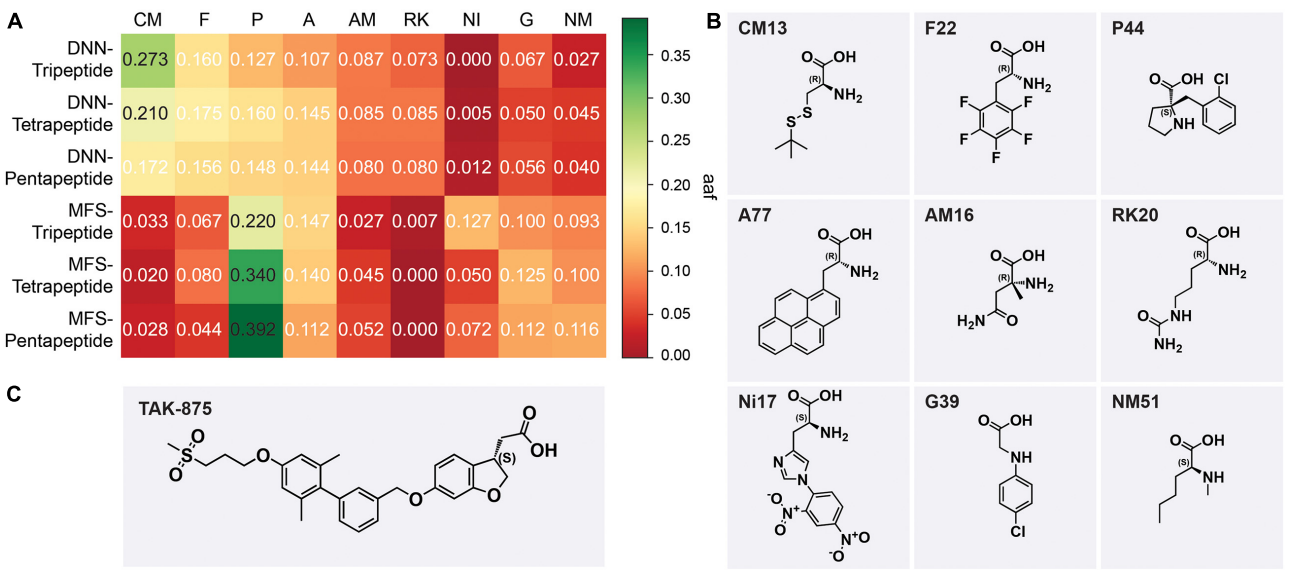

FIGURE 7 | (A) The aaf of MSF and deep neural network (DNN) on three peptides. **(B)** The most frequent amino acids from nine preferred amino acids. **(C)** The chemical scaffold of TAK-875.

aaf of P in MFS-Pentapeptide reached 0.392, which was the highest value among all samples. P reaches high *aaf* of 0.220 and 0.340 in MFS-Tripeptide and MFS-Tetrapeptide, respectively (**Figure 7A**). DNN and MFS both showed a preference for P and A, but DNN showed a lower tendency for NI, G, and NM, which were preferred by MFS. DNN was more stable than MFS in the *aaf* of three different length peptides. Most of the molecules in the data set used to construct the model are analogs of TAK-875, all of which contain ring structures, and many analogs contain sulfone groups, sulfur heterocycles, or carboxyl

groups (**Figures 7B,C**). The two AAs categories including P and A that DNN and MFS commonly prefer were molecules with five-membered heterocyclic or aromatic rings. The most preferred CM AAs of DNN were cysteine and methionine derivatives, both of which contained sulfur groups. Compared with MFS, DNN successfully captured the sulfur group features of the data set molecules. We noticed that some molecules in the data set contained halogen elements. F22 and P44 are observed with the highest frequency among the F and P AAs preferred by DNN, which shows that DNN has paid attention to the halogen element features of the molecule (**Figure 7B**).

Molecular Docking

Amino acid preference statistics showed that MFS paid attention to molecular skeleton information, and DNN could pay attention to the details of the molecule. We combined the results of the two models to select candidate peptides for docking. The intersection of the top 1% (1,000) of the two models of the tripeptide, tetrapeptide, and pentapeptide ranked by MFS and DNN was selected. The intersection of peptide samples contains 39 tripeptides, 16 tetrapeptides, and 7 pentapeptides. The GBVI scoring function that estimates the free energy of ligand binding according to a given posture is used to assess docking posture (Naïm et al., 2007) (**Table 1**). The GBVI scores of the top three peptides numbered 4-15, 5-1, and 4-4 reached −10.2063, −9.62029, and −9.57896, respectively. As shown in **Figure 8A**, the 4-15 carboxyl group forms a hydrogen bond with the hydrogen on the backbone of Cys136. The three benzene rings of 4-15 form π–H interactions with Val81, Trp174, and Leu135. Phe87 forms a π–H interaction with the main chain hydrogen of 4-15. The docking pose of 5-1 is shown in **Figure 8B**. The benzene ring in 5-1 forms π–H interaction with Val84, Leu138, and Trp174. The benzene ring of Phe142 forms a π–H interaction with 5-1. The interaction between 4-4 and GPR40 is shown in **Figure 8C**. The quinoline ring of 4-4 forms 3 π–H interactions with Leu138 and Trp174. The benzene ring of Phe142 forms a π–H interaction with 4-4. The H-bond is found between Val84 and the carboxyl of 4-4. As a control, TAK-875 was also evaluated by the GBVI method. The crystal structure of TAK-875 has abnormal van der Waals interaction between atoms. The energy minimization was performed on the crystal structure to optimize the interaction within the structure. The repaired structure shows that the GBVI of TAK-875 has been reduced from −1.4554 to −9.7494. The pose of TAK-875 is shown in **Figure 8D**. To be specific, the carboxyl of TAK-875 formed a salt bridge with Arg183 and Arg258. The benzene ring in TAK-875 interacted with Val84 by forming π–H interaction. The binding of TAK-875 to GPR40 mainly relied on two strong salt bridges. The fixation of the three peptides at the binding site mainly relied on π–H interaction, hydrogen bonding, and van der Waals force. Compared with peptides, TAK-875 had a linear structure that allowed it to penetrate deeply into the binding pocket to form salt bridge interactions. In addition, the peptide exhibited higher solvent exposure than TAK-875 due to the residues of the peptide anchored on the outer surface of GPR40. The receptor solvent exposure of the peptide is also higher than that of TAK-875. The solvent exposure of the GPR40 residues after binding with the peptide is further reduced, indicating that the peptide binding to GPR40 is primarily dependent on hydrophobic interactions.

TABLE 1 | GBVI (GBVI/WSA dG scoring) of the top 10 ranked peptides and TAK-875 in the docking results.

Name	Ranking	GBVI	Sequence
4-15	1	−10.2063	(G28)(NI42)(L18)(CM25)
5-1	2	−9.62029	(P80)(G35)(P40)(F117)(AM18)
4-4	3	−9.57896	(P131)(P107)(AM47)(A60)
4-10	4	−9.43213	(A109)(Y40)(CM28)(P103)
4-1	5	−9.38494	(P44)(G22)(L09)(F87)
5-2	6	−9.17657	(P95)(G32)(G34)(A96)(CM25)
3-12	7	−9.16672	(P93)(G28)(W026)
3-13	8	−9.04828	(P97)(A108)(P91)
5-3	9	−8.88673	(RK20)(G31)(L04)(P40)(W030)
4-5	10	−8.76586	(A109)(G19)(P52)(NM26)
TAK-875		−9.74940	

GBVI/WSA, generalized Born/volume integral/weighted surface area.

Site-Directed Mutagenesis Optimization and Re-Docking Evaluation

The high affinity of TAK-875 came from the ionic and hydrogen bonds between its carboxyl group and Arg183 and Arg258. The carboxyl group was at the end of the TAK-875 chain, and the chain is firmly inserted between the two α-helices (**Figure 8D**). The NI42 AA of 4-15 with the lowest GBVI enters the target site in a similar posture, but it fails to form strong ionic or hydrogen bonds (**Figure 8A**). To this end, the SDM method was carried out to optimize the performance of candidate peptides. NI42 that successfully penetrated into GPR40 is defined as the mutation site, and 41 AAs with a carboxyl chain similar to that of TAK-875 are used for SDM (**Supplementary Table 5** and **Figure 9**). A rough mutation evaluation without the refinement of Amber10:EHT force field shows that Li01, DE30, DE29, and LI02 have better GBVI scores than NI42 (**Figure 10**). The method of directly replacing AAs did not use a force field to adjust the conformation, so all the 41 mutant conformations were preserved, and the flexible docking was performed again. The results show that the DE20 and AG02 mutants with low GBVI formed ionic and hydrogen bonds (**Table 2**).

Based on **Figure 11A**, Arg183 and Arg258 also play a significant role in the interaction between DE20 mutant and GPR40 by forming the salt bridge or ionic interaction. The H-bonds were found between Leu135, Val84, and DE20 mutant. The benzene ring of the DE20 mutant forms a π–H interaction with Val84. In **Figure 11B**, the interaction between AG02 mutant and GPR40 is shown. Interestingly, the carboxyl moiety of AG02 mutant formed a salt bridge with Arg183 comparable with TAK-875. In addition, the AG02 mutant formed a strong ionic interaction with Arg258. The Ala88 and Leu138 interacted with AG02 mutant by H-bond. Less solvent exposure was observed on

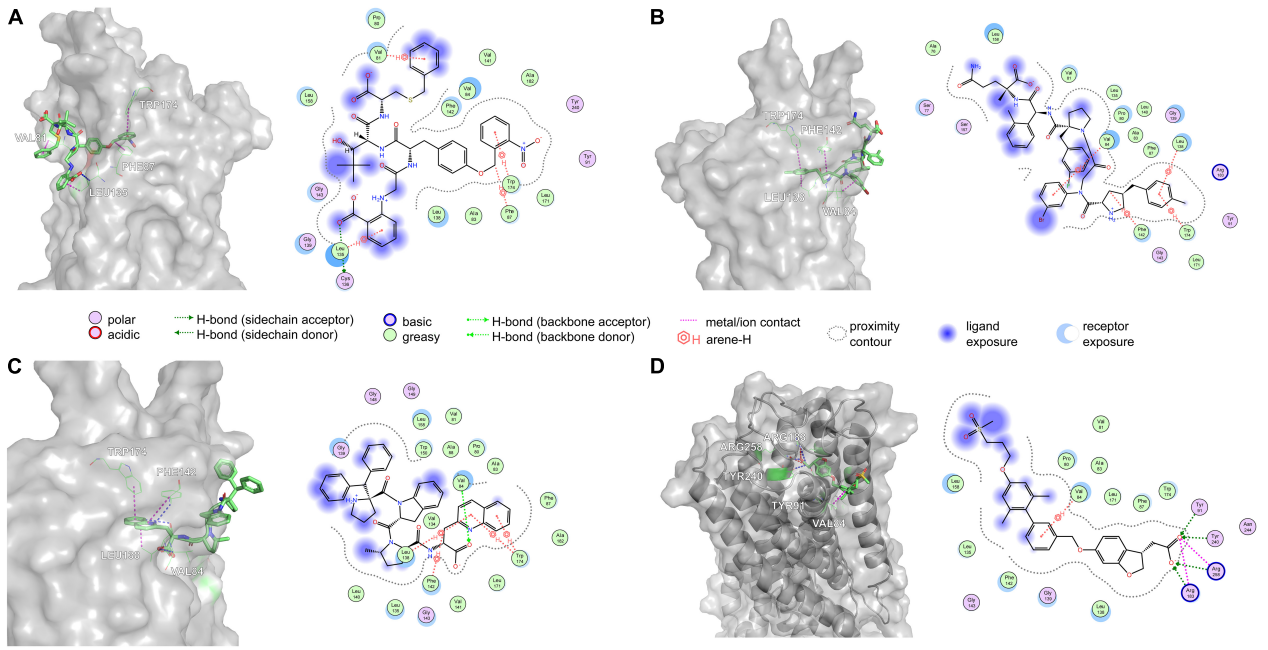

FIGURE 8 | The top three poses generated by flexible docking and the pose of TAK-875 in the crystal structure after energy minimization. In 3D pose diagrams, the red dash lines represent ionic bonds, magenta dash lines represent π–H interaction, and blue dash lines represent H-bonds. **(A)** 4-15, **(B)** 5-1, **(C)** 4-4, and **(D)** TAK-875.

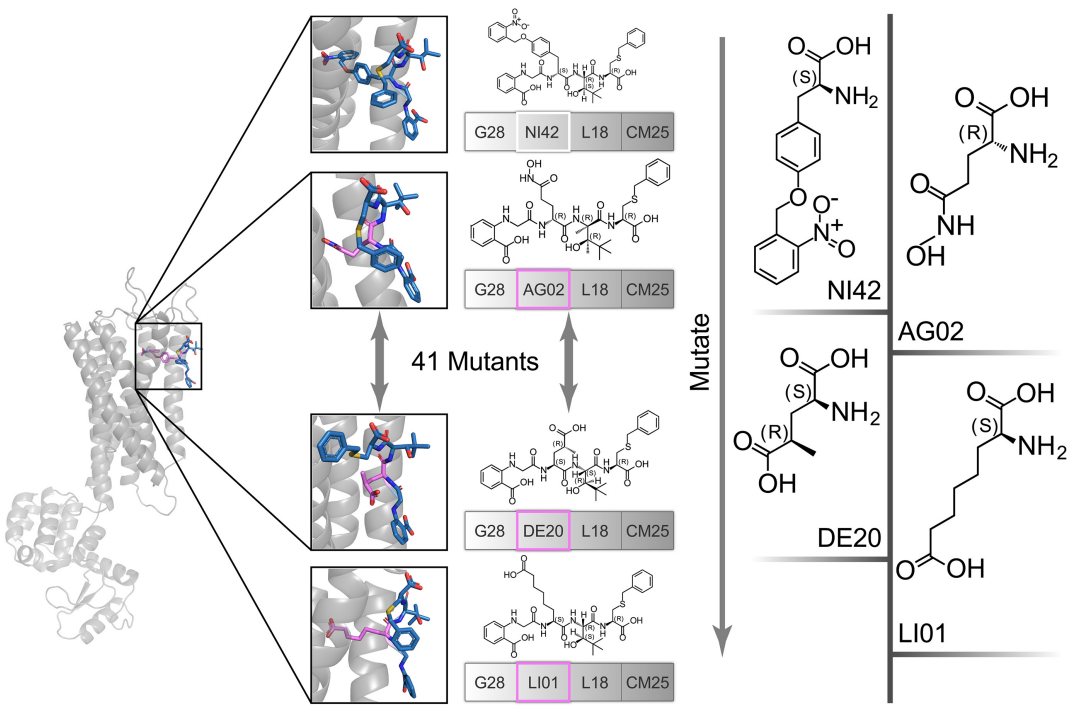

FIGURE 9 | The NI42 amino acid of 4-15 was defined as the mutation site, and 41 mutations were performed.

DE20 mutant and AG02 mutant similar to TAK-875. LI01 with the carboxyl group attached to the long alkyl chain showed the best performance in SDM but poor performance after re-docking. The re-docking pose of LI01 mutant in GPR40 is illustrated in **Figure 11C**. The side chain of LI01 mutant formed π–H and H-bond interaction with GPR40, which fixed LI01 mutant in

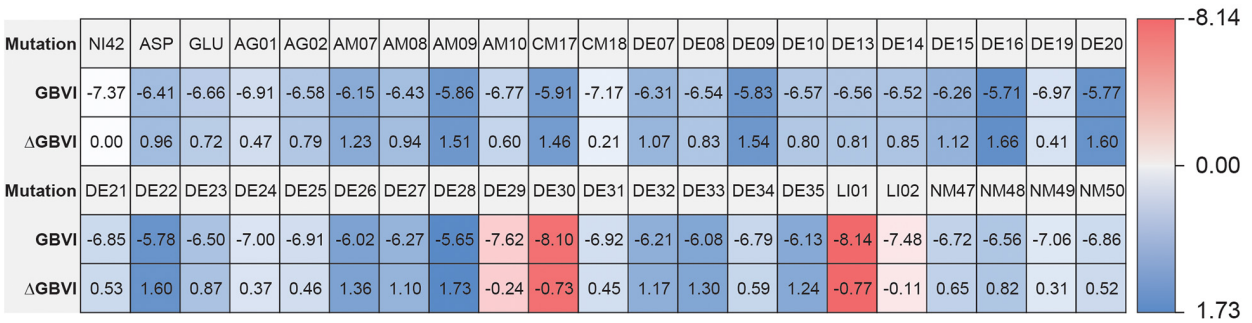

FIGURE 10 | Site-directed mutagenesis result.

TABLE 2 | The results of re-dock and energy minimization of AG02, DE20, and LI01 mutants.

Mutated amino acid	GBVI	Hydrogen/Ionic bond
AG02	−8.8651	Yes
DE20	−8.8189	Yes
LI01	−8.4173	No
AG02 (energy minimization)	−10.043	Yes
DE20 (energy minimization)	−10.404	Yes
LI01 (energy minimization)	−9.1861	Yes

GBVI, generalized Born/volume integral.

GPR40. However, the carboxyl group of LI01 did not form ionic or hydrogen bond interactions with ARG residues as expected. The AG02 and DE20 mutants successfully formed ionic and hydrogen bonds by increasing the GBVI score from −10.2063 to −8.8651 and −8.8189, respectively. The absence of ionic or hydrogen bonds in the GPR40–LI01 mutant complex results in a lower GBVI score at −8.4173 (**Table 2**). Standard energy minimization of the TAK-875 crystal structure was performed on three mutants to compare their performance. When energy minimization was done, the GBVI scores of the AG02 mutant and DE20 mutant were attained to −10.043 and −10.404, respectively. Both mutants showed expected performance. The carboxyl end of the LI01 mutant successfully contacted the ARG residues and formed ionic and hydrogen bonds, but the pockets might not be gathered to this extent, and it was difficult for the LI01 mutant to form ionic and hydrogen bonds. One solution worth considering was to simplify the side chain of the peptide outside the pocket and further extend the fatty chain where the carboxyl group was located. Finally, 4-15, 5-1, 4-4, DE20 mutant, and AG02 mutant are considered as potential active peptides that are analyzed in MD simulations (**Supplementary Figure 7**).

Molecular Dynamics Simulations of Five Peptides and Control

A 10-ns MD simulation was run on five peptides and the control. The structure at 10 ns shows that 5-1 and 4-4 are separated from the binding site (**Supplementary Figures 8D,E**), which indicated that the binding stability of the two under simulated physiological conditions was insufficient. The GBVI of the structure at 10 ns was calculated. The 5-1 and 4-4 that were separated from the binding site showed poor GBVI. The GBVI values of 4-15, AG02 mutant, DE20 mutant, and the control that remained at the binding site are −9.196, −8.564, −7.335, and −8.542, respectively (**Supplementary Figures 8A–C,F** and **Table 3**). The GBVI of all peptides increased, but the increase of the GBVI of the peptides remaining in the binding site was smaller, among which 4-15 showed the best GBVI maintenance ability. The two peptides leaving the binding site were excluded due to insufficient stability, and the remaining three peptides and the control were further analyzed.

The AG02 is selected as a representative example for MD analysis (**Figure 12**). RMSD measured the average positional change of all atoms between two structures. Based on the initial structure, the RMSD of all ligands and complexes was calculated. The RMSD calculated based on the protein and the complex was almost the same, so only the RMSD data of the complex were retained. AG02 mutant, DE20 mutant, and the control as ligands maintain relatively stable RMSD values throughout the simulation process (**Supplementary Figures 9B–D**). As a ligand, 4-15 showed a large increase in RMSD at about 3 ns then decreased and stabilized after 6 ns. When the RMSD of the 4-15 ligand is stable, the value is the largest among the four ligands, which indicates that the largest posture change occurred during the simulation (**Supplementary Figure 9A**). However, 4-15 retained the best GBVI at the end of the simulation, which might indicate that it was adjusted to a stable and high-affinity conformation. After the RMSD of the four simulated complexes was compared, the control complex and the DE20 complex show a stable trend at the end of the simulation (**Supplementary Figure 9**). The RMSD fluctuation of the AG02 complex in the later stage was larger than the former two. The 4-15 complex with the best affinity had a RMSD mutation in the late simulation stage, which might indicate that the conformation of the 4-15 complex will continue to change. MSD, the mean of the squared displacements of all atoms, was used to analyze the changes in the positions of proteins and ligands. The MSD values of the proteins and ligands in the control complex are the most stable

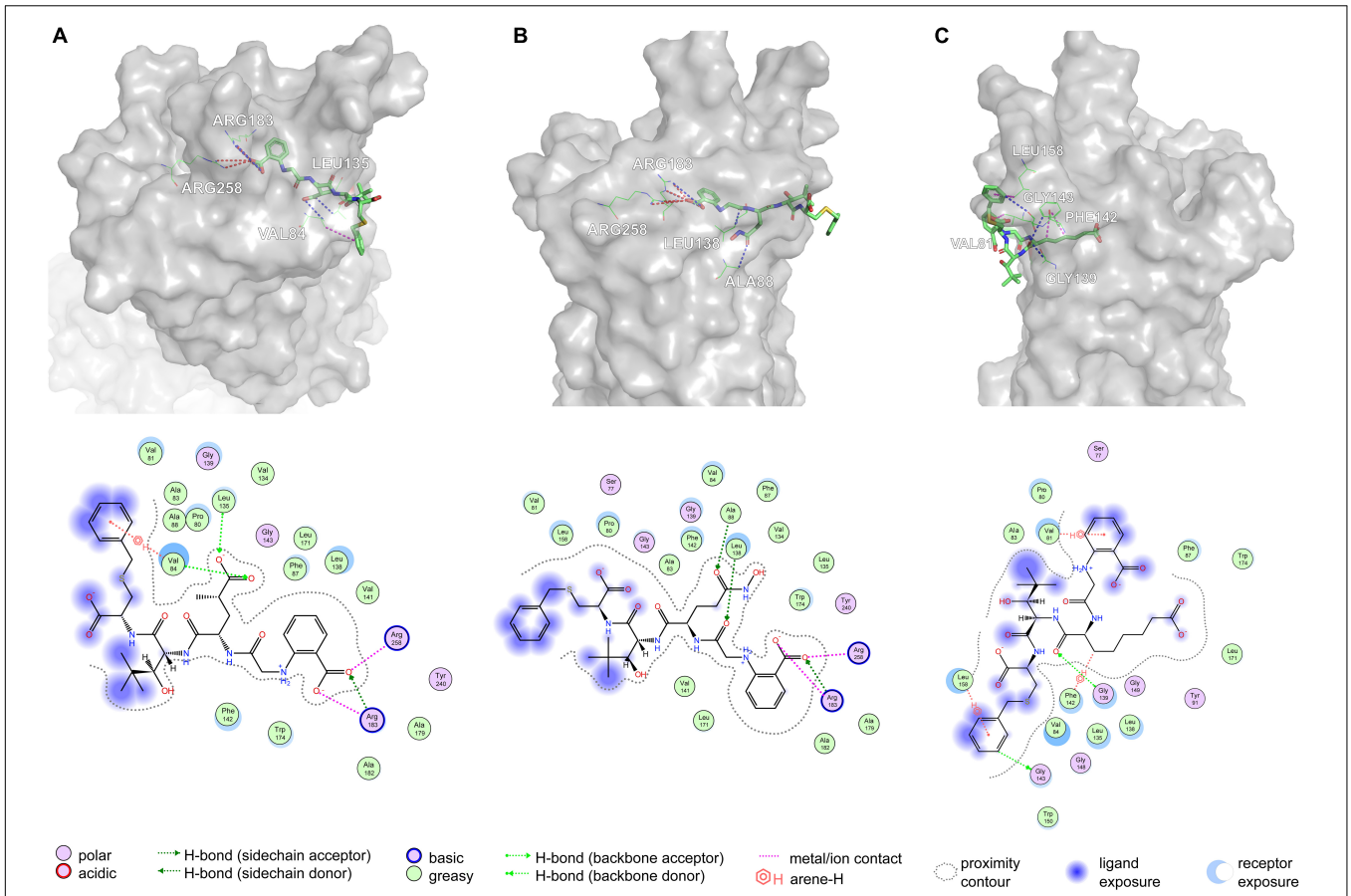

FIGURE 11 | Poses are generated by the flexible docking of mutants. In 3D pose diagrams, the red dash lines represent ionic bonds, magenta dash lines represent π–H interaction, and blue dash lines represent H-bonds. **(A)** DE20 mutant, **(B)** AG02 mutant, and **(C)** LI01 mutant.

(**Supplementary Figure 10**). The MSD changes of the proteins and ligands of the AG02 complex and the DE20 complex have similar trends, while the MSDs of the two components of the 4-15 complex are quite different (**Supplementary Figure 10A**). The protein and ligand of the 4-15 complex might have greater relative displacements resulting in low stability. Gyrate reflects the volume and shape of the molecule, and an increase in gyrate indicates that the system have expanded. The gyrate of DE20 mutant and the control is more stable than the other two molecules (**Supplementary Figure 11**). The *X*-axis component of the control was lower than the *Y*- and *Z*-axes, and its gyrate mainly derived from the plane where the *Y*- and *Z*-axes were located, which was related to the linear structure of the control. The gyrate of 4-15 entered a period of stability when the simulation was approaching the late stage but changed at the end of the simulation. The gyrate of the AG02 mutant was maintained in a relatively large interval during the entire simulation process, and the changes in the three-axis components of the AG02 mutant were also maintained in a range (**Supplementary Figure 11B**). The gyrates of the protein components of the three complexes other than 4-15 show a stable trend throughout the simulation process (**Supplementary Figure 12**). The protein component of the 4-15 complex expanded in volume at about 7 ns and then shrank. This might be due to the process of 4-15 adjusting its conformation to a higher affinity.

TABLE 3 | Comparison of peptide and control at the beginning and end of molecular dynamics simulation.

Name	GBVI at the beginning of MD	GBVI at the end of MD	Depart from GPR40
4-15	−10.206	−9.196	No
5-1	−9.620	−5.913	Yes
4-4	−9.579	−5.765	Yes
AG02	−10.043	−8.564	No
DE20	−10.404	−7.335	No
Control	−9.749	−8.542	No

GBVI, generalized Born/volume integral.

Similarly, the SASA of 4-15 is different from that of the other three ligands in the whole simulation process (**Supplementary Figure 13**). After 6 ns, the SASA of 4-15 dropped sharply, indicating that its conformation became tighter. At the end of the simulation, the 4-15 SASA returned to the level before 6 ns. 4-15 had undergone a large degree of conformation

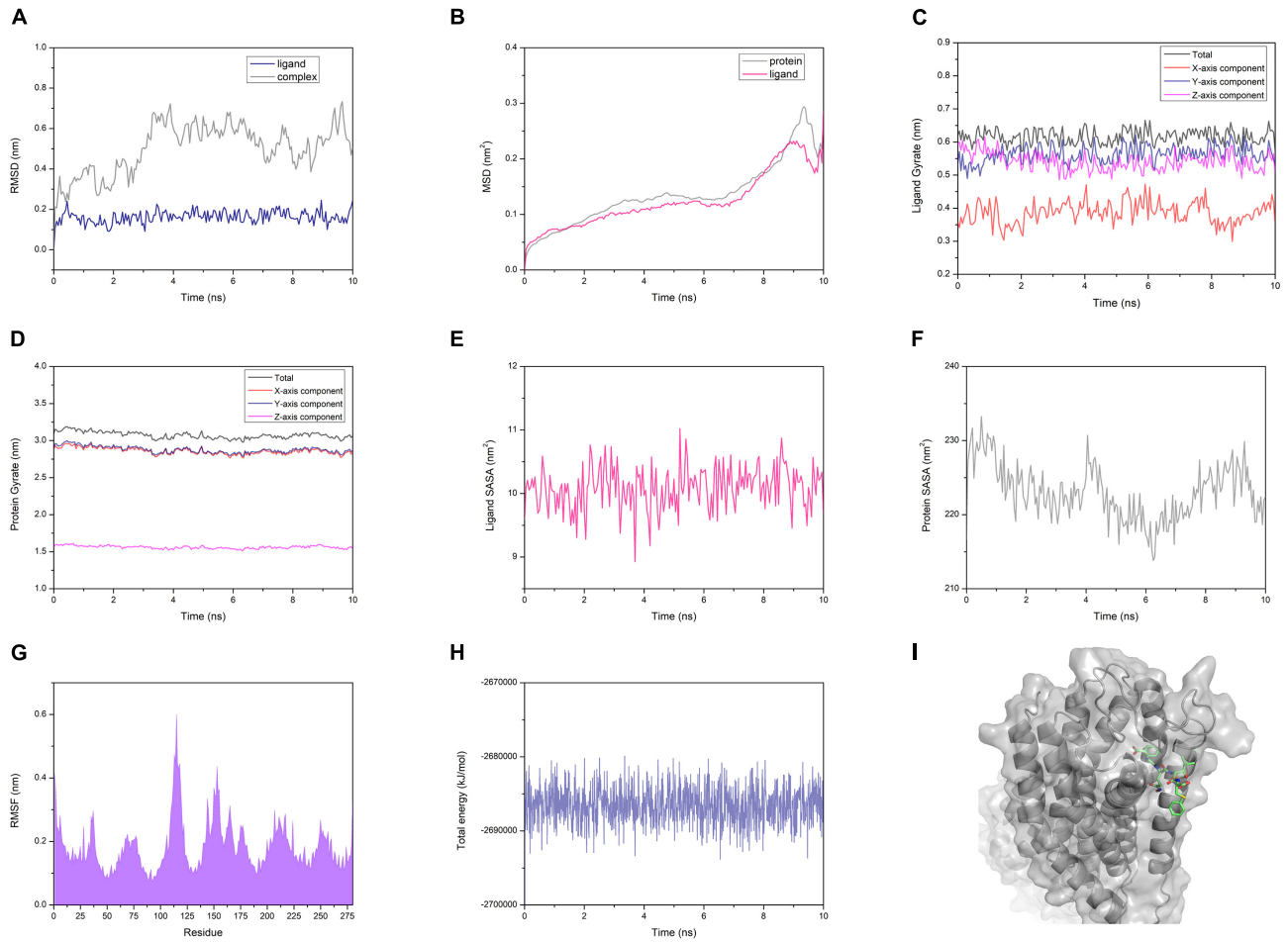

FIGURE 12 | (A) Root mean square deviation (RMSD) of the AG02 mutant and the complex. **(B)** Mean square displacement (MSD) of the AG02 mutant and GPR40 in the complex. **(C)** Gyrate of the AG02 mutant in the complex. **(D)** Gyrate of the GPR40 in the AG02 mutant complex. **(E)** Solvent-accessible surface area (SASA) of the AG02 mutant in the complex. **(F)** SASA of the GPR40 in the AG02 mutant complex. **(G)** Root mean square fluctuation (RMSF) of the GPR40 in the AG02 mutant complex. **(H)** The total energy of the AG02 mutant complex. **(I)** The AG02 mutant complex structures at 10 ns.

adjustment between 6 and 10 ns and maintained a high affinity at the end of the simulation. The SASA calculated based on the protein composition shows that 4-15 had the most stable trend (**Supplementary Figure 14**). This might be due to AG02, DE20, and the control mainly relying on the combination of salt bridge and GPR40, while 4-15 mainly relies on van der Waals interaction. 4-15 had the most stable hydrophobic interaction. RMSF reflected the average position change amplitude of the residue atoms in 10 ns. The protein residues of the four complexes all have similar RMSF distributions (**Supplementary Figure 15**). The residues numbered 75-85 and 130-140 showed lower RMSF. This region was where the binding cleft was located, which indicated that the residues at this location had higher stability due to binding with the ligand. The residues numbered 183 and 258 are arginine acids that form a salt bridge, and the RMSF recessed appears adjacent to these two residues (**Supplementary Figure 15**). The degree of depression of 4-15 near residues 183 and 258 was lower than that of the other three ligands, which might be due to 4-15 relying on van der Waals interaction instead of forming a salt bridge with arginine. The 4-15 complex has a total energy similar to that of the control, and the other two peptide complexes have a total energy lower than that of the control (**Supplementary Figure 16**). In addition, the total energy fluctuation of the peptide complex was similar to that of the control. 4-15, AG02 mutant, and DE20 mutant showed good performance similar to TAK-875 in MD simulations, and the three peptides were considered as potential GPR-40 agonists.

DISCUSSION

In this study, CNN can effectively extract local features by local receptive fields. CNN reduces complexity by sharing weights. It is a topological structure that uses spatial relationships to reduce the number of parameters, thereby improving the training efficiency of feedforward neural networks. Therefore, CNN can successfully realize the deep structure and effectively control the

occurrence of overfitting. To be able to perform the CNN, the 153 molecular features were converted to 1D sequences. We attempted to maximize the use of feature information through the deep structure of 1D CNN. However, the performance of CNN on the GPR40 agonist data set was less efficient than that of the three-layer DNN with a fully connected structure. A total of 153 features are independent according to their specific meanings (**Supplementary Table 2**). Local features were very important for sound signal, vibration signal, and text processing. Compared with global information extraction, local detail extraction could be used for model training more efficiently on signals like sound. But for the quantitative physical and chemical properties and composition information of molecules, the significance of the transformation and extraction of multiple features by the convolutional layer was not as great as the former. The molecular feature sequence lacked overall spatial information because 153 features had no spatial correlation. This would cause the local receptive field to extract the meaningless characteristics of neighboring spatial information. Although it had a deeper network structure, the partial failure of the local receptive field and the simplification of the connection structure might be the reason for the performance degradation of CNN. CNN was an excellent feature extractor, but the processing and optimization of 2D features with high independence and low noise and no adjacent spatial information would not get positive feedback. The feedback of PCA feature dimensionality reduction and LASSO feature selection on DNN also supported this view, and both methods led to variable degrees of performance degradation. The MSE shock of CNN at the end of the training was stronger than that of DNN; this is possibly because the data set is too small and the batch size of CNN is smaller than that of DNN.

For small data sets, the performance of MOE 2D molecular features was better than that of Morgan fingerprint features. The information content of a single MOE 2D descriptor was more complex than Morgan fingerprints, and the highly integrated features reduced the difficulty of convergence for the model. The 1,024-bit Morgan fingerprint was more suitable for large data sets. Although the data set had undergone the necessary preprocessing, the noise of EC50 labels measured by different laboratories could not be ignored. The instruments, methods, and materials used by the researcher during the label determination process would all affect the label. The error of the label and the size of the data set were the main reasons that restrict the accuracy of the DNN. How to obtain high-quality data sets was still an important issue in the development of AI.

Compared with that by non-processing, the number of new PCA features obtained by orthogonal projection is significantly reduced. Still, the apparent decline of DNN performance indicated that important information was lost in the PCA processing. The LASSO regression estimator retained 83 features with nonzero coefficients, and DNN showed a slight loss of accuracy. The model was not optimized for accuracy after the preprocessing of the features was completed, which might be due to less noise in the features.

For all the scoring functions, there was a noticeable feature from the result that the order of the value from each scoring function is Max > Dis/Ave > Min, which was consistent with their definition. The "Must match" function was so strict that none of the entities in the testing set match the fingerprint model. In some distance, a high standard of the scoring function is not always appropriate for the fingerprint method. For finding the novel compounds as GPR40 agonists, a high standard might lead one to miss potent candidates in screening. In the "Min" function, the scores were low and close to each other, which were not identical to the "Max" function. The model that could distinguish active entities from inactive entities is our goal. Therefore, the "Max" function was chosen to be the scoring function in this study. For the fingerprint type, the high absolute value of k is a key characteristic to evaluate the quality of each fingerprint type, and the GpiDAPH3 showed gorgeous output in this study.

The inputs of DNN are some quantitative molecular features, and different weights are assigned to the features after training. Compared with DNN, MFS recognizes the common features of data sets. Most molecules in the data set have similar main body skeletons, so the active molecules exported by MFS have skeleton similarity. DNN can have different tendencies in the main body skeleton and detailed features through weight distribution. Here, DNN tended to feature details, but access to the GPR40 binding site required certain linearity of the molecule. Therefore, the two models were combined to limit the linear and affinity groups of the peptides. In addition, DNN combined with MFS to predict peptides reduced the influence of label noise in the data set to a certain extent. For large data sets, it may be difficult for the MFS to extract a sufficient number of common features, while the DNN will have better performance due to its complex network structure.

The docking results show that the peptides are difficult to form an ion–hydrogen bond interaction similar to that of TAK-875, which might be due to the steric hindrance given by the peptide backbone and the peptide side chain. In contrast, the molecular structure of TAK-875 was roughly linear with almost no branches. The linear structure helped TAK-875 penetrate deep into GPR40 and formed ionic and hydrogen bonds with ARG183 and ARG258. As little steric hindrance as possible was necessary to pass through the narrow binding cleft. The data sets used for DNN and MFS contained a large number of TAK-875 analogs. DNN and MFS extracted high-frequency features, such as benzene ring, heterocyclic ring, carboxyl group, halogen, and sulfur element. Linear peptides contained at least one carboxyl group, which was the advantage of peptides to form ionic or hydrogen bonds. The main chain of the peptide was composed of repeating units of carbon-amide bonds, which meant that the groups preferred by the model could only exist in the side chain. The preference groups that exist only in the side chain led to the fact that the peptides selected by DNN and MFS were simple linear structures and much more complicated than TAK-875. The complex side-chain structure of peptides causes it proneness to molecular–residue spatial conflicts when passing through the binding cleft, which was not conducive to the deepening of the carboxyl-terminal or side chain ionic groups of the peptide.

It is worth noting that the single-point mutation of the AA within the binding cleft is an effective strategy to form ionic

bonds or hydrogen bonds. Moreover, a sufficiently long chain with a carboxyl terminus is necessary, which is essential for the peptide to reach ARG183 and ARG258. However, the long-chain carboxyl AAs of the LI01 mutant failed to reach the residues of ARG183 and ARG258. This is because the complex moiety outside the alpha helix of the LI01 mutant prevented the mutant from approaching GPR40. Interestingly, the mutant AAs of the AG02 mutant and the DE20 mutant did not form ionic bonds or hydrogen bonds with ARG residues as expected. Instead, the mutant binds to GPR40 in another position, and the mutant's G28 passes through the alpha helix to form ionic and hydrogen bonds (**Figures 11A,B**).

The five peptides after flexible docking were all inserted into the binding cleft by one residue, and the remaining peptide residues on the outer surface had different effects on the affinity of peptides. The two main interactions of 4-15 were formed by CM25 and G28 on the outer surface. The affinity of 5-1 was mainly derived from two interactions: the π–H interaction formed by the G35 residue on the outer surface. The peptide residues on the outer surface of 4-4 contributed little to the affinity; and P107 and P131, respectively, formed only weak hydrogen bonds and π–H interactions. Most of the affinity was derived from the salt bridge formed by the G28 residue and the GPR40 residue entering the binding cleft for the two candidate mutants. The binding modes of peptides can be divided into two types: the binding mode is dominated by external surface residues; the other is the mode where a single residue penetrates the binding cleft. The mode of a single residue entering the binding pocket profoundly depends on the strong salt bridge. The mode dominated by residues on the outer surface is more dependent on van der Waals interactions. The two models may have different specificities and affinities, which can provide references for advanced peptide design.

4-4 and 5-1 broke away from the binding site in MD; even they obtain low GBVI upon the flexible docking. The GBVI of other ligands increases to varying degrees in MD (**Table 3**). This might be caused by conditions similar to those of the environment in the human body used by MD. The temperature of 310K increased the instability of the system. MD showed that the stability of peptides that relied on van der Waals interaction was lower than that of peptides that relied on salt bridges. Peptides that relied on salt bridges needed to enter the binding site as deep as possible to contact the arginine residues, which might be the main reason for their high stability. The peptides of the two binding modes (4-15 and mutants) showed different characteristics in many aspects of the MD analysis results. Although peptides that relied on salt bridges showed higher stability, peptides that relied on van der Waals interactions could achieve higher affinity by complex interactions.

CONCLUSION

In summary, we developed a novel protocol to rationally design peptides and to identify a peptide database that may show potency for the activation of GPR40. Machine learning combined with MFS could efficiently distinguish between active and inactive molecules. The comparison results of the two machine learning methods showed that the DNN had better performance than the 1D CNN on the peptide activity prediction task based on small data sets. We found that the MFS model focused on the main skeleton of the chemical structure, and the DNN was able to pay attention to more structural details, so the combination of the two strategies could comprehensively scan the chemical structures. Besides, the SDM approach successfully optimized the interaction between the lead peptides and GPR40 to make the peptide more comparable with the active compound. Then, flexible docking, a credible method to evaluate the affinity, was performed to confirm the candidates; and five peptides were finally selected for MD simulations. Three peptides showing good stability in MD simulations were selected as promising leads against T2DM. The strategy concept described here can efficiently discover new active peptides and require only a small amount of computing resources, cost-effective for scale-up assessments in peptide drug development.

DATA AVAILABILITY STATEMENT

The original contributions presented in the study are included in the article/**Supplementary Material**, further inquiries can be directed to the corresponding authors.

AUTHOR CONTRIBUTIONS

JW, XC, and ZC conceived the idea, designed the study, and wrote the manuscript. JW and ZW directed the project, provided technical support, and corrections to the manuscript. XC and ZC performed all the experiments and analyzed the data. XC and ZC revised the manuscript according to the comments of JW and other co-authors. All authors contributed to the article and approved the submitted version.

FUNDING

This work was supported in part by the National Natural Science Foundation of China (82001887 to JW and 81900105 to ZW). JW was supported by a grant from the Hundred Talents Program (75110-18841227) from the Sun Yat-sen University and the Guangdong Basic and Applied Basic Research Foundation (2019A1515110326).

ACKNOWLEDGMENTS

The authors are grateful to Shaohua Ji and Jieyu Chen for their technical assistance and discussions.

SUPPLEMENTARY MATERIAL

The Supplementary Material for this article can be found online at: https://www.frontiersin.org/articles/10.3389/fbioe.2021.694100/full#supplementary-material

REFERENCES

Abraham, M. J., Murtola, T., Schulz, R., Páll, S., Smith, J. C., Hess, B., et al. (2015). GROMACS: High performance molecular simulations through multi-level parallelism from laptops to supercomputers. *SoftwareX* 1-2, 19–25. doi: 10.1016/j.softx.2015.06.001

Berman, H. M., Westbrook, J., Feng, Z., Gilliland, G., Bhat, T. N., Weissig, H., et al. (2000). The protein data bank. *Nucleic Acids Res.* 28, 235–242. doi: 10.1093/nar/28.1.235

Blad, C. C., Tang, C., and Offermanns, S. (2012). G protein-coupled receptors for energy metabolites as new therapeutic targets. *Nat. Rev. Drug Discov.* 11, 603–619. doi: 10.1038/nrd3777

Brooks, B. R., Brooks, C. L. III, Mackerell, A. D. Jr., Nilsson, L., Petrella, R. J., Roux, B., et al. (2009). CHARMM: the biomolecular simulation program. *J. Comput. Chem.* 30, 1545–1614. doi: 10.1002/jcc.21287

Cai, C., Guo, P., Zhou, Y., Zhou, J., Wang, Q., Zhang, F., et al. (2019). Deep learning-based prediction of drug-induced cardiotoxicity. *J. Chem. Inform. Model.* 59, 1073–1084. doi: 10.1021/acs.jcim.8b00769

Case, D. A., Darden, T. A., Cheatham, T. E., Simmerling, C. L., Wang, J., Duke, R. E., et al. (2008). *Amber 10*. San Francisco CA: University of California.

Cereto-Massagué, A., Ojeda, M. J., Valls, C., Mulero, M., Garcia-Vallvé, S., and Pujadas, G. (2015). Molecular fingerprint similarity search in virtual screening. *Methods* 71, 58–63. doi: 10.1016/j.ymeth.2014.08.005

Chatterjee, S., Khunti, K., and Davies, M. J. (2017). Type 2 diabetes. *Lancet* 389, 2239–2251. doi: 10.1016/S0140-6736(17)30058-2

Chen, C., Li, H., and Long, Y.-Q. (2016). GPR40 agonists for the treatment of type 2 diabetes mellitus: The biological characteristics and the chemical space. *Bioorg. Med. Chem. Lett.* 26, 5603–5612. doi: 10.1016/j.bmcl.2016.10.074

Esteva, A., Chou, K., Yeung, S., Naik, N., Madani, A., Mottaghi, A., et al. (2021). Deep learning-enabled medical computer vision. *NPJ Digit. Med.* 4:5. doi: 10.1038/s41746-020-00376-2

Gerber, P. R., and Müller, K. (1995). MAB, a generally applicable molecular force field for structure modelling in medicinal chemistry. *J. Comput. Aided Mol. Des.* 9, 251–268. doi: 10.1007/bf00124456

Grechishnikova, D. (2021). Transformer neural network for protein-specific de novo drug generation as a machine translation problem. *Sci. Rep.* 11:321. doi: 10.1038/s41598-020-79682-4

Hessler, G., and Baringhaus, K.-H. (2018). Artificial intelligence in drug design. *Molecules (Basel, Switzerland)* 23:2520. doi: 10.3390/molecules23102520

Ishida, S., Terayama, K., Kojima, R., Takasu, K., and Okuno, Y. (2019). Prediction and interpretable visualization of retrosynthetic reactions using graph convolutional networks. *J. Chem. Inform. Model.* 59, 5026–5033. doi: 10.1021/acs.jcim.9b00538

Kim, M., Gu, G. J., Koh, Y.-S., Lee, S.-H., Na, Y. R., Seok, S. H., et al. (2018). Fasiglifam (TAK-875), a G protein-coupled receptor 40 (GPR40) agonist, may induce hepatotoxicity through reactive oxygen species generation in a GPR40-dependent manner. *Biomol. Therap.* 26, 599–607. doi: 10.4062/biomolther.2017.225

Kingma, D. P., and Ba, J. (2014). Adam: a method for stochastic optimization. *arXiv* [Preprint] arXiv:1412.6980,

Krishna, A. G., and Anuradha, K. G. (2020). CoMFA, CoMSIA and HQSAR Analysis of 3-aryl-3-ethoxypropanoic acid derivatives as GPR40 modulators. *Curr. Drug Discov. Technol.* 17, 100–118. doi: 10.2174/1570163815666180829144431

Landrum, G. (2016). *RDKit: Open-Cource Cheminformatics Software*.

LeCun, Y., Bengio, Y., and Hinton, G. (2015). Deep learning. *Nature* 521, 436–444. doi: 10.1038/nature14539

Li, X., Xu, Y., Lai, L., and Pei, J. (2018). Prediction of human cytochrome p450 inhibition using a multitask deep autoencoder neural network. *Mol. Pharm.* 15, 4336–4345. doi: 10.1021/acs.molpharmaceut.8b00110

Li, Z., Zhou, Z., and Zhang, L. (2020). Current status of GPR40/FFAR1 modulators in medicinal chemistry (2016–2019): a patent review. *Expert Opin. Therap. Pat.* 30, 27–38. doi: 10.1080/13543776.2020.1698546

Mancini, A. D., and Poitout, V. (2015). GPR40 agonists for the treatment of type 2 diabetes: life after 'TAKing' a hit. *Diabetes Obes. Metab.* 17, 622–629. doi: 10.1111/dom.12442

Mendez, D., Gaulton, A., Bento, A. P., Chambers, J., De Veij, M., Félix, E., et al. (2018). ChEMBL: towards direct deposition of bioassay data. *Nucleic Acids Res.* 47, D930–D940. doi: 10.1093/nar/gky1075

Muegge, I., and Mukherjee, P. (2016). An overview of molecular fingerprint similarity search in virtual screening. *Expert Opin. Drug Discov.* 11, 137–148. doi: 10.1517/17460441.2016.1117070

Naik, H., Lu, J., Cao, C., Pfister, M., Vakilynejad, M., and Leifke, E. (2013). Pharmacometric approaches to guide dose selection of the novel GPR40 agonist TAK-875 in subjects with type 2 diabetes mellitus. *CPT: Pharm. Syst. Pharmacol.* 2:22. doi: 10.1038/psp.2012.23

Naik, H., Vakilynejad, M., Wu, J., Viswanathan, P., Dote, N., Higuchi, T., et al. (2012). Safety, tolerability, pharmacokinetics, and pharmacodynamic properties of the GPR40 agonist TAK-875: results from a double-blind, placebo-controlled single oral dose rising study in healthy volunteers. *J. Clin. Pharmacol.* 52, 1007–1016. doi: 10.1177/0091270011409230

Naïm, M., Bhat, S., Rankin, K. N., Dennis, S., Chowdhury, S. F., Siddiqi, I., et al. (2007). Solvated interaction energy (SIE) for scoring protein- ligand binding affinities. 1. Exploring the parameter space. *J. Chem. Inform. Model.* 47, 122–133. doi: 10.1021/ci600406v

Nair, V., and Hinton, G. E. (2010). "Rectified linear units improve restricted boltzmann machines," in *Proceedings of the 27th International Conference on International Conference on Machine Learning*, (Madison WI).

Nutan, S., Sunita, B., and Tejpal Singh, C. (2017). Recent advances in development of GPR40 modulators (FFA1/FFAR1): an emerging target for type 2 diabetes. *Mini Rev. Med. Chem.* 17, 947–958. doi: 10.2174/1389557517666170120152917

Sharma, A., Kumar, R., Ranjta, S., and Varadwaj, P. K. (2021). SMILES to smell: decoding the structure–odor relationship of chemical compounds using the deep neural network approach. *J. Chem. Inform. Model.* 61, 676–688. doi: 10.1021/acs.jcim.0c01288

Soliman, K., Grimm, F., Wurm, C. A., and Egner, A. (2021). Predicting the membrane permeability of organic fluorescent probes by the deep neural network based lipophilicity descriptor DeepFl-LogP. *Sci. Rep.* 11:6991. doi: 10.1038/s41598-021-86460-3

Sriram, K., and Insel, P. A. (2018). G Protein-coupled receptors as targets for approved drugs: how many targets and how many drugs? *Mol. Pharmacol.* 93, 251–258. doi: 10.1124/mol.117.111062

Srivastava, A., Yano, J., Hirozane, Y., Kefala, G., Gruswitz, F., Snell, G., et al. (2014). High-resolution structure of the human GPR40 receptor bound to allosteric agonist TAK-875. *Nature* 513, 124–127. doi: 10.1038/nature13494

Sun, C., Zhang, M., Wu, R., Lu, J., Xian, G., Yu, Q., et al. (2021). A convolutional recurrent neural network with attention framework for speech separation in monaural recordings. *Sci. Rep.* 11:1434. doi: 10.1038/s41598-020-80713-3

Tibshirani, R. (2011). Regression shrinkage and selection via the lasso: a retrospective. *J. R. Stat. Soc. Ser. B (Statistical Methodology)* 73, 273–282. doi: 10.1111/j.1467-9868.2011.00771.x

Vilar, S., Cozza, G., and Moro, S. (2008). Medicinal chemistry and the molecular operating environment (MOE): application of QSAR and molecular docking to drug discovery. *Curr. Topics Med. Chem.* 8, 1555–1572. doi: 10.2174/156802608786786624

Wang, J., Wang, A. Z., Lv, P., Tao, W., and Liu, G. (2018). Advancing the pharmaceutical potential of bioinorganic hybrid lipid-based assemblies. *Adv. Sci. (Weinh)* 5:1800564. doi: 10.1002/advs.201800564

Wang, J., Zope, H., Islam, M. A., Rice, J., Dodman, S., Lipert, K., et al. (2020). Lipidation approaches potentiate adjuvant-pulsed immune surveillance: a design rationale for cancer nanovaccine. *Front. Bioeng. Biotechnol.* 8:787. doi: 10.3389/fbioe.2020.00787

Yabuki, C., Komatsu, H., Tsujihata, Y., Maeda, R., Ito, R., Matsuda-Nagasumi, K., et al. (2013). A novel antidiabetic drug, fasiglifam/TAK-875, acts as an ago-allosteric modulator of FFAR1. *PLoS One* 8:e76280. doi: 10.1371/journal.pone.0076280

Yang, X., Wang, Y., Byrne, R., Schneider, G., and Yang, S. (2019). Concepts of Artificial Intelligence for Computer-Assisted Drug Discovery. *Chemical Reviews* 119, 10520–10594. doi: 10.1021/acs.chemrev.8b00728

Zhang, Z., Park, C. Y., Theesfeld, C. L., and Troyanskaya, O. G. (2021). An automated framework for efficiently designing deep convolutional neural networks in genomics. *Nat. Mach. Intell.* 3, 392–400. doi: 10.1038/s42256-021-00316-z

Zheng, Y., Ley, S. H., and Hu, F. B. (2018). Global aetiology and epidemiology of type 2 diabetes mellitus and its complications. *Nat. Rev. Endocrinol.* 14, 88–98. doi: 10.1038/nrendo.2017.151

Zoete, V., Cuendet, M. A., Grosdidier, A., and Michielin, O. (2011). SwissParam: A fast force field generation tool for small organic molecules. *J. Comput. Chem.* 32, 2359–2368. doi: 10.1002/jcc.21816

Zorzi, A., Middendorp, S. J., Wilbs, J., Deyle, K., and Heinis, C. (2017). Acylated heptapeptide binds albumin with high affinity and application as tag furnishes long-acting peptides. *Nat. Commun.* 8:16092. doi: 10.1038/ncomms16092

Conflict of Interest: The authors declare that the research was conducted in the absence of any commercial or financial relationships that could be construed as a potential conflict of interest.

Copyright © 2021 Chen, Chen, Xu, Lyu, Li, Li, Wang and Wang. This is an open-access article distributed under the terms of the Creative Commons Attribution License (CC BY). The use, distribution or reproduction in other forums is permitted, provided the original author(s) and the copyright owner(s) are credited and that the original publication in this journal is cited, in accordance with accepted academic practice. No use, distribution or reproduction is permitted which does not comply with these terms.

frontiers in Bioengineering and Biotechnology

REVIEW
published: 24 June 2021
doi: 10.3389/fbioe.2021.707479

Antioxidant Therapy and Antioxidant-Related Bionanomaterials in Diabetic Wound Healing

Wenqian Zhang[1,2], Lang Chen[1,2], Yuan Xiong[1,2], Adriana C. Panayi[3], Abudula Abududilibaier[1,2], Yiqiang Hu[1,2], Chenyan Yu[1,2], Wu Zhou[1,2], Yun Sun[2,4], Mengfei Liu[1,2], Hang Xue[1,2], Liangcong Hu[1,2], Chenchen Yan[1,2], Xuedong Xie[1,2], Ze Lin[1,2], Faqi Cao[1,2], Bobin Mi[1,2]* and Guohui Liu[1,2]**

[1] Department of Orthopaedics, Union Hospital, Tongji Medical College, Huazhong University of Science and Technology, Wuhan, China, [2] Hubei Province Key Laboratory of Oral and Maxillofacial Development and Regeneration, Wuhan, China, [3] Division of Plastic Surgery, Brigham and Women's Hospital and Harvard Medical School, Boston, MA, United States, [4] Department of Neurosurgery, Union Hospital, Tongji Medical College, Huazhong University of Science and Technology, Wuhan, China

OPEN ACCESS

Edited by:
Junqing Wang,
Sun Yat-sen University, China

Reviewed by:
Ren Xu,
Xiamen University, China
Tao Yu,
Shanghai Tongji Hospital, Tongji University School of Medicine, China

***Correspondence:**
Faqi Cao
13971293030@163.com
Bobin Mi
mibobin@hust.edu.cn
Guohui Liu
liuguohui@hust.edu.cn

Specialty section:
This article was submitted to Biomaterials, a section of the journal Frontiers in Bioengineering and Biotechnology

Received: 10 May 2021
Accepted: 03 June 2021
Published: 24 June 2021

Citation:
Zhang W, Chen L, Xiong Y, Panayi AC, Abududilibaier A, Hu Y, Yu C, Zhou W, Sun Y, Liu M, Xue H, Hu L, Yan C, Xie X, Lin Z, Cao F, Mi B and Liu G (2021) Antioxidant Therapy and Antioxidant-Related Bionanomaterials in Diabetic Wound Healing. Front. Bioeng. Biotechnol. 9:707479. doi: 10.3389/fbioe.2021.707479

Ulcers are a lower-extremity complication of diabetes with high recurrence rates. Oxidative stress has been identified as a key factor in impaired diabetic wound healing. Hyperglycemia induces an accumulation of intracellular reactive oxygen species (ROS) and advanced glycation end products, activation of intracellular metabolic pathways, such as the polyol pathway, and PKC signaling leading to suppression of antioxidant enzymes and compounds. Excessive and uncontrolled oxidative stress impairs the function of cells involved in the wound healing process, resulting in chronic non-healing wounds. Given the central role of oxidative stress in the pathology of diabetic ulcers, we performed a comprehensive review on the mechanism of oxidative stress in diabetic wound healing, focusing on the progress of antioxidant therapeutics. We summarize the antioxidant therapies proposed in the past 5 years for use in diabetic wound healing, including Nrf2- and NFκB-pathway-related antioxidant therapy, vitamins, enzymes, hormones, medicinal plants, and biological materials.

Keywords: wound healing, antioxidative therapy, oxidative stress, bionanomaterials, diabetes mellitus

INTRODUCTION

Type II Diabetes (T2DM) is characterized by chronic hyperglycemia and is associated with significant vasculopathy (Brownlee, 2001). T2DM is a worldwide healthcare problem with increasing global prevalence (NCD Risk Factor Collaboration (Ncd-RisC), 2016). Foot ulcers, a lower-extremity complication of T2DM with high recurrence rates, is a substantial burden for patients with T2DM and society as a whole (Armstrong et al., 2017). The lifetime risk of a patient with T2DM developing a foot ulcer is estimated to be as high as 25% (Singh et al., 2005), and it is believed that every 30 s worldwide a lower limb is amputated as a consequence of T2DM (Boulton et al., 2005). An effective therapeutic approach that can improve wound healing in T2DM has the potential to revolutionize medicine.

Wound healing is the precise interplay of complex biological and molecular events including cell migration, cell proliferation, and extracellular matrix (ECM) deposition. The process is classically divided into four overlapping phases of coagulation, inflammation, migration-proliferation (including matrix deposition), and remodeling (Falanga, 2005). Wound healing requires the combined function of different cells including platelets, neutrophils, monocytes, macrophages, endothelial cells, keratinocytes, fibroblasts, and myofibroblasts. However, these processes and healing stages have been shown to be dysfunctional in patients with T2DM and collectively lead to overall impaired healing of acute wounds predisposing the patients to chronic, non-healing wounds such as diabetic foot ulcers (Avishai et al., 2017).

Oxidative stress is one of the main mechanisms involved in chronic diabetic foot ulcers. The concept of oxidative stress was introduced by H. Sies in 1985, who defined it as a shift in the prooxidant-antioxidant balance in favor of the former. Oxidative stress now also refers to an imbalance between oxidants and antioxidants in favor of oxidants, leading to a disruption of redox signaling and molecular damage (Sies, 2015). Oxidative stress can be classified into different subgroups ranging from physiological oxidative stress to excessive and toxic oxidative burden (Lushchak, 2014). Oxygen-dependent redox-sensitive signaling processes are an integral component of the healing cascade. Oxidative stress is necessary for wound disinfection and promotes wound healing by facilitating hemostasis, inflammation, angiogenesis, granulation tissue formation, wound closure, and development and maturation of the extracellular matrix(ECM) (Schafer and Werner, 2008; Sen and Roy, 2008). However, excessive and uncontrolled oxidative stress results in sustaining and deregulating inflammation, playing a central role in the pathogenesis of chronic non-healing wounds (Bryan et al., 2012). In diabetic wounds, ROS production through several ROS-generating enzymes is elevated, resulting in impaired wound healing processes via increased cell apoptosis and senescence with ongoing oxidative stress, lipid peroxidation, protein modification, and DNA damage (Schafer and Werner, 2008).

Given the importance of oxidative stress in the pathology of diabetic ulcers, this comprehensive review will focus on oxidative stress in diabetic wound healing, paying particular attention to the progress of antioxidant therapies in the past 5 years (**Table 1**).

OXIDATIVE STRESS IN WOUND HEALING

Normal Wound Healing

Wound healing is a precise integration of complex biological and molecular events including cell migration, cell proliferation, and ECM deposition. It can be divided into the four overlapping phases of coagulation, inflammation, migration-proliferation (including matrix deposition), and remodeling (Falanga, 2005). As has been reported in numerous studies, wound healing is the joint effort of various cells including platelets, neutrophils, monocytes, macrophages, endothelial cells, keratinocytes, fibroblasts, and myofibroblasts.

In the coagulation phase, platelets, together with a meshwork of polymerized fibrinogen (fibrin), fibronectin, vitronectin, and thrombospondin, participate in the construction of fibrin plugs, providing a temporary wound coverage to protect the wound and defend bacteria (Singer and Clark, 1999). During their incorporation within the plug, platelets aggregate and release a wide range of growth factors such as platelet-derived growth factor (PDGF), epidermal growth factor (EGF) and transforming growth factor-β (TGF-β) (Rodrigues et al., 2019).

During the inflammation phase, neutrophils and monocytes, recruited by PDGF, aid in microorganism killing and produce several key growth factors and mediators to promote wound healing (Singer and Clark, 1999). Neutrophils secrete proteolytic enzymes and release reactive oxygen species (ROS) into the wound bed to combat invading bacteria. Neutrophils also release important cytokines, such as TGF- β1, monocyte chemoattractant protein 1, and fragments of ECM proteins to recruit monocytes (Mirza and Koh, 2015). Monocytes, recruited to the wound, differentiate into pro-inflammatory macrophages to aid in the inflammatory process by phagocytosing dead neutrophils, cellular debris and bacteria (Schafer and Werner, 2008). These leukocytes also secrete new growth factors and cytokines such as TGF- β1, fibroblast growth factor (FGF), PDGF, and vascular endothelial growth factor (VEGF) aiding in the migration-proliferation phase (Mirza and Koh, 2015).

In the migration-proliferation phase, keratinocytes start migrating with the disassembly of hemidesmosomes, and a keratinocyte proliferative burst is followed to close the defect and create a new epidermis (re-epithelialization) (Martin, 1997). Fibroblasts convert into myofibroblasts that secrete ECM proteins, aiding in closure of the wound (Bainbridge, 2013; Quan et al., 2013). Endothelial cells also play a crucial role in this phase. Endothelial cells proliferate, migrate, and branch to form new blood vessels (Falanga, 2005), allowing re-supply of oxygen and other nutrients. While new blood vessels form, endothelial cells, together with macrophages and fibroblasts, form the early granulation tissue that begins the process of contraction (Martin, 1997). Due to expression of α- smooth muscle actin in microfilament bundles or stress fibers, myofibroblasts exhibit contractile properties, promoting contraction and maturation of the granulation tissue (Bainbridge, 2013). Granulation tissue lays down collagen, eventually resulting in scar formation (Bainbridge, 2013; Landen et al., 2016; Tracy et al., 2016).

The remodeling phase is the last phase in healing. In this phase, synthesis of ECM is considerably reduced, and synthesized components are modified as the matrix is remodeled. Excess cells undergo apoptosis and are removed by resident macrophages and histiocytes (Schafer and Werner, 2008). With the development of the recovery process, granulation tissue rich in type III collagen is replaced by a less vascularized and more resistant tissue rich in type I collagen (Singer and Clark, 1999). The newly formed tissue is strong due to the tensile strength of various components of the ECM and fibroblasts of the scar tissues (Stadelmann et al., 1998). Elastin, which is absent in the granulation tissue and normally contributes to skin elasticity, reappears in this phase

TABLE 1 | Antioxidant therapies used in diabetic wounds reported in the past 5 years (2016–2020).

Category	Therapy	Mechanism	Effects	References
Nrf2-pathway-related	siKeap1	Inhibit Keap1, increase Nrf2 nuclear translocation	Accelerate wound healing, improve redox homeostasis, and promote angiogenesis	Soares et al., 2016
	Lipoproteoplex	Deliver siKeap1	Restore Nrf2 antioxidant function, Accelerate wound healing, augment reduction-oxidation homeostasis	Rabbani et al., 2017
	Exosomes from ADSCs overexpressing Nrf2	Increase Nrf2 level	Prevent senescence of EPCs, inhibit ROS and inflammatory cytokine formation and promote angiogenesis	Li et al., 2018b
NFκB-pathway-related	miR-146a	Decrease levels of phosphorylated IκB-α, phosphorylated NFκB, and total NFκB	/	Zgheib et al., 2019; Niemiec et al., 2020; Sener et al., 2020
	SRT1720	Activate SIRT1	Accelerate wound healing and promote angiogenesis	Li et al., 2019;
Vitamins	Vitamins E and C	Restore the antioxidant enzyme activities, reduce ROS levels	Accelerate wound healing	Pessoa et al., 2016
	Mono-epoxy-tocotrienol-α	Antioxidant effects	Increase the expression of genes involved in cell growth, motility, angiogenesis and mitochondrial function	Xu et al., 2017
	Folic acid	Suppress oxidative stress	Accelerate wound healing and promote collagen deposition	Zhao et al., 2018
	SkQ1	Suppress mitochondrial ROS production	Accelerate wound healing and promote epithelization, granulation tissue formation, and angiogenesis	Demyanenko et al., 2017
Enzymes	SOD	Catalyze the decomposition of superoxide radicals into hydrogen peroxide	Accelerate wound healing	Zhang et al., 2018
	HO-1	Cleaves the α-methene bridges of heme to produce equimolar amounts of biliverdin and carbon monoxide	Inhibit inflammatory cytokine formation, increase antioxidants and promote angiogenesis	Chen et al., 2016b; Kumar et al., 2019
Hormones	17β-estradiol	Regulate energy homeostasis and glucose metabolism	Reduce excessive ROS formation and facilitate cell survival	Oh et al., 2019
	5α-dihydrotestosterone	Regulate energy homeostasis and glucose metabolism	Increase the proportion of type I and type III collagen fibers and superoxide dismutase levels	Goncalves et al., 2016
Medicinal plants	Dimethyl fumarate	Activate Nrf2	Decrease oxidative damage and inflammation, and accelerate wound healing	Li et al., 2018b
	RTA 408	Upregulate expression of Nrf2 target genes	Accelerate wound healing and promote re-epithelialization	Rabbani et al., 2018
	Genistein	Activate Nrf2, downregulate NFκB	Accelerate wound healing	Eo et al., 2016
	Asiatic acid	Downregulate NFκB activation and reduce pro-inflammatory cytokines	Attenuate prolonged inflammation and Accelerate wound healing	Han et al., 2019
	Syringic acid	Suppress NFκB activation and the inflammatory response	Accelerate wound healing	Ren et al., 2019
	Hydroethanolic extract of strychnos pseudoquina	Modulate oxidative status and microstructural reorganization	Accelerate wound healing	Sarandy et al., 2017
	Deoxyshikonin	Exert antioxidant activity and promote phosphorylation of ERK and p38 and VEGFR-2 expression	Accelerate wound healing	Park et al., 2018
	Quercetin	Suppress oxidative stress and enhance the antioxidant defense system	Accelerate wound healing	Ahmed et al., 2018
Biological materials	SOD-loaded hydrogel	Sustained release of SOD with high activity	Promote re-epithelialization and collagen deposition	Zhang et al., 2018
	CONP-loaded GelMA hydrogel	Uptake exudate, scavenge free radicals	Accelerate wound healing	Augustine et al., 2021
	Edaravone-loaded alginate-based nanocomposite hydrogel	Downregulate ROS levels	Accelerate wound healing	Fan et al., 2019

(Continued)

TABLE 1 | Continued

Category	Therapy	Mechanism	Effects	References
	Injectable, self-healable zwitterionic cryogel	Sustained release of miRNA-146a-CNPs	Accelerate wound healing	Sener et al., 2020
	Nanosilk	Deliver CNP-miR146a to the wound bed	Downregulate proinflammatory signaling and promote pro-fibrotic processes	Niemiec et al., 2020
	AA-PL scaffolds	Relieve the high oxidative stress, inflammation and infection	Promote angiogenesis, extracellular matrix formation and re-epithelization	Han et al., 2019
	tFNAs	Activate the Akt/Nrf2/HO-1 signaling pathway	Control inflammation, prevent oxidative damage, facilitate angiogenesis	Lin et al., 2020
	Berberine nanohydrogel	Activate SIRT1, inhibit the expression of NFκB	Accelerate wound healing, reduce inflammation, promote angiogenesis	Zhang et al., 2020

(Bainbridge, 2013; Landen et al., 2016; Tracy et al., 2016). The skin barrier is re-established to protect the newly formed tissue from the environment (Loots et al., 1998). The remodeling phase proclaims the termination of wound healing.

Oxidative Stress Impairs Diabetic Wound Healing

Individuals with diabetes demonstrate disturbances in all four individual healing stages that collectively lead to an overall impaired wound healing predisposing to chronic non-healing wounds such as diabetic foot ulcers (Avishai et al., 2017). Several studies have highlighted that impaired wound healing in diabetes is associated with the elevated levels of oxidative stress (Martin, 1996; Schafer and Werner, 2008). Hyperglycemia induces an increase in intracellular ROS generation, activating intracellular metabolic pathways, such as the polyol pathway and PKC signaling, leading to suppression of antioxidant enzymes and compounds (Evans et al., 2002). Excessive ROS generation in diabetes is also due to acute rises in serum glucose and accumulation of advanced glycation end products (AGEs) (Monnier et al., 2006). AGEs are potent prooxidants, a risk factor for injury and chronic ulcers. In chronic diabetic wounds, redox homeostasis is damaged by excessive ROS generation, causing loss of antioxidants and resulting in cell oxidative damage and wound healing inhibition (Wlaschek and Scharffetter-Kochanek, 2005; Zhang et al., 2018). The impacts of oxidative stress on the individual phase of wound healing are summarized as follows.

In the inflammation phase, oxidative stress in wounds influences the normal function of macrophages and neutrophils, resulting in prolonged inflammation. The increased number of neutrophils results in the production of ROS and excessive oxidative stress during inflammation, which damages the surrounding cells, tissues, and fibroblasts (Park et al., 2018). Oxidative stress also influences the macrophage differentiation and polarization impairing wound healing. T2DM induces pathological hematopoietic stem cells (HSCs) oxidant stress that can reduce the number and function of terminally differentiated inflammatory cells. Yan et al. (2018) reported that T2DM induces oxidant stress in HSC through a Nox-2-dependent mechanism and decreases microRNA let-7d-3p, which, in turn, upregulates the expression of Dnmt1. Increased Dnmt1 expression results in the downregulation of the genes responsible for HSC differentiation to monocytes/macrophages, and consequently reduces macrophage infiltration, driving polarization toward M1 macrophages (pro-inflammatory function), which causes excessive and prolonged inflammation in murine diabetic wounds (Khanna et al., 2010; Gallagher et al., 2015). Moreover, diabetic fibrocytes show a pro-inflammatory phenotype, which also contributes to arrest the process at the inflammatory phase (Falanga, 2005).

In the migration-proliferation phase, oxidative stress exerts its effects on endothelial cells, keratinocytes and fibroblasts, resulting in endothelial dysfunction, abnormal keratinocyte migration and proliferation, as well as impaired fibroblast proliferation, migration, differentiation. Oxidative stress is commonly implicated as an important unifying mechanism in endothelial dysfunction, which underlies both the micro- and macrovascular complications of T2DM (Rochette et al., 2014). Oxidative stress is a cell damage related factor that causes damage to proteins, lipids, and DNA in the cells, leading to cell death and subsequent tissue dysfunction (Long et al., 2016). Oxidative stress alters the functional capacity of endothelial nitric oxide synthase (eNOS) and directly degrades vasoprotective nitric oxide (NO) by ROS, resulting in diminished bioavailability of NO and endothelial dysfunction (Roberts and Porter, 2013). Oxidative stress also impairs keratinocytes. High-glucose environments disturb keratinocyte function including migration and proliferation. Gap junction abnormalities increase oxidative stress (Hu and Lan, 2016). Higher oxidative stress is associated with increased production of Interleukin (IL)-8 in high glucose–treated keratinocytes, which is responsible for recruiting neutrophils and impaired wound healing (Lan et al., 2013). Oxidative stress contributes to antiangiogenic molecule thrombospondin-1 (TSP1) DNA hypomethylation in keratinocytes exposed to hyperglycemia, resulting in overexpression of TSP1 that impairs proper wound healing (Lan et al., 2016). Oxidative stress also impairs fibroblasts. Increased free radical generation and lack of antioxidant defenses interfere with fibroblast proliferation (Schafer and Werner, 2008). Diabetic fibrocytes also demonstrate reduced expression of the C-X-C motif and C-C motif chemokine receptors (CXCR)4, (CCR)5, and CCR7 with weak migration in response to their ligands (CXCL)12, (CCL) 5, and CCL21

(Walker et al., 2018). Diabetic fibrocytes lose the ability to differentiate into myofibroblast-like cells on stimulation by growth factors that promote wound healing (Walker et al., 2018).

In the remodeling phase, oxidative stress impairs collagen deposition and ECM remodeling. Delayed diabetic wound healing is characterized by an increase in matrix metalloproteinase (MMPs) and a reduction in some growth factors, such as TGF-β1 (Jude et al., 2002; Blakytny and Jude, 2006; Long et al., 2016). TGF-β1 signaling works as the regulator in a series of biological processes of skin regeneration and wound healing, such as angiogenesis and re-epithelialization (Amento and Beck, 1991). High levels of ROS impair collagen production and tissue growth, resulting in halted wound closure (Loo et al., 2012). Interference of ECM production is highlighted through disruption of TGF-β1 signaling (Davies, 2005; He et al., 2014). High ROS levels affect ECM remodeling by regulating MMP expression (Hantke et al., 2002), which remodels tissue through proteolytic degradation (Caley et al., 2015). Excessive MMP activity inhibits the remodeling process and delays wound healing (Ravanti and Kahari, 2000).

Taken together, the impact of oxidative stress induced by hyperglycemia is widespread impairing the majority of cells and mechanisms involved in wound healing.

ANTIOXIDANT THERAPY IN DIABETIC WOUND HEALING

The Nrf2 Pathway and Antioxidant Therapy

The nuclear factor erythroid–related factor 2 (Nrf2)/kelch-like erythroid cell–derived protein 1 (Keap1) pathway encompasses a central cellular defense mechanism that maintains redox homeostasis, but is disrupted in T2DM (Kensler et al., 2007; Soares et al., 2016). Nrf2 is a transcription factor regulating a wide range of genes influencing redox homeostasis, metabolism and repair (Hayes and Dinkova-Kostova, 2014). Keap1 is a Cul-E3 ligase regulating the progress of Nrf2 turnover and the ability of Nrf2 to translocate to the nucleus and activate the cellular antioxidant response (Wakabayashi et al., 2004). Keap1 functions as an intracellular ROS sensor and oxidants and electrophiles modify its cysteine residues. Under unstressed conditions, Keap1 interacts with Nrf2 and the cell's actin cytoskeleton to sequester Nrf2 to the cytoplasm and promote ubiquitination and degradation of Nrf2 (Choi et al., 2014; Zoja et al., 2014). In the presence of oxidative stress, certain cysteine-rich oxidant and electrophile sensing regions of Keap1 are covalently modified, preventing Nrf2 ubiquitination. Nrf2 dissociates from its repressor Keap1, translocating to the nucleus and forming heterodimers with the Maf protein in the nucleus binding to Maf recognition element sequences, such as the antioxidant response element (ARE) and electrophile response element (EpRE) (Surh et al., 2005). Nrf2 responds to oxidative stress by activating key genes including NAD(P)H quinone oxidoreductase 1 (NQO1), manganese superoxide dismutase (MnSOD), heme oxygenase 1 (HO-1), glutamate cysteine ligase (GCL), and glutathione S-transferases (GSTs) (Baird and Dinkova-Kostova, 2011; Ruiz et al., 2013).

Since the Nrf2/Keap1 pathway is one of the master switch systems in oxidative stress (Sies, 2015), therapies based on Nrf2/Keap1 pathway have been reported. Keap1 is an important target in antioxidant therapy. Topical delivery of siRNAs is considered to be effective in diabetic wound treatment due to its temporary limitation to local applications and extrachromosomal function. Soares et al. (2016) reported that application of siRNA against Keap1 improved the redox homeostasis and accelerated diabetic tissue regeneration to near-normal levels by upregulating Nrf2-downstream antioxidant gene products such as NQO1 and MnSOD. Biomaterials designed to improve delivery efficiency of siKeap1 also show excellent effect in diabetic wound healing with severe oxidative stress. Rabbani et al. (2017) constructed a novel lipoproteoplex (LPP) nanoparticle, with optimal siRNA complexation, minimal cytotoxicity, and increased transfection efficacy. Application of this LPP complexing siKeap1 restored Nrf2 antioxidant function, accelerated diabetic tissue regeneration, and augmented reduction-oxidation homeostasis in murine diabetic wounds. Together, these studies suggest that targeted therapeutic strategies that reduce Keap1 expression may be an ideal, rapidly translatable way to treat cutaneous defects in T2DM.

Nrf2 is a central regulator of redox mechanisms. Firstly, topical application of Nrf2 activators provides a practical therapeutic intervention in diabetic wound healing. Sulforaphane (SF) and cinnamaldehyde (CA) are two known activators of NRF2 (Wu et al., 2013, 2016; Jiang et al., 2014), shown to be effective in ameliorating diabetic wound healing in a mouse model (Long et al., 2016). Likewise, Li et al. (2018b) showed that Dimethyl fumarate (DMF), a potent activator of NRF2, minimized oxidative damage and inflammation, and accelerated diabetic wound healing by producing DMF-elevated antioxidants and neutralizing ROS-induced excessive free radicals. Improving Nrf2 expression level in diabetic wound tissue is also a promising therapeutic strategy. RTA 408, a semi-synthetic oleanane triterpenoid, has been shown to have cytoprotective effects in human and rat skin through upregulation of Nrf2 target genes (Reisman et al., 2014, 2015). Rabbani et al. (2018) reported that application of 0.1% RTA 408 led to accumulation of Nrf2 in the nucleus, in conjunction with induction of the key antioxidant NQO1, and reversed the delayed healing trend of full thickness cutaneous wounds, significantly reducing the time to re-epithelialization in Leprdb/db mice. Genistein, an isoflavone in legumes with estrogen-like and antioxidative effects, accelerated wound healing in diabetic ICR mice by elevating Nrf2 and its related markers such as HO-1, GPx, catalase, and SODs (Wang et al., 1996; Eo et al., 2016). Additionally, carriers with Nrf2 have been shown to be excellent therapeutic strategies in diabetic wound healing. Li et al. (2018a) isolated the exosomes from Nrf2 overexpression adipose-derived stem cells (ADSCs). Compared with exosomes that originated from wild-type ADSCs, treatment with exosomes derived from ADSCs overexpressing Nrf2 were more effective in increasing granulation tissue formation, angiogenesis, and reducing inflammation and oxidative stress-related proteins detected in the wound beds of diabetic rats

(Li et al., 2018a). Therefore, Nrf2 is a pertinent therapeutic target in diabetic wound healing.

Studies reveal the importance of the Nrf2/Keap1 pathway in antioxidant use in diabetic wound healing. The aforementioned studies provide insight that Nrf2 and Keap1 can be significant targets in gene and molecular therapy of diabetic wound healing (**Figure 1**).

The NFκB Pathway and Antioxidant Therapy

The nuclear factor κB (NFκB) signaling pathway is known for its pro–inflammatory and pro–oxidant functions, and is reported as a master switch system in oxidative stress (Sies, 2015). Oxidative stress as well as inflammation activate the NFκB complex, which in turn is related to the cellular redox state (Hirota et al., 1999). Increasing expressions of NFκB genes and proteins contribute to enhanced oxidative stress (Mariappan et al., 2010).

The NFκB is a transcription factor consisting of homo- and heterodimers of five distinct proteins, the REL subfamily proteins (p65/RELA, RELB, and c-REL) and the NFκB subfamily proteins (p50 and p52) (Mitchell et al., 2016; Lingappan, 2018). NFκB is normally localized in the cytoplasm as a heterodimer such as p50/p65 (RelA). The Rel homology domain (RHD) in NFκB reacts on dimerization, recognition and binding to DNA as well as interaction with the inhibitory κB (IκB) proteins. IκB proteins bind to and block the nuclear localization signal of NFκB, resulting in sequestering of p65 in the cytoplasm and inhibiting the transcriptional activity of NFκB (Vallabhapurapu and Karin, 2009). IκB proteins possess nuclear export signals removing NFκB proteins from the nucleus, strictly regulating the pathway. Inflammatory signals (such as TNF-α or lipopolysaccharide) induce phosphorylation of IκB proteins by upstream kinases (IKK), resulting in the ubiquitination and degradation of IκB. Active NFκB translocates to the nucleus and activates the target genes (Zhang et al., 2017). NFκB induces the expression of inflammatory cytokines such as tumor necrosis factor alpha (TNF-α) (Yao et al., 1997), interleukin 1 beta (IL-1β) (Goto et al., 1999), interleukin 6 (IL-6) (Libermann and Baltimore, 1990), cyclooxygenase 2 (COX-2) (Kim et al., 2000), and

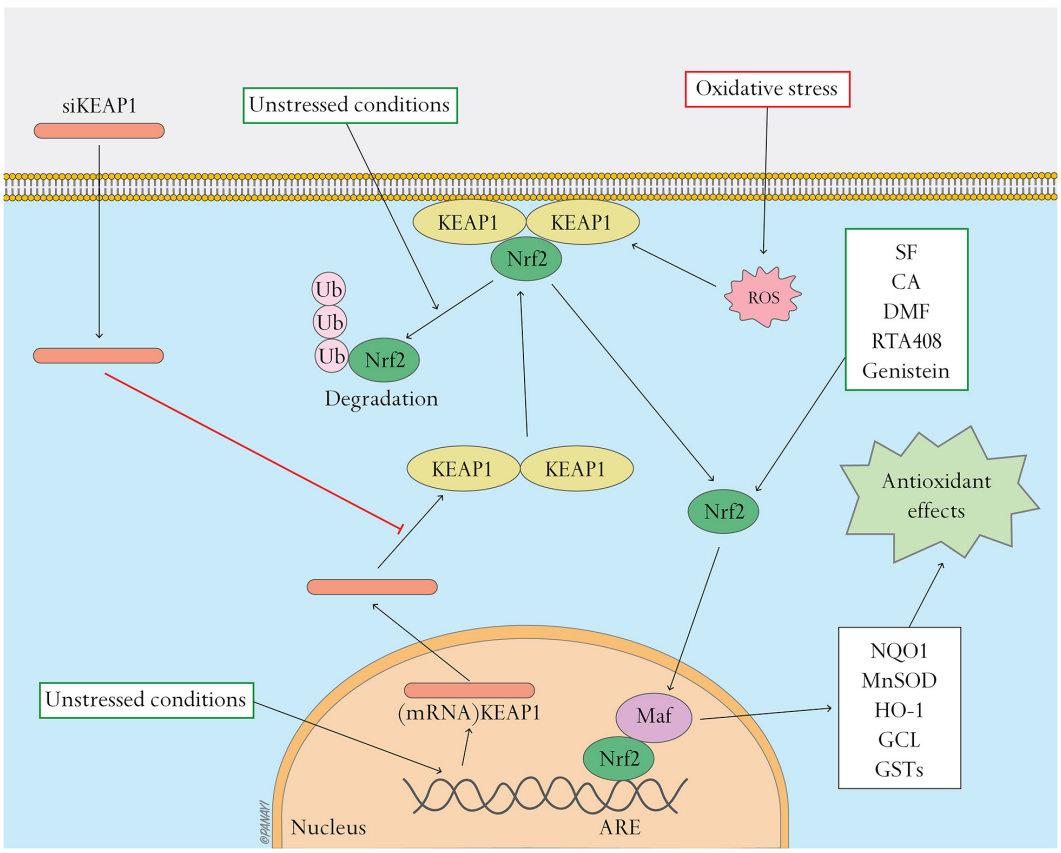

FIGURE 1 | Nrf2 pathway and related antioxidant therapy. Nrf2 pathway and related antioxidant therapy. This figure shows the activation of the Nrf2 pathway and effects of antioxidant therapy targeting this pathway. Under unstressed conditions, Keap1 interacts with Nrf2 and the cell's actin cytoskeleton to keep Nrf2 inactive in the cytoplasm and promote ubiquitination and degradation of Nrf2. Oxidative stress causes Nrf2 to detach from Keap1 and translocate to the nucleus where it heterodimerizes with Maf. The Nrf2-Maf heterodimer binds to ARE to induce the expression of antioxidant and metabolic genes including NQO1, MnSOD, HO-1, GCL, and GSTs. Oxidative stress can be regulated by activating the Nrf2 pathway. siKeap1 downregulates the levels of Keap1 by incorporating into an RNA-induced silencing complex (RISC) and inducing degradation of the complementary mRNA of Keap1. Nrf2 activators, such as SF, CA, DMF, RTA408 and genistein, stimulate the Nrf2 pathway and ameliorate oxidative stress.

inducible nitric oxide synthase (iNOS) (Taylor et al., 1998). The NFκB pathway also induces NADPH oxidase (NOX-2) subunit gp91phox and exacerbates oxidative stress (Anrather et al., 2006). Studies have reported that expression of NFκB pathway genes is upregulated in diabetic rats, triggering downstream expression of inflammatory cytokines (such as TNF-α, IL-1β, and IL-8) and delaying wound healing (Ren et al., 2019). NFκB also regulates the NOD-like receptor protein-3 (NLRP3) inflammasome (Bauernfeind et al., 2009), which is a target mechanism in promoting wound healing during the early stages (Weinheimer-Haus et al., 2015). It should be noted that although the NFκB pathway also has antioxidant functions and targets such as MnSOD (Kairisalo et al., 2007; Lingappan, 2018), current therapeutic strategies focus on suppression of the NFkB pathway in diabetic wound healing. NFκB has been considered as a crucial molecule contributing to end-organ damage T2DM. Therapeutic strategies related to the NFκB pathway are as follows.

Application of miR-146a against the NFκB pathway in wound healing has been reported. miR-146a is an anti-inflammatory microRNA known for its inhibitory effect on the NFκB pro-inflammatory signaling pathway, known to be decreased in diabetic wound healing (Xu et al., 2012). miR-146a targets and represses tumor necrosis factor receptor-associated factor 6 (TRAF6) and interleukin-1 receptor-associated kinase 1 (IRAK1), key adapter molecules in NFκB pathway activation (Xu et al., 2012; Xie et al., 2018). Enhancing expression of miR-146a can decrease levels of phosphorylated IκB-α, phosphorylated NFκB and total NFκB (Chen et al., 2013). miR-146a in conjugation with cerium oxide nanoparticles (CNP) has been proposed as a therapy for diabetic wound healing. CNP-miR146a improved wound healing in a murine and porcine diabetic wound model (Zgheib et al., 2019). CNP-miR146a combined with an efficient delivery system, such as nanosilk (Niemiec et al., 2020) or self-healable zwitterionic cryogels (Sener et al., 2020), demonstrated efficacy in accelerating diabetic wound healing.

SIRT1 (Sirtuin 1) is an important target in diabetic wound healing, and antagonizes the effect of NFκB pathway. SIRT1, a NAD-dependent class III histone deacetylase, suppresses binding of NFκB to inflammation-related gene promoters and its transcriptional activities by deacetylating the p65 subunit at lysine (Yeung et al., 2004). Downregulation of SIRT1 leads to hyperacetylation of p65, resulting in inflammation (Yeung et al., 2004; Kauppinen et al., 2013). Low expression of SIRT1 has been shown in diabetic rats and human umbilical vein endothelial cells (HUVECs) under hyperglycemia conditions (Yerra et al., 2017; Li et al., 2019). Therapeutic strategies of diabetic wound healing targeting the SIRT1 have been reported in recent years. Resveratrol, a well-known SIRT1 activator, accelerates wound healing by attenuating oxidative stress-induced impairment of cell proliferation and migration (Zhou et al., 2021). SIRT1 inhibits the expression of matrix metalloproteinase-1 and −3, delaying wound healing. Likewise, SIRT1 is a target of berberine, an eminent traditional Chinese and Ayurvedic medicine (Feng et al., 2019). Zhang et al. (2020) reported a novel berberine nanohydrogel that activates SIRT1, inhibiting the expression of NFκB and ameliorating diabetic wound healing through effective reduction of inflammation and promotion of angiogenesis. SRT1720, a specific SIRT1 activator, demonstrating locally improved wound healing and angiogenesis in STZ-induced diabetic mice (Li et al., 2019).

Several plant medicines that promote diabetic wound healing by regulating the NFκB pathway have been reported in recent years. Asiatic acid, the most active substance in the extracts of Chinese herbal compound Centella asiatica (Coldren et al., 2003), attenuates prolonged inflammation by downregulating NFκB activation in RAW 264.7 macrophage cells and reducing pro-inflammatory cytokine IL-1β, TNF-a and IL-6 (Yun et al., 2008). Han et al. (2019) reported that application of Asiatic acid together with aligned poly (L-lactic acid) electrospun scaffolds as drug-delivery system can accelerate re-epithelization, angiogenesis and ECM formation by relieving the high oxidative stress and inflammation in diabetic wounds. Likewise, syringic acid is involved in the suppression of NFκB activation and the inflammatory response to improve wound healing (Ren et al., 2019). Similarly, genistein promotes angiogenesis and accelerates healing related to the regulation of the NFκB pathway (Eo et al., 2016).

In summary, overactivation of NFκB pathway impairs wound healing in T2DM. Recent studies demonstrate that miR-146a and SIRT1 can be therapy targets in suppression of activated NFκB pathway and promotion of diabetic wound healing (**Figure 2**).

Vitamins and Other Endogenous Molecules

Endogenous molecules such as glutathione, ubiquinones, uric acid, and lipoic acid, as well as vitamins E and C (ascorbic acid), carotinoids, and phenolic compounds have direct antioxidant effects and are involved in the regulation of the redox balance in skin wound healing (Schafer and Werner, 2008). As oxidative stress plays a major role in impaired diabetic wound healing, use of antioxidants to improve healing by modulating inflammation and the antioxidant system with no effect on glycemia is promising. Use of antioxidant vitamins, such as Vitamins E and C, has been reported to promote diabetic wound healing in recent studies. Vitamin E (α-tocopherol) interacts directly with peroxyl radicals, superoxide and singlet oxygen to protect cell membranes against lipid peroxidation, while vitamin C recycles the tocopherol radical, enhances its antioxidant activity, and generates dehydroascorbic acid to reduce oxidative stress (Maritim et al., 2003). Oral administration of vitamins E and C effectively restored the antioxidant enzyme activities, reducing ROS levels and accelerating wound closure in diabetic mice (Pessoa et al., 2016). Likewise, tocotrienols belong to the vitamin E-family. A study has reported that mono-epoxy-tocotrienol-α showed beneficial effects on wound healing in a diabetic (db/db) mouse model by increasing the expression of genes involved in cell growth, motility, angiogenesis, and mitochondrial function (Xu et al., 2017). Similarly, folic acid, a vitamin with direct antioxidant effects, improved collagen deposition and promoted wound healing via suppression of oxidative stress in diabetic mice (Zhao et al., 2018). Together,

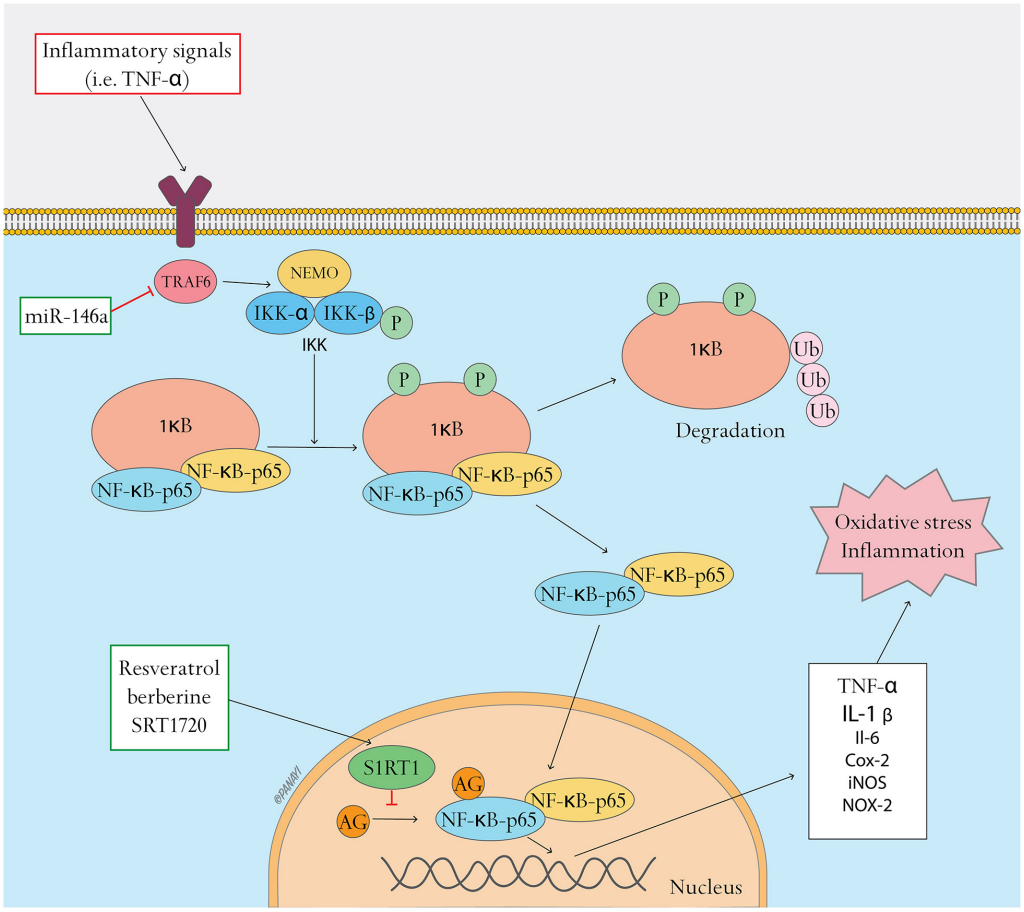

FIGURE 2 | NFκB pathway and related antioxidant therapy. NFκB pathway and related antioxidant therapy. This figure shows the activation of the NFκB pathway and the effects of antioxidant therapy targeting this pathway. In resting state, NFκB dimers form a complex with the inhibitory protein IκB, which is located in the cytoplasm. Inflammatory signals (such as TNF-α) induce phosphorylation of IκB through upstream kinases (IKK), resulting in the ubiquitination and degradation of IκB. Active NFκB translocates to the nucleus and activates target genes including TNF-α, IL-1β, IL-6, COX-2, iNOS, and NOX-2, resulting in oxidative stress and inflammation. Oxidative stress can be regulated by inhibiting the NFκB pathway. MiR-146a can target and repress tumor necrosis factor receptor-associated factor 6 (TRAF6), inhibiting the activation of IKK and the NFκB pathway. SIRT1 activators, such as resveratrol, berberine and SRT1720, suppress binding of NFκB to inflammation-related gene promoters and their transcriptional activities by activating SIRT1, a NAD-dependent class III histone deacetylase that leads to deacetylation of the p65 subunit.

these studies indicate the importance of antioxidant vitamins in diabetic wound healing.

Overproduction of mitochondrial ROS (mtROS) is linked to the damaging effects of hyperglycemia (Giacco and Brownlee, 2010), and mitochondria-targeted antioxidants can be helpful in diabetic wound healing. Demyanenko et al. (2017) reported that administration of the mitochondria-targeted antioxidant SkQ1 suppressed oxidative stress, accelerated wound closure and stimulated epithelization, granulation tissue formation, and angiogenesis.

Therefore, administration of vitamins and other endogenous antioxidant molecules is an effective therapy method in diabetic wound healing that should be considered.

Antioxidant Enzymes

Antioxidant enzymes play a crucial role in oxidative stress and chronic diabetic wounds (Panayi et al., 2020). Major antioxidant enzymes include superoxide dismutase (SOD), catalase, glutathione peroxidase, and heme oxygenase. In recent years, studies have reported the application of antioxidant enzymes in diabetic wound healing.

Superoxide dismutase is an antioxidant enzyme involved in oxidative stress. As an endogenous factor capable of scavenging free radicals, SOD catalyzes the decomposition of superoxide radicals into hydrogen peroxide which is converted into water and oxygen (Maier and Chan, 2002). However, SOD is expressed at inadequate levels in diabetic wound healing, resulting in excessive oxidative stress and impaired wound healing. In recent years, studies have reported use of SOD in diabetic wound healing, with SOD-loaded effectively promoting the repair of chronic diabetic wounds (Zhang et al., 2018).

HO-1, which is involved in the production of antioxidant enzymes associated with Nrf2 activation (Lee et al., 2011), is an important therapeutic target. HO-1 has protective

effects on various cells and tissues while induction of HO-1 is a crucial event in the defense against cellular stress by maintaining anti-oxidant/oxidant homeostasis (Choi and Alam, 1996; Molavi and Mehta, 2004; Abraham and Kappas, 2008). HO-1 cleaves the α-methene bridges of heme to produce equimolar amounts of biliverdin and carbon monoxide (CO) (Maines and Kappas, 1977). Under the catalyzation of NADPH biliverdin reductase, biliverdin is transformed into bilirubin. Both bilirubin and biliverdin are powerful antioxidants (Jansen et al., 2010). CO functions as a gaseous signaling molecule that elicits an anti-inflammatory and anti-oxidative response (Ryter and Choi, 2009). Studies have shown the effect of HO-1 regulation in diabetic wound healing. Chen et al. (2016b) reported that use of hemin, a strong inducer of HO-1, can accelerate wound closure by reducing inflammatory cytokines such as TNF-α and IL-6, increasing antioxidants, and promoting angiogenesis in diabetic rat wounds. On the other hand, application of in-protoporphyrin IX (SnPPIX), a HO-1 inhibitor, exacerbated the oxidative stress conditions and delayed wound contraction in non-diabetic mice (Kumar et al., 2019). Together, studies in recent years have confirmed the efficacy of HO-1 regulation in diabetic wound healing.

Overall, regulation of the expression and activity of antioxidant enzymes is a promising therapy for diabetic wound healing.

Hormones

Some hormones have been reported to be useful in diabetic wound healing. 17β-estradiol (E2) regulates energy homeostasis and glucose metabolism, which play a crucial role in regulating antioxidant enzyme expression and redox states (Bellanti et al., 2013). E2 can act as a cytoprotective antioxidant and has been shown to reduce excessive ROS formation, facilitating cell survival in a high glucose environment. Transplantation of hUCB-MSCs combined with E2 treatment can promote wound healing and angiogenesis through ERα-induced Nrf2 and Sirt3 signaling (Oh et al., 2019). Similarly, 5α-dihydrotestosterone has a positive antioxidant effect in secondary wound healing in diabetic rats, increasing the proportion of type I and type III collagen fibers and the level of SOD (Goncalves et al., 2016).

Medicinal Plants

Medicinal plants, as well as their preparations and active compounds, have been utilized in wound healing and have been shown to regulate different metabolic pathways (Fronza et al., 2009; Kant et al., 2015). Some medicinal plants and their active compounds can modify the processes in the redox signaling pathway promoting diabetic wound healing. Medicinal plant compounds such as genistein and dimethyl fumarate accelerate wound healing through stimulation of the Nrf2 pathway and through other anti-inflammatory and antioxidant properties (Eo et al., 2016; Long et al., 2016). Medicinal plant compounds such as asiatic acid, syringic acid, and genistein accelerate the healing process through downregulation of the NFκB pathway (Eo et al., 2016; Han et al., 2019; Ren et al., 2019). Hydroethanolic extract of the strychnos pseudoquina has been shown to accelerate wound healing through modulating the oxidative status and microstructural reorganization in diabetic rats (Sarandy et al., 2017). Deoxyshikonin, the major angiogenic compound extracted from Lithospermi Radix, can exert antioxidant activities and promote phosphorylation of ERK and p38 and VEGFR-2 expression in diabetic wound healing (Park et al., 2018). Quercetin, a flavonoid plant ingredient, enhances organized granulation and fibrillar collagen formation by limiting prolonged inflammation, improving the glycemic state, increasing the insulin level, suppressing oxidative stress and enhancing the antioxidant defense system (Ahmed et al., 2018).

The application of medicinal plants in diabetic wound healing is a therapeutic strategy that has garnered attention in studies of recent years as using alternative therapies and natural remedies in faster wound healing upsurges in recent years. Medicinal plants and their active compounds with anti-inflammatory and antioxidant properties demonstrate a positive effect on diabetic wound healing.

Biological Materials in Antioxidant Therapy

Hydrogels

Hydrogel is a promising material for wound healing, which possesses air permeability, moisture retention, possibility to load bioactive agents and the capability to absorb wound exudate and cool the wound surface leading to pain relief for patients (Gong et al., 2013; Zhang et al., 2018). Application of antioxidant-loaded hydrogels in diabetic wound healing has been developed. Superoxide dismutase (SOD)-loaded hydrogels have been shown to be effective in decreasing ROS generation and oxidative stress in chronic wounds. Zhang et al. (2018) constructed a novel SOD-loaded antioxidant hydrogel which exhibited sustained release of SOD with high activity in diabetic wound healing. The SOD-loaded hydrogel promoted healing of diabetic wounds by accelerating re-epithelialization and increasing collagen deposition. Similarly, Augustine et al. (2021) developed a biodegradable gelatin methacryloyl (GelMA) hydrogel patch incorporated with cerium oxide nanoparticles, which showed adequate exudate uptake capacity, effective free radical scavenging activity and capacity to establish a suitable microenvironment for cell proliferation in the wound healing of diabetic rats. Likewise, Alginate hydrogels have been particularly promising for use in wound healing owing to their good biocompatibility and ease of gelation (Lee and Mooney, 2012). Fan et al. (2019) developed a nanocomposite alginate hydrogel eluding the radical free scavenger edaravone with use of Eudragit nanoparticles to enhance the Edaravone's solubility and stability. The Edaravone-eluting nanocomposite hydrogel downregulated ROS levels in diabetic mice and promoted wound healing in a dose-dependent manner. Sener et al. (2020) constructed a biomaterial system of zwitterionic cryogels laden with the anti-inflammatory and antioxidant CNP-miR146a, demonstrating efficacy and viability in the wound healing of diabetic mice. Taken

together, antioxidant-loaded hydrogels are feasible therapies in diabetic wound healing.

Nanobiopolymers

Nanobiopolymers, such as nanocellulose, nanochitin, nanosilk, nanostarch, and microbial nanobiopolymers, which are produced by living organisms, have received widely scientific and engineering interests for their sustainable and biodegradable properties in recent years (Yang et al., 2019). Nanosilk, characterized by a high strength-to-density ratio and an ability to exhibit strain hardening, shows significant application in diabetic wound healing. Niemiec et al. (2020) prepared nanosilk-based materials on silk fibroin, a biocompatible polymer that can be fabricated into a nanostructure. The Nanosilk preparation showed effective delivery of CNP-miR146a to the wound bed, which downregulated pro-inflammatory signaling and promoted pro-fibrotic processes, ultimately accelerating diabetic wound healing.

Scaffolds

Scaffolds are regarded as promising materials for tissue engineering, and improved results have been reported in diabetic wound healing in studies of recent years. The 3D fibrous scaffolds of poly(lactic acid-co-glycolic acid) (PLGA) fabricated by liquid-collecting electrospinning have been used to simulate the ECM microenvironment, providing mechanical support for cell adhesion and promoting cell growth in wounds (Chen et al., 2016a). Han et al. (2019) utilized an asiatic acid -embedded aligned porous poly(L-lactic acid) electrospun fibrous scaffold (AA-PL), to promote angiogenesis, ECM formation and re-epithelization by relieving the high oxidative stress, inflammation and infection in diabetic wound healing.

Framework Nucleic Acids

Framework nucleic acids (FNAs) – biocompatible and biodegradable nucleic acids – show advantages in tailorable functionality and multiple modifiability, which can be applied to drug delivery and nanomedicine (Lin et al., 2020). Lin et al. (2020) demonstrated that framework nucleic acids (tFNAs) attenuated inflammation, prevented oxidative damage, and promoted angiogenesis in diabetic wound healing.

Therefore, studies in recent years have reported multiple combinations of antioxidant therapy and biological materials in diabetic wound healing. This provides insight that biological materials loaded with antioxidant agents can decrease oxidative stress and promote healing and are promising for diabetic wound healing.

CONCLUSION AND PROSPECTS

Numerous studies have highlighted the promising potential of antioxidant therapy in diabetic wound healing given the central role of oxidative stress in the pathology of chronic diabetic wounds. This review summarizes the antioxidant therapy that has been studied for use in diabetic wound healing in the past 5 years. The NFκB and Nrf2/Keap1 pathways are key pathways in oxidative stress, therefore therapies targeting these pathways have been shown to effectively promote diabetic wound healing. Antioxidants and enzymes with direct antioxidant effects can downregulate oxidative stress and accelerate diabetic wound closure. Hormones can regulate energy homeostasis and glucose metabolism to relieve oxidative stress. Medicinal plants with anti-inflammatory and antioxidant properties have been shown to improve diabetic wound healing. Biological materials loaded with antioxidant agents decrease oxidative stress and promote diabetic wound healing. Despite the rapid development in the field of antioxidant therapy for diabetic wound healing, a complete cure for diabetic ulcers has yet to be developed. As the evidence from recent years is largely based on animal experiments, further research on the use of antioxidant therapy in humans, as well as the function of antioxidants at the genomic and molecular level, is necessary to elucidate the key roles of oxidative stress and redox homeostasis in diabetic wound healing.

AUTHOR CONTRIBUTIONS

FC, BM, and GL: conceptualization and funding acquisition. LC and YX: formal analysis. AA, YH, and CY: investigation. WZ, YS, ML, HX, LH, and CY: resources and supervision. XX and ZL: validation. WZ: visualization and writing (original draft). AP: writing (review and editing). All authors contributed to the article and approved the submitted version.

FUNDING

This work was supported by the National Science Foundation of China (Nos. 82002313 and 82072444), the National Key Research & Development Program of China (Nos. 2018YFC2001502 and 2018YFB1105705), Hubei Province Key Laboratory of Oral and Maxillofacial Development and Regeneration (No. 2020kqhm008), the Health Commission of Hubei Province (No. WJ2019Z009), and the Wuhan Union Hospital "Pharmaceutical Technology nursing" special fund (No. 2019xhyn021).

REFERENCES

Abraham, N. G., and Kappas, A. (2008). Pharmacological and clinical aspects of heme oxygenase. *Pharmacol. Rev.* 60, 79–127. doi: 10.1124/pr.107.07104

Ahmed, O. M., Mohamed, T., Moustafa, H., Hamdy, H., Ahmed, R. R., and Aboud, E. (2018). Quercetin and low level laser therapy promote wound healing process in diabetic rats via structural reorganization and modulatory effects on inflammation and oxidative stress. *Biomed. Pharmacother.* 101, 58–73. doi: 10.1016/j.biopha.2018.02.040

Amento, E. P., and Beck, L. S. (1991). Tgf-beta and wound healing. *Ciba Found Symp.* 157, 115–123. doi: 10.1002/9780470514061.ch8

Anrather, J., Racchumi, G., and Iadecola, C. (2006). Nf-kappab regulates phagocytic nadph oxidase by inducing the expression of gp91phox. *J. Biol. Chem.* 281, 5657–5667. doi: 10.1074/jbc.M506172200

Armstrong, D. G., Boulton, A. J. M., and Bus, S. A. (2017). Diabetic foot ulcers and their recurrence. *N. Engl. J. Med.* 376, 2367–2375. doi: 10.1056/NEJMra1615439

Augustine, R., Zahid, A. A., Hasan, A., Dalvi, Y. B., and Jacob, J. (2021). Cerium oxide nanoparticle-loaded gelatin methacryloyl hydrogel wound-healing patch with free radical scavenging activity. *ACS Biomater. Sci. Eng.* 7, 279–290. doi: 10.1021/acsbiomaterials.0c01138

Avishai, E., Yeghiazaryan, K., and Golubnitschaja, O. (2017). Impaired wound healing, Facts and hypotheses for multi-professional considerations in predictive, preventive and personalised medicine. *EPMA J.* 8, 23–33. doi: 10.1007/s13167-017-0081-y

Bainbridge, P. (2013). Wound healing and the role of fibroblasts. *J. Wound Care* 22, 407–408. doi: 10.12968/jowc.2013.22.8.407

Baird, L., and Dinkova-Kostova, A. T. (2011). The cytoprotective role of the keap1-nrf2 pathway. *Arch. Toxicol.* 85, 241–272. doi: 10.1007/s00204-011-0674-5

Bauernfeind, F. G., Horvath, G., Stutz, A., Alnemri, E. S., MacDonald, K., Speert, D., et al. (2009). Cutting edge, Nf-kappab activating pattern recognition and cytokine receptors license nlrp3 inflammasome activation by regulating nlrp3 expression. *J. Immunol.* 183, 787–791. doi: 10.4049/jimmunol.0901363

Bellanti, F., Matteo, M., Rollo, T., De Rosario, F., Greco, P., Vendemiale, G., et al. (2013). Sex hormones modulate circulating antioxidant enzymes, Impact of estrogen therapy. *Redox. Biol.* 1, 340–346. doi: 10.1016/j.redox.2013.05.003

Blakytny, R., and Jude, E. (2006). The molecular biology of chronic wounds and delayed healing in diabetes. *Diabet. Med.* 23, 594–608. doi: 10.1111/j.1464-5491.2006.01773.x

Boulton, A. J. M., Vileikyte, L., Ragnarson-Tennvall, G., and Apelqvist, J. (2005). The global burden of diabetic foot disease. *Lancet* 366, 1719–1724. doi: 10.1016/S0140-6736(05)67698-2

Brownlee, M. (2001). Biochemistry and molecular cell biology of diabetic complications. *Nature* 414, 813–820. doi: 10.1038/414813a

Bryan, N., Ahswin, H., Smart, N., Bayon, Y., Wohlert, S., and Hunt, J. A. (2012). Reactive oxygen species (ros)–a family of fate deciding molecules pivotal in constructive inflammation and wound healing. *Eur. Cell Mater.* 24, 249–265. doi: 10.22203/eCM.v024a18

Caley, M. P., Martins, V. L., and O'Toole, E. A. (2015). Metalloproteinases and wound healing. *Adv. Wound Care (New Rochelle)* 4, 225–234. doi: 10.1089/wound.2014.0581

Chen, G., Umelo, I. A., Lv, S., Teugels, E., Fostier, K., Kronenberger, P., et al. (2013). Mir-146a inhibits cell growth, cell migration and induces apoptosis in non-small cell lung cancer cells. *PLoS One* 8:e60317. doi: 10.1371/journal.pone.0060317

Chen, H., Peng, Y., Wu, S., and Tan, L. P. (2016). Electrospun 3d fibrous scaffolds for chronic wound repair. *Materials (Basel)* 9:272. doi: 10.3390/ma9040272

Chen, Q. Y., Wang, G. G., Li, W., Jiang, Y. X., Lu, X. H., and Zhou, P. P. (2016). Heme oxygenase-1 promotes delayed wound healing in diabetic rats. *J. Diab. Res.* 2016:9726503. doi: 10.1155/2016/9726503

Choi, A. M., and Alam, J. (1996). Heme oxygenase-1, Function, regulation, and implication of a novel stress-inducible protein in oxidant-induced lung injury. *Am. J. Respir. Cell Mol. Biol.* 15, 9–19. doi: 10.1165/ajrcmb.15.1.8679227

Choi, B. H., Kang, K. S., and Kwak, M. K. (2014). Effect of redox modulating nrf2 activators on chronic kidney disease. *Molecules* 19, 12727–12759. doi: 10.3390/molecules190812727

Coldren, C. D., Hashim, P., Ali, J. M., Oh, S. K., Sinskey, A. J., and Rha, C. (2003). Gene expression changes in the human fibroblast induced by *Centella asiatica* triterpenoids. *Planta Med.* 69, 725–732. doi: 10.1055/s-2003-42791

Davies, M. J. (2005). The oxidative environment and protein damage. *Biochim. Biophys. Acta* 1703, 93–109. doi: 10.1016/j.bbapap.2004.08.007

Demyanenko, I. A., Zakharova, V. V., Ilyinskaya, O. P., Vasilieva, T. V., Fedorov, A. V., Manskikh, V. N., et al. (2017). Mitochondria-targeted antioxidant skq1 improves dermal wound healing in genetically diabetic mice. *Oxid. Med. Cell Longev.* 2017:6408278. doi: 10.1155/2017/6408278

Eo, H., Lee, H. J., and Lim, Y. (2016). Ameliorative effect of dietary genistein on diabetes induced hyper-inflammation and oxidative stress during early stage of wound healing in alloxan induced diabetic mice. *Biochem. Biophys. Res. Commun.* 478, 1021–1027. doi: 10.1016/j.bbrc.2016.07.039

Evans, J. L., Goldfine, I. D., Maddux, B. A., and Grodsky, G. M. (2002). Oxidative stress and stress-activated signaling pathways, A unifying hypothesis of type 2 diabetes. *Endocr. Rev.* 23, 599–622. doi: 10.1210/er.2001-0039

Falanga, V. (2005). Wound healing and its impairment in the diabetic foot. *Lancet* 366, 1736–1743. doi: 10.1016/S0140-6736(05)67700-8

Fan, Y., Wu, W., Lei, Y., Gaucher, C., Pei, S., Zhang, J., et al. (2019). Edaravone-loaded alginate-based nanocomposite hydrogel accelerated chronic wound healing in diabetic mice. *Mar. Drugs* 17:285. doi: 10.3390/md17050285

Feng, X., Sureda, A., Jafari, S., Memariani, Z., Tewari, D., Annunziata, G., et al. (2019). Berberine in cardiovascular and metabolic diseases, From mechanisms to therapeutics. *Theranostics* 9, 1923–1951. doi: 10.7150/thno.30787

Fronza, M., Heinzmann, B., Hamburger, M., Laufer, S., and Merfort, I. (2009). Determination of the wound healing effect of calendula extracts using the scratch assay with 3t3 fibroblasts. *J. Ethnopharmacol.* 126, 463–467. doi: 10.1016/j.jep.2009.09.014

Gallagher, K. A., Joshi, A., Carson, W. F., Schaller, M., Allen, R., Mukerjee, S., et al. (2015). Epigenetic changes in bone marrow progenitor cells influence the inflammatory phenotype and alter wound healing in type 2 diabetes. *Diabetes Metab. Res. Rev.* 64, 1420–1430. doi: 10.2337/db14-0872

Giacco, F., and Brownlee, M. (2010). Oxidative stress and diabetic complications. *Circ. Res.* 107, 1058–1070. doi: 10.1161/CIRCRESAHA.110.223545

Goncalves, R. V., Novaes, R. D., Sarandy, M. M., Damasceno, E. M., da Matta, S. L., de Gouveia, N. M., et al. (2016). 5alpha-dihydrotestosterone enhances wound healing in diabetic rats. *Life Sci.* 152, 67–75. doi: 10.1016/j.lfs.2016.03.019

Gong, C., Wu, Q., Wang, Y., Zhang, D., Luo, F., Zhao, X., et al. (2013). A biodegradable hydrogel system containing curcumin encapsulated in micelles for cutaneous wound healing. *Biomaterials* 34, 6377–6387. doi: 10.1016/j.biomaterials.2013.05.005

Goto, M., Katayama, K. I., Shirakawa, F., and Tanaka, I. (1999). Involvement of nf-kappab p50/p65 heterodimer in activation of the human pro-interleukin-1beta gene at two subregions of the upstream enhancer element. *Cytokine* 11, 16–28. doi: 10.1006/cyto.1998.0390

Han, Y., Jiang, Y., Li, Y., Wang, M., Fan, T., Liu, M., et al. (2019). An aligned porous electrospun fibrous scaffold with embedded asiatic acid for accelerating diabetic wound healing. *J. Mater. Chem. B* 7, 6125–6138. doi: 10.1039/C9TB01327J

Hantke, B., Lahmann, C., Venzke, K., Fischer, T., Kocourek, A., Windsor, L. J., et al. (2002). Influence of flavonoids and vitamins on the mmp- and timp-expression of human dermal fibroblasts after uva irradiation. *Photochem. Photobiol. Sci.* 1, 826–833. doi: 10.1039/B207731K

Hayes, J. D., and Dinkova-Kostova, A. T. (2014). The nrf2 regulatory network provides an interface between redox and intermediary metabolism. *Trends Biochem. Sci.* 39, 199–218. doi: 10.1016/j.tibs.2014.02.002

He, T., Quan, T., Shao, Y., Voorhees, J. J., and Fisher, G. J. (2014). Oxidative exposure impairs tgf-beta pathway via reduction of type ii receptor and smad3 in human skin fibroblasts. *Age (Dordr)* 36:9623. doi: 10.1007/s11357-014-9623-6

Hirota, K., Murata, M., Sachi, Y., Nakamura, H., Takeuchi, J., Mori, K., et al. (1999). Distinct roles of thioredoxin in the cytoplasm and in the nucleus. a two-step mechanism of redox regulation of transcription factor nf-kappab. *J. Biol. Chem.* 274, 27891–27897. doi: 10.1074/jbc.274.39.27891

Hu, S. C., and Lan, C. E. (2016). High-glucose environment disturbs the physiologic functions of keratinocytes, Focusing on diabetic wound healing. *J. Dermatol. Sci.* 84, 121–127. doi: 10.1016/j.jdermsci.2016.07.008

Jansen, T., Hortmann, M., Oelze, M., Opitz, B., Steven, S., Schell, R., et al. (2010). Conversion of biliverdin to bilirubin by biliverdin reductase contributes to endothelial cell protection by heme oxygenase-1-evidence for direct and indirect antioxidant actions of bilirubin. *J. Mol. Cell Cardiol.* 49, 186–195. doi: 10.1016/j.yjmcc.2010.04.011

Jiang, T., Tian, F., Zheng, H., Whitman, S. A., Lin, Y., Zhang, Z., et al. (2014). Nrf2 suppresses lupus nephritis through inhibition of oxidative injury and the nf-kappab-mediated inflammatory response. *Kidney Int.* 85, 333–343. doi: 10.1038/ki.2013.343

Jude, E. B., Blakytny, R., Bulmer, J., Boulton, A. J., and Ferguson, M. W. (2002). Transforming growth factor-beta 1, 2, 3 and receptor type i and ii in diabetic foot ulcers. *Diabet. Med.* 19, 440–447. doi: 10.1046/j.1464-5491.2002.00692.x

Kairisalo, M., Korhonen, L., Blomgren, K., and Lindholm, D. (2007). X-linked inhibitor of apoptosis protein increases mitochondrial antioxidants through

nf-kappab activation. *Biochem. Biophys. Res. Commun.* 364, 138–144. doi: 10.1016/j.bbrc.2007.09.115

Kant, V., Gopal, A., Kumar, D., Pathak, N. N., Ram, M., Jangir, B. L., et al. (2015). Curcumin-induced angiogenesis hastens wound healing in diabetic rats. *J. Surg. Res.* 193, 978–988. doi: 10.1016/j.jss.2014.10.019

Kauppinen, A., Suuronen, T., Ojala, J., Kaarniranta, K., and Salminen, A. (2013). Antagonistic crosstalk between nf-kappab and sirt1 in the regulation of inflammation and metabolic disorders. *Cell. Signal.* 25, 1939–1948. doi: 10.1016/j.cellsig.2013.06.007

Kensler, T. W., Wakabayashi, N., and Biswal, S. (2007). Cell survival responses to environmental stresses via the keap1-nrf2-are pathway. *Annu. Rev. Pharmacol. Toxicol.* 47, 89–116. doi: 10.1146/annurev.pharmtox.46.120604.141046

Khanna, S., Biswas, S., Shang, Y., Collard, E., Azad, A., Kauh, C., et al. (2010). Macrophage dysfunction impairs resolution of inflammation in the wounds of diabetic mice. *PLoS One* 5:e9539. doi: 10.1371/journal.pone.0009539

Kim, H. J., Kim, K. W., Yu, B. P., and Chung, H. Y. (2000). The effect of age on cyclooxygenase-2 gene expression, Nf-kappab activation and ikappabalpha degradation. *Free Radic. Biol. Med.* 28, 683–692. doi: 10.1016/S0891-5849(99)00274-9

Kumar, D., Jena, G. R., Ram, M., Lingaraju, M. C., Singh, V., Prasad, R., et al. (2019). Hemin attenuated oxidative stress and inflammation to improve wound healing in diabetic rats. *Naunyn Schmiedebergs Arch. Pharmacol.* 392, 1435–1445. doi: 10.1007/s00210-019-01682-7

Lan, C. C., Huang, S. M., Wu, C. S., Wu, C. H., and Chen, G. S. (2016). High-glucose environment increased thrombospondin-1 expression in keratinocytes via DNA hypomethylation. *Transl. Res.* 169, 91–101.e1–e3. doi: 10.1016/j.trsl.2015.11.002

Lan, C. C., Wu, C. S., Huang, S. M., Wu, I. H., and Chen, G. S. (2013). High-glucose environment enhanced oxidative stress and increased interleukin-8 secretion from keratinocytes, new insights into impaired diabetic wound healing. *Diabetes Metab. Res. Rev.* 62, 2530–2538. doi: 10.2337/db12-1714

Landen, N. X., Li, D., and Stahle, M. (2016). Transition from inflammation to proliferation, a critical step during wound healing. *Cell Mol. Life. Sci.* 73, 3861–3885. doi: 10.1007/s00018-016-2268-0

Lee, K. Y., and Mooney, D. J. (2012). Alginate, properties and biomedical applications. *Prog. Polym. Sci.* 37, 106–126. doi: 10.1016/j.progpolymsci.2011.06.003

Lee, S., Park, Y., Zuidema, M. Y., Hannink, M., and Zhang, C. (2011). Effects of interventions on oxidative stress and inflammation of cardiovascular diseases. *World J. Cardiol.* 3, 18–24. doi: 10.4330/wjc.v3.i1.18

Li, X., Wu, G., Han, F., Wang, K., Bai, X., Jia, Y., et al. (2019). Sirt1 activation promotes angiogenesis in diabetic wounds by protecting endothelial cells against oxidative stress. *Arch. Biochem. Biophys.* 661, 117–124. doi: 10.1016/j.abb.2018.11.016

Li, X., Xie, X., Lian, W., Shi, R., Han, S., Zhang, H., et al. (2018). Exosomes from adipose-derived stem cells overexpressing nrf2 accelerate cutaneous wound healing by promoting vascularization in a diabetic foot ulcer rat model. *Exp. Mol. Med.* 50:29. doi: 10.1038/s12276-018-0058-5

Li, Y., Ma, F., Li, H., Song, Y., Zhang, H., Jiang, Z., et al. (2018). Dimethyl fumarate accelerates wound healing under diabetic condition. *J. Mol. Endocrinol.* 61, 163–172. doi: 10.1530/JME-18-0102

Libermann, T. A., and Baltimore, D. (1990). Activation of interleukin-6 gene expression through the nf-kappa b transcription factor. *Mol. Cell. Biol.* 10, 2327–2334. doi: 10.1128/MCB.10.5.2327

Lin, S., Zhang, Q., Li, S., Zhang, T., Wang, L., Qin, X., et al. (2020). Antioxidative and angiogenesis-promoting effects of tetrahedral framework nucleic acids in diabetic wound healing with activation of the akt/nrf2/ho-1 pathway. *ACS Appl Mater Interfaces* 12, 11397–11408. doi: 10.1021/acsami.0c00874

Lingappan, K. (2018). Nf-kappab in oxidative stress. *Curr. Opin. Toxicol.* 7, 81–86. doi: 10.1016/j.cotox.2017.11.002

Long, M., Rojo de la Vega, M., Wen, Q., Bharara, M., Jiang, T., Zhang, R., et al. (2016). An essential role of nrf2 in diabetic wound healing. *Diabetes Metab. Res. Rev.* 65, 780–793. doi: 10.2337/db15-0564

Loo, A. E., Wong, Y. T., Ho, R., Wasser, M., Du, T., Ng, W. T., et al. (2012). Effects of hydrogen peroxide on wound healing in mice in relation to oxidative damage. *PLoS One* 7:e49215. doi: 10.1371/journal.pone.0049215

Loots, M. A., Lamme, E. N., Zeegelaar, J., Mekkes, J. R., Bos, J. D., and Middelkoop, E. (1998). Differences in cellular infiltrate and extracellular matrix of chronic diabetic and venous ulcers versus acute wounds. *J. Invest. Dermatol.* 111, 850–857. doi: 10.1046/j.1523-1747.1998.00381.x

Lushchak, V. I. (2014). Free radicals, reactive oxygen species, oxidative stress and its classification. *Chem. Biol. Interact.* 224, 164–175. doi: 10.1016/j.cbi.2014.10.016

Maier, C. M., and Chan, P. H. (2002). Role of superoxide dismutases in oxidative damage and neurodegenerative disorders. *Neuroscientist* 8, 323–334. doi: 10.1177/107385840200800408

Maines, M. D., and Kappas, A. (1977). Enzymatic oxidation of cobalt protoporphyrin ix, Observations on the mechanism of heme oxygenase action. *Biochemistry* 16, 419–423. doi: 10.1021/bi00622a012

Mariappan, N., Elks, C. M., Sriramula, S., Guggilam, A., Liu, Z., Borkhsenious, O., et al. (2010). Nf-kappab-induced oxidative stress contributes to mitochondrial and cardiac dysfunction in type ii diabetes. *Cardiovasc. Res.* 85, 473–483. doi: 10.1093/cvr/cvp305

Maritim, A. C., Sanders, R. A., and Watkins, J. B. III (2003). Diabetes, oxidative stress, and antioxidants, a review. *J. Biochem. Mol. Toxicol.* 17, 24–38. doi: 10.1002/jbt.10058

Martin, A. (1996). The use of antioxidants in healing. *Dermatol. Surg.* 22, 156–160. doi: 10.1111/j.1524-4725.1996.tb00499.x

Martin, P. (1997). Wound healing–aiming for perfect skin regeneration. *Science* 276, 75–81. doi: 10.1126/science.276.5309.75

Mirza, R. E., and Koh, T. J. (2015). Contributions of cell subsets to cytokine production during normal and impaired wound healing. *Cytokine* 71, 409–412. doi: 10.1016/j.cyto.2014.09.005

Mitchell, S., Vargas, J., and Hoffmann, A. (2016). Signaling via the nfkappab system. *Wiley Interdiscip. Rev. Syst. Biol. Med.* 8, 227–241. doi: 10.1002/wsbm.1331

Molavi, B., and Mehta, J. L. (2004). Oxidative stress in cardiovascular disease, Molecular basis of its deleterious effects, its detection, and therapeutic considerations. *Curr. Opin. Cardiol.* 19, 488–493. doi: 10.1097/01.hco.0000133657.77024.bd

Monnier, L., Mas, E., Ginet, C., Michel, F., Villon, L., Cristol, J. P., et al. (2006). Activation of oxidative stress by acute glucose fluctuations compared with sustained chronic hyperglycemia in patients with type 2 diabetes. *JAMA* 295, 1681–1687. doi: 10.1001/jama.295.14.1681

NCD Risk Factor Collaboration (Ncd-RisC) (2016). Worldwide trends in diabetes since 1980, a pooled analysis of 751 population-based studies with 4.4 million participants. *Lancet* 387, 1513–1530.

Niemiec, S. M., Louiselle, A. E., Hilton, S. A., Dewberry, L. C., Zhang, L., Azeltine, M., et al. (2020). Nanosilk increases the strength of diabetic skin and delivers cnp-mir146a to improve wound healing. *Front. Immunol.* 11:590285. doi: 10.3389/fimmu.2020.590285

Oh, J. Y., Choi, G. E., Lee, H. J., Jung, Y. H., Chae, C. W., Kim, J. S., et al. (2019). 17beta-estradiol protects mesenchymal stem cells against high glucose-induced mitochondrial oxidants production via nrf2/sirt3/mnsod signaling. *Free Radic. Biol. Med.* 130, 328–342. doi: 10.1016/j.freeradbiomed.2018.11.003

Panayi, A. C., Endo, Y., Karvar, M., Sensharma, P., Haug, V., Fu, S., et al. (2020). Low mortality oxidative stress murine chronic wound model. *BMJ Open Diabetes Res. Care* 8, e001221. doi: 10.1136/bmjdrc-2020-001221

Park, J. Y., Shin, M. S., Hwang, G. S., Yamabe, N., Yoo, J. E., Kang, K. S., et al. (2018). Beneficial effects of deoxyshikonin on delayed wound healing in diabetic mice. *Int. J. Mol. Sci.* 19:3660. doi: 10.3390/ijms19113660

Pessoa, A. F., Florim, J. C., Rodrigues, H. G., Andrade-Oliveira, V., Teixeira, S. A., Vitzel, K. F., et al. (2016). Oral administration of antioxidants improves skin wound healing in diabetic mice. *Wound Repair Regen.* 24, 981–993. doi: 10.1111/wrr.12486

Quan, T., Wang, F., Shao, Y., Rittie, L., Xia, W., Orringer, J. S., et al. (2013). Enhancing structural support of the dermal microenvironment activates fibroblasts, endothelial cells, and keratinocytes in aged human skin in vivo. *J. Invest. Dermatol.* 133, 658–667. doi: 10.1038/jid.2012.364

Rabbani, P. S., Ellison, T., Waqas, B., Sultan, D., Abdou, S., David, J. A., et al. (2018). Targeted nrf2 activation therapy with rta 408 enhances regenerative capacity of diabetic wounds. *Diabetes. Res. Clin. Pract.* 139, 11–23. doi: 10.1016/j.diabres.2018.02.021

Rabbani, P. S., Zhou, A., Borab, Z. M., Frezzo, J. A., Srivastava, N., More, H. T., et al. (2017). Novel lipoproteoplex delivers keap1 sirna based gene therapy to accelerate diabetic wound healing. *Biomaterials* 132, 1–15. doi: 10.1016/j.biomaterials.2017.04.001

Ravanti, L., and Kahari, V. M. (2000). Matrix metalloproteinases in wound repair (review). *Int. J. Mol. Med.* 6, 391–407. doi: 10.3892/ijmm.6.4.391

Reisman, S. A., Goldsberry, A. R., Lee, C. Y., O'Grady, M. L., Proksch, J. W., Ward, K. W., et al. (2015). Topical application of rta 408 lotion activates nrf2 in human skin and is well-tolerated by healthy human volunteers. *BMC Dermatol.* 15:10. doi: 10.1186/s12895-015-0029-7

Reisman, S. A., Lee, C. Y., Meyer, C. J., Proksch, J. W., Sonis, S. T., and Ward, K. W. (2014). Topical application of the synthetic triterpenoid rta 408 protects mice from radiation-induced dermatitis. *Radiat Res.* 181, 512–520. doi: 10.1667/RR13578.1

Ren, J., Yang, M., Xu, F., Chen, J., and Ma, S. (2019). Acceleration of wound healing activity with syringic acid in streptozotocin induced diabetic rats. *Life Sci.* 233:116728. doi: 10.1016/j.lfs.2019.116728

Roberts, A. C., and Porter, K. E. (2013). Cellular and molecular mechanisms of endothelial dysfunction in diabetes. *Diab. Vasc. Dis. Res.* 10, 472–482. doi: 10.1177/1479164113500680

Rochette, L., Zeller, M., Cottin, Y., and Vergely, C. (2014). Diabetes, oxidative stress and therapeutic strategies. *Biochim. Biophys. Acta* 1840, 2709–2729. doi: 10.1016/j.bbagen.2014.05.017

Rodrigues, M., Kosaric, N., Bonham, C. A., and Gurtner, G. C. (2019). Wound healing, a cellular perspective. *Physiol. Rev.* 99, 665–706. doi: 10.1152/physrev.00067.2017

Ruiz, S., Pergola, P. E., Zager, R. A., and Vaziri, N. D. (2013). Targeting the transcription factor nrf2 to ameliorate oxidative stress and inflammation in chronic kidney disease. *Kidney Int.* 83, 1029–1041. doi: 10.1038/ki.2012.439

Ryter, S. W., and Choi, A. M. (2009). Heme oxygenase-1/carbon monoxide, From metabolism to molecular therapy. *Am. J. Respir. Cell Mol. Biol.* 41, 251–260. doi: 10.1165/rcmb.2009-0170TR

Sarandy, M. M., Novaes, R. D., Xavier, A. A., Vital, C. E., Leite, J., Melo, P. V. F., et al. (2017). Hydroethanolic extract of strychnos pseudoquina accelerates skin wound healing by modulating the oxidative status and microstructural reorganization of scar tissue in experimental type i diabetes. *Biomed. Res. Int.* 2017:9538351. doi: 10.1155/2017/9538351

Schafer, M., and Werner, S. (2008). Oxidative stress in normal and impaired wound repair. *Pharmacol. Res.* 58, 165–171. doi: 10.1016/j.phrs.2008.06.004

Sen, C. K., and Roy, S. (2008). Redox signals in wound healing. *Biochim. Biophys. Acta* 1780, 1348–1361. doi: 10.1016/j.bbagen.2008.01.006

Sener, G., Hilton, S. A., Osmond, M. J., Zgheib, C., Newsom, J. P., Dewberry, L., et al. (2020). Injectable, self-healable zwitterionic cryogels with sustained microrna - cerium oxide nanoparticle release promote accelerated wound healing. *Acta Biomater.* 101, 262–272. doi: 10.1016/j.actbio.2019.11.014

Sies, H. (2015). Oxidative stress, a concept in redox biology and medicine. *Redox. Biol.* 4, 180–183. doi: 10.1016/j.redox.2015.01.002

Singer, A. J., and Clark, R. A. (1999). Cutaneous wound healing. *N. Engl. J. Med.* 341, 738–746. doi: 10.1056/NEJM199909023411006

Singh, N., Armstrong, D. G., and Lipsky, B. A. (2005). Preventing foot ulcers in patients with diabetes. *JAMA* 293, 217–228. doi: 10.1001/jama.293.2.217

Soares, M. A., Cohen, O. D., Low, Y. C., Sartor, R. A., Ellison, T., Anil, U., et al. (2016). Restoration of nrf2 signaling normalizes the regenerative niche. *Diabetes Metab. Res. Rev.* 65, 633–646. doi: 10.2337/db15-0453

Stadelmann, W. K., Digenis, A. G., and Tobin, G. R. (1998). Physiology and healing dynamics of chronic cutaneous wounds. *Am. J. Surg.* 176, 26S–38S. doi: 10.1016/S0002-9610(98)00183-4

Surh, Y. J., Kundu, J. K., Na, H. K., and Lee, J. S. (2005).). Redox-sensitive transcription factors as prime targets for chemoprevention with anti-inflammatory and antioxidative phytochemicals. *J. Nutr.* 135, 2993S–3001S. doi: 10.1093/jn/135.12.2993S

Taylor, B. S., de Vera, M. E., Ganster, R. W., Wang, Q., Shapiro, R. A., Morris, S. M. Jr., et al. (1998). Multiple nf-kappab enhancer elements regulate cytokine induction of the human inducible nitric oxide synthase gene. *J. Biol. Chem.* 273, 15148–15156. doi: 10.1074/jbc.273.24.15148

Tracy, L. E., Minasian, R. A., and Caterson, E. J. (2016). Extracellular matrix and dermal fibroblast function in the healing wound. *Adv. Wound Care (New Rochelle)* 5, 119–136. doi: 10.1089/wound.2014.0561

Vallabhapurapu, S., and Karin, M. (2009). Regulation and function of nf-kappab transcription factors in the immune system. *Annu. Rev. Immunol.* 27, 693–733. doi: 10.1146/annurev.immunol.021908.132641

Wakabayashi, N., Dinkova-Kostova, A. T., Holtzclaw, W. D., Kang, M. I., Kobayashi, A., Yamamoto, M., et al. (2004). Protection against electrophile and oxidant stress by induction of the phase 2 response, fate of cysteines of the keap1 sensor modified by inducers. *Proc. Natl. Acad. Sci. U S A.* 101, 2040–2045. doi: 10.1073/pnas.0307301101

Walker, A., Nissen, E., and Geiger, A. (2018). Migratory, metabolic and functional alterations of fibrocytes in type 2 diabetes. *IUBMB Life* 70, 1122–1132. doi: 10.1002/iub.1920

Wang, T. T., Sathyamoorthy, N., and Phang, J. M. (1996). Molecular effects of genistein on estrogen receptor mediated pathways. *Carcinogenesis* 17, 271–275. doi: 10.1093/carcin/17.2.271

Weinheimer-Haus, E. M., Mirza, R. E., and Koh, T. J. (2015). Nod-like receptor protein-3 inflammasome plays an important role during early stages of wound healing. *PLoS One* 10:e0119106. doi: 10.1371/journal.pone.0119106

Wlaschek, M., and Scharffetter-Kochanek, K. (2005). Oxidative stress in chronic venous leg ulcers. *Wound Repair Regen.* 13, 452–461. doi: 10.1111/j.1067-1927.2005.00065.x

Wu, P., Yan, Y., Ma, L. L., Hou, B. Y., He, Y. Y., Zhang, L., et al. (2016). Effects of the nrf2 protein modulator salvianolic acid a alone or combined with metformin on diabetes-associated macrovascular and renal injury. *J. Biol. Chem.* 291, 22288–22301. doi: 10.1074/jbc.M115.712703

Wu, W., Qiu, Q., Wang, H., Whitman, S. A., Fang, D., Lian, F., et al. (2013). Nrf2 is crucial to graft survival in a rodent model of heart transplantation. *Oxid. Med. Cell Longev.* 2013:919313. doi: 10.1155/2013/919313

Xie, Y., Chu, A., Feng, Y., Chen, L., Shao, Y., Luo, Q., et al. (2018). Microrna-146a, A comprehensive indicator of inflammation and oxidative stress status induced in the brain of chronic t2dm rats. *Front. Pharmacol.* 9:478. doi: 10.3389/fphar.2018.00478

Xu, C., Bentinger, M., Savu, O., Moshfegh, A., Sunkari, V., Dallner, G., et al. (2017). Mono-epoxy-tocotrienol-alpha enhances wound healing in diabetic mice and stimulates in vitro angiogenesis and cell migration. *J. Diabetes Complications* 31, 4–12. doi: 10.1016/j.jdiacomp.2016.10.010

Xu, J., Wu, W., Zhang, L., Dorset-Martin, W., Morris, M. W., Mitchell, M. E., et al. (2012). The role of microrna-146a in the pathogenesis of the diabetic wound-healing impairment, correction with mesenchymal stem cell treatment. *Diabetes Metab. Res. Rev.* 61, 2906–2912. doi: 10.2337/db12-0145

Yan, J., Tie, G., Wang, S., Tutto, A., DeMarco, N., Khair, L., et al. (2018). Diabetes impairs wound healing by dnmt1-dependent dysregulation of hematopoietic stem cells differentiation towards macrophages. *Nat. Commun.* 9:33. doi: 10.1038/s41467-017-02425-z

Yang, N., Zhang, W., Ye, C., Chen, X., and Ling, S. (2019). Nanobiopolymers fabrication and their life cycle assessments. *Biotechnol. J.* 14:e1700754. doi: 10.1002/biot.201700754

Yao, J., Mackman, N., Edgington, T. S., and Fan, S. T. (1997). Lipopolysaccharide induction of the tumor necrosis factor-alpha promoter in human monocytic cells. Regulation by egr-1, c-jun, and nf-kappab transcription factors. *J. Biol. Chem.* 272, 17795–17801. doi: 10.1074/jbc.272.28.17795

Yerra, V. G., Kalvala, A. K., and Kumar, A. (2017). Isoliquiritigenin reduces oxidative damage and alleviates mitochondrial impairment by sirt1 activation in experimental diabetic neuropathy. *J. Nutr. Biochem.* 47, 41–52. doi: 10.1016/j.jnutbio.2017.05.001

Yeung, F., Hoberg, J. E., Ramsey, C. S., Keller, M. D., Jones, D. R., Frye, R. A., et al. (2004). Modulation of nf-kappab-dependent transcription and cell survival by the sirt1 deacetylase. *EMBO J.* 23, 2369–2380. doi: 10.1038/sj.emboj.7600244

Yun, K. J., Kim, J. Y., Kim, J. B., Lee, K. W., Jeong, S. Y., Park, H. J., et al. (2008). Inhibition of lps-induced no and pge2 production by asiatic acid via nf-kappa b inactivation in raw 264.7 macrophages, Possible involvement of the ikk and mapk pathways. *Int. Immunopharmacol.* 8, 431–441. doi: /10.1016/j.intimp.2007.11.003

Zgheib, C., Hilton, S. A., Dewberry, L. C., Hodges, M. M., Ghatak, S., Xu, J., et al. (2019). Use of cerium oxide nanoparticles conjugated with microrna-146a to correct the diabetic wound healing impairment. *J. Am. Coll. Surg.* 228, 107–115. doi: 10.1016/j.jamcollsurg.2018.09.017

Zhang, L., Ma, Y., Pan, X., Chen, S., Zhuang, H., and Wang, S. (2018). A composite hydrogel of chitosan/heparin/poly (gamma-glutamic acid) loaded with superoxide dismutase for wound healing. *Carbohydr. Polym.* 180, 168–174. doi: 10.1016/j.carbpol.2017.10.036

Zhang, P., He, L., Zhang, J., Mei, X., Zhang, Y., Tian, H., et al. (2020). Preparation of novel berberine nano-colloids for improving wound healing of diabetic rats by acting sirt1/nf-kappab pathway. *Colloids Surf B Biointerfaces* 187:110647. doi: 10.1016/j.colsurfb.2019.110647

Zhang, Q., Lenardo, M. J., and Baltimore, D. (2017). 30 years of nf-kappab, A blossoming of relevance to human pathobiology. *Cell* 168, 37–57. doi: 10.1016/j.cell.2016.12.012

Zhao, M., Zhou, J., Chen, Y. H., Yuan, L., Yuan, M. M., Zhang, X. Q., et al. (2018). Folic acid promotes wound healing in diabetic mice by suppression of oxidative stress. *J. Nutr. Sci. Vitaminol. (Tokyo)* 64, 26–33. doi: doi.org/10.3177/jnsv.64.26

Zhou, X., Ruan, Q., Ye, Z., Chu, Z., Xi, M., Li, M., et al. (2021). Resveratrol accelerates wound healing by attenuating oxidative stress-induced impairment of cell proliferation and migration. *Burns* 47, 133–139. doi: 10.1016/j.burns.2020.10.016

Zoja, C., Benigni, A., and Remuzzi, G. (2014). The nrf2 pathway in the progression of renal disease. *Nephrol. Dial. Transplant.* 29(Suppl. 1), i19–i24. doi: 10.1093/ndt/gft224

Conflict of Interest: The authors declare that the research was conducted in the absence of any commercial or financial relationships that could be construed as a potential conflict of interest.

Copyright © 2021 Zhang, Chen, Xiong, Panayi, Abududilibaier, Hu, Yu, Zhou, Sun, Liu, Xue, Hu, Yan, Xie, Lin, Cao, Mi and Liu. This is an open-access article distributed under the terms of the Creative Commons Attribution License (CC BY). The use, distribution or reproduction in other forums is permitted, provided the original author(s) and the copyright owner(s) are credited and that the original publication in this journal is cited, in accordance with accepted academic practice. No use, distribution or reproduction is permitted which does not comply with these terms.

frontiers in Bioengineering and Biotechnology

REVIEW
published: 21 July 2021
doi: 10.3389/fbioe.2021.723490

Hydrogel-By-Design: Smart Delivery System for Cancer Immunotherapy

Rongwei Cui[1,2], Qiang Wu[1], Jing Wang[3], Xiaoming Zheng[1], Rongying Ou[4], Yunsheng Xu[5], Shuxin Qu[2] and Danyang Li[1]**

[1]Research Center, The Seventh Affiliated Hospital, Sun Yat-sen University, Shenzhen, China, [2]Key Lab of Advanced Technologies of Materials, Ministry of Education, School of Material Science and Engineering, Southwest Jiaotong University, Chengdu, China, [3]School of Life Sciences, Northwestern Polytechnical University, Xi'an, China, [4]Department of Gynaecology and Obstetrics, The First Affiliated Hospital of Wenzhou Medical University, Wenzhou, China, [5]Department of Dermatovenereology, The Seventh Affiliated Hospital, Sun Yat-sen University, Shenzhen, China

Immunotherapy has emerged as a promising strategy for cancer treatment, in which durable immune responses were generated in patients with malignant tumors. In the past decade, biomaterials have played vital roles as smart drug delivery systems for cancer immunotherapy to achieve both enhanced therapeutic benefits and reduced side effects. Hydrogels as one of the most biocompatible and versatile biomaterials have been widely applied in localized drug delivery systems due to their unique properties, such as loadable, implantable, injectable, degradable and stimulus responsible. Herein, we have briefly summarized the recent advances on hydrogel-by-design delivery systems including the design of hydrogels and their applications for delivering of immunomodulatory molecules (e.g., cytokine, adjuvant, checkpoint inhibitor, antigen), immune cells and environmental regulatory substances in cancer immunotherapy. We have also discussed the challenges and future perspectives of hydrogels in the development of cancer immunotherapy for precision medicine at the end.

Keywords: hydrogels, smart delivery, cancer immunotherapy, immunomodualtors, immune cells, environmental regulatory substance

OPEN ACCESS

Edited by:
Junqing Wang,
School of Pharmaceutical Sciences (Shenzhen) Sun Yat-sen University, China

Reviewed by:
Rongrong Jin,
Sichuan University, China
Changqiang Wu,
North Sichuan Medical College, China

****Correspondence:***
Shuxin Qu
qushuxin@swjtu.edu.cn
Danyang Li
lidy55@mail.sysu.edu.cn

Specialty section:
This article was submitted to Biomaterials, a section of the journal Frontiers in Bioengineering and Biotechnology

Received: *10 June 2021*
Accepted: *09 July 2021*
Published: *21 July 2021*

Citation:
Cui R, Wu Q, Wang J, Zheng X, Ou R, Xu Y, Qu S and Li D (2021) Hydrogel-By-Design: Smart Delivery System for Cancer Immunotherapy. Front. Bioeng. Biotechnol. 9:723490. doi: 10.3389/fbioe.2021.723490

INTRODUCTION

In the past decade, cancer immunotherapy has shifted the paradigm for the treatment of cancers that it activates patients' own immune systems to attack and kill cancers. Till now, cancer immunotherapy includes five main classes, immune checkpoint blockade (ICB) therapy, lymphocyte promoting cytokine therapy, chimeric antigen receptor T-cell (CAR-T) therapy, agonistic antibodies and cancer vaccines (Chao et al., 2019; Tang et al., 2021; Yang et al., 2020). The success of those therapies relies on the administration of corresponding biomacromolecules such as checkpoint inhibitors, cytokines, antibodies or T cells and vaccines (Li et al., 2020; Tang et al., 2021). However, high dose or multiple injections involved in conventional drug administration methods may introduce many problems such as safety issues and efficacy (Chao et al., 2019). For instance, the toxicity caused by the delivery agents and the complex tumor microenvironments are still challenges for the development of suitable delivery systems for cancer immunotherapy (Vigata et al., 2020). Therefore, novel delivery approaches could increase the accumulation of immune therapeutics in targeted sites, enabling more effective treatment and reduced side effects (Qiu et al., 2020). Biomaterials such as lipids (Yang et al., 2020), polymers (Munoz et al., 2021), polypeptides and hydrogels (Hoffman, 2012; Munoz et al., 2021) have played vital roles as smart delivery systems for cancer immunotherapy. The unique physicochemical properties of hydrogel have attracted broad attentions of researchers (Hoffman, 2012; Pal et al., 2013).

Firstly, hydrogels are formed by hydrophilic polymer chains absorbing large amounts of water (Ahmed, 2015; Oliva et al., 2017). The water content could reach 90%, which provides a suitable physiological environment for the cargoes (Akhtar et al., 2016; Xie et al., 2021). Hydrogels with excellent biocompatibility highly mimic the properties of nature tissues because of their high water content (Salah et al., 2020). Furthermore, the softness and rubbery properties of hydrogels minimize inflammatory reaction of surrounding cells. Especially for CAR-T therapy, cell viability could be guaranteed which is the basis for its immune function (Palucka and Banchereau, 2012; Seliktar, 2012; Monette et al., 2016; Zeng et al., 2021). Secondly, the availability of functional groups and the adjustable of the formed network structure of hydrogels allow carrying cargoes with various types and via different magnitude of interaction forces (Qiu et al., 2020). For example, Leach et al. developed an injectable multi-domain peptide-based hydrogel that can carry cyclic dinucleotides and STING (stimulator of interferon genes) agonists through electrostatic interactions (Leach et al., 2018). Additionally, the injectable properties of hydrogels through quick sol-gel phase transition or *in situ* chemical polymerization render them implantable in the body with minimal surgical wounds and the *in situ* entrapment of therapeutic molecules or cells by simple syringe injection at target sites (Overstreet et al., 2012; Leach et al., 2019; Vigata et al., 2020). Yu *et al.* summarized the status and development trend of injectable hydrogel-based cancer immunotherapy and claimed that injectable hydrogels have unprecedented potential to realize the inhibition of tumor growth at the systemic level and prevent the occurrence of side effects through local administration (Chao et al., 2019). Moreover, hydrogels respond immediately to various external stimuli and undergo morphological changes, which realize sustained and controlled release of therapeutics for cancer immunotherapy (Lin and Metters, 2006; Ma et al., 2021). Novel pH-responsive hydrogels with high swelling property at acidic pH were shown to release drug at a relative fast rate by adjusting the ratio of chitosan and alginate polymers with poly (vinyl alcohol) (Andrade et al., 2021). In addition, the advantages of ease of synthesis, and low raw material prices also make hydrogels a very promising delivery agent for multiple immunological therapeutics (Ahmed, 2015).

This review concentrates on the state-of-the-art of hydrogels applied in cancer immunotherapy as efficient, biocompatible, controllable local drug delivery platforms. The following sections discussed the design principles of hydrogels for delivery therapeutics for cancer immunotherapy, which include the choice of polymer feedstock, the strength of the interaction force between the polymer network, the polymer modification etc. In addition, specific applications of hydrogels in cancer immunotherapy that classified by the carrying cargos which includes cytokines, adjuvant, checkpoint inhibitors, antigen, cells and environmental regulatory substance were discussed and summarized. At last, the development trend, main challenges and clinical application potential of hydrogel-based delivery systems for cancer immunotherapy were discussed.

CHARACTERISTICS OF HYDROGELS AS DELIVERY SYSTEMS FOR CANCER IMMUNOTHERAPY

Cancer immunotherapy mainly aims to achieve the following purposes, e.g., enhancing the functions of antigen presenting cells, promoting the production of protective T-cells and overcoming immunosuppression (Zou, 2006; Tang et al., 2021). The corresponding therapeutics commonly used in cancer immunotherapy, such as biologically antigenic proteins or peptides, nucleic acids, natural or synthetic adjuvants, and immune cells require the delivery systems to retain their activities and functions (Zhang et al., 2018; Chao et al., 2019).

Hydrogel is a particularly appealing type of drug delivery system because of its unique characters, providing the delivered immunological therapeutics with a physiological environment that highly mimics the natural conditions (**Figure 1**; Hori et al., 2008; Hickey et al., 2019). These desirable properties include loadable (**Figure 2A**), implantable/injectable (**Figure 2B**), degradable (**Figure 2C**) and stimulus-responsible (**Figure 2D**). Hydrogels as drug delivery systems can be divided into two categories according to their component sources: synthetic and natural (Chao et al., 2019). Commonly used synthetic hydrogels are hydroxyethyl methacrylate (pHEMA), poly(vinyl alcohol) (PVA), and poly(ethylene glycol) (PEG). These components often have stimulus response characteristics such as temperature sensitivity, so that the hydrogel can be polymerized or degraded *in situ* (Rizzo and Kehr, 2021). Natural hydrogels include polysaccharides (such as hyaluronic acid and alginate), proteins (such as gelatine and collagen), and DNA. This type of hydrogel has extremely high biocompatibility. The large number of hydroxyl, carboxyl and amino groups in the composition also makes it capable of loading a variety of drugs (Choudhury et al., 2018; Hauptstein et al., 2020). In this part, we focused on the key characters of hydrogels influencing the delivery of therapeutics for cancer immunotherapy.

Loadable

First of all, hydrogel has the capability to easily encapsulate hydrophilic drugs due to its high water content. The water content of the hydrogel is related to the type of polymers. Natural polymers such as hyaluronic acid-based hydrogel can achieve 99% water content (Tu et al., 2019; Dorishetty et al., 2020). Secondly, the crosslinked network of hydrogel could prevent the drugs from leaking out and impede penetration of various proteins that may degrade the loaded biological drugs (Pal et al., 2013). This feature means the hydrogel can be loaded with highly labile macromolecular drugs (for example, recombinant proteins and monoclonal antibodies). According to David J. Mooney, the space between polymer molecules in the network (referred to as the mesh size) is tunable from around 5 to around 100 nm (Li and Mooney, 2016). Importantly, the network can retain the drugs in the "mesh" before the state of the hydrogel changes. The mesh size of hydrogels can be adjusted by the molecular weight and concentration of the polymer (**Figure 2A**). In general, the higher the molecular weight and the concentration, the smaller the mesh size can be achieved to

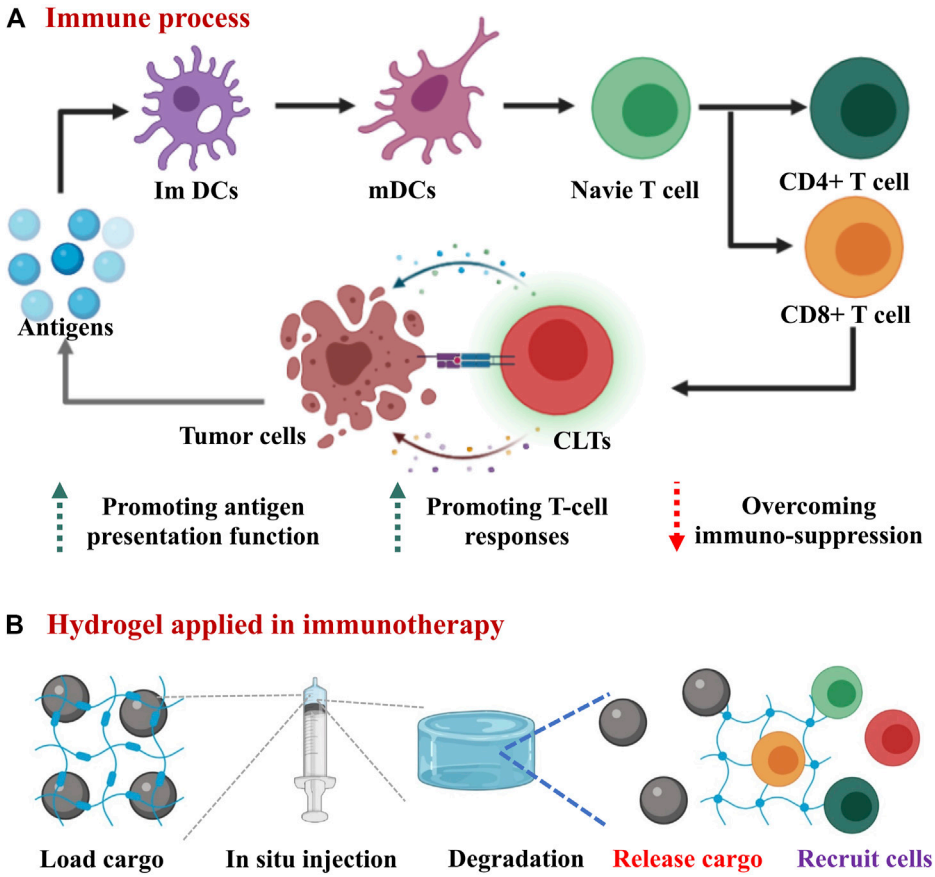

FIGURE 1 | Overview scheme of hydrogels applied in cancer immunotherapy. **(A)** The schematic diagram of the immune response in the body: antigens are processed by immature dendritic cells (ImDCs), then mature dendritic cells (mDCs) presented antigens to T cells. $CD8^+$ T cells further differentiate into cytotoxic T lymphocytes (CTLs) to directly kill tumor cells. **(B)** hydrogels applied in immunotherapy: the hydrogel carrying various cargos is injected into the tumor site and then undergoes degradation, thereby releasing drugs and recruting immune cells to tumor site.

encapsulate the smaller size of drugs. Finally, there are various interactions (**Figure 2A**) between the drugs and the polymer chains which could be designed *via* diverse strategies such as covalent conjugation, electrostatic interactions and hydrophobic associations (Li and Mooney, 2016). The interactions between hydrogels and drugs are important to maintain the functions and activities of the loaded cargos when designing hydrogels. For instance, Dror *et al.* claimed the bioactivities of hydrogels could be achieved through immobilizing growth factors and/or small molecules such as RGD peptide (Arginine-Glycine-Aspartic acid) to the backbone polymer. With facilitainge the interactions with cellular and extracellular biomolecules, the hydrogel can also carry immune cells for therapeutic purposes(Chao et al., 2019; Li et al., 2020).

Implantable

Immunotherapeutics on their own typically require repeated high-dose injections that often result in off target effects with limited efficacy. Implantable scaffolds formed by hydrogel possess powerful synergies with anti-cancer immunotherapies because they allow for discrete localization and controlled release of immunotherapeutic agents, which have been shown various applications to improve outcomes in the treatment of cancers *via* immunotherapy (Buwalda et al., 2014; Rizzo and Kehr, 2021). Among various strategies, implantable hydrogel can form robust tablet-like scaffolds that are surgically implanted into a tumor resection site, releasing immunoregulatory "cargos" and recruiting immune cells into the porous matrix of the scaffold for further biological programming (Li et al., 2020). In order to prepare hydrogels into implantable scaffold with different mechanical, degradation, and slow-release properties, the cross-linking process needs to be adjusted. Because of the covalent bonds presented between the polymer chains, chemical cross-linking is one of the highly resourceful methods for the formation of hydrogels with excellent mechanical strength (Tie et al., 2020). The hydrogel formed in this method usually degrades slower, so that the release rate of the carried immune drug is relatively slow. Simultaneously, literatures show that hydrogel with a large elastic modulus is beneficial for adhesion and spread of immune cells on its surface, while not being conducive for migration of immune cells into its three-dimensional interior of the hydrogel (Seliktar, 2012;

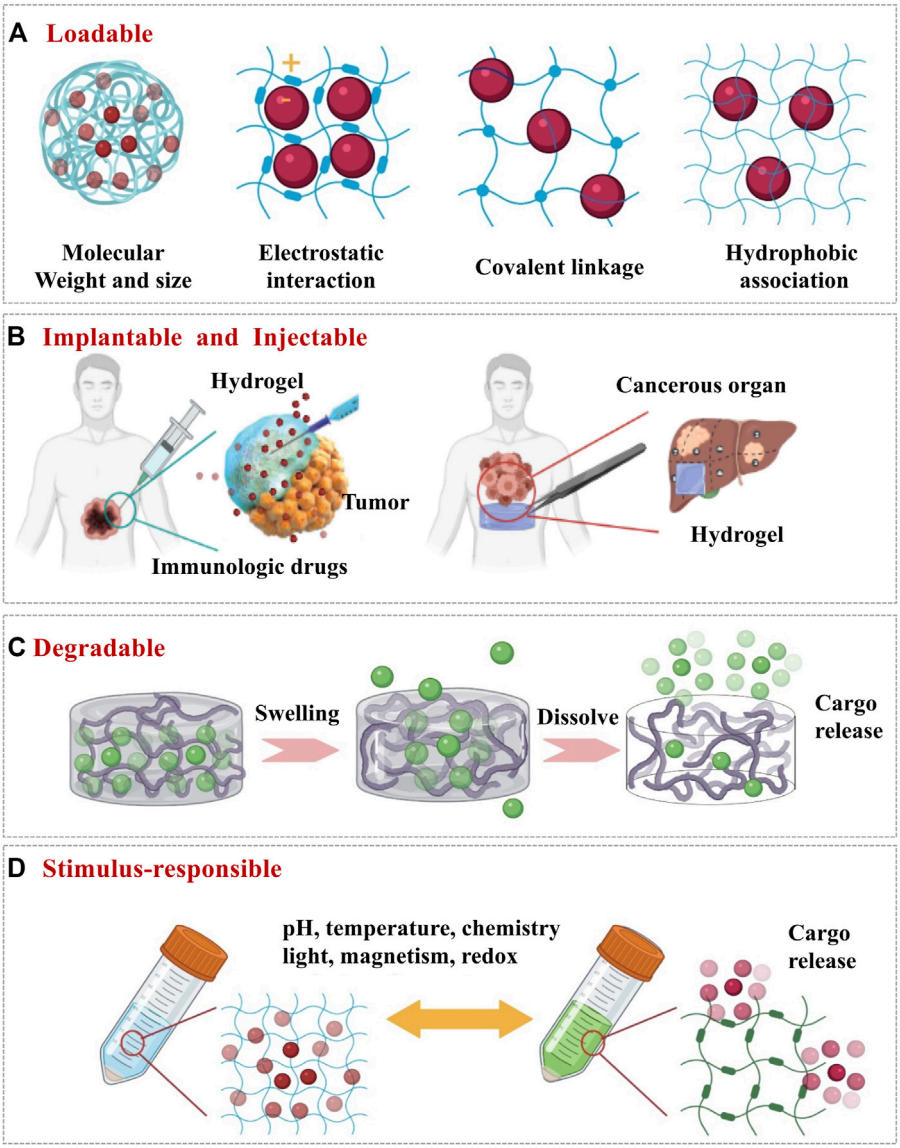

FIGURE 2 | The design of hydrogel by altering its physicochemical properties as delivery systems for cancer immunotherapy. **(A)** Loadable: ensure that the immune cargo can stay in the hydrogel when it does not need to be released. **(B)** Implantable and injectable: ensure that the hydrogel can reach the tumor site in a minimally invasive, non-surgical way and stays at the tumor site for drug release. **(C)** Degradable: hydrogel degrades for releasing the encapsulated drugs. **(D)** Stimulus-responsible: to achieve controlled release of the drugs from hydrogel upon external stimuli.

Ahearne, 2014; Simona et al., 2015). Since physical cross-linking is relatively mild and avoids the use of cross-linking agents, it is much more friendly to loaded immunotherapy-related biologically active components such as cytokines and immune cells. The interaction forces formed between physical cross-links include hydrogen bonds, hydrophobic interactions and ionic interactions. These weak interaction forces are extremely easy to be destroyed, which makes the drug delivery system easy to degrade and results in relatively rapid drug release (Buwalda et al., 2014). The most advanced application of implantable hydrogels in immunotherapy is enhance adoptive T cell (ATC) immunotherapy because it is able to support T cell viability and localize the desired immune response (Oh et al., 2016). Stephan *et al.* synthesized a calcium cross-linked alginate scaffold containing synthetic collagen mimic peptides, which can promote the adhesion and migration of T cells and also increase the expansion and dispersion of T cells to the tumor resection bed (Hori et al., 2008; Rastogi and Kandasubramanian, 2019).

Injectable

Injectable hydrogels formed *in situ* by chemical polymerization or sol–gel phase transition have been widely concerned in drug delivery and cancer immunotherapy (Chao et al., 2019).

Injectable means the materials are flowable before injection but rapidly turn into gels once injected (**Figure 2B**). Such materials have been widely used because of a few distinct advantages (Rizzo and Kehr, 2021). Firstly, they can be positioned and delivered following the needle, which is a simpler and less traumatic process that avoids unnecessary tissue damage and complications related to inflammation. Secondly, with their viscoelastic properties, injectable materials can move and flow, conforming to any available space before forming into a persisting implant. Koshy *et al.* reported an injectable gelatin cryogels derived from natural collagen, which were shown to be easily administered without a surgical procedure, promoting infiltration and proliferation of immune cells with controlled release of granulocyte-macrophage colony-stimulating factor (GM-CSF) (Duong et al., 2020). Thirdly, it is easy to encapsulate cells or drugs.

At present, rapid construction of injectable and biocompatible hydrogels with proper mechanical properties remains a challenge. Many methods including thermal gelation, ionic interaction, physical self-assembly and photopolymerization have been employed for preparation of injectable hydrogels *in situ* (Lei and Tang, 2019; Duong et al., 2020). The "click" reaction, with easy preparation and rapid reaction rate, has emerged as one of the most versatile and innovative technologies (Lei and Tang, 2019). Due to the fast reaction rate and mild reaction conditions, click chemistry is often used to fabricate bio-orthogonal hydrogels, which are highly suitable as carriers for delivering immunotherapy related drugs. In a study by Xu *et al.*, two types of biodegradable and injectable hydrogels using thiol–Michael addition reaction were found to be capable of carrying cells and allowing them function when reaching the designated site (Liu et al., 2020). In addition, Brudno *et al.* confirmed that utilizing biorthogonal click chemistry to link the functionalized hydrogel with modified anti-cancer pro-drug agents *in situ* (Ma et al., 2021). In clinical immunotherapy, injectable and implantable can exist simultaneously once the hydrogel is delivered to the tumor site through the needle, the hydrogel can spontaneously form a high-strength scaffold. Kim *et al.* have developed an injectable cancer vaccine scaffold based on mesoporous silica rods. The system is an ingenious compromise between implantable stents and injectable biomaterials. When injected subcutaneously, it self-assembles into a unique pocket-like reservoir *in situ*, allowing extended load factor release (Chao et al., 2019).

Degradable

When used as drug delivery system in cancer immunotherapy, hydrogels mainly release drugs at tumor sites in two ways: hydrogel degradation and hydrogel swelling (Oliva et al., 2017). As the network degrades, the mesh size increases, allowing drugs to diffuse out of the hydrogel (**Figure 2C**). Hydrogels undergo local or bulk dissolution *via* a number of mechanisms (such as hydrolysis, proteolysis, disentanglement, or environmental triggers), whilst degradation can occur in the polymer backbone or at the crosslinks, and is typically mediated by hydrolysis or enzyme activity (Tan and Marra, 2010; Vojtova et al., 2019). The hydrogel can be passively degraded or can be actively degraded in response to a certain stimulus, achieving the controlled release of immune "cargos", which will be discussed in more detail in the next section. Furthermore, the degradation process should also not be too short nor too long because the short degradation of hydrogels will cause the explosive release of the drugs and long degradation which will inactivate the immune drugs or cause inflammation in the body. On the other hand, the biodegradation of hydrogels is essential for biomedical applications where controlled *in vivo* absorption and/or local lysis is required to facilitate cell movement and morphogenesis. For biodegradability, the most common method is to introduce labile bonds in hydrogels either in the cross-links, or the network backbones. Unstable linkages may be cleaved in physiological conditions, either chemically or enzymatically, typically by hydrolysis. Hu *et al.* reported that a hyaluronic acid hydrogel carries PD-L1antibody (aPD-L1) which is grafted onto the platelet. When the hydrogel is injected into the tumor site, inflammation will initiate platelet activation and release aPD-L1, which achieves a controlled release (Hu et al., 2021).

Stimulus-Responsible

Those hydrogels with stimulus-responsive properties can be used as a drug delivery system in cancer immunotherapy, in which drug release is triggered upon external stimulis (Bajpai et al., 2008; Andrade et al., 2021) such as pH, temperature, and biomolecule concentration (**Figure 2D**). The cross-linking process of the hydrogel can respond to external stimuli. One of the most representative example is the novel thermogelling poly(lactic-co-glycolic acid)–poly(ethylene glycol)–poly(lactic-co-glycolic acid) (PLGA–PEG–PLGA) triblock copolymer, which exhibits a sol–gel transition with increasing temperature (Li et al., 2021). Jiang *et al.* incorporated multifunctional dendritic nanoparticles into a injectable thermosensitive hydrogel matrix (PLGA-PEG-PLGA triblock copolymers) to construct a localized drug delivery system for combining chemotherapy and immunotherapy (Vojtova et al., 2019). It is noteworthy that the dendritic nanoparticles-in-hydrogel delivery system gels at physiological temperature, thus allowing for sustained release of drugs. Ultimately, this system showed remarkable efficacy in treating triple negative breast cancer in mice model with 86% tumor growth inhibition. Additionally, the degradation process of hydrogel can respond to external stimuli. In response to pathological cues, hydrogel undergoes degradation upon external stimuli, followed by the release of the drugs which was precisely controlled by the pathological need. Gajanayake *et al.* developed a hydrogel that can release the immunosuppressant tacrolimus responsively to deal with proteolytic enzymes overexpressed in inflammation. Within 14 days, drugs in the hydrogel can be completely released, while the drug release rate in phosphate buffered saline for 28 days is less than 10%. Immunosuppressive drug tacrolimus was encapsulated in hydrogelS responsive to proteolytic enzymes which are overexpressed in inflammation. Within 14 days, complete drug release was achieved without burst release, whilst the drug release in phosphate-buffered saline was below 10% over 28 days (Oliva et al., 2017). The swelling behaviour of hydrogels can be affected by various external physicochemical

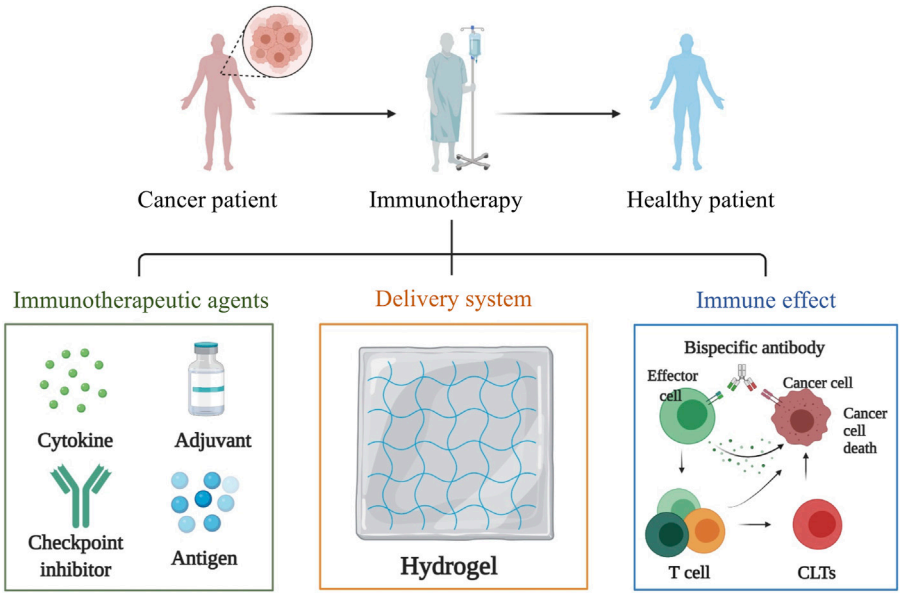

FIGURE 3 | Hydrogels applied in the delivery of immunomodulatory molecules which include cytokine, adjuvant, checkpoint inhibitor and antigen. These immunomodulatory molecules can be loaded to the biocompatible hydrogel in a simple and gentle way to ensure the biological activity of these immunomodulatory factors, enabling them to exert their immune effects.

conditions, which have been widely exploited in controlled drug delivery. pH responsive swelling is particularly important for cancer delivery systems because it allows targeted drug release in solid tumors where tumour microenvironments are typically more acidic than normal tissues (Andrade et al., 2021). Other stimuli responsive swelling mechanisms have also been exploited for controlled drug delivery. For example, a temperature responsive nanogel was fibricated to deliver the chemotherapy drug cisplatin to breast cancer that the temperature was believed to be slightly higher than the normal ones (Li et al., 2021) In some other cases, the drug carried by the hydrogel responds to stimuli. Natalie *et al.* incorporated gold nanoparticles decorated with 5-fluorouracil (5-FU)-hairpin DNA into dendrimer-dextran hydrogels to silence multidrug resistance protein-1 (MRP1). When the hairpin is opened by hybridizing with a complementary target (MRP1 mRNA), this interaction becomes weaker, allowing simultaneous release of the drug and knockout of the gene encoding the protein responsible for drug resistance (Ding et al., 2019). These smart properties of hydrogels mentioned above make hydrogel attractive and praisable as drug delivery systems for cancer immunotherapy.

APPLICATIONS OF HYDROGELS AS DELIVERY SYSTEMS FOR CANCER IMMUNOTHERAPY

Delivery of Immunomodulatory Molecules

A wide variety of immunotherapeutic agents, from small molecule drugs to macromolecular drugs and even cells, can be incorporated into the hydrogel for enhanced cancer immunotherapy. In this section, we discussed the application of hydrogel as delivery system for immunomodulatory molecules such as cytokine, adjuvant, checkpoint inhibitor and antigen (**Figure 3**).

Cytokine

In cancer immunotherapy, cytokines can be used to either activate or suppress the immune response against tumors (Chao et al., 2019). For example, Interleukin-12 (IL-12), a heterodimeric cytokine composed of two polypeptides with disulfide linkage, enhances the immune response of Th1, the maturation of cytotoxic T lymphocytes, the stimulation of natural killer cells, and the production of interferon-γ (IFN-γ). To overcome the main impediment of cytokines' short half-life *in vivo*, Shimizu *et al.* encapsulated IL-12 in a cholesterol-bearing pullulan (CHP) nanogel. After the mice were subcutaneously injected with murine IL-12-loaded CHP nanogel (CHP/rmIL-12), the concentration of serum rmIL-12 stays relatively high for 12–24 h (Shimizu et al., 2008). GM-CSF, also known as colony stimulating factor 2 (CSF2), is a monomeric glycoprotein that secretes by macrophages, T cells, mast cells, natural killer cells, endothelial cells, and fibroblasts. Doo Sung Lee *et al.* have designed an injectable smart hydrogels composed of levodopa and poly(ε-caprolactone-co-lactide)ester-functionalized hyaluronic acid (HA-PCLA) that loaded with OVA expressing plasmid (pOVA) and GM-CSF to boost the maturation of dendritic cells (DCs). By the controlled release of pOVA and GM-CSF through a single subcutaneous injection, the hydrogel system effectively eliminated the B16/OVA melanoma tumors (Leach et al., 2018).

Adjuvant

Chemotherapy and radiotherapy can induce immunogenic cell death (ICD), such antitumor immune response would be further amplified if there are concurrent immune adjuvants inside the tumor. Adjuvants are nonspecific immunostimulants, which enhance the body's immune response when combined with antigens. For example, Hou *et al.* used genetically engineered polypeptide hydrogel PC10ARGD as a sustained-release system that delivered Bestatin which is an immune adjuvant for mammary carcinoma treatment. The hydrogel serves as a drug delivery depot for sustained drug release of Bestatin, which further inhibits tumour metastases and microvessel formation but amplified T lymphocytes function (Hou et al., 2020). Liu *et al.* developed a smart hydrogel based on alginate, which hybridized with immunoadjuvant CpG oligonucleotide and conjugated with an adenosine triphosphate (ATP)-specific aptamer. Once intratumoral injection, this hydrogel gelled *in situ* and released the CpG oligonucleotide, achieving remarkable synergistic tumor elimination as well as generating long-lasting immune memory to prevent recurrences (Wu et al., 2021).

Checkpoint Inhibitor

Immunological checkpoints are a class of immunosuppressive molecules that can regulate the intensity and duration of immune responses, thereby avoiding damage of normal tissues. During the occurrence and development of tumors, immune checkpoints become one of the main regulators for immune tolerance (Yu et al., 2018). Immune checkpoint blockade therapy is an approach that regulates the activity of T cells through a series of channels such as cosuppression or costimulation signals to kill tumor cells. The most commonly used therapeutic drugs are programmed death receptors 1/programmed death receptor-ligand 1 (PD-1/PD-L1) and cytotoxic T lymphocyte-associated antigen-4 (CTLA-4) inhibitors. Activated T cells express PD-1 to recognize and remove abnormal or cancerous cells. However, tumor cells inactivate the T cells that recognize tumor antigens by expressing PD-1 ligands that bind to PD-1, thereby evading immune system attacks. Therefore, tumor cell death can be induced by blocking inhibitors of PD-1 or its ligand. CTLA-4 is another immune checkpoint that reduces T-cell activation and promotes tumor progression by binding to its ligands. Inhibitors against CTLA-4 and its ligands block their interactions to increase T-cell activity and thereby clear tumors (Kazemi et al., 2021; Tang et al., 2021). Immune checkpoint inhibitors can cause side effects to many normal organs. Therefore, a large number of studies have used hydrogel as delivery system to locally release immune checkpoint inhibitors at the tumor site to solve the above problems. Chen *et al.* developed an anti-inflammatory nanofiber hydrogel self-assembled by steroid drugs for local delivery of (αPD-L1). Effective therapeutic effects were observed with inhibition both local tumors and abscopal tumors once injected with αPDL1-loaded hydrogel.

Antigen

Low immunogenicity and tumor heterogeneity greatly limit the therapeutic effect of tumor vaccines. In view of this, Zhu *et al.* prepared a new type of injectable adhesive hydrogel based on thermosensitive nanogels containing catechol groups and loaded with MnO_2 nanoparticles. After intratumoral injection, the concentrated nanogel dispersion transformed into an adhesive hydrogel *in situ*. The photothermal effect of the loaded MnO_2 nanoparticles induces immunogenic cell death and releases a large amount of autologous tumor-derived protein antigens under near-infrared radiation. These antigens captured by the hydrogel are ideal immunostimulatory substances to avoid the consequences of tumor heterogeneity. They also recruit more dendritic cells to stimulate a strong and durable anti-tumor immune response mediated by $CD8^+$ T cells (Song et al., 2018). Wang *et al.* used polypeptide hydrogel loaded with tumor cell lysates (TCL) as antigens, Toll-like receptors 3 (TLR3) agonist, polyinosinic:polycytidylic acid [poly(I:C)] to construct the vaccines, which robustly recruit, activate and mature DCs *in vitro* and *in vivo* by sustained release of TCL and poly (I:C). The antigen persistence at the injection site and antigen drainage to lymph nodes were significantly improved by hydrogel (Song et al., 2018).

Delivery of Immune Cells

Localized delivery using hydrogels in immunotherapy provides adjustable microenvironments for immune cells as it enables the recruitment, expansion, and activation of immune cells *in vitro* and *in vivo* (**Figure 4**; Weiden et al., 2018; Yang et al., 2018) It is reported that a thermosensitive chitosan hydrogel for the delivery of tumor-infiltrating lymphocytes and activated $CD8^+$ T cells**.** To provide a suitable physical condition for the proliferation of immune cells, the gelation process and mechanical strength of the hydrogel could be precisely tuned by varying the concentration of sodium bicarbonate. The *in vitro* T-cell expansion experiment revealed that hydrogel platform with a larger pore size and higher stiffness promoted the viability and proliferation of the encapsulated T cells (Hickey et al., 2019). DCs can either be activated in hydrogels *in vitro* before implantation, or by immobilizing stimuli within the gels *in vivo* (Yang et al., 2018). Verbeke *et al.* designed an injectable alginate hydrogel system that allows DCs to be enriched locally *in vivo* without activation or maturation. Similarly, alginate hydrogels was designed to carry and releas antigen-loaded DCs when injected subcutaneously in mice (Hori et al., 2008). Besides DCs, macrophages also playws a major role as antigen-presenting cells in tumor vaccination. Muraoka *et al.* developed a cholesteryl pullulan-based hydrogel to deliver peptide-based antigens to macrophages (Chao et al., 2019). The antigens were successfully delivered to $CD8^+$ cytotoxic T cells by this immunologically inert hydrogel.

Passive immunotherapy uses components of immune system to target specific cancers without necessarily involving an immune response. Since the first clinical trial 28 years ago, tumor-infiltrating lymphocytes (TILs) have been widely applied for the treatment of metastatic melanoma. Meanwhile remarkable research efforts have been focusd on adopative cell therapy (ACT), which heavily relies on the administration of allogeneic T cells (Monette et al., 2016). Furthermore, genetically modified tumor-specific T cells have been developed to overcome the limitation of TIL expansion and the augment ACT-mediated

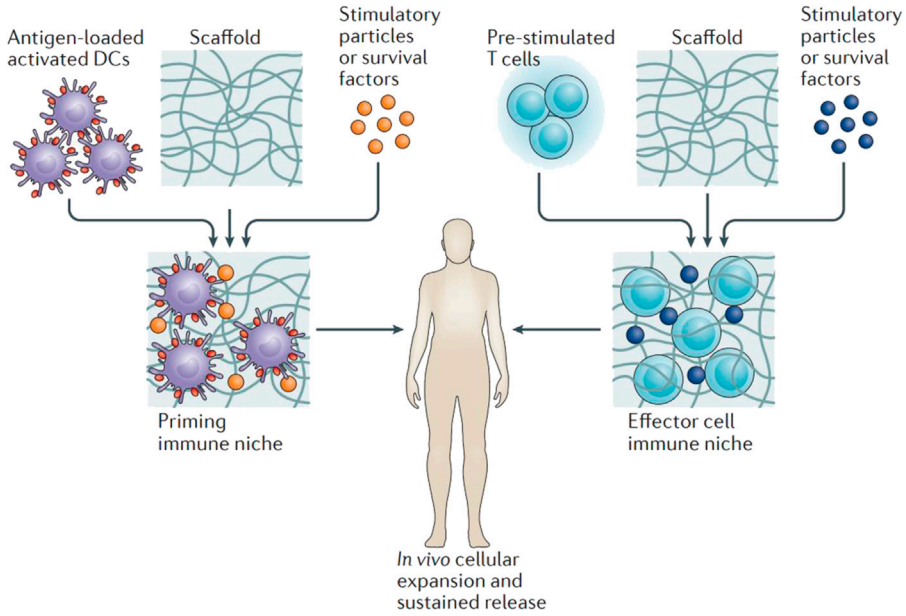

FIGURE 4 | Hydrogels applied in the delivery of immune cells. Antigen-loaded activated dendritic cells or pre-stimulated tumour-specific T cells are loaded to hydrogel scaffolds *ex vivo*. Stimulatory agents were encapsulated to support cell survival, activation and expansion. After administration of the matrix close to the tumour site, potent immune cells proliferate within the scaffold and are released continuously into the tissue environment. Reproduced with permission Weiden et al. (2018). Copyright 2018 Nature.

immunotherapy. Compared with systemic delivery, which is likely to result in T cells infiltrating to noncancerous tissues, localized administration using hydrogels into tumor sites improves delivery efficiency and sustained release of T cells. The feasibility of a thermosensitive, amine-reactive oligo(ethylene glycol) methacrylate-based hydrogel was investigated as a T cell carrier. Additionally, an injectable thermogel based on chitosan was developed with the purpose of encapsulating, expanding, and delivering cytotoxic T cells (Jiang et al., 2018).

Delivery of Environmental Regulatory Substances

Practically, in addition to carrying the above-mentioned cytokines, immune adjuvants, checkpoint inhibitors, and immune cells that directly stimulate immunity, the hydrogel can also carry environmental regulation substances to regulate the tumor microenvironment. For example, acidic extracellular pH promotes immune evasion and tumor progression. Therefore, antagonizing tumor acidity can be a powerful approach in cancer immunotherapy. Hyung-seung *et al.* used Pluronic F-127 as a $NaHCO_3$ releasing carrier to focally alleviate extracellular tumor acidity (**Figure 5A**). In a mouse tumor model, intratumoral treatment with pH modulating injectable gel (pHe-MIG) generates immune-favorable TME, as evidenced by the decrease of immune-suppressive cells and increase of tumor infiltrating $CD8^+$ T cells (Jin et al., 2019). It has also been suggested that implantable hydrogel can be engineered to investigate specific aspects of the tumor microenvironment, either singularly or in combination. It is known that lactate, a metabolite byproduct of anaerobic glycolysis, is known to reprogram immune cells, resulting in increased tumor survival. Riley *et al.* (**Figure 5B**) designed and synthesized a peptide hydrogel loaded with GM-CSF and poly-(lactic-co-glycolic acid)/(lactic acid) microparticles which can generate the localized lactate concentrations (~2–22 mM) and cellular makeup of the tumor microenvironment, following subcutaneous implantation in mice and causing significant immunological effects (Allen et al., 2020). Jiang *et al.* incorporated multifunctional dendritic nanoparticles into a injectable hydrogel matrix which is composed with thermosensitive triblock copolymers to construct a localized drug delivery system for combining gas-therapy and immunotherapy (**Figure 5C**). The dendritic scaffolds were used to deliver arginine-rich molecules (L-Arg) to M1 macrophages, which produce the cytotoxic substance nitric oxide (NO), and subsequently induce tumor cell destruction (Jiang et al., 2018).

CONCLUSION AND PERSPECTIVES

Immunotherapy is a type of approach that utilizes the body's own immune system to combat cancer, demonstrating to be effective or completely alleviating some solid or hematological malignant tumors. Hydrogels exhibited excellent promise for cancer immunotherapy since they are loadable, implantable, injectable, biodegradable and stimuli-responsive (Bu et al., 2019). These properties guarantee hydrogels higher

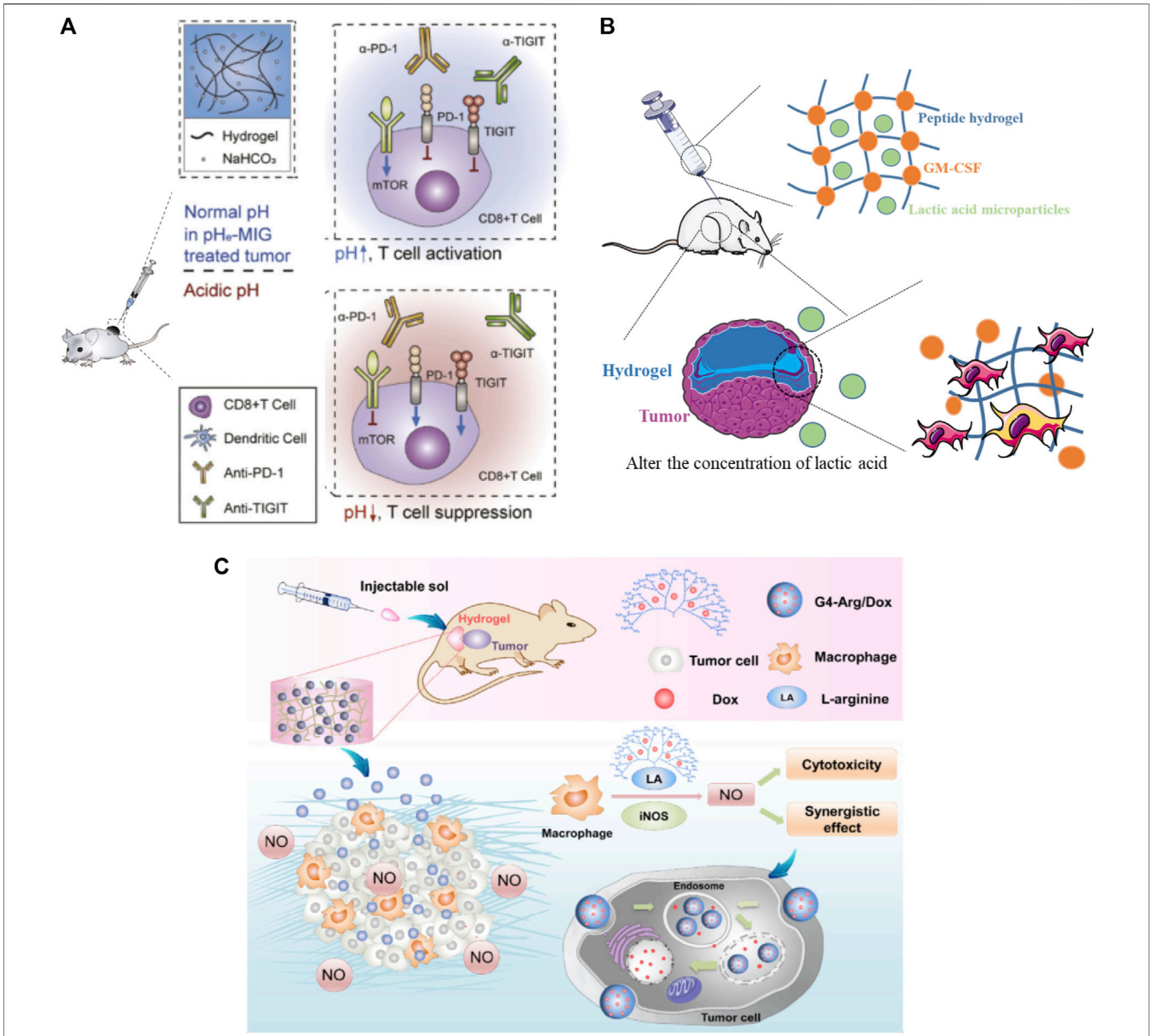

FIGURE 5 | Hydrogels applied in the delivery of environmental regulatory substance. **(A)** Pluronic F-127 was used as a $NaHCO_3$ releasing carrier to focally alleviate extracellular tumor acidity. Reproduced with permission Jin et al. (2019). Copyright 2019 Elsevier Ltd. **(B)** A lactic acid-producing hydrogel system was design to change the concentration of lactic acid at the tumor site to interrogate immune cell modulation in cancer-like environments. Reproduced with permission Allen et al. (2020). Copyright. 2020. The Royal Society of Chemistry. **(C)** A dendritic scaffolds were designed to enrich arginine molecules and provide the inducible nitric oxide synthase (iNOS) substrate, L-Arg, to M1 macrophages, which can produce the cytotoxic substance nitric oxide (NO) and subsequently induce tumor cell destruction through immunotherapy. Reproduced with permission Jiang et al. (2018). Copyright 2018 springer.

immunological drug loading efficiency and drug stability, more controllable drug release profiles, and easier to combine immunotherapy with other treatment methods (Yang et al., 2020). In this review, we focus on how the characteristics of hydrogels have been applied to deliver cytokines, adjuvants, checkpoint inhibitors, antigens, cells, and environmental regulatory substance in cancer immunotheraoy. These reported hydrogel systems are able to prolong the residence time of immunotherapy factors at tumor sites, as well as protect bioactive molecules from denaturation or degradation, thus improving the efficacy of immunotherapy.

In spite of the successful exploration of hydrogel drug delivery systems for cancer immunotherapy, several challenges still need to be considered for the future development and potential applications. Firstly, the controlled release of drug from hydrogels still remains as an issue since immunological drug are released by diffusion and hydrogel degradation, both of which are uncontrollable processes. Those hydrogels are responsive to

stimulation can release immunological drugs, but the research in this area is only limited to *in vitro* experiments or rely heavily on the intrinsic tumor microenvironment. Once the hydrogel implanted into the body, it will be important to find out if same type of response properties exists *in vivo*. Secondly, although hydrogel materials have demonstrated good biocompatibility and biodegradability, higher biocompatibility is needed when used to deliver immunological drugs. In clinical application, the safety of the delivery agents is extremely crucial, particularly in cancer immunotherapy, those bioactive molecules or cells discussed above require an environment that is similar to physiological conditions more than other drugs. Thirdly, there are some issues that need to be considered in clinical aspects: 1) multiple imaging-guided injection techniques should be developed for deep-sited tumors administration; 2) The dose of immune drugs is also a vital parameter. For *in vitro* experiments, a drug dose is usually chosen based on the effectiveness of the drug. In clinical practice, however, a strict dose screening should be performed according to the drug release curve of the hydrogel. High concentration of anticancer agents can also cause severe acute injury to the healthy parenchyma due to the burst release. If the drug release from the hydrogel does not proceed at a uniform rate, it can also lead to increase the risk of drug resistance; 3) It will be feasible to construct the final system on the basis of approved clinical materials as it is also more likely to get clinical approval.

In summary, the delivery systems based on hydrogels have exhibited excellent promises for cancer immunotherapy as the unique characteristics of hydrogels ensure locally and sustainably delivering immunotherapeutic agents to target tumor sites with reduced drug dose and side effects. However, challenges still exist, which requires experts from multidisciplinary fields work more closely. We believe this smart delivery system will continue contributing in tomour threatment *via* immunotherapy as well as other aspects for improving human health.

AUTHOR CONTRIBUTIONS

Conception of the work: RC, SQ and DL; Drafting the article: RC and DL; Critical revision of the article: RC, QW, JW, XZ, RO, YX, SQ and DL.

FUNDING

This work is supported by the following programs: National Natural Science Foundation of China (Grant Nos. 52035012, 81771531, 81871129, 82072862, 82072863, 61805158), the Basic Research Foundation Key Project of Sichuan Province (2021JY0046) and Research Start-up Grant of SAHSYSU (ZSQYBRJH0019).

REFERENCES

Ahearne, M. (2014). Introduction to Cell-Hydrogel Mechanosensing. *Interf. Focus.* 4 (2), 20130038. doi:10.1098/rsfs.2013.0038

Ahmed, E. M. (2015). Hydrogel: Preparation, Characterization, and Applications: A Review. *J. Adv. Res.* 6 (2), 105–121. doi:10.1016/j.jare.2013.07.006

Akhtar, M. F., Hanif, M., and Ranjha, N. M. (2016). Methods of Synthesis of Hydrogels . . . A Review. *Saudi Pharm. J.* 24 (5), 554–559. doi:10.1016/j.jsps.2015.03.022

Allen, R., Ivtchenko, E., Thuamsang, B., Sangsuwan, R., and Lewis, J. S. (2020). Polymer-loaded Hydrogels Serve as Depots for Lactate and Mimic "cold" Tumor Microenvironments. *Biomater. Sci.* 8 (21), 6056–6068. doi:10.1039/d0bm01196g

Andrade, F., Roca-Melendres, M. M., Durán-Lara, E. F., Rafael, D., and Schwartz, S., Jr. (2021). Stimuli-Responsive Hydrogels for Cancer Treatment: The Role of pH, Light, Ionic Strength and Magnetic Field. *Cancers* 13 (5), 1164. doi:10.3390/cancers13051164

Bajpai, A. K., Shukla, S. K., Bhanu, S., and Kankane, S. (2008). Responsive Polymers in Controlled Drug Delivery. *Prog. Polym. Sci.* 33 (11), 1088–1118. doi:10.1016/j.progpolymsci.2008.07.005

Bu, L.-L., Yan, J., Wang, Z., Ruan, H., Chen, Q., Gunadhi, V., et al. (2019). Advances in Drug Delivery for post-surgical Cancer Treatment. *Biomaterials* 219, 119182. doi:10.1016/j.biomaterials.2019.04.027

Buwalda, S. J., Boere, K. W. M., Dijkstra, P. J., Feijen, J., Vermonden, T., and Hennink, W. E. (2014). Hydrogels in a Historical Perspective: from Simple Networks to Smart Materials. *J. Controlled Release* 190, 254–273. doi:10.1016/j.jconrel.2014.03.052

Chao, Y., Chen, Q., and Liu, Z. (2019). Smart Injectable Hydrogels for Cancer Immunotherapy. *Adv. Funct. Mater.* 30 (2), 1902785. doi:10.1002/adfm.201902785

Choudhury, D., Tun, H. W., Wang, T., and Naing, M. W. (2018). Organ-Derived Decellularized Extracellular Matrix: A Game Changer for Bioink Manufacturing?. *Trends Biotechnol.* 36 (8), 787–805. doi:10.1016/j.tibtech.2018.03.003

Ding, F., Huang, X., Gao, X., Xie, M., Pan, G., Li, Q., et al. (2019). A Non-cationic Nucleic Acid Nanogel for the Delivery of the CRISPR/Cas9 Gene Editing Tool. *Nanoscale* 11 (37), 17211–17215. doi:10.1039/c9nr05233j

Dorishetty, P., Dutta, N. K., and Choudhury, N. R. (2020). Bioprintable Tough Hydrogels for Tissue Engineering Applications. *Adv. Colloid Interf. Sci.* 281, 102163. doi:10.1016/j.cis.2020.102163

Duong, H. T. T., Thambi, T., Yin, Y., Kim, S. H., Nguyen, T. L., Phan, V. H. G., et al. (2020). Degradation-regulated Architecture of Injectable Smart Hydrogels Enhances Humoral Immune Response and Potentiates Antitumor Activity in Human Lung Carcinoma. *Biomaterials* 230, 119599. doi:10.1016/j.biomaterials.2019.119599

Hauptstein, J., Böck, T., Bartolf-Kopp, M., Forster, L., Stahlhut, P., Nadernezhad, A., et al. (2020). Hyaluronic Acid-Based Bioink Composition Enabling 3D Bioprinting and Improving Quality of Deposited Cartilaginous Extracellular Matrix. *Adv. Healthc. Mater.* 9 (15), 2000737. doi:10.1002/adhm.202000737

Hickey, J. W., Dong, Y., Chung, J. W., Salathe, S. F., Pruitt, H. C., Li, X., et al. (2019). Engineering an Artificial T-Cell Stimulating Matrix for Immunotherapy. *Adv. Mater.* 31 (23), 1807359. doi:10.1002/adma.201807359

Hoffman, A. S. (2012). Hydrogels for Biomedical Applications. *Adv. Drug Deliv. Rev.* 64, 18–23. doi:10.1016/j.addr.2012.09.010

Hori, Y., Winans, A. M., Huang, C. C., Horrigan, E. M., and Irvine, D. J. (2008). Injectable Dendritic Cell-Carrying Alginate Gels for Immunization and Immunotherapy. *Biomaterials* 29 (27), 3671–3682. doi:10.1016/j.biomaterials.2008.05.033

Hou, X.-l., Dai, X., Yang, J., Zhang, B., Zhao, D.-h., Li, C.-q., et al. (2020). Injectable Polypeptide-Engineered Hydrogel Depot for Amplifying the Anti-tumor Immune Effect Induced by Chemo-Photothermal Therapy. *J. Mater. Chem. B* 8 (37), 8623–8633. doi:10.1039/d0tb01370f

Hu, Q., Li, H., Archibong, E., Chen, Q., Ruan, H., Ahn, S., et al. (2021). Inhibition of post-surgery Tumour Recurrence via a Hydrogel Releasing CAR-T Cells and Anti-PDL1-conjugated Platelets. *Nat. Biomed. Eng.* doi:10.1038/s41551-021-00712-1

Jiang, L., Ding, Y., Xue, X., Zhou, S., Li, C., Zhang, X., et al. (2018). Entrapping Multifunctional Dendritic Nanoparticles into a Hydrogel for Local Therapeutic Delivery and Synergetic Immunochemotherapy. *Nano Res.* 11 (11), 6062–6073. doi:10.1007/s12274-018-2123-8

Jin, H.-s., Choi, D.-s., Ko, M., Kim, D., Lee, D.-h., Lee, S., et al. (2019). Extracellular pH Modulating Injectable Gel for Enhancing Immune Checkpoint Inhibitor Therapy. *J. Controlled Release* 315, 65–75. doi:10.1016/j.jconrel.2019.10.041

Kazemi, M. H., Najafi, A., Karami, J., Ghazizadeh, F., Yousefi, H., Falak, R., et al. (2021). Immune and Metabolic Checkpoints Blockade: Dual Wielding against Tumors. *Int. Immunopharmacology* 94, 107461. doi:10.1016/j.intimp.2021.107461

Leach, D. G., Dharmaraj, N., Piotrowski, S. L., Lopez-Silva, T. L., Lei, Y. L., Sikora, A. G., et al. (2018). STINGel: Controlled Release of a Cyclic Dinucleotide for Enhanced Cancer Immunotherapy. *Biomaterials* 163, 67–75. doi:10.1016/j.biomaterials.2018.01.035

Leach, D. G., Young, S., and Hartgerink, J. D. (2019). Advances in Immunotherapy Delivery from Implantable and Injectable Biomaterials. *Acta Biomater.* 88, 15–31. doi:10.1016/j.actbio.2019.02.016

Lei, K., and Tang, L. (2019). Surgery-free Injectable Macroscale Biomaterials for Local Cancer Immunotherapy. *Biomater. Sci.* 7 (3), 733–749. doi:10.1039/c8bm01470a

Li, J., Luo, Y., Li, B., Xia, Y., Wang, H., and Fu, C. (2020). Implantable and Injectable Biomaterial Scaffolds for Cancer Immunotherapy. *Front. Bioeng. Biotechnol.* 8, 612950. doi:10.3389/fbioe.2020.612950

Li, J., and Mooney, D. J. (2016). Designing Hydrogels for Controlled Drug Delivery. *Nat. Rev. Mater.* 1 (12). doi:10.1038/natrevmats.2016.71

Li, L., He, Y., Zheng, X., Yi, L., Nian, W., and Abadi, P. P. (2021). Progress on Preparation of pH/Temperature-Sensitive Intelligent Hydrogels and Applications in Target Transport and Controlled Release of Drugs. *Int. J. Polym. Sci.* 2021, 1–14. doi:10.1155/2021/1340538

Lin, C.-C., and Metters, A. T. (2006). Hydrogels in Controlled Release Formulations: Network Design and Mathematical Modeling. *Adv. Drug Deliv. Rev.* 58 (12-13), 1379–1408. doi:10.1016/j.addr.2006.09.004

Liu, Y., Liu, M., Zhang, Y., Cao, Y., and Pei, R. (2020). Fabrication of Injectable Hydrogels via Bio-Orthogonal Chemistry for Tissue Engineering. *New J. Chem.* 44 (27), 11420–11432. doi:10.1039/d0nj02629h

Ma, H., He, C., and Chen, X. (2021). Injectable Hydrogels as Local Depots at Tumor Sites for Antitumor Immunotherapy and Immune-Based Combination Therapy. *Macromol. Biosci.* 21, 2100039. doi:10.1002/mabi.202100039

Monette, A., Ceccaldi, C., Assaad, E., Lerouge, S., and Lapointe, R. (2016). Chitosan Thermogels for Local Expansion and Delivery of Tumor-specific T Lymphocytes towards Enhanced Cancer Immunotherapies. *Biomaterials* 75, 237–249. doi:10.1016/j.biomaterials.2015.10.021

Muñoz, N. M., Williams, M., Dixon, K., Dupuis, C., McWatters, A., Avritscher, R., et al. (2021). Influence of Injection Technique, Drug Formulation and Tumor Microenvironment on Intratumoral Immunotherapy Delivery and Efficacy. *J. Immunother. Cancer* 9 (2), e001800. doi:10.1136/jitc-2020-001800

Oh, S. H., An, D. B., Kim, T. H., and Lee, J. H. (2016). Wide-range Stiffness Gradient PVA/HA Hydrogel to Investigate Stem Cell Differentiation Behavior. *Acta Biomater.* 35, 23–31. doi:10.1016/j.actbio.2016.02.016

Oliva, N., Conde, J., Wang, K., and Artzi, N. (2017). Designing Hydrogels for On-Demand Therapy. *Acc. Chem. Res.* 50 (4), 669–679. doi:10.1021/acs.accounts.6b00536

Overstreet, D. J., Dutta, D., Stabenfeldt, S. E., and Vernon, B. L. (2012). Injectable Hydrogels. *J. Polym. Sci. B Polym. Phys.* 50 (13), 881–903. doi:10.1002/polb.23081

Pal, K., Singh, V. K., Anis, A., Thakur, G., and Bhattacharya, M. K. (2013). Hydrogel-Based Controlled Release Formulations: Designing Considerations, Characterization Techniques and Applications. *Polymer-Plastics Technology Eng.* 52 (14), 1391–1422. doi:10.1080/03602559.2013.823996

Palucka, K., and Banchereau, J. (2012). Cancer Immunotherapy via Dendritic Cells. *Nat. Rev. Cancer* 12 (4), 265–277. doi:10.1038/nrc3258

Qiu, H., Guo, H., Li, D., Hou, Y., Kuang, T., and Ding, J. (2020). Intravesical Hydrogels as Drug Reservoirs. *Trends Biotechnol.* 38 (6), 579–583. doi:10.1016/j.tibtech.2019.12.012

Rastogi, P., and Kandasubramanian, B. (2019). Review of Alginate-Based Hydrogel Bioprinting for Application in Tissue Engineering. *Biofabrication* 11 (4), 042001. doi:10.1088/1758-5090/ab331e

Rizzo, F., and Kehr, N. S. (2021). Recent Advances in Injectable Hydrogels for Controlled and Local Drug Delivery. *Adv. Healthc. Mater.* 10 (1), 2001341. doi:10.1002/adhm.202001341

Salah, M., Tayebi, L., Moharamzadeh, K., and Naini, F. B. (2020). Three-dimensional Bio-Printing and Bone Tissue Engineering: Technical Innovations and Potential Applications in Maxillofacial Reconstructive Surgery. *Maxillofac. Plast. Reconstr. Surg.* 42 (1), 18. doi:10.1186/s40902-020-00263-6

Seliktar, D. (2012). Designing Cell-Compatible Hydrogels for Biomedical Applications. *Science* 336 (6085), 1124–1128. doi:10.1126/science.1214804

Shimizu, T., Kishida, T., Hasegawa, U., Ueda, Y., Imanishi, J., Yamagishi, H., et al. (2008). Nanogel DDS Enables Sustained Release of IL-12 For Tumor Immunotherapy. *Biochem. Bioph. Res. Co.* 367, 330–335. doi:10.1016/j.bbrc.2007.12.112

Simona, B. R., Hirt, L., Demkó, L., Zambelli, T., Vörös, J., Ehrbar, M., et al. (2015). Density Gradients at Hydrogel Interfaces for Enhanced Cell Penetration. *Biomater. Sci.* 3 (4), 586–591. doi:10.1039/c4bm00416g

Song, H., Huang, P., Niu, J., Shi, G., Zhang, C., Kong, D., et al. (2018). Injectable Polypeptide Hydrogel for Dual-Delivery of Antigen and TLR3 Agonist to Modulate Dendritic Cells *In Vivo* and Enhance Potent Cytotoxic T-Lymphocyte Response against Melanoma. *Biomaterials* 159, 119–129. doi:10.1016/j.biomaterials.2018.01.004

Tan, H., and Marra, K. G. (2010). Injectable, Biodegradable Hydrogels for Tissue Engineering Applications. *Materials* 3 (3), 1746–1767. doi:10.3390/ma3031746

Tang, T., Huang, X., Zhang, G., Hong, Z., Bai, X., and Liang, T. (2021). Advantages of Targeting the Tumor Immune Microenvironment over Blocking Immune Checkpoint in Cancer Immunotherapy. *Sig Transduct Target. Ther.* 6 (1), 72. doi:10.1038/s41392-020-00449-4

Tie, S., Zhang, X., Wang, H., Song, Y., and Tan, M. (2020). Procyanidins-Loaded Complex Coacervates for Improved Stability by Self-Crosslinking and Calcium Ions Chelation. *J. Agric. Food Chem.* 68 (10), 3163–3170. doi:10.1021/acs.jafc.0c00242

Tu, Y., Chen, N., Li, C., Liu, H., Zhu, R., Chen, S., et al. (2019). Advances in Injectable Self-Healing Biomedical Hydrogels. *Acta Biomater.* 90, 1–20. doi:10.1016/j.actbio.2019.03.057

Vigata, M., Meinert, C., Hutmacher, D. W., and Bock, N. (2020). Hydrogels as Drug Delivery Systems: A Review of Current Characterization and Evaluation Techniques. *Pharmaceutics* 12 (12), 1188. doi:10.3390/pharmaceutics12121188

Vojtova, L., Michlovska, L., Valova, K., Zboncak, M., Trunec, M., Castkova, K., et al. (2019). The Effect of the Thermosensitive Biodegradable PLGA-PEG-PLGA Copolymer on the Rheological, Structural and Mechanical Properties of Thixotropic Self-Hardening Tricalcium Phosphate Cement. *Ijms* 20 (2), 391. doi:10.3390/ijms20020391

Weiden, J., Tel, J., and Figdor, C. G. (2018). Synthetic Immune Niches for Cancer Immunotherapy. *Nat. Rev. Immunol.* 18 (3), 212–219. doi:10.1038/nri.2017.89

Wu, Y., Li, Q., Shim, G., and Oh, Y.-K. (2021). Melanin-loaded CpG DNA Hydrogel for Modulation of Tumor Immune Microenvironment. *J. Controlled Release* 330, 540–553. doi:10.1016/j.jconrel.2020.12.040

Xie, Z., Shen, J., Sun, H., Li, J., and Wang, X. (2021). Polymer-based Hydrogels with Local Drug Release for Cancer Immunotherapy. *Biomed. Pharmacother.* 137, 111333. doi:10.1016/j.biopha.2021.111333

Yang, F., Shi, K., Jia, Y.-p., Hao, Y., Peng, J.-r., and Qian, Z.-y. (2020). Advanced Biomaterials for Cancer Immunotherapy. *Acta Pharmacol. Sin* 41 (7), 911–927. doi:10.1038/s41401-020-0372-z

Yang, P., Song, H., Qin, Y., Huang, P., Zhang, C., Kong, D., et al. (2018). Engineering Dendritic-Cell-Based Vaccines and PD-1 Blockade in Self-Assembled Peptide Nanofibrous Hydrogel to Amplify Antitumor T-Cell Immunity. *Nano Lett.* 18 (7), 4377–4385. doi:10.1021/acs.nanolett.8b01406

Yu, S., Wang, C., Yu, J., Wang, J., Lu, Y., Zhang, Y., et al. (2018). Injectable Bioresponsive Gel Depot for Enhanced Immune Checkpoint Blockade. *Adv. Mater.* 30 (28), 1801527. doi:10.1002/adma.201801527

Zeng, Y., Xiang, Y., Sheng, R., Tomás, H., Rodrigues, J., Gu, Z., et al. (2021). Polysaccharide-based Nanomedicines for Cancer Immunotherapy: A Review. *Bioactive Mater.* 6 (10), 3358–3382. doi:10.1016/j.bioactmat.2021.03.008

Zhang, R., Billingsley, M. M., and Mitchell, M. J. (2018). Biomaterials for Vaccine-Based Cancer Immunotherapy. *J. Controlled Release* 292, 256–276. doi:10.1016/j.jconrel.2018.10.008

Zou, W. (2006). Regulatory T Cells, Tumour Immunity and Immunotherapy. *Nat. Rev. Immunol.* 6 (4), 295–307. doi:10.1038/nri1806

Conflict of Interest: The authors declare that the research was conducted in the absence of any commercial or financial relationships that could be construed as a potential conflict of interest.

The handling editor declared a shared affiliation, though no other collaboration, with several of the authors RC, QW, YX and DL at the time of the review.

Copyright © 2021 Cui, Wu, Wang, Zheng, Ou, Xu, Qu and Li. This is an open-access article distributed under the terms of the Creative Commons Attribution License (CC BY). The use, distribution or reproduction in other forums is permitted, provided the original author(s) and the copyright owner(s) are credited and that the original publication in this journal is cited, in accordance with accepted academic practice. No use, distribution or reproduction is permitted which does not comply with these terms.

frontiers in Bioengineering and Biotechnology

ORIGINAL RESEARCH
published: 30 July 2021
doi: 10.3389/fbioe.2021.721617

Polypyrrole-Coated Magnetite Vortex Nanoring for Hyperthermia-Boosted Photothermal/Magnetothermal Tumor Ablation Under Photoacoustic/Magnetic Resonance Guidance

Jianfeng Bao[1†], Shuangshuang Guo[2†], Xiangyang Zu[3], Yuchuan Zhuang[4], Dandan Fan[2], Yong Zhang[1], Yupeng Shi[1], Zhenyu Ji[2], Jingliang Cheng[1] and Xin Pang[1]**

[1] Functional Magnetic Resonance and Molecular Imaging Key Laboratory of Henan Province, Department of Magnetic Resonance Imaging, First Affiliated Hospital of Zhengzhou University, Zhengzhou University, Zhengzhou, China, [2] Henan Institute of Medical and Pharmaceutical Sciences, Zhengzhou University, Zhengzhou, China, [3] College of Medical Technology and Engineering, Henan University of Science and Technology, Luoyang, China, [4] Department of Imaging Sciences, University of Rochester Medical Center, Rochester, NY, United States

Photothermal/magnetothermal-based hyperthermia cancer therapy techniques have been widely investigated, and associated nanotechnology-assisted treatments have shown promising clinical potentials. However, each method has some limitations, which have impeded extensive applications. For example, the penetration ability of the photothermal is not satisfactory, while the heating efficiency of the magnetothermal is very poor. In this study, a novel magnetite vortex nanoring nanoparticle-coated with polypyrrole (denoted as nanoring Fe_3O_4@PPy-PEG) was first synthesized and well-characterized. By combining photothermal and magnetothermal effects, the performance of the dual-enhanced hyperthermia was significantly improved, and was thoroughly examined in this study. Benefiting from the magnetite vortex nanoring and polypyrrole, Fe_3O_4@PPy-PEG showed excellent hyperthermia effects (SAR = 1,648 Wg^{-1}) when simultaneously exposed to the alternating magnetic field (300 kHz, 45 A) and near-infrared (808 nm, 1 W cm^{-2}) laser. What is more, nanoring Fe_3O_4@PPy-PEG showed a much faster heating rate, which can further augment the antitumor effect by incurring vascular disorder. Besides, Fe_3O_4@PPy-PEG exhibited a high transverse relaxation rate [60.61 mM^{-1} S^{-1} (Fe)] at a very low B_0 field (0.35 T) and good photoacoustic effect. We believe that the results obtained herein can significantly promote the development of multifunctional nanoparticle-mediated magnetic and photo induced efficient hyperthermia therapy.

Keywords: magnetite vortex nanoring, magnetic hyperthermia, photothermal hyperthermia, theranostics, multimodal imaging

OPEN ACCESS

Edited by:
Junqing Wang,
Sun Yat-sen University, China

Reviewed by:
Gang Liu,
Xiamen University, China
Jun Deng,
Army Medical University, China
Yanling Wei,
Army Medical University, China

***Correspondence:**
Jingliang Cheng
fccchengjl@zzu.edu.cn
Xin Pang
pangxin116@163.com

[†] These authors have contributed equally to this work

Specialty section:
This article was submitted to Biomaterials, a section of the journal Frontiers in Bioengineering and Biotechnology

Received: *07 June 2021*
Accepted: *29 June 2021*
Published: *30 July 2021*

Citation:
Bao J, Guo S, Zu X, Zhuang Y, Fan D, Zhang Y, Shi Y, Ji Z, Cheng J and Pang X (2021) Polypyrrole-Coated Magnetite Vortex Nanoring for Hyperthermia-Boosted Photothermal/Magnetothermal Tumor Ablation Under Photoacoustic/Magnetic Resonance Guidance. Front. Bioeng. Biotechnol. 9:721617. doi: 10.3389/fbioe.2021.721617

INTRODUCTION

Hyperthermia therapy (HT), which is well known as a "green" cancer therapy method, has been widely used as a treatment for cancer in all phases and almost all kinds of cancer in clinical trials (van der Horst et al., 2018; Helderman et al., 2019). HT has a long history of treating disease and owing to nanotechnology-enabled advancements, it has attracted more attention of researchers in recent years. Nanoparticle-aided HTs have demonstrated controllability and efficient efficiency, which allow time- and region-specific treatment with maximum therapeutic effect and minimum side effects (Al-Ahmady and Kostarelos, 2016; Sharma et al., 2019; Zhang et al., 2020). Among various heating strategies, alternating magnetic field (AMF)- and near infrared (NIR)-induced HTs have been most studied and are generally considered as the most appropriate approaches. Thus, nanoparticles with high thermal effects, such as Au (Ma et al., 2016; Sun et al., 2017), Ag (Das et al., 2016; He et al., 2020), copper (Wang et al., 2018), carbon (Hong et al., 2015), iron (Wang et al., 2005; Tong et al., 2017; Cotin et al., 2019; Zhang et al., 2020), and organic materials [cyanine dyes (Yoon et al., 2017; Chu et al., 2020), porphyrins (Hiroto et al., 2017), and conjugated polymer (Zhou et al., 2013; Shi et al., 2020)], have been designed and successfully synthesized, and the corresponding NIR/AMF-triggered HTs have led to fruitful results in treatment of various diseases. However, both the NIR and the AMF have their own limitations. For example, most AMFs need high concentration heating agents (1–2 M), which may raise concern for clinical application. While for the photothermal, the NIR laser light has been confined to the superficial tumor for a long time. Thus, inspired by the aforementioned problems, we presented a combination of top-down approach to realize the two thermal effects triggered by one nanocomposite to compensate for each other to realize the optimized heating efficiency. Furthermore, multifunctional nanoparticles that can increase both thermal efficiencies have been merely reported in the literature (Espinosa et al., 2016; Ma et al., 2019; Yang et al., 2019).

In this study, a novel core-shell magnetic vortex nanoring coated with polypyrrole (PPy) Fe_3O_4@PPy-PEG composites was designed and successfully synthesized for photothermal/magnetothermal therapy against cancer. We chose PPy in this study because of its good photothermal performance, photostability, and outstanding biocompatibility. The characterization and photothermal, and magnetothermal properties of the proposed nanoring composites were explored in an aqueous suspension. The cytotoxicity and dual heating effects were also assessed *in vitro* cancer cells and *in vivo* solid tumors. After treatments, histological analysis was then carried out on the tumors and main organs to further evaluate the therapy efficiency and toxicity. Moreover, since medical imaging techniques could monitor the status and provide spatial and functional information of the tumor, imaging-guided cancer therapy may be promising to increase the accuracy of cancer therapy. To this end, the nanoring Fe_3O_4@PPy-PEG was also investigated for magnetic resonance imaging (MRI) and photoacoustic imaging (PAI) contrast enhancement both *in vitro* and *in vivo*. An extremely high transverse relaxation rate (60.61 mM^{-1} S^{-1}) was observed with a clinical open scanner equipped with a very low 0.35 T permanent magnet. The results showed that guiding by high resolution of soft tissue enhanced MRI/PAI images, and that nanoring Fe_3O_4@PPy-PEG enabled efficient ablation of tumor unaccompanied by obviously adverse effects with AMF plus NIR-triggered dual-enhanced hyperthermia. Lastly, this study provides an effective strategy for mechanism-based dual-enhancement HTs and suggests the promising potential of such multifunctional nanotheranostics applicable for clinical applications.

RESULTS AND DISCUSSION

Synthesis and Preparation of Nanoring Fe_3O_4@PPy-PEG

Nanoring Fe_3O_4@PPy-PEG was synthesized, as shown in **Scheme 1**. As shown in the TEM (**Figure 1A**) and SEM (**Supplementary Figure 1**) images, nanoring α-Fe_2O_3 was first obtained according to the previous study using oil bath with uniform morphology. The SEM results revealed that synthesized nanoring has an average size: height = 67 ± 21 nm, inner diameter = 41 ± 18 nm, external diameter = 93 ± 27 nm, and the wall thickness is 26 ± 12 nm by manual measurement of 30 nanoparticles (NPs) in SEM images. Then, the orange color nanoring α-Fe_2O_3 was reduced to black color magnetic nanoring Fe_3O_4 as shown in **Figure 1C**. Compared with nanoring α-Fe_2O_3, no obvious difference was found in the morphology and the geometry for the nanoring Fe_3O_4 in SEM and TEM images as shown in **Supplementary Figure 1**. After the nanoring Fe_3O_4 coated with PPy and PEG, a thin shadow layer was clearly observed on the ring surface in TEM image as shown in **Figure 1B** and the shadow layer can be attributed to the PPy coating and PEGylation. The thickness of PPy is around 12 nm. As shown in **Figure 1C**, the saturation magnetization (*Ms*) of the obtained nanoring Fe_3O_4@PPy-PEG was 76.7 emu g^{-1}, which was much larger than that of the conventional SPIO. The good magnetic properties indicate that favorable magnetic hyperthermia and transverse relaxation effects can be expected and the proposed Fe_3O_4@PPy-PEG nanoring may also have a great potential in MRI-guided cancer magnetic hyperthermal therapy. The zeta potential and hydrodynamic size of the nanoring Fe_3O_4@PPy-PEG measured by dynamic light scatter (DLS) in saline were determined to be about −10.3 mV and 192 nm, respectively, which are larger than those under TEM observations. The narrow size distribution indicated NPs without obvious aggregation. Moreover, the ICP-OES analysis revealed that the Fe_3O_4:PPy of the nanoring composite is 1:3.28.

The crystal structure of the nanoring α-Fe_2O_3, Fe_3O_4 and Fe_3O_4@PPy-PEG was determined by X-ray diffraction (XRD) (**Supplementary Figure 2**) analysis, which revealed that all the peaks can be well-indexed to a single phase of hematite (JCPDS no. 33-0664) for the initially as-prepared product (nanoring α-Fe_2O_3). In contrast, the reduced product shows a cubic inverse spinel phase, which can be identified as Fe_3O_4

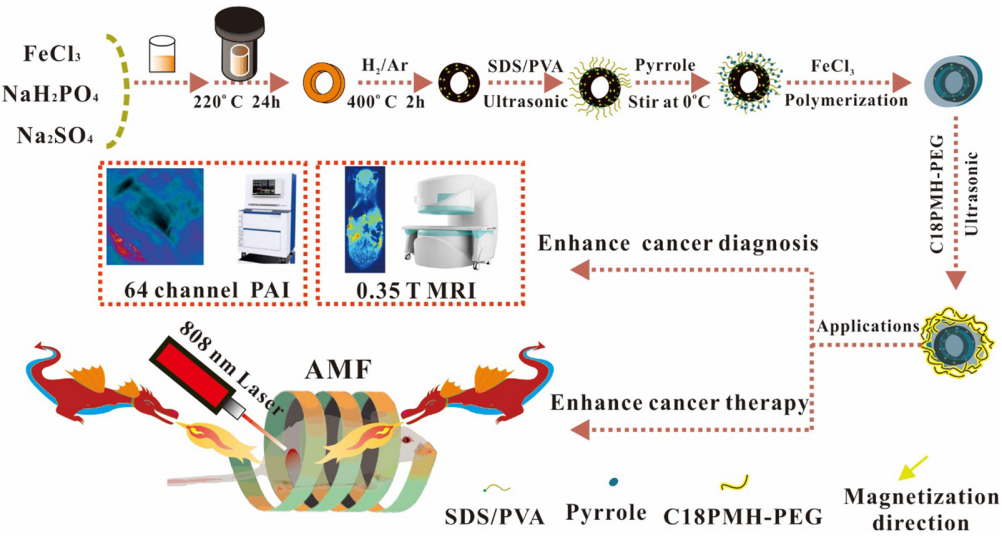

SCHEME 1 | Schematic illustration of the formation process for nanoring Fe_3O_4@PPy-PEG nanoparticles and their applications for cancer theranostics.

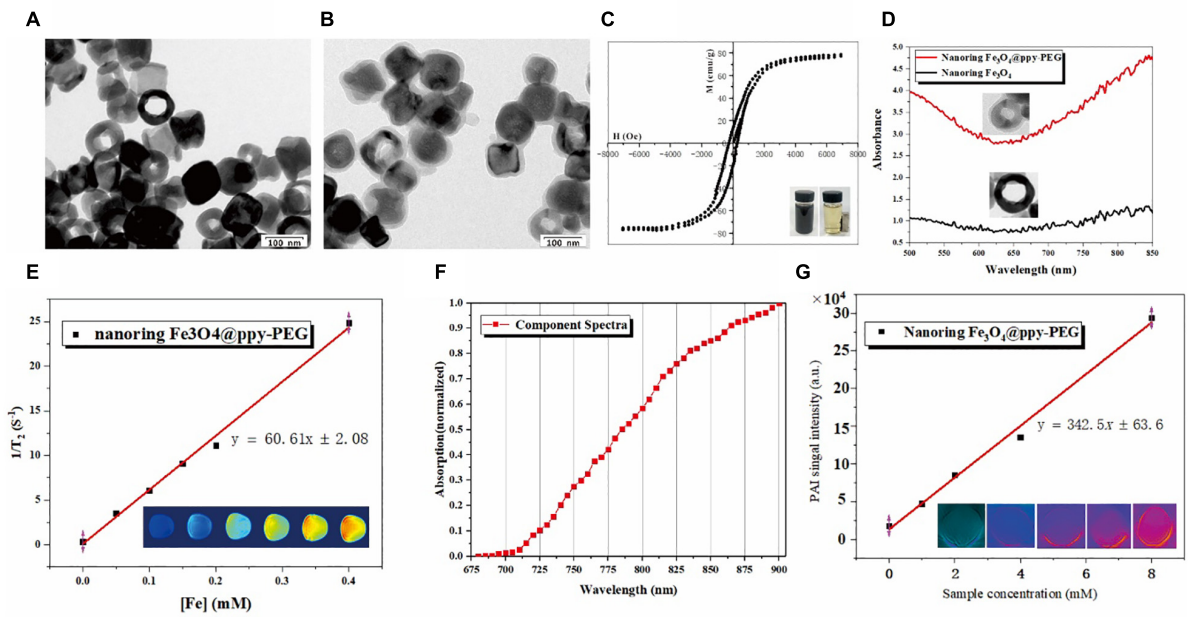

FIGURE 1 | Characterization of nanoring Fe_3O_4@PPy-PEG and its magnetic, photothermal properties. **(A,B)** Are morphology of nanoring Fe_3O_4 and Fe_3O_4@PPy-PEG determined by TEM. **(C)** Magnetization loops of nanoring Fe_3O_4@PPy-PEG and its photos in water with and without magnet. **(D)** UV-vis spectra of nanoring Fe_3O_4 and nanoring Fe_3O_4@PPy-PEG. **(E)** Transverse relaxation rate of Fe_3O_4@PPy-PEG obtained at very low B_0 field strength (0.35 T) and corresponding T_2_weighted images. **(F)** Photoacoustic spectrum from 680 to 980 nm with 5 nm step length in the water of Fe_3O_4@PPy-PEG. **(G)** Photoacoustic imaging of the phantom with different concentrations of Fe_3O_4@PPy-PEG at 830 nm excited wavelength. The graph presents the linear regression of the mean values of the photoacoustic signal amplitude as a function of nanoring Fe_3O_4@PPy-PEG aqueous dispersion. The hydrodynamic diameters of the prepared nanoring Fe_3O_4@PPy-PEG in the PBS and cell culture medium for 5 days are explored, and the results show good stability and dispersibility in both solvents (**Supplementary Figure 3**).

(JCPDS no. 19-0629). After coating with the PPy and PEG, a broad envelope peak shows up at the low-angle region in XRD patterns, which come from the PPy according to the previous studies (Wang et al., 2013; Das et al., 2019) and does not change the crystallinity of nanoring Fe_3O_4.

As shown in **Figure 1C**, the magnetic property of Fe_3O_4@PPy-PEG was preliminary validated using a magnet. When placed a magnet nearby, the black nanoring was rapidly attracted to the magnet side. What's more, the measured high saturation magnetization value (76.7 emu g^{-1}) further indicated that the

synthesized nanoring has a potential for enhancing T2W MR imaging.

As shown in **Figure 1D**, compared with the nude nanoring, Fe_3O_4, PPy-PEG coated nanoring shows a significantly elevated absorption peak in IR window, which means the proposed as-prepared nanoring Fe_3O_4@PPy-PEG may hold a great potential for PAI-guided cancer PTT treatment.

As shown in **Figure 1E**, T_2 relaxation rate was measured on 0.35 T, [60.61 mM^{-1} S^{-1}(Fe)] as a function of Fe concentration for nanoring Fe_3O_4@PPy-PEG. In the corresponding T_2-weighted (T_2W) images (bottom), higher nanoring concentration show lower MR signals, and reduced nanoring of Fe_3O_4 show the lowest MR signal. The *in vitro* phantom quantitative experiments prove the proposed nanoring Fe_3O_4@PPy-PEG can be used as a high-performance MR T_2 contrast agent. In order to further validate and verify the synthesized sample's capability in clinical applications, we also scanned the sample using a 3.0 T MRI scanner, and the T_2 relaxation rate (R_2) on 3.0T is 85.28 mM^{-1} S^{-1} (Fe) (**Supplementary Figure 5**). This result indicates that the proposed synthesized sample can be used on both 0.35T and 3.0T MRI scanner.

As shown in **Figure 1F**, the PAI signal intensity increases with the increase in the excitation wavelength from 680 to 900 nm. It not only proves the nanoring Fe_3O_4@PPy-PEG may be used as PAI contrast agent but also indicates high PAI signal intensity can be obtained in the long wavelength region, which alleviates the effects of the physiological artifacts. Thus, 900 nm was selected as the excitation wavelength for the following phantom and animal studies. Thus, as shown in **Figure 1G** using 900 nm excitation wavelength, we found a clearly linear relationship between the PAI signals and the corresponding sample concentrations, which is beneficial to following *in vivo* quantitative imaging. Furthermore, it can be directly seen that the brightness of PA images (bottom) of the aqueous phantoms increases with the concentrations and the signal intensity is pretty high even at the low concentration, which further confirmed the outstanding PA property of nanoring Fe_3O_4@PPy-PEG, and it may be attributed to the synergistic effects of black color magnetite (Ting et al., 2014; Lu et al., 2018) and PPy (Liang et al., 2015; Lin et al., 2018). The results demonstrate that the proposed nanoring Fe_3O_4@PPy-PEG is a promising candidate for photoacoustic imaging at the

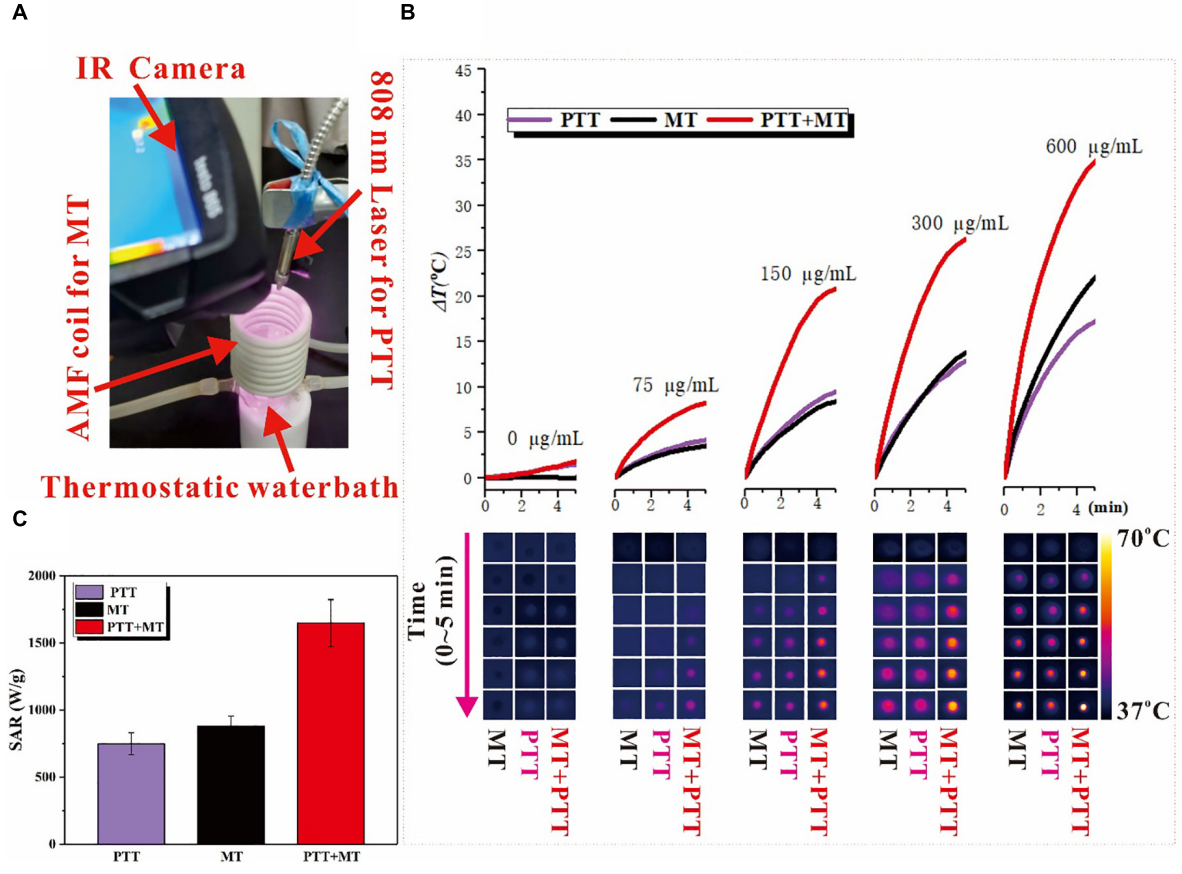

FIGURE 2 | (A) Photo of the home-made dual hyperthermia cancer therapy system, combined the photothermal and magnetothermal therapy. In the photo, the red arrows indicate four parts: IR Camera, AMF coil for MT, 808 nm Laser for PTT, and Thermostatic water bath. **(B)** Heating capacity [SAR (Wg^{-1})] in MT, PTT, and dual mode. **(C)** Temperature increase for different concentration nanoring Fe_3O_4@PPy-PEG after 5 min of each treatment and corresponding thermal images acquired by IR camera at different time points.

NIR window where the excitation laser pulse can penetrate to the deeper tissues.

Photothermal and Magnetic Thermal Properties of Fe_3O_4@PPy-PEG

The photothermal effects of Fe_3O_4@PPy-PEG were investigated by photo-irradiating Fe_3O_4@PPy-PEG in saline (200 μl, 75, 150, 300, and 600 $\mu g ml^{-1}$) with an 808-nm laser (1 W cm^{-2}). The solution exhibited a rapid temperature increase, reaching about 55°C in 5 min with irradiation (**Figures 2A,C**). The photo-irradiating temperature change curves and thermal images of sample and control over times are shown in **Figures 2A,B**. It should be noticed that beside the much higher final plateaus of the dual thermal actions, the temperature increase rate was also obviously faster, which possibly augments the antitumor effects and shortens the treatment duration (Hasegawa et al., 2001; Szasz et al., 2006) in the following study. The results proved that the proposed nanoring Fe_3O_4@PPy-PEG may hold a potential as a high efficiency photothermal conversion agent. The magnetic thermal property of Fe_3O_4@PPy-PEG was also investigated *in vitro* by AMF. From **Figure 2B**, we found that higher concentration of the Fe_3O_4@PPy-PEG saline solution shows a steeper temperature change curve as expected.

As shown in **Supplementary Figure 4**, the heating capacities of the nanoring Fe_3O_4@PPy-PEG triggered by MT and PTT were studied with different magnetic strength and laser power separately, and both parameters can adjust the heating hyperthermia efficiency. As expected, the SAR increases with the magnetic field strength in the MT-mode and increases with the laser power as well in the PTT-mode. Furthermore, in the dual model shown in **Figure 2C**, the SAR is significantly higher than PTT and MT and far beyond 1,000 (Wg^{-1}), which is consistent within some previous studies (Das et al., 2016; Del Sol-Fernández et al., 2019).

Cancer Cell Cytotoxicity

The cell viability of the different concentrations of Fe_3O_4@PPy-PEG and corresponding various treatment conditions were explored *in vitro* with 4T1 cells. As shown in **Figure 3A**, the cell viability slightly decreased when the concentration of the samples increased. However, no significant cytotoxicity for

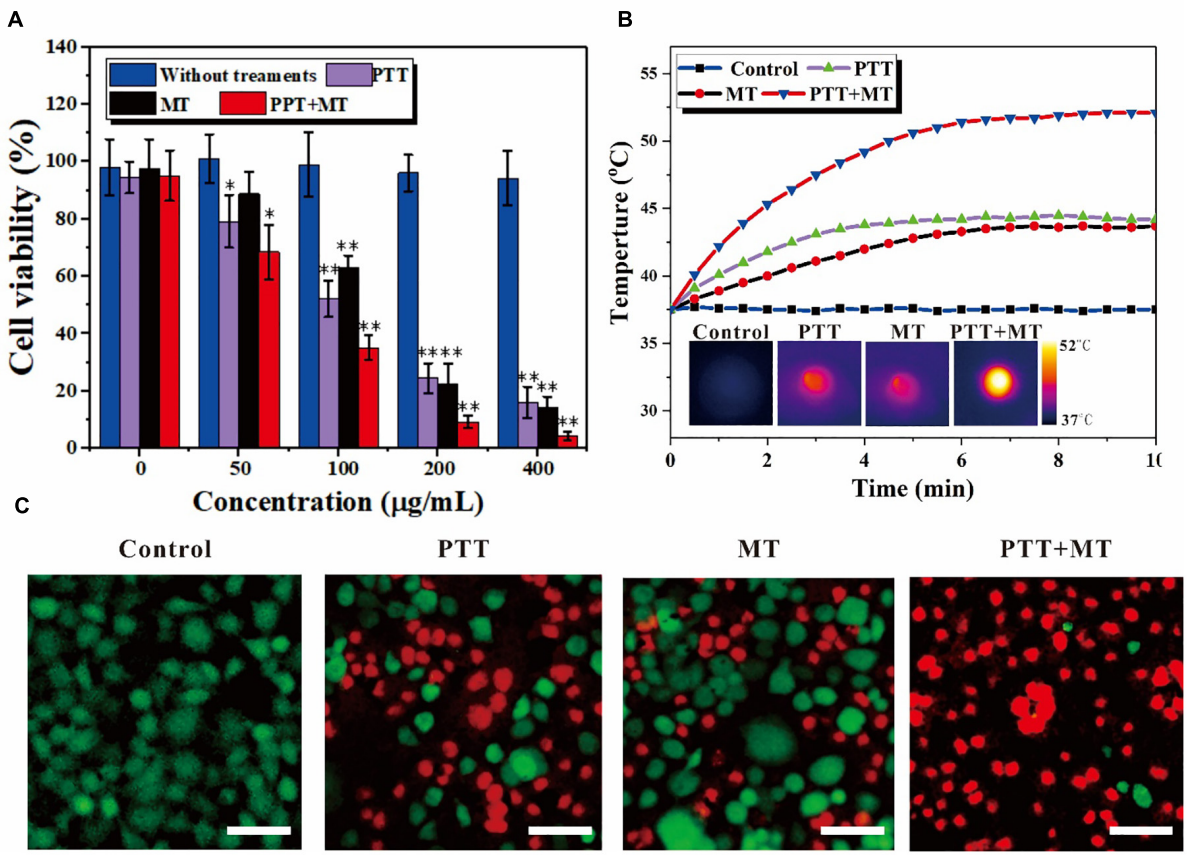

FIGURE 3 | *In vitro* nanoring Fe_3O_4@PPy-PEG-mediated heating for 4T1 cells. **(A)** Relative cell viabilities after incubation with samples in the presence of a magnet with or without photo thermal (808 nm 5 W cm^{-2}) and magneto thermal (300 kHz 30 A) for 10 min, $^*p < 0.05$ and $^{**}p < 0.01$. **(B)** Temperature curves of 4T1 cells incubated with nanoring Fe_3O_4@PPy-PEG, at a final concentration 200 $\mu g ml^{-1}$, and subject to an AFM (300 kHz, 30 A), NIR-Laser irradiation (808 nm, 0.5 W cm^{-2}) or both treatments simultaneously and corresponding IR images. **(C)** Representative fluorescence images of 4T1 cells co-stained with calcein-AM/PI (live is green/dead is red) standing. Scale bar, 100 μm.

Fe_3O_4@PPy-PEG was observed, which indicated good cellular affinity of the proposed nanoring. The cytocompatibility assay also indicated that the proposed nanoring is relatively safe for *in vivo* application. Compared with the control group (0 $\mu g ml^{-1}$), no obvious death was observed in 4T1 cells incubated with Fe_3O_4@PPy-PEG, even if being treated with the high concentration (400 $\mu g ml^{-1}$), which the cell viability remains high of 94.2%. Subsequently, *in vitro* nanoparticle-mediated ablation effects triggered by AMF and NIR were explored. As shown in **Figure 3A**, the cell viability was almost equal to that of the control group after different treatments without the nanoparticles, which indicates that neither NIR (808 nm, 0.5 W cm^{-2}) or AMF (300 kHz 30 A) will lead to apparent cell death. In contrast, when the nanoring Fe_3O_4@PPy-PEG was introduced, obvious cell cytotoxicity was observed with the same treatments as the control group. As expected, the cell viability decreased obviously with increasing the concentration of the nanoring Fe_3O_4@PPy-PEG for each therapy method. Importantly, the combined therapy of photothermal and magnetic hyperthermal were also examined, and the results can be seen in **Figure 3A**. The cell viability decreases rapidly when the concentration of the nanoring Fe_3O_4@PPy-PEG increases, and there is a dramatic decrease in the cell viability after combined therapy was observed for all concentrations. The temperature elevation was recorded for all treatments, as shown in **Figure 3B**. The temperature increases remarkably higher and faster using the dual mode than the MT or NIR mode alone. Thus, the combination therapy was preliminary proved to be more efficient than monotherapy for *in vitro* cell experiments.

To intuitively display and visualize the cancer cell kill abilities of the proposed nanoring, cell live/dead staining with calcein AM/PI was used, as shown in **Figure 3C**. The results are consistent with cell viability assessments under same conditions, and further confirmed the good cytocompatibility of nanoring Fe_3O_4@PPy-PEG and obvious cell death (red fluorescence) with each treatment. Noteworthy is that much higher cell death of the combined therapy was observed compared with that of monotherapy, which was consistent with the MTT results. When we used the dual hyperthermia, almost all cells incubated with the nanoring Fe_3O_4@PPy-PEG were ablated to death, which indicated the best effect in killing cancer cells. In summary, by combining the two complementary HT method (PTT and MT), we achieved a high antiproliferative efficiency, which indicated that the proposed dual HT method can significantly inhibit the tumor grow *in vitro*.

MR and PA Imaging

Attributed to the excellent T_2-weighted MRI and PA dual contrast-enhancing performance in the phantom of the proposed nanoring Fe_3O_4@PPy-PEG, as well as the very low cytotoxicity

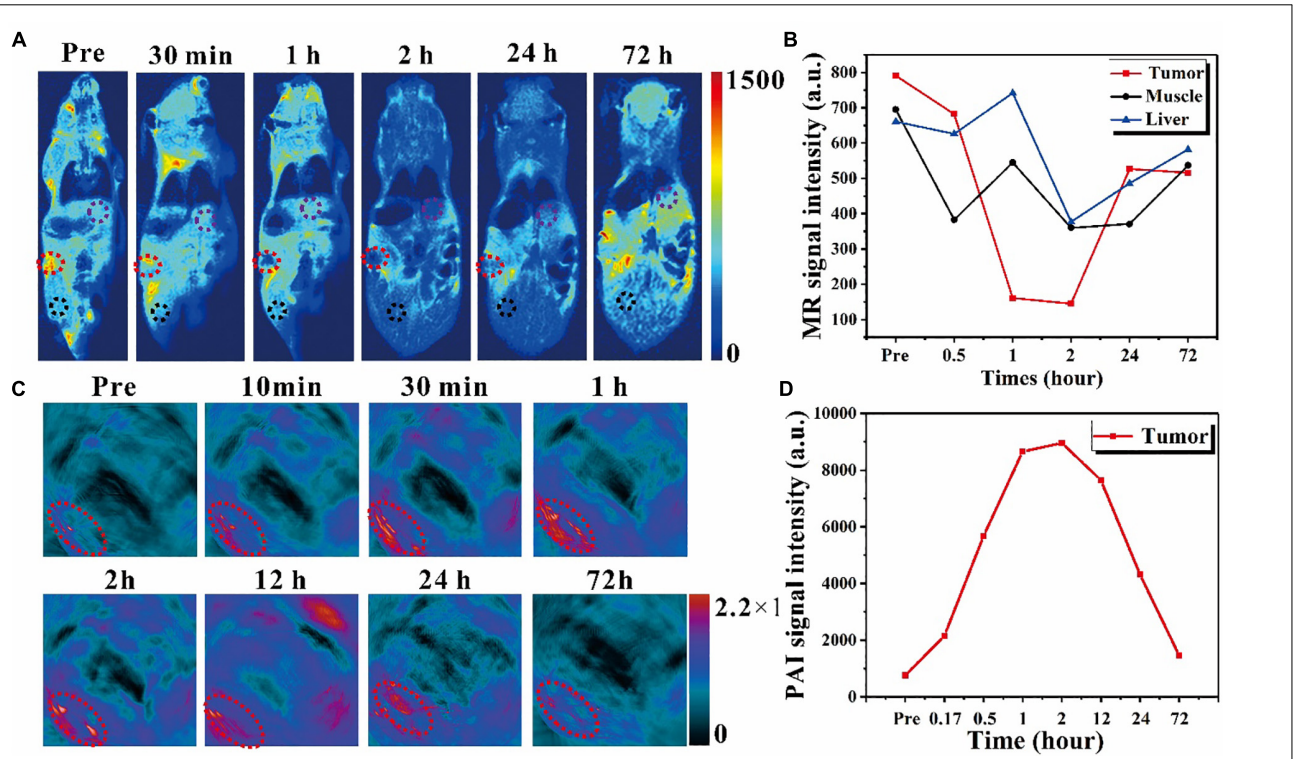

FIGURE 4 | *In vivo* exploration of the dual imaging modalities enhancement caused by nanoring Fe_3O_4@PPy-PEG on 4T1 tumor-bearing mice. **(A)** *In vivo* T_2-weighted MR images with IV injection with 200 μl 2 $mg ml^{-1}$ samples for up to 72 h. The red dotted circle denotes the tumor site, and the black and purple circle denotes the muscle and liver regions for acquiring the MR signal intensity. **(B)** MR signal intensity changes in different organs before and after administration. **(C)** PAI images acquired at different time points before and after the IV injection of samples. The exciting light wavelength of PAI is 900 nm, and the red circle denotes the tumor region. **(D)** PAI signal intensity changes over time for the tumor site.

verified by the *in vitro* experiments, the *in vivo* contrast enhancement capability and tumor accumulation behavior were then explored. It should be noted that before the *in vivo* studies, the hemocompatibility of the proposed nanoparticle was also assessed *in vitro*. As shown in **Supplementary Figure 6** and **Supplementary Table 1**, no visible hemolytic effects were observed, which further confirmed the good biocompatibility of the materials, indicating the promising potential for *in vivo* applications.

Next, the *in vivo* MR experiment was performed on a tumor bearing mouse, as shown in **Figure 4A**; and in order to compare the signal intensity changes, all the scan parameters, which can also affect the final image contrast and signal intensity, were consistent across different time points. The T_2W coronal MR images were obtained at different time points before and after Fe_3O_4@PPy-PEG injection (200 μl, 2 $mgml^{-1}$). It can be seen that cancer sites (red dotted circles) were significantly darker after 2-h injection, and almost recovered after 3 days of injection. To quantitatively analyze the signal change over time, several regions of interest (ROIs) were manually placed in the tumor, liver (purple circle), and muscles (black circle) regions to extract the signal values. The average signal intensities of these tissues were plotted at different time points, as shown in **Figure 4B**. Compared with muscle and liver, the tumor site showed remarkably signal attenuation after about 1–2-h administration, which indicated that the nanoring Fe_3O_4@PPy-PEG produced high native contrasts on T_2W MR images. Furthermore, it should be noticed that the signal intensity falls to the lowest point after

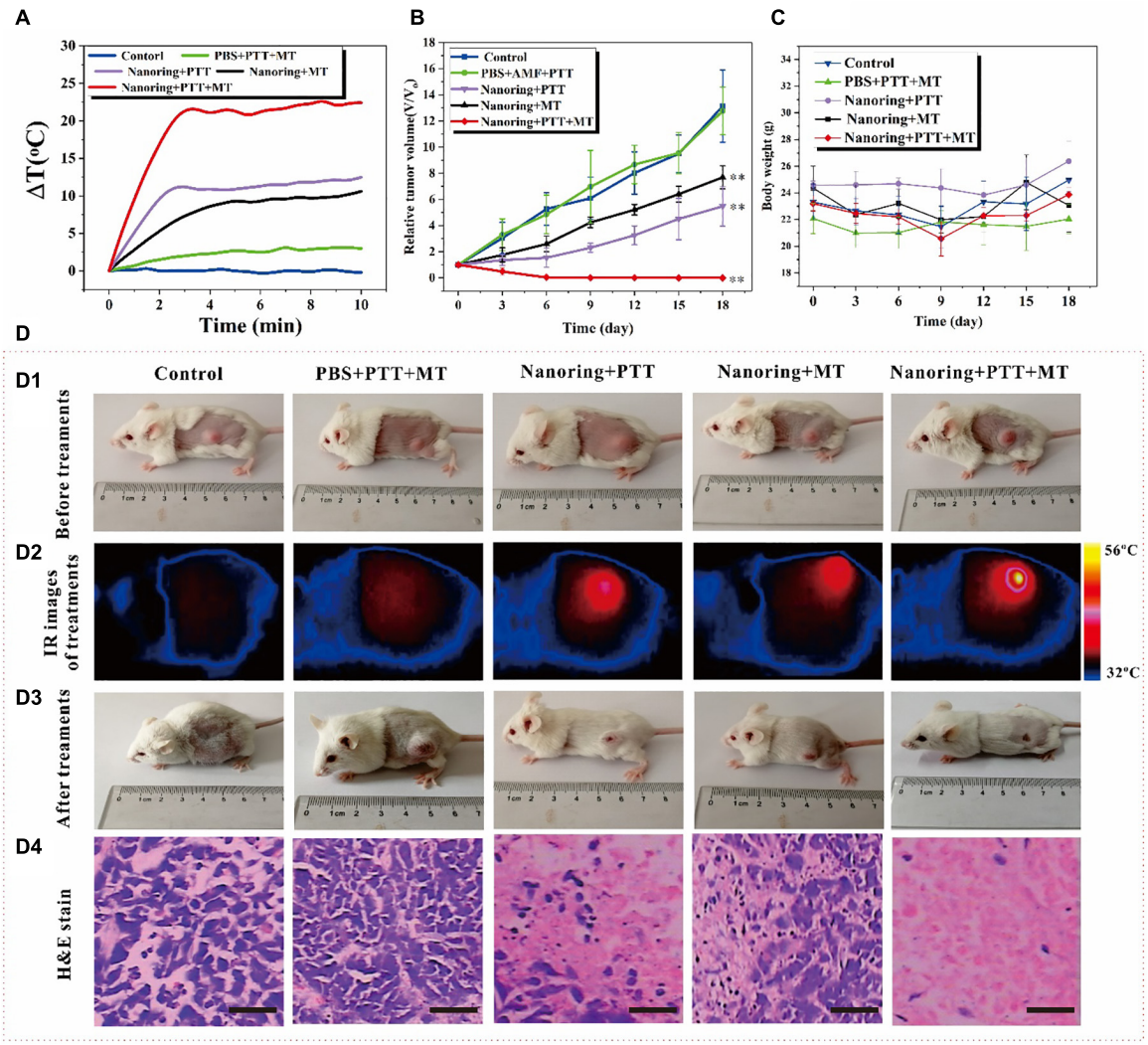

FIGURE 5 | Antitumor effects of the proposed nanoring Fe_3O_4@PPy-PEG through hyperthermia (PTT and AMF separately or jointly) in 4T1 mice. **(A)** Thermal elevation curves for each treatment group. **(B)** Body weight recorded in 18 days and **(C)** relative tumor growth curves. Data are presented as mean ± SD, and the significance of differences was set at $^{**}p < 0.01$. **(D)** According to different treatment protocols to implement grouping and subsequent experiments, **(D1)** photos of the mice before treatments, **(D2)** reprehensive IR images of tumor bearing mice injected intratumorally with 50 μl PBS or 200 μgml^{-1} sample, **(D3)** photos of the mice after 18 days for different treatments, and **(D4)** representative H and E staining of tumor section of each group. Scale bar, 100 μm.

2-h injection, which indicates the maximum accumulation of the nanoring Fe_3O_4@PPy-PEG and implied that the NIR or AMF induced therapy must work the best at that time point. The *in vivo* results demonstrated the nanoring structure could serve as an excellent negative contrast agent for very low magnetic field MRI scanner.

Due to the tremendous amount and broad absorption in the NIR window in UV-vis spectrum and photothermal characteristic, the nanoring Fe_3O_4@PPy-PEG playing a PAI contrast agent role for enhancing PAI images was explored *in vitro* and *in vivo*. For the *in vivo* experiments shown in **Figure 4C** with 900 nm excitation laser pulse and IV injection, the tumor (denoted with red dash circles) was remarkably enhanced gradually and reached the maximum value at 2 h post injection and then declined. The quantitative analysis of the mean signal intensity curve of the tumor is shown in **Figure 4D**. It should be noticed that the temporal signal enhancements and decline reflect the dynamic accumulation and excretion process of the nanoring Fe_3O_4@PPy-PEG in the tumor site, which can be used to precisely guide the subsequent tumor treatments. From **Figure 4B**, the MR signal intensity of the tumor reached to the lowest points at around 2 hours, while **Figure 4D** showed that the PAI signal intensity peaked also around 2 hours. Both results indicate the maximum nanoparticles accumulation in the cancer site appeared in 2 hours after injection. From this result, we can then optimize when to apply the external PTT and MT treatments. These results demonstrated that the proposed nanoring Fe_3O_4@PPy-PEG possessed excellent MR and PA imaging capabilities *in vivo*.

In vivo Cancer Combined Therapy

Encouraged by the remarkable *in vitro* cell-killing ability through high-performance thermal effects *via* the combined PTT and MT method mediated by the proposed nanoring Fe_3O_4@PPy-PEG, *in vivo* animal experiments were carried out to evaluate and compare the cancer therapy efficiency of different hyperthermia therapies. As illustrated in **Figure 5A**, cancer-bearing mice were randomly separated into five groups. Each group includes five mice with prescribed treatments. The tumor temperature under different therapies was monitored using a thermal camera, because the high thermal efficiency is a key factor for tumor ablation efficiency. **Figure 5A** shows the curve of the temperature changes over 10 min. After about 3 min, the dual hyperthermia therapy method heats the tumor region higher than 55°C, which is sufficient to cause tumor cell ablation *in vivo*. In contrast, for the mice treated with single thermal method, the temperature only shows no obvious increase in the PBS group. Furthermore, consistent with the *in vitro* results, both the heating rate and the final temperature are remarkably higher for the dual hyperthermia method than those of each method alone, and are both beneficial for HT efficiency. The relative tumor volume of each mouse was calculated with cancer length and width in 18-day treatment; and as shown in **Figure 5B**, at the end of the experiment, the mean value of the relative cancer volume was significantly lower in the NIR + AMF group, which shows extraordinary tumor suppression and almost realizes complete tumor reduction compared with the other groups. On the other hand, the group with AMF or NIR shows relative smaller value of relative cancer volume than the control groups. Since loss of body weight is a clinical sign of toxic symptoms, the body weight was recorded, and no notable or statistically significant differences in the mean body weight were found between the groups, as shown in **Figure 5C**. It is obvious that AMF + NIR shows almost disappeared tumors, and the control group shows huge tumors. In order to better display the *in vivo* treatment procedures and results, reprehensive photos and images are shown in **Figure 5D**. To further evaluate the efficacy and safety of the HTs, after the second treatments, one mouse in each group was randomly chosen and sacrificed. Besides the tumor, major organs such as heart, liver, spleen, lung, and kidney were extracted for hematoxylin and eosin (H and E) staining. As shown in **Figure 5d4**, the therapy group showed the large area of cell death, but no obvious damages or inflammation lesions were observed in the major organs (**Supplementary Figure 7**). These preliminary results indicated that the proposed Fe_3O_4@PPy-PEG is an efficient and safe nanoplatform for cancer therapy. Consequently, these preliminary results suggest that the nanoring Fe_3O_4@PPy-PEG may serve as a potential clinically translatable nanotheranostics for highly dual effective HTs.

CONCLUSION

In summary, a novel iron oxide-based theranostic nanosystem was reported for efficiently enhanced MRI/PAI-guided photo-magnetic hyperthermia therapies. By simply reducing the ring shape of α-Fe_2O_3, uniform hollow magnetite Fe_3O_4 was obtained with excellent magnetic properties. After coating with PPy, the nanoring Fe_3O_4@PPy-PEG showed intensive absorption and light-to-heat conversion efficiency. Remarkably, the heat-generating ability, both heating rate and peak value, was significantly higher for the dual thermal actions compared with either one. Cell culture results suggested excellent biocompatibility of the nanoparticle itself but with high level of cytotoxicity upon being remotely activated with AMF and NIR. An extremely high transverse rate (R_2 = 60.61 mM S^{-1}) was observed *in vitro*, and good contrast effects were proved for *in vivo* experiments with a very low magnetic-filed 0.35 T clinical MR scanner. Interestingly, the nanoring also showed good PAI effect for the *in vitro* and *in vivo* experiments. In particular, under AMF and NIR stimulation conditions, the boosting heat induced complete tumor ablation and largely suppressed cancer growth for *in vivo* experiments. In brief, this study not only demonstrates the nanoring Fe_3O_4@PPy-PEG is a highly effective nanocomposite for imaging-guided photo-magnetic HT, it also provides a fundamental guideline for developing a hollow iron oxide-based multifunctional theragnostic nanoplatform for cancer-efficient hyperthermia therapy and monitoring.

MATERIALS AND METHODS

Materials

Unless specified, the chemicals were purchased from several commercial companies and used without further purification. $FeCl_3$, NaH_2PO_4, Na_2SO_4, and pyrrole were purchased from

Aladdin Company (Shanghai, China). The murine breast cancer cell line (4T1) was purchased from Shanghai Bioleaf Biotechnology Co., Ltd. (Shanghai, China). Poly (vinyl alcohol) (PVA) and sodium dodecylbenzene sulfonate (SDBS) were purchased from Macklin Chemical Co. (Shanghai, China). The DAPI kit and calcein-AM/PI kit were purchased from Biyuntian Bio-Technology Co., Ltd. (Shanghai, China), and 3-(4,5-dimethyl-2-thiazyl)-2, 5-diphenyl-2H-tetrazolium bromide (MTT) was purchased from Solarbio (Beijing, China). The fetal bovine serum (FBS), Roswell Park Memorial Institute-1640 (RPMI-1640) medium, and (calcein-AM)/propidium iodide (PI) was purchased from Thermo Fisher Scientific Inc. (Waltham, MA, United States), which was used without further purification. PL-PEG-COOH (DSPE-PEG2000 carboxylic acid) was purchased from Avanti Polar Lipids, Inc. (Alabaster, AL, United States).

Preparations of Nanoring Fe_3O_4@PPy-PEG NPs

The synthesis approach of the basic hollow α-Fe_2O_3 nanoring NPs was a simple hydrothermal method derived from previous study (Jia et al., 2008). As shown in **Scheme 1**, 259.2 mg $FeCl_3$, 1.728 mg NaH_2PO_4, and 6.248 mg Na_2SO_4 were mixed together in an 80-mL aqueous solution with distilled water. After vigorously stirring for 30 min, the mixture was transferred into a hydrothermal reactor liner with a capacity of 100 ml for hydrothermal treatment at 220°C in oil bath for 24 h. The autoclave was cooled to room temperature at the end of the experiments, and the orange precipitate was separated by centrifugation (10,000 r min^{-1}), washed with distilled water and absolute ethanol eight times, and dried under vacuum at 80°C for the following procedures.

For the reduction experiment on powdered α-Fe_2O_3 nanoring, the as-prepared nanoparticles (1 g) were flattened on the bottom of a quartz boat, which was placed in the middle part of a quartz tube and kept horizontally in the furnace. A mixed gas of 5% hydrogen and 95% argon was passed through the quartz tube at a rate of 1 L min^{-1} for 20 min to remove other gases. Then, the system was heated to 400°C at a speed of 10°C min^{-1} and kept at that temperature for 2 h before being cooled down to room temperature (Peng et al., 2012).

After reduction, the nanoring NPs were coated with PPy. The PPy monomer was oxidized by $FeCl_3$, which triggered the following PPy polymerization on the surface of Fe_3O_4 nanoring. Briefly, 10 mg sodium dodecyl benzene sulfonate (SDBS) and 30 mg PVA were completely dissolved in 10 ml water, and then 10 mg as-prepared Fe_3O_4 nanoring was added into the solution. Then, the solution was ultrasonicated at maximum power for 1 h to ensure full dispersion of the sample. Then, a 20-μl PPy monomer was added to the solution and stirred for another 2 h. After that, 40 mg of 2 ml $FeCl_3$ solution was added to the mixture solution dropwise and then stirred at room temperature for 48 h to obtain the final product nanoring Fe_3O_4@PPy. The raw product was washed eight times with deionized water and collected with magnet. To improve biocompatibility, polyethylene glycol (PEG) was modified on the nanoring Fe_3O_4@PPy according to the previous study (Wang et al., 2013).

Characterization

A tabletop ultracentrifuge (Beckman Coulter TL120, Beckman Coulter, Brea, CA, United States) was used for NP purification and isolation. Particle morphology and size were measured using a field emission scanning electron microscope (FE-SEM, JEOL, JSM-6700F, 15 kV, Tokyo, Japan) and a transmission electron microscope (TEM, JEOL, JEM-2100, 200 kV, Tokyo, Japan). The magnetic character of NP was measured at 300 K in a superconducting quantum interference device (SQUID) magnetometer (Quantum Design MPMS-5S, Quantum Design Inc., San Diego, CA, United States). XRD was measured using a Bruker D8 Advance diffractometer (Bruker GmbH, Karlsruhe, Germany) at room temperature. Nanodrop 8000 (Thermo Fisher Scientific Inc., Waltham, MA, United States) was used to obtain the UV-Vis spectrum. Magnetic properties were measured by Physical Property Measurement System [PPMS-9T (EC-II), Quantum Design Inc., San Diego, CA, United States]. Inductively Coupled Plasma-Optical Emission Spectroscopy (ICP-OES, Optima 2100, PerkinElmer, Waltham, MA, United States) was used to determine metal elements. An ASPG-10A-II (Shuangping Power Supply Technology Co., Ltd., Shenzhen, China) high-frequency alternating magnetic field (AMF) system was applied in this study with F = 300 kHz and I = 5–45 A. An 80-nm NIR laser source LWIRL808-8W (Beijing Laserwave Optoelectronics Technology Co., Ltd., Beijing, China) was applied to conduct photothermal experiments. A thermal infrared camera (Thermal Imager TESTO 869, Testo SE & Co., KGaA, Darmstadt, Germany) was used to record temperature changes. The MRI data were obtained on a clinical open permanent magnet scanner (XGY-OPER, Ningbo Xingaoyi Co., Ningbo, China). The PAI data were obtained using a preclinical 64-TF multispectral optoacoustic tomography (MSOT, iThera Medical, Munich, Germany) system with the spectral region from 680 to 980 nm and 150-μm resolution.

Hyperthermia Effect Evaluation

The photothermal conversion ability of the Fe_3O_4@PPy-PEG nanoring was excited using an 808 nm NIR laser system. Saline and samples with various concentrations (75, 150, 300, and 600 μgml^{-1}) in Eppendorf tubes were irradiated under the 808 nm laser with a power of 1 W cm^{-2}. Similarly, the magnetothermal effect was assessed using a high-frequency AMF system (SPG-10A-II, 300 kHz,45 A). Samples with the same concentration as PTT were placed in the center of the coil, and then AMF was applied. For the photo/magneto joint thermal effects, the different concentration sample was placed in the coil, and then AMF and laser exactions were applied at the same time for 5 min, as shown in **Figure 2A**. The temperature and corresponding thermal image were recorded at real-time for 5 min for all the experiments. To prove the heating process of the proposed nanoring, Fe_3O_4@PPy-PEG can be easily controlled by adjusting the dual-mode parameters, as shown in **Supplementary Figure 4**, the heating efficiency for each hyperthermia modality

was assessed with various magnetic field strength (70–560 Oe) and laser power (0.3–2 W cm^{-2}).

The efficiency of photothermal and magnetothermal is classically expressed in terms of specific absorption rate (SAR). The SAR value is defined as the power dissipation per unit mass of iron (Wg^{-1}) and was calculated using the following equation:

$$SAR = C\frac{V_S}{m}\frac{dT}{dt}$$

where C is the heat capacity of the medium (water is commonly considered to be 4184 $Jkg^{-1}\cdot°C$), V_S is the mass of the suspension, m is the iron content of the suspension, and $\frac{dT}{dt}$ is the measured temperature elevation rate at the initial 60 s linear slope (Ebrahimisadr et al., 2018).

Cell Experiments

The cytotoxicity of nanoring Fe_3O_4@PPy-PEG and different therapy efficiency were evaluated *in vitro*. 4T1 cells were cultured in a 20-ml RPMI-1640 medium containing 10% FBS, 15 mg penicillin, and 25 mg streptomycin at 37°C in a humidified 5% CO_2 atmosphere. The medium was replaced every 1–2 days (Liu et al., 2018).

For the standard MTT and cell hyperthermia experiments, 4T1 cells were first seeded in a 96-well plate at a density of 1×10^4 cells $well^{-1}$. The plate was then maintained in a CO_2 incubator at 37°C with 5% CO_2 for another 24 h. Then, a different amount of nanoring Fe_3O_4@PPy-PEG was added to the medium, and the 4T1 cells were cultured for another 24 h before other experiments. For standard MTT assay, all wells were added with 100 μl 5 mg ml^{-1} MTT dissolved in PBS and was incubated and gently shaken for 4 h. Then, 100 ml dimethyl sulfoxide was added into all the wells, and the absorbance was quantified at 570 nm using an enzyme-linked immunosorbent assay (ELISA) plate reader (model 550, Bio-Rad Laboratories, Inc., Hercules, CA, United States). PBS was added to the control group, and the background absorbance was adjusted for the bias caused by the dark color nanoring Fe_3O_4@PPy-PEG. According to the previous study (Wang et al., 2013), a magnet was placed under the well to enhance the cellular uptake of the proposed multifunctional nanoparticle internalization for another 30 min. Then, after carefully washing, the PTT (808 nm, 0.5 W cm^{-2}) and magnetic hyperthermia therapy (300 kHz, 30 A) were applied separately or jointly for 10 min after. After 4-h incubation, standard MTT assay was performed as well (Yang et al., 2016). In order to visualize the cell death caused by different treatments, cells were further stained with calcein AM/PI (Ma et al., 2012).

Tumor-Bearing Mice Preparation

All mice are 4 weeks old female Balb/c mice (∼18 g) purchased from Beijing Huafukang Biological Science and Technology Stock Co., Ltd. (Beijing, China), and 4T1 cells (1×10^6) suspended in 50-μL PBS were subcutaneously injected into the left hind limb of each mouse (Hill et al., 2016). After about 1 week, the volume of the tumor is about 80∼100 mm^3, and predesigned treatments protocols can be applied. It should be noted that in order to make the nanoring Fe_3O_4@PPy-PEG enriched in the cancer site, a small circular magnet (diameter ø = 8 mm) was placed on the tumor surface immediately for 12 h after the intravenous (IV) injection of the sample.

MRI and PAI Enhancement Experiments

Because the saturation magnetization (*Ms*) value of the obtained nanoring Fe_3O_4@PPy-PEG is relatively high (76.7 emu g^{-1}), the corresponding transverse relaxation rate (R_2) value of MRI is expected high as well even at lower field permanent magnet MR scanners. It is also well known that the R_2 value is not only depending on the material itself but also on the main magnetic field strength (B_0) of the measurement MRI scanner. That is, R_2 decreases as the B_0 decreases. Thus, different from most previous studies, all MRI experiments in this study were performed on a 0.35 Tesla, which is the lowest B_0 for clinical use, an open permanent magnet scanner (XGY-OPER, Ningbo Xingaoyi Co., Ningbo, China). In order to calculate the R_2, different concentration (0–2 $mgml^{-1}$) of nanoring Fe_3O_4@PPy-PEG was dispersed in an aqueous solution and fixed with 0.8% agarose gel in 2-ml EP tubes. Then, the phantoms were scanned with Carr–Purcell–Meiboom–Gill (CPMG) pulse sequence in a single coronal slice with the following parameters: repetition time (TR) = 4,000 ms, echo time (TE) = 12, 24, 48, 72, 96, 108, 120, 132, 168, 180, and 192 ms, bandwidth = 50 kHz, matrix = 128 × 128, and slice thickness = 5 mm. After acquisition, T_2 fitting was carried out using the non-linear curve-fitting method and the reciprocal of T_2 is R_2.

Animal MRI experiments were performed with a 4T1 cancer-bearing mouse and a small animal coil. Before and after tail vein IV injection of 200 μl 2 mg m^{-1} nanoring Fe_3O_4@PPy-PEG, mouse was scanned with T_2W fast spins echo method at predefined time points with the following parameters: TR = 3,000 ms, effective TE = 40 ms, echo train length (ETL) = 12, matrix = 128 × 128, and field of view (FOV) = 50 mm× 50 mm. The signal intensity of the tumor and any other organs was extracted using the ImageJ software package (Rasband W., National Institutes of Health, United States) for future quantitative analysis.

The PAI experiments were performed in a real-time whole-body mouse imaging multispectral optoacoustic tomography (MOST) system with 64 channels. In order to determine the optimal excited laser wavelength, a phantom containing 0.1 $mgml^{-1}$ nanoring Fe_3O_4@PPy-PEG was scanned using wavelength sweep mode from 680 to 900 nm with 5-nm step width, and the PAI signal intensity was recorded for each wavelength. After that, different concentrations of nanoring Fe_3O_4@PPy-PEG (0–2 $mgml^{-1}$) aqueous phantoms were prepared and scanned at the wavelength that the PAI signal intensity is maximized.

4T1 cancer beard mouse was scanned with the same protocol as the phantoms before and after IV injection of 200 μl 2 mg ml^{-1} sample at predefined time points. The signal intensity of cancer was recorded for further analysis.

In vivo Cancer Therapy Assessment

The *in vivo* cancer therapy efficiency of the proposed nanoring Fe_3O_4@PPy-PEG was assessed on 4T1 cancer-bearing mice on the left hind limb. When the cancer volume reached about 80∼100 mm^3, the mice were randomly allocated into five groups (five mice for each group): (i) control group without any treatment; (ii) PBS + AMF + PTT; (iii) nanoring Fe_3O_4@PPy-PEG + PTT; (iv) nanoring Fe_3O_4@PPy-PEG + AMF; (v) nanoring Fe_3O_4@PPy-PEG + PTT + AMF. Nanoring Fe_3O_4@PPy-PEG 5 mg mL^{-1} was intratumorally injected into the mice at a dosage of 5 mg kg^{-1}. After injection, the hyperthermia treatments including PTT (808 nm, 0.5 W cm^{-2}, 20 min) and AMF (300 kHz, 30 A, 20 min) therapies, were performed as above designed for each group. To enhance the therapy outcomes, same treatments were applied to the corresponding group the day after first therapy day. The mice weight, and the length and width of each cancer were recorded every 3 days for 15 days before and after the second therapy. The tumor volume was calculated using the formula: $width^2 \times length/2$ (Wang et al., 2019).

H and E Staining

Two days after the second time therapy, one mouse in each group was randomly sacrificed, and the tumor and other main organs (heart, liver, spleen, lungs, and kidney) were extracted for further hematoxylin and eosin (H and E) stain to explore whether there are obvious damages.

Statistic Analyzing

All the statistical analyses were performed using SPSS 7.0 (IBM Corporation, Armonk, NY, United States). Group differences were determined by independent samples *t*-tests. Statistical significance was accepted at the 0.05 level ($^*p < 0.05$ and $^{**}p < 0.01$).

DATA AVAILABILITY STATEMENT

The original contributions presented in the study are included in the article/**Supplementary Material**, further inquiries can be directed to the corresponding authors.

ETHICS STATEMENT

The animal study was reviewed and approved by the Institutional Animal Care and Use Committee of Zhengzhou University.

AUTHOR CONTRIBUTIONS

XP and JC designed the project. JB, SG, and XZ performed the experiments and analyzed the data. JB, DF, YoZ, YS, and ZJ interpreted the data and wrote the manuscript. YuZ and ZJ revised the manuscript. All authors contributed to the article and approved the submitted version.

FUNDING

This study was supported by the National Natural Science Foundation of China (Grant Nos. 81601470, 81901808, and 82001955), Key Scientific and Technological Project of Henan Province (Grant No. 212102310235), and the Key Research Projects of Henan Higher Education (Grant No. 19B310004).

SUPPLEMENTARY MATERIAL

The Supplementary Material for this article can be found online at: https://www.frontiersin.org/articles/10.3389/fbioe.2021.721617/full#supplementary-material

REFERENCES

Al-Ahmady, Z., and Kostarelos, K. (2016). Chemical components for the design of temperature-responsive vesicles as cancer therapeutics. *Chem. Rev.* 116, 3883–3918. doi: 10.1021/acs.chemrev.5b00578

Chu, C., Yu, J., En, R., Ou, S., Zhang, Y., Wu, Y., et al. (2020). Multimodal photoacoustic imaging-guided regression of corneal neovascularization: a non-invasive and safe strategy. *Adv. Sci.* 7:2000346. doi: 10.1002/advs.202000346

Cotin, G., Perton, F., Blanco-Andujar, C., Pichon, B., Mertz, D., and Begin-Colin, S. (2019). *Design of Anisotropic Iron-Oxide-Based Nanoparticles for Magnetic Hyperthermia*. Amsterdam: Elsevier.

Das, R., Rinaldi-Montes, N., Alonso, J., Amghouz, Z., Garaio, E., García, J. A., et al. (2016). Boosted hyperthermia therapy by combined AC magnetic and photothermal exposures in Ag/Fe3O4 nanoflowers. *ACS Appl. Mater. Interfaces* 8, 25162–25169. doi: 10.1021/acsami.6b09942

Das, R., Sypu, V. S., Paumo, H. K., Bhaumik, M., Maharaj, V., and Maity, A. (2019). Silver decorated magnetic nanocomposite (Fe3O4@PPy-MAA/Ag) as highly active catalyst towards reduction of 4-nitrophenol and toxic organic dyes. *Appl. Catalysis B Environ.* 244, 546–558. doi: 10.1016/j.apcatb.2018.11.073

Del Sol-Fernández, S., Portilla-Tundidor, Y., Gutiérrez, L., Odio, O. F., Reguera, E., Barber, D. F., et al. (2019). Flower-like Mn-doped magnetic nanoparticles functionalized with αvβ3-integrin-ligand to efficiently induce intracellular heat after alternating magnetic field exposition, triggering glioma cell death. *ACS Appl. Mater. Interfaces* 11, 26648–26663. doi: 10.1021/acsami.9b08318

Ebrahimisadr, S., Aslibeiki, B., and Asadi, R. (2018). Magnetic hyperthermia properties of iron oxide nanoparticles: the effect of concentration. *Physica C Superconductivity Appl.* 549, 119–121. doi: 10.1016/j.physc.2018.02.014

Espinosa, A., Di Corato, R., Kolosnjaj-Tabi, J., Flaud, P., Pellegrino, T., and Wilhelm, C. (2016). Duality of iron oxide nanoparticles in cancer therapy: amplification of heating efficiency by magnetic hyperthermia and photothermal bimodal treatment. *ACS Nano* 10, 2436–2446. doi: 10.1021/acsnano.5b07249

Hasegawa, T., Gu, Y., Takahashi, T., Hasegawa, T., and Yamamoto, I. (2001). "Enhancement of hyperthermic effects using rapid heating," in *Thermotherapy for Neoplasia, Inflammation, and Pain*, eds M. Kosaka, T. Sugahara, and K. L. Schmidt (Berlin: Springer), 439–444. doi: 10.1007/978-4-431-67035-3_49

He, X., Peng, C., Qiang, S., Xiong, L.-H., Zhao, Z., Wang, Z., et al. (2020). Less is more: Silver-AIE core@shell nanoparticles for multimodality cancer imaging and synergistic therapy. *Biomaterials* 238:119834. doi: 10.1016/j.biomaterials.2020.119834

Helderman, R., Löke, D., Kok, H. P., Oei, A., Tanis, P., Franken, N., et al. (2019). Variation in clinical application of hyperthermic intraperitoneal chemotherapy: a review. *Cancers* 11:78. doi: 10.3390/cancers11010078

Hill, T. K., Kelkar, S. S., Wojtynek, N. E., Souchek, J. J., Payne, W. M., Stumpf, K., et al. (2016). Near infrared fluorescent nanoparticles derived from hyaluronic

acid improve tumor contrast for image-guided surgery. *Theranostics* 6, 2314–2328. doi: 10.7150/thno.16514

Hiroto, S., Miyake, Y., and Shinokubo, H. (2017). Synthesis and functionalization of porphyrins through organometallic methodologies. *Chem. Rev.* 117, 2910–3043. doi: 10.1021/acs.chemrev.6b00427

Hong, G., Diao, S., Antaris, A. L., and Dai, H. (2015). Carbon nanomaterials for biological imaging and nanomedicinal therapy. *Chem. Rev.* 115, 10816–10906. doi: 10.1021/acs.chemrev.5b00008

Jia, C.-J., Sun, L.-D., Luo, F., Han, X.-D., Heyderman, L. J., Yan, Z.-G., et al. (2008). Large-scale synthesis of single-crystalline iron oxide magnetic nanorings. *J. Am. Chem. Soc.* 130, 16968–16977. doi: 10.1021/ja805152t

Liang, X., Li, Y., Li, X., Jing, L., Deng, Z., Yue, X., et al. (2015). PEGylated polypyrrole nanoparticles conjugating gadolinium chelates for dual-modal MRI/Photoacoustic imaging guided photothermal therapy of cancer. *Adv. Funct. Mater.* 25, 1451–1462. doi: 10.1002/adfm.201402338

Lin, Q., Yang, Y., Ma, Y., Zhang, R., Wang, J., Chen, X., et al. (2018). Bandgap engineered Polypyrrole–Polydopamine hybrid with intrinsic raman and photoacoustic imaging contrasts. *Nano Lett.* 18, 7485–7493. doi: 10.1021/acs.nanolett.8b02901

Liu, W., Liu, T., Zou, M., Yu, W., Li, C., He, Z., et al. (2018). Aggressive man-made red blood cells for hypoxia-resistant photodynamic therapy. *Adv. Mater.* 30:1802006. doi: 10.1002/adma.201802006

Lu, M., Cheng, X., Jiang, J., Li, T., Zhang, Z., Tsauo, C., et al. (2018). Dual-modal photoacoustic and magnetic resonance tracking of tendon stem cells with PLGA/iron oxide microparticles in vitro. *PLoS One* 13:e0193362. doi: 10.1371/journal.pone.0193362

Ma, N., Jiang, Y.-W., Zhang, X., Wu, H., Myers, J. N., Liu, P., et al. (2016). Enhanced radiosensitization of gold nanospikes via hyperthermia in combined cancer radiation and photothermal therapy. *ACS Appl. Mater. Interfaces* 8, 28480–28494. doi: 10.1021/acsami.6b10132

Ma, X., Tao, H., Yang, K., Feng, L., Cheng, L., Shi, X., et al. (2012). A functionalized graphene oxide-iron oxide nanocomposite for magnetically targeted drug delivery, photothermal therapy, and magnetic resonance imaging. *Nano Res.* 5, 199–212. doi: 10.1007/s12274-012-0200-y

Ma, X., Wang, Y., Liu, X.-L., Ma, H., Li, G., Li, Y., et al. (2019). Fe3O4–Pd Janus nanoparticles with amplified dual-mode hyperthermia and enhanced ROS generation for breast cancer treatment. *Nanoscale Horiz.* 4, 1450–1459. doi: 10.1039/c9nh00233b

Peng, W., Zhu, S., Wang, W., Zhang, W., Gu, J., Hu, X., et al. (2012). 3D network magnetophotonic crystals fabricated on morpho butterfly wing templates. *Adv. Funct. Mater.* 22, 2072–2080. doi: 10.1002/adfm.201103032

Sharma, S. K., Shrivastava, N., Rossi, F., Tung, L. D., and Thanh, N. T. K. (2019). Nanoparticles-based magnetic and photo induced hyperthermia for cancer treatment. *Nano Today* 29:100795. doi: 10.1016/j.nantod.2019.100795

Shi, X., Zhang, Y., Tian, Y., Xu, S., En, R., Bai, S., et al. (2020). Multi-responsive bottlebrush-like unimolecules self-assembled nano-riceball for synergistic sono-chemotherapy. *Small Methods* 5:2000416. doi: 10.1002/smtd.202000416

Sun, H., Su, J., Meng, Q., Yin, Q., Chen, L., Gu, W., et al. (2017). Cancer cell membrane-coated gold nanocages with hyperthermia-triggered drug release and homotypic target inhibit growth and metastasis of breast cancer. *Adv. Funct. Mater.* 27:1604300. doi: 10.1002/adfm.201604300

Szasz, A., Szasz, O., Szasz, N., Baronzio, G., and Hager, E. (2006). "Physical background and technical realizations of hyperthermia," in *Hyperthermia in Cancer Treatment: a Primer*, eds G. F. Baronzio and E. D. Hager. Berlin: Springer, 27–59. doi: 10.1007/978-0-387-33441-7_3

Ting, P., Huang, C., and Li, M. (2014). "NIR-activated iron oxides as a new multi-functional contrast agent of photoacoustic imaging," in *Proceedings of the SPIE 8943, 89434E*, San Francisco

Tong, S., Quinto, C. A., Zhang, L., Mohindra, P., and Bao, G. (2017). Size-dependent heating of magnetic iron oxide nanoparticles. *ACS Nano* 11, 6808–6816. doi: 10.1021/acsnano.7b01762

van der Horst, A., Versteijne, E., Besselink, M. G. H., Daams, J. G., Bulle, E. B., Bijlsma, M. F., et al. (2018). The clinical benefit of Hyperthermia in pancreatic cancer: a systematic review. *Int. J. Hyperthermia* 34, 969–979. doi: 10.1080/02656736.2017.1401126

Wang, C., Xu, H., Liang, C., Liu, Y., Li, Z., Yang, G., et al. (2013). Iron Oxide @ polypyrrole nanoparticles as a multifunctional drug carrier for remotely controlled cancer therapy with synergistic antitumor effect. *ACS Nano* 7, 6782–6795. doi: 10.1021/nn4017179

Wang, D., Dong, H., Li, M., Cao, Y., Yang, F., Zhang, K., et al. (2018). Erythrocyte–cancer hybrid membrane camouflaged hollow copper sulfide nanoparticles for prolonged circulation life and homotypic-targeting Photothermal/Chemotherapy of melanoma. *ACS Nano* 12, 5241–5252. doi: 10.1021/acsnano.7b08355

Wang, X., Gu, H., and Yang, Z. (2005). The heating effect of magnetic fluids in an alternating magnetic field. *J. Magn. Magn. Mater.* 293, 334–340. doi: 10.1016/j.jmmm.2005.02.028

Wang, Z., Gai, S., Wang, C., Yang, G., Zhong, C., Dai, Y., et al. (2019). Self-assembled zinc phthalocyanine nanoparticles as excellent photothermal/photodynamic synergistic agent for antitumor treatment. *Chem. Eng. J.* 361, 117–128. doi: 10.1016/j.cej.2018.12.007

Yang, F., Skripka, A., Tabatabaei, M. S., Hong, S. H., Ren, F., Huang, Y., et al. (2019). Magnetic photoluminescent nanoplatform built from large-pore Mesoporous silica. *Chem. Mater.* 31, 3201–3210. doi: 10.1021/acs.chemmater.9b00028

Yang, Y., Liu, J., Liang, C., Feng, L., Fu, T., Dong, Z., et al. (2016). Nanoscale metal–organic particles with rapid clearance for magnetic resonance imaging-guided photothermal therapy. *ACS Nano* 10, 2774–2781. doi: 10.1021/acsnano.5b07882

Yoon, H.-J., Lee, H.-S., Lim, J.-Y., and Park, J.-H. (2017). Liposomal indocyanine green for enhanced photothermal therapy. *ACS Appl. Mater. Interfaces* 9, 5683–5691. doi: 10.1021/acsami.6b16801

Zhang, Y., Wang, X., Chu, C., Zhou, Z., Chen, B., Pang, X., et al. (2020). Genetically engineered magnetic nanocages for cancer magneto-catalytic theranostics. *Nat. Commun.* 11:5421.

Zhou, J., Lu, Z., Zhu, X., Wang, X., Liao, Y., Ma, Z., et al. (2013). NIR photothermal therapy using polyaniline nanoparticles. *Biomaterials* 34, 9584–9592. doi: 10.1016/j.biomaterials.2013.08.075

Conflict of Interest: The authors declare that the research was conducted in the absence of any commercial or financial relationships that could be construed as a potential conflict of interest.

Publisher's Note: All claims expressed in this article are solely those of the authors and do not necessarily represent those of their affiliated organizations, or those of the publisher, the editors and the reviewers. Any product that may be evaluated in this article, or claim that may be made by its manufacturer, is not guaranteed or endorsed by the publisher.

Copyright © 2021 Bao, Guo, Zu, Zhuang, Fan, Zhang, Shi, Ji, Cheng and Pang. This is an open-access article distributed under the terms of the Creative Commons Attribution License (CC BY). The use, distribution or reproduction in other forums is permitted, provided the original author(s) and the copyright owner(s) are credited and that the original publication in this journal is cited, in accordance with accepted academic practice. No use, distribution or reproduction is permitted which does not comply with these terms.

frontiers in Bioengineering and Biotechnology

ORIGINAL RESEARCH
published: 19 August 2021
doi: 10.3389/fbioe.2021.707208

Biomimetic Black Phosphorus Nanosheet-Based Drug Delivery System for Targeted Photothermal-Chemo Cancer Therapy

Jinxiu Cao†, Junyang Qi†, Xun Lin, Yue Xiong, Fumei He, Wenbin Deng and Gan Liu**

School of Pharmaceutical Sciences (Shenzhen), Sun Yat-sen University, Guangzhou, China

OPEN ACCESS

Edited by:
Jianxun Ding,
Changchun Institute of Applied Chemistry (CAS), China

Reviewed by:
Saji Uthaman,
Iowa State University, United States
Dezhong Zhou,
Xi'an Jiaotong University, China
Guoqing Pan,
Jiangsu University, China
Yan Ma,
Hefei University of Technology, China

***Correspondence:**
Gan Liu
liugan5@mail.sysu.edu.cn
Wenbin Deng
dengwb5@mail.sysu.edu.cn

†These authors have contributed equally to this work and share first authorship

Specialty section:
This article was submitted to Biomaterials, a section of the journal Frontiers in Bioengineering and Biotechnology

Received: *09 May 2021*
Accepted: *07 July 2021*
Published: *19 August 2021*

Citation:
Cao J, Qi J, Lin X, Xiong Y, He F, Deng W and Liu G (2021) Biomimetic Black Phosphorus Nanosheet-Based Drug Delivery System for Targeted Photothermal-Chemo Cancer Therapy. Front. Bioeng. Biotechnol. 9:707208. doi: 10.3389/fbioe.2021.707208

As a biodegradable material, black phosphorus (BP) has been considered as an efficient agent for cancer photothermal therapy. However, its systemic delivery faces several hurdles, including rapid degradation in blood circulation, quick clearance by the immune system, and low delivery sufficiency to the tumor site. Here, we developed a biomimetic nanoparticle platform for *in vivo* tumor-targeted delivery of BP nanosheets (BP NSs). Through a biomimetic strategy, BP NSs were utilized to coordinate with the active species of oxaliplatin (1,2-diaminocyclohexane) platinum (II) (DACHPt) complexions, and the nanoparticles were further camouflaged with mesenchymal stem cell (MSC)–derived membranes. We showed that the incorporation of DACHPt not only decelerated the BP degradation but also enhanced the antitumor effect by combining the photothermal effect with chemotoxicity. Furthermore, MSC membrane coating increased the stability, dispersibility, and tumor-targeting properties of BP/DACHPt, significantly improving the antitumor efficacy. In short, our work not only provided a new strategy for *in vivo* tumor-targeted delivery of BP NSs but also obtained an enhanced antitumor effect by combining photothermal therapy with chemotherapy.

Keywords: biomimetic nanoparticles, black phosphorus, drug-self-stabilization, mesenchymal stem cell membrane, combined chemo-photothermal cancer therapy, targeted delivery

INTRODUCTION

Owing to its distinctive structure and excellent physicochemical properties, black phosphorus (BP), an emerging member of the two-dimensional nanomaterials family has attracted extensive research interests in cancer photothermal therapy (Luo G. et al., 2019; Gao, et al., 2020; Hu, et al., 2020; Qi, et al., 2020). Compared with existing nanomaterials such as graphene and MoS_2, BP offers a much larger surface-to-volume ratio due to its puckered lattice configuration (Ray 2016) and, therefore, has great potential as a superior drug nanocarrier, especially for cancer combination therapies (Luo M. et al., 2019; Wang, et al., 2020). Moreover, BP can easily degrade into nontoxic phosphorus compounds, such as phosphate, phosphonate, and other P_XO_Y (Huang, et al., 2016; Zhang, et al., 2018), showing good biodegradability and safety *in vivo* (Shao, et al., 2018; Xue, et al., 2020). However, *in vivo* adoption of BP faces several hurdles, such as rapid degradation in blood circulation (Abate, et al., 2018), quick clearance by the immune system (Qu, et al., 2017), and low delivery sufficiency to the tumor site (Mitchell, et al., 2021).

Although multiple modification strategies have been developed for BP nanosheets (BP NSs) to improve their therapeutic effect, developing a stable and targeted BP NS-based multifunctional drug

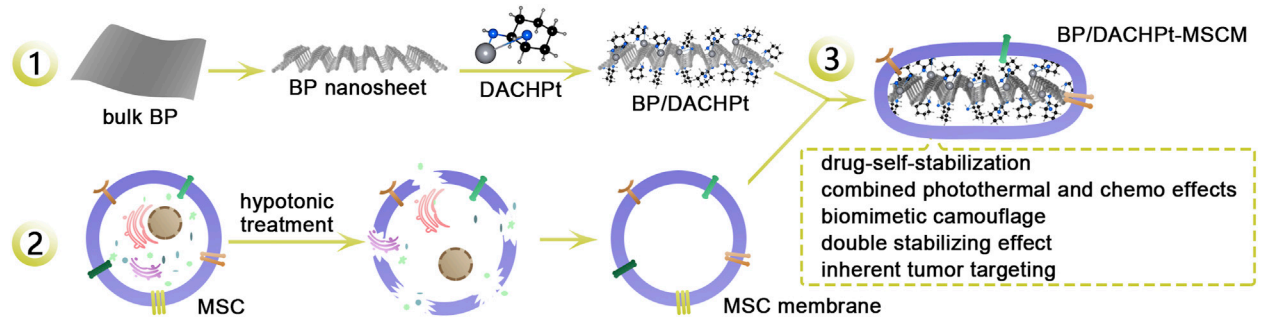

FIGURE 1 | Schematic showing the preparation of biomimetic BP/DACHPt-MSCM nanoparticles for targeted photothermal-chemo cancer therapy. 1: BP NSs prepared with bulk BP coordination with DACHPt to synthesize BP/DACHPt nanoparticles. 2: Extraction of MSC membranes by hypotonic treatment. 3: Ultrasonication mediated self-assembly of MSC membrane on the surface of BP/DACHPt nanoparticle to yield BP/DACHPt-MSCM nanoparticles.

delivery system is still a challenging task. For example, as a common method to modify BP NSs, the PEGylation can effectively reduce their aggregation and keep them stable (Ou, et al., 2018; Wan, et al., 2020), but this electrostatic adsorption of polyelectrolytes onto BP NSs is instable upon intravenous administration due to the desorption. On the other hand, although chemical modification is a valid way to enhance the ambient stability of BP NSs by passivating their surface P atoms, it cannot improve the dispersion of BP NSs, leading to quick clearance of BP by the immune system. For example, we previously used the active species of oxaliplatin (1,2-diaminocyclohexane) platinum (II) (DACHPt) complexion to coordinate with exposed lone pair electrons of BP NSs (Liu G. et al.,. 2019). This strategy markedly stabilized BP NSs and meanwhile introduced chemotherapeutics DACHPt with a high loading efficiency, which showed more significant synergistic antitumor effects. However, in a complex physiological environment, this is still not an ideal delivery system requiring BP protection from immune attack and targeted delivery at tumor sites.

Recently, owing to its ability of directly inheriting complex membrane surface molecules from the source cell, the cell membrane camouflaging of nanoparticles has emerged as an attractive strategy for imparting nanoparticles a wide range of functionalities, including a prolonged circulation time (Wang, et al., 2018), modulated immune responses (Gao, et al., 2015), and specific targeting (Zhang, et al., 2018). Among the popular cell candidates, mesenchymal stem cells (MSCs) have received close attention due to their unique migration ability and intrinsic tumor tropism, which are primarily mediated by diverse surface receptors on their membranes (Momin, et al., 2010). In addition, ease of isolation from *in vitro* culture (Kusuma, et al., 2015) and safety in allogeneic transplantation (Noriega, et al., 2017; Tsumanuma, et al., 2016) are also the advantages of MSCs to be the source of membrane. Based on these properties, MSC membrane-coated nanoparticles have obtained a very good effect in targeting tumor and prolonging circulation time (Gao, et al., 2016a; Gao, et al., 2016b).

Accordingly, we designed a biomimetic tumor-targeted BP nanoplatform, called as BP/DACHPt-MSCM (**Figure 1**). In this nanoplatform, the active species of platinum-based anticancer drugs (DACHPt) was utilized to coordinate with BP NSs to form BP/DACHPt nanoparticles, and it was further camouflaged with MSC-derived membrane. We demonstrated that BP/DACHPt-MSCM had good dispersibility, much enhanced stability, and efficient tumor targeting. *In vitro* cytotoxicity results showed the combination of chemotherapy and photothermal therapies resulted in an excellent ability to inhibit the tumor cell growth.

MATERIALS AND METHODS

Materials

The bulk BP was purchased from Nanjing MKNANO Technology Co., Ltd. (Nanjing, China). $DACHPtCl_2$, N-methyl-2-pyrrolidone (NMP), and fluorescein isothiocyanate (FITC) were purchased from Macklin Biochemical Co., Ltd. (Shanghai, China). $AgNO_3$ was purchased from J&K Chemical (Shanghai, China). Phycoerythrin (PE) anti-human CD73 antibody, PE anti-human CD90 antibody, PE anti-human CD105 antibody, FITC anti-human CD44 antibody, FITC anti-human CD45 antibody, and FITC anti-human HLA-DR antibody were purchased from Elabscience (Texas, United States). Tris-HCl was purchased from Beijing Solarbio Science & Technology Co., Ltd. (Beijing, China). Phenylmethylsulphonyl fluoride (PMSF) was purchased from Shanghai Aladdin Biochemical Technology Co., Ltd. (Shanghai, China). 1,1'-Dioctadecyl-3,3,3',3'-tetramethylindodicarbocyanine,4-chlorobenzenesulfonate salt (DiD) was purchased from Coolaber Technology Co., Ltd. (Beijing, China). Cell Counting Kit-8 (CCK-8) was purchased from ApexBio (Houston, United States). Dead Cell Apoptosis Kit (Annexin V-FITC) and propidium iodide (PI) were purchased from Jiangsu KeyGEN Biotechnology Co., Ltd. (Jiangsu, China). Fetal bovine serum (FBS), high-glucose Dulbecco's modified eagle medium (H-DMEM), alpha minimum essential medium (α-MEM), penicillin–streptomycin, trypsin-EDTA, and phosphate buffer saline solution (PBS) (pH 7.4) were obtained from Gibco Life Technologies (AG, Switzerland). All other commercially available chemicals and reagents were used as received.

Synthesis and Characterization of BP NSs

To prepare BP NSs, the bulk BP was ground to powder in a mortar, which was then dispersed in NMP (2 mg/ml) and sonicated for 4 h by a probe sonicator (on/off cycle: 5 s/5 s and 25% power) in an ice bath, followed by ultrasonication with a Kunshan KQ-600 GDV bath sonicator for 10 h (frequency: 40 kHz, power: 300 W) to perform liquid exfoliation. Next, the solution was centrifuged for 15 min at 7,000 rpm and the supernatant containing BP NSs was collected. Afterward, the supernatant was centrifuged for 15 min at 12,000 rpm and the precipitate was dispersed in NMP for further use.

Transmission electron microscopy (TEM) was performed using an FEI Tecnai G2 Spirit microscope operated at 120 kV. Atomic force microscopy (AFM) was carried out using the Bruker Dimension Fastscan microscope.

Synthesis and Characterization of BP/DACHPt

BP/DACHPt was prepared as per our method described previously (Liu M. et al., 2019). Briefly, $AgNO_3$ (10 mM) was mixed with $DACHPtCl_2$ in DI water (molar ratio: $AgNO_3$/$DACHPtCl_2$ = 2) in the dark at room temperature (RT) by stirring for 24 h. After the reaction, the mixture was centrifuged to remove generated AgCl precipitate. The supernatant was filtered through a micropore film and freeze-dried. Next, BP NSs dispersed in NMP (2 mg/ml) was mixed with DACHPt (mass ratio: DACHPt/BP NSs = 2) in the dark at RT for 12 h. Then, BP/DACHPt was harvested by centrifugation and washed with deionized (DI) water.

Raman spectroscopy was conducted using a Renishaw inVia Qontor confocal Raman microscope with the wavelength laser of 532 nm as the light source. X-ray photoelectron spectroscopy (XPS) was performed using the ESCALab250 spectrometer with Al Kα radiation.

Cell Culture

MSCs, derived from human placental chorionic villi, were cultured in α-MEM supplemented with 10% FBS. The A549 cells were incubated in H-DMEM containing 1% penicillin–streptomycin and 10% FBS. All cells were maintained at 37 C in a humid atmosphere with 5% CO2.

Characterization of MSCs

The bright-field image of MSCs was obtained by a NIKON ECLIPSE Ti2 fluorescence microscope. The immunophenotype of MSCs was estimated by Beckman Coulter CytoFLEX flow cytometry (FACS). Briefly, the cells were collected and stained for 30 min at 4 C with FITC-labeled or PE-labeled monoclonal antibodies against CD73, CD90, CD44, CD105, CD45, and HLA-DR.

Derivation and Characterization of MSC Membranes

To generate MSC membranes, MSCs were harvested by scraping and cleaned twice with PBS by mild centrifugation at 700 g for 5 min. The cells were resuspended in a hypotonic buffer containing 10 mM Tris-HCl and 1 mM PMSF. The cell suspension was homogenized in an ice bath with a Dounce homogenizer for 10 min. Next, the solution was centrifuged at 4,000 g for 10 min, and the collected supernatant was recentrifuged at 20,000 g for 30 min. The obtained MSC membranes were once washed with PBS and suspended in PBS with PMSF for further use. The TEM image was performed using a Hitachi HC-1 microscope operated at 80 kV.

Preparation and Characterization of MSC Membrane-Coated BP/DACHPt Nanoparticles (BP/DACHPt-MSCM)

To synthesize biomimetic BP/DACHPt-MSCM nanoparticles, BP/DACHPt dispersed in PBS was mixed with MSC membranes in a mass ratio of 4:1. Notably, the concentration of MSC membranes was represented by that of the membrane protein measured with the BCA assay. After vortexing for 1 min, the mixture was sonicated for 5 min by a bath sonicator (frequency: 40 kHz, power: 100 W) to yield BP/DACHPt-MSCM nanoparticles.

TEM images were performed using an FEI Tecnai G2 Spirit microscope operated at 120 kV. The zeta potentials were determined using the NanoBrook 90PlusPALS phase analysis light scattering. Confocal microscopy images were obtained by a NIKON ECLIPSE Ti2 fluorescence microscope.

Stability Study of BP Formulations

To test the changes in the hydration particle size and UV–vis absorption during the degradation process of three BP formulations (BP NSs, BP/DACHPt, and BP/DACHPt-MSCM), these BP formulations with the same internal BP concentration were pre-dispersed in air-exposed water for different periods. At each time point, the hydration particle size of the samples was measured by using the NanoBrook 90PlusPALS phase analysis light scattering and the UV–vis absorption from 400 to 850 nm of the samples was measured by using the PerkinElmer LAMBDA 365 UV/Vis spectrophotometer. To acquire the TEM images of BP/DACHPt-MSCM after NIR irradiation, the BP/DACHPt-MSCM dispersed in DI water was irradiated with 808 nm NIR laser (power density: 1.0 W/cm^2) for 10 min followed by dripping onto the surface of a copper grid and the TEM images were obtained using an FEI Tecnai G2 Spirit microscope operated at 120 kV. To test the photothermal stability of BP NSs, BP/DACHPt, and BP/DACHPt-MSCM, these three BP formulations having 30 μg/ml of BP were pre-dispersed in air-exposed water by stirring for different time durations (0, 12, 24, 48, and 72 h). At each time point, the photothermal conversion ability of the distinct BP formulations was tested by monitoring their temperature changes using a Fluke Ti450 infrared thermal imaging camera under Shanxi KaiSite KS-810F-8000 808-nm NIR laser irradiation (power: 1.0 W/cm^2, duration: 10 min). The dispersity of BP NSs, BP/DACHPt, and BP/DACHPt-MSCM nanoparticles that had the same amount of BP was evaluated in DI water, PBS, and DMEM containing 10% FBS for 12 h at RT.

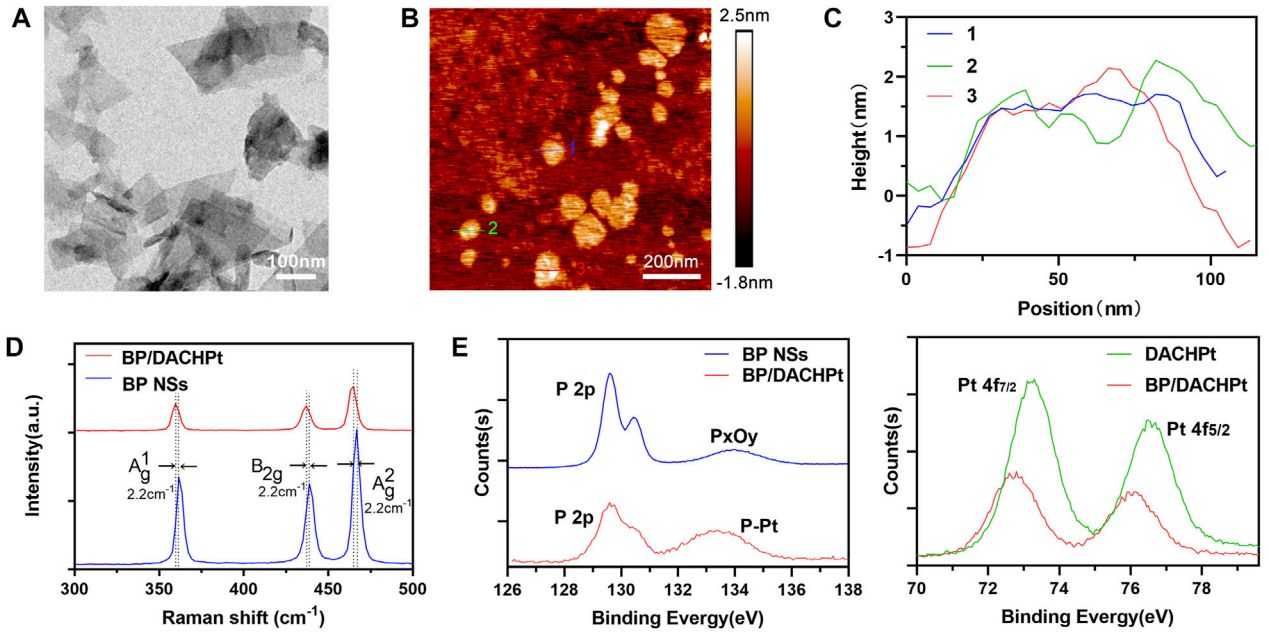

FIGURE 2 | Characterization of BP NSs and BP/DACHPt. **(A)** Transmission electron microscopy (TEM) image of BP NSs. **(B)** Atomic force microscopy (AFM) image of BP NSs. **(C)** Height profiles of the three randomly chosen lines in B. **(D)** Raman spectra of BP/DACHPt and BP NSs. **(E)** HR-XPS spectra of P 2p and Pt 4f.

Cellular Uptake of Nanoparticles

The cellular uptake of nanoparticles was estimated by FACS using CytExpert software. Briefly, the bare or MSC membranes coated FITC-conjugated BP/DACHPt nanoparticles were incubated with the A549 cells for 1, 2, 3, or 4 h, respectively. In addition, for green fluorescent dye FITC loading, 1 mg/ml of BP/DACHPt was mixed with FITC (10 μg/ml) in NMP and then stirred at room temperature for 12 h. The excess unloading was washed away via rinsing with NMP and DI water. Then, the cells were washed thrice before collection and the fluorescence was estimated by FACS.

CCK-8 Assay

The Cell Counting Kit-8 (CCK-8) assay was used to quantify the antitumor effect of freshly prepared BP-based formulations by estimating the viability of A549 cells. The A549 cells (1×10^4 cells/well) were seeded into 96-well plates and cultured overnight. Then, the cells were cultured with BP, BP/DACHPt, or BP/DACHPt-MSCM (having internal BP concentration of 0, 1.875, 3.750, 7.500, 15.000, and 30.000 μg/ml) for 24 h without any irradiation. On the other hand, the A549 cells in the NIR irradiation group were incubated with the concentration of 0, 1.875, 3.750, 7.500, 15.000, and 30.000 μg/ml for 4 h followed by irradiating with 808 nm NIR laser (power density: 1.0 W/cm^2) for 10 min. Then, the cells were cultured for another 8 h at 37 C. Last, the CCK-8 solution was added to each well and the absorbance was measured at 450 nm by a PerkinElmer VICTOR NivoTM Multimode Plate Reader.

To assess the effect of combined therapy of DACHPt and BP, we calculated the combination index (CI) (Chou 2010) with respect to experimental parameters (IC_{50}) by using the formula $CI = C_{DACHPt,50}/IC_{50,DACHPt} + C_{BP,50}/IC_{50,BP}$. $C_{DACHPt,50}$ and $C_{BP,50}$ refer to the drug concentration of DACHPt and BP when 50% cell inhibition was induced in the combined group. $IC_{50,\ DACHPt}$ and $IC_{50,\ BP}$ are the drug concentrations resulting in 50% inhibition with a single DACHPt or BP. The concentration of DACHPt and BP in BP/DACHPt was calculated after quantifying their concentration of Pt and P elements by Thermoscientific inductively coupled plasma mass spectrometry. CI allows quantitative determination of drug interactions, where CI < 1, = 1, and >1 indicate synergism, additive effect, and antagonism, respectively.

Calcein-AM/PI Assay

The antitumor effect of freshly prepared BP formulations at a certain concentration was tested by the Calcein-AM/PI assay. Briefly, the A549 cells (1×10^4 cells/well) were seeded into 96-well plates and cultured overnight. Subsequently, the cells were incubated with BP, BP/DACHPt, or BP/DACHPt-MSCM (an internal BP concentration of 7.5 μg/ml) for 24 h without irradiation. On the other hand, the A549 cells in NIR irradiation group were incubated with the internal BP concentration of 15.0 μg/ml for 4 h followed by 808 nm NIR irradiation (power density: 1.0 W/cm^2, duration: 10 min) and further incubated for another 8 h at 37 C. Afterward, to explore the antitumor effect, the cells were co-stained with Calcein-AM/PI by a NIKON ECLIPSE Ti2 fluorescence microscope.

RESULTS AND DISCUSSION

Synthesis and Characterization of BP NSs and BP/DACHPt

The morphology of BP NSs prepared by a liquid exfoliation method was observed by TEM and AFM. As shown in the TEM

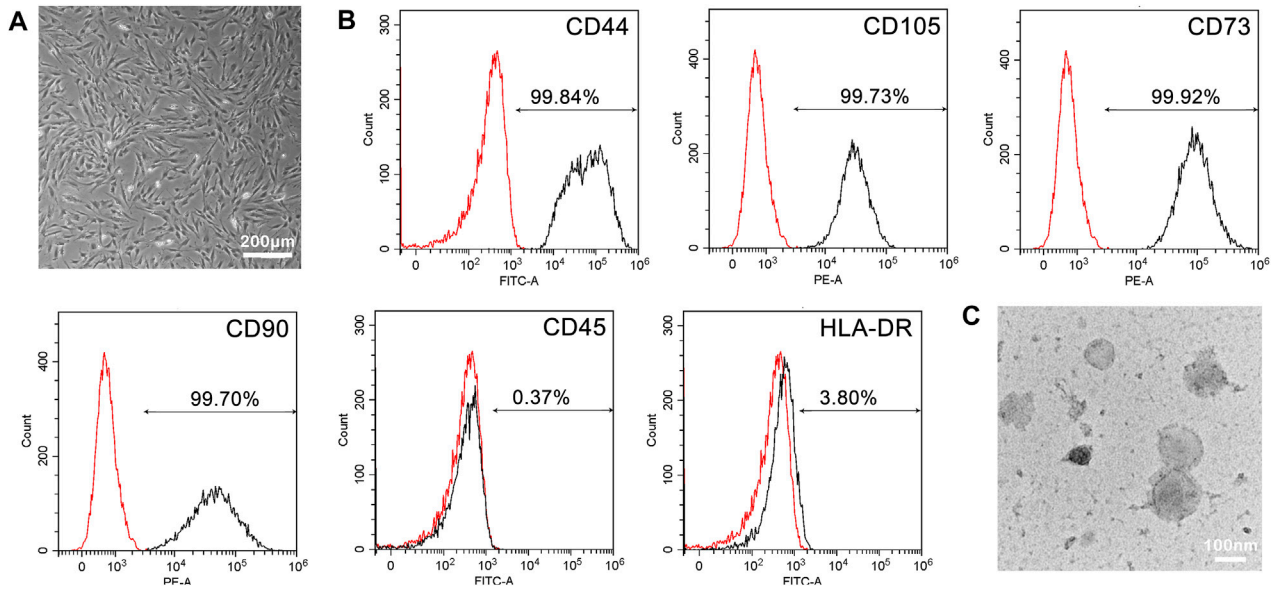

FIGURE 3 | Characterization of MSCs and MSC membranes. **(A)** Bright-field microscopy image of MSCs. **(B)** Expression of MSCs cell surface markers. Histograms showing the expression of CD44, CD105, CD73, CD90, CD45, and HLA-DR. The black and red represent the MSC marker antibody and the corresponding control antibody staining, respectively. **(C)** TEM image of MSC membranes.

image (**Figure 2A**), BP NSs exhibited a nanosheet structure with the size of 100–400 nm. The topographic morphology of BP NSs was shown in AFM image (**Figure 2B**). The heights of three randomly selected BP NSs were 0.8–2.3 nm (**Figure 2C**), indicating that BP NSs had few layers. Next, to confirm the interaction between DACHPt and BP NSs, the structural changes in BP/DACHPt and BP NSs were tested by Raman spectroscopy. There were three characteristic peaks in the spectrum of BP/DACHPt, relating to the one out-of-plane mode A_g^1 at 359.7 cm^{-1} and two in-plane modes of B_{2g} at 436.9 cm^{-1} and A_g^2 at 465.0 cm^{-1} (**Figure 2D**). In contrast to BP NSs, the A_g^1, B_{2g}, and A_g^2 peaks of BP/DACHPt showed a red-shift of about 2.2 cm^{-1}. This indicated that the Pt–P bonds suppressed the oscillation of surface P atoms decreasing the corresponding scattering energy. The Pt–P coordination was further evaluated by X-ray photoelectron spectroscopy (XPS), while BP NSs and DACHPt were used as controls. The P 2p core level spectrum of BP NSs showed three peaks, corresponding to P $2p_{3/2}$ at 129.58 eV and P $2p_{1/2}$ at 130.43 eV which were the characteristic peak of BP crystal (Ni, et al., 2018) (**Figure 2E**). In addition, the oxidized P species (P_xO_y) sub-bands is located at 133.98 eV, indicating the slight oxidation of BP NSs surface (Tao, et al., 2017). Accordingly, the P 2p peak at 129.60 eV of BP/DACHPt is attenuated whereas the peak at 133.8 eV is enhanced, which can be attributed to the formation of P^{5+} species via the coordination between DACHPt and P atoms on the surface of BP/DACHPt. Meanwhile, the Pt 4f signals of DACHPt and BP/DACHPt were also measured. DACHPt showed two characteristic Pt peaks ($4f_{7/2}$ and $4f_{5/2}$) at 73.30 and 76.50 eV (Fojtů et al., 2017). Owing to the electron donation from Pt (II) metal center to P, this set of doublets in BP/DACHPt was shifted toward lower binding energies of 72.80 and 75.95 eV. All these results verified the successful coordination between DACHPt and BP NSs.

Characterization of MSCs and MSC Membranes

Considering that the real MSCs is the prerequisite for the extracted membranes to carry out expected functions, we evaluated the morphology and cell surface markers of chorionic villi-derived MSCs (CV-MSCs). In **Figure 3A**, CV-MSCs showed the characteristic fibroblast-like morphology as of MSCs. Furthermore, FACS analysis of phenotypic markers revealed that the cultured MSCs strongly (> 99%) expressed CD44, CD105, CD73, and CD90, while lacked expression (< 5%) of CD45 and HLA-DR surface molecules (**Figure 3B**). These results were in agreement with the recommendations of the MSCs by the International Society for Cellular Therapy (ISCT) (Dominici, et al., 2006), validating the reliability of MSCs source. Subsequently, MSC membranes were extracted by hypotonic treatment, followed by density gradient centrifugation. As showed in **Figure 3C**, the membranes exhibited a vesicle structure.

Synthesis and Characterization of BP/DACHPt-MSCM

To prepare the MSC membrane-coated BP/DACHPt nanoparticles, MSC membranes assembly on the surface of BP/DACHPt nanoparticle was driven by ultrasonication. As showed in **Figure 4A**, MSC membranes completely covered the BP/DACHPt nanoparticles forming a distinctive lemma. The zeta potential characterization (**Figure 4B**) showed that the surface charge of BP/DACHPt nanoparticles (−19.7 mV)

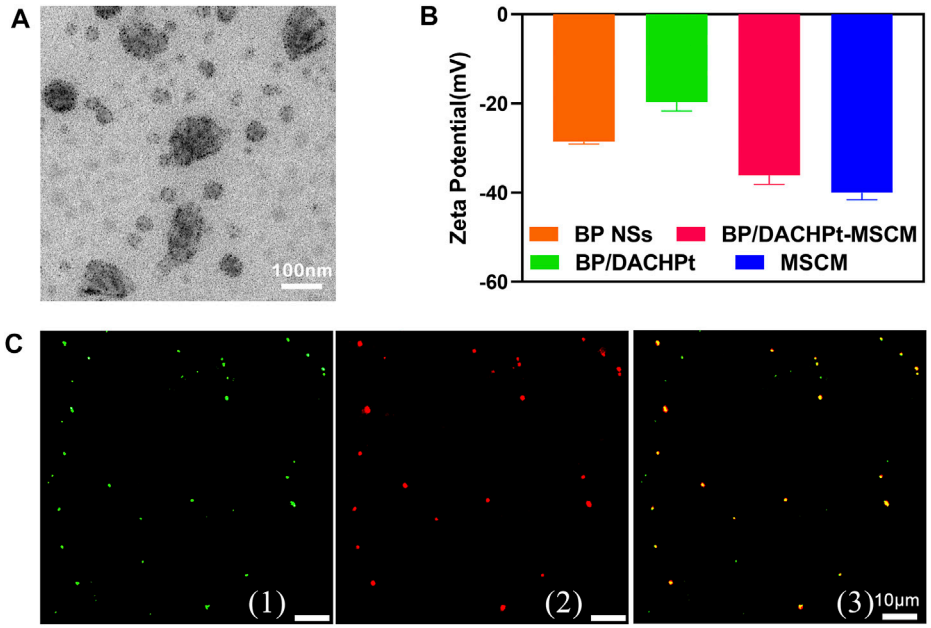

FIGURE 4 | Characterization of biomimetic nanoparticles. **(A)** TEM image of BP/DACHPt-MSCM nanoparticles. **(B)** Zeta potential of BP NSs, BP/DACHPt nanoparticles, MSC membranes, and BP/DACHPt-MSCM nanoparticles. Data present mean ± s.d. (n = 3). **(C)** Confocal images of fluorescence-labeled BP/DACHPt-MSCM nanoparticles: (1) the green, (2) red, and (3) yellow are the fluorescence of encapsulated BP/DACHPt nanoparticles, MSC membranes, and merged fluorescence, respectively.

was lower than that of BP (−28.5 mV), while after encapsulation, the surface charge of BP/DACHPt-MSCM (−36.1 mV) increased significantly, nearly equivalent to that of MSC membranes (−40.0 mV). This clearly demonstrated the successful development of BP/DACHPt-MSCM. For visual analysis of encapsulation, BP/DACHPt nanoparticles and MSC membranes were stained with FITC and DiD, respectively, and evaluated by fluorescence microscopy. As shown in **Figure 4C**, the green fluorescence of BP/DACHPt was almost completely overlapping with the red fluorescence of MSC membranes, indicating a high encapsulation rate of MSC membranes.

Stability Assessments of BP/DACHPt-MSCM Nanoparticles

To examine the effect of coordination with DACHPt and encapsulation with MSC membranes on the stability of BP NSs, the absorption of BP NSs, BP/DACHPt, and BP/DACHPt-MSCM solutions in air-exposed water were monitored at respective time points. At the beginning, the spectra of these three BP formulations exhibit broad absorption from UV to NIR regions (Pan, et al., 2020) (**Figures 5A–C**). With extended time, the absorbance of BP NSs in air-exposed water plummets (**Figure 5A**). After 24, 48, and 72 h of dispersion, the absorbance becomes only 80, 58 and 40%, respectively, of the original one (**Figure 5D**), suggesting that BP NSs rapidly and continuously degraded. In contrast, the absorbance of BP/DACHPt and BP/DACHPt-MSCM kept more stable (**Figures 5B,C**), with 62 and 78% retained even after 72 h, respectively (**Figure 5D**). Therefore, the stability in air-exposed water improved from BP, BP/DACHPt to BP/DACHPt-MSCM in sequence.

To study whether NIR irradiation destructed the surface morphology of BP/DACHPt-MSCM, the morphology of BP/DACHPt-MSCM after NIR irradiation was observed by TEM. As showed in **Figure 5E**, the membranes still completely covered the BP NSs, indicating that the BP/DACHPt-MSCM could be stable with no change in the surface morphology under NIR irradiation.

In consideration of the BP, formulations would undergo a period of blood circulation under physiological conditions before performing photothermal therapy, the temperature changes at respective time points of BP NSs, BP/DACHPt, and BP/DACHPt-MSCM solutions in air-exposed water after irradiating by 808 nm NIR laser (power density: 1.0 W/cm^2, duration: 10 min) were recorded using an IR thermal camera. In the case of BP NSs, the temperature rose by 21.5°C after irradiation in the beginning of the dispersion, but only by 7°C at 12 h time point. After 72°h, irradiation barely raised the temperature, indicating the attenuation of photothermal performance along with BP NSs degradation (**Figure 5F**). In contrast, BP/DACHPt was more photothermally stable, allowing a temperature increase by 18.2°C after 12°h, but the temperature rise decreased markedly in the next three days, only 3.7°C after 72 h (**Figure 5G**). Interestingly, encapsulation with MSC membranes significantly improved the photothermal stability of BP/DACHPt, enabling the temperature increase by 19°C after 72 h (**Figure 5H**). Collectively, this dual protection of

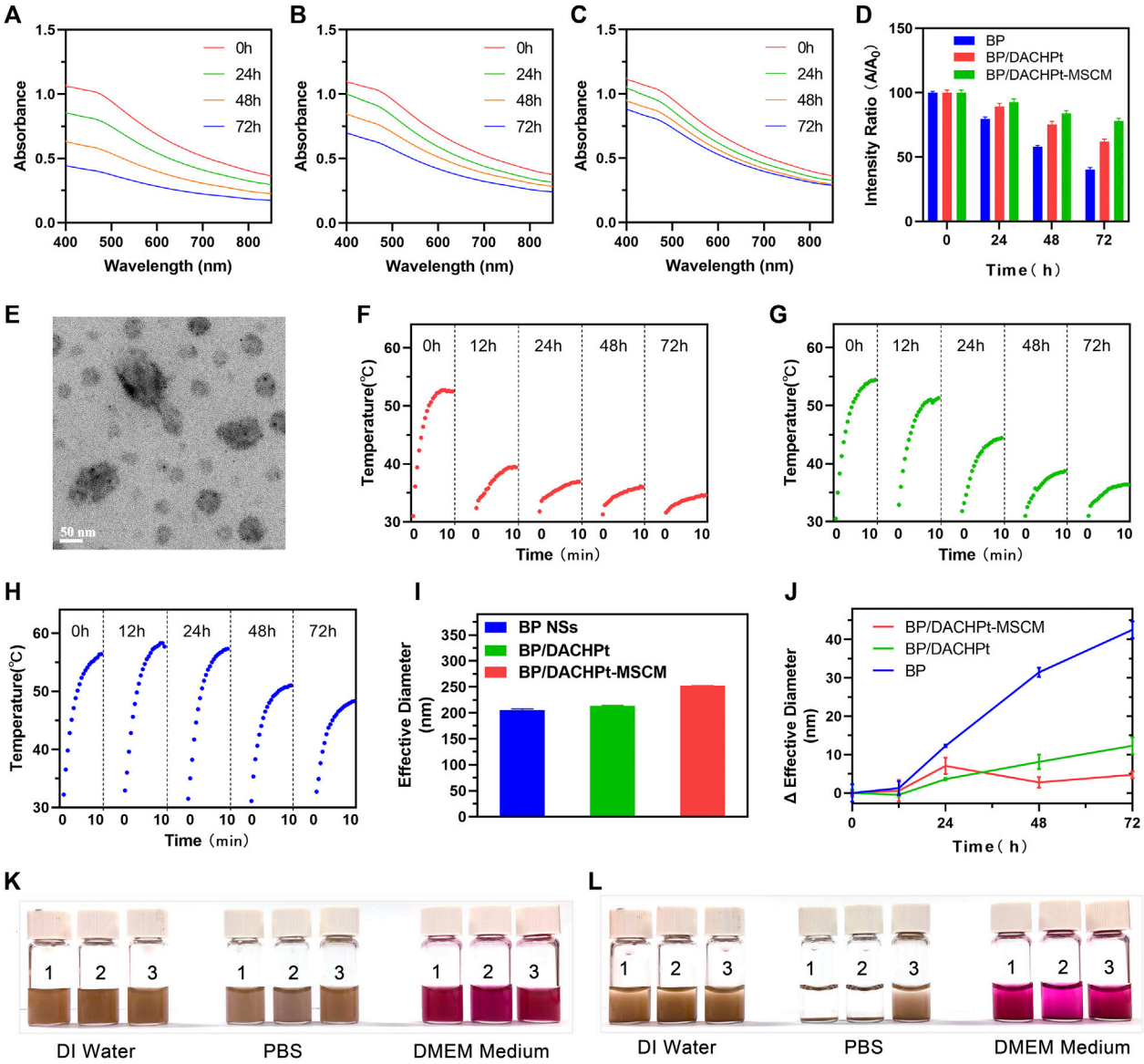

FIGURE 5 | Enhanced stability of BP/DACHPt-MSCM nanoparticles. Absorption spectra of **(A)** BP NSs, **(B)** BP/DACHPt, and **(C)** BP/DACHPt-MSCM dispersed in air-exposed water for 0, 24, 48, and 72 h. **(D)** Average variation of the absorption ratios at 420, 440, and 460 nm (A/A_0) of BP, BP/DACHPt, and BP/DACHPt-MSCM. **(E)** TEM image of BP/DACHPt-MSCM with NIR irradiation. Photothermal heating curves of **(F)** BP NSs, **(G)** BP/DACHPt, and **(H)** BP/DACHPt-MSCM dispersed in air-exposed water for 0, 12, 24, 48, and 72 h after laser irradiation for 10 min (808 nm, 1.0 W/cm^2). **(I)** Diameter of three BP formulations (BP NSs, BP/DACHPt, and BP/DACHPt-MSCM) dispersed in air-exposed water at the beginning (0 h). **(J)** Changes in Diameter of three BP formulations dispersed in air-exposed water for 12, 24, 48, and 72 h. Images showing the dispersibility of (1) BP NSs, (2) BP/DACHPt, and (3) BP/DACHPt-MSCM in DI water, PBS, and DMEM cell culture medium at **(K)** 0 and **(L)** 12 h.

DACHPt coordination and MSC membrane coating significantly improved the photothermal stability of BP NSs.

To test the changes in the hydration particle size of BP NSs, BP/DACHPt, and BP/DACHPt-MSCM for 72°h, the hydration particle size of these three BP formulations in air-exposed water were measured at each time point. As shown in **Figure 5I**, the particle diameter of freshly prepared three BP formulations were about 205.6, 213.8, and 252.3°nm, respectively. With an extended time, the diameter of BP NSs increased continuously (**Figure 5J**). After 72 h of dispersion, the diameter increased by about 42.5°nm, suggesting that BP NSs markedly and continuously aggregated in air-exposed water. In contrast, the diameter of BP/DACHPt kept more stable, with increasing by about just 12.3 nm after 72°h, manifesting that the BP NSs was much more likely to aggregate than the BP/DACHPt in air-exposed DI water. For BP/DACHPt-MSCM, the increase of particle diameter was maintained below 7 nm within 72°h, especially after 48 and 72°h, the changes of particle diameter were less than those of BP/DACHPt, showing good stability of BP/DACHPt-MSCM in air-exposed water.

Next, we examined the dispersity of BP/DACHPt-MSCM nanoparticles after standing in DI water, PBS, and DMEM

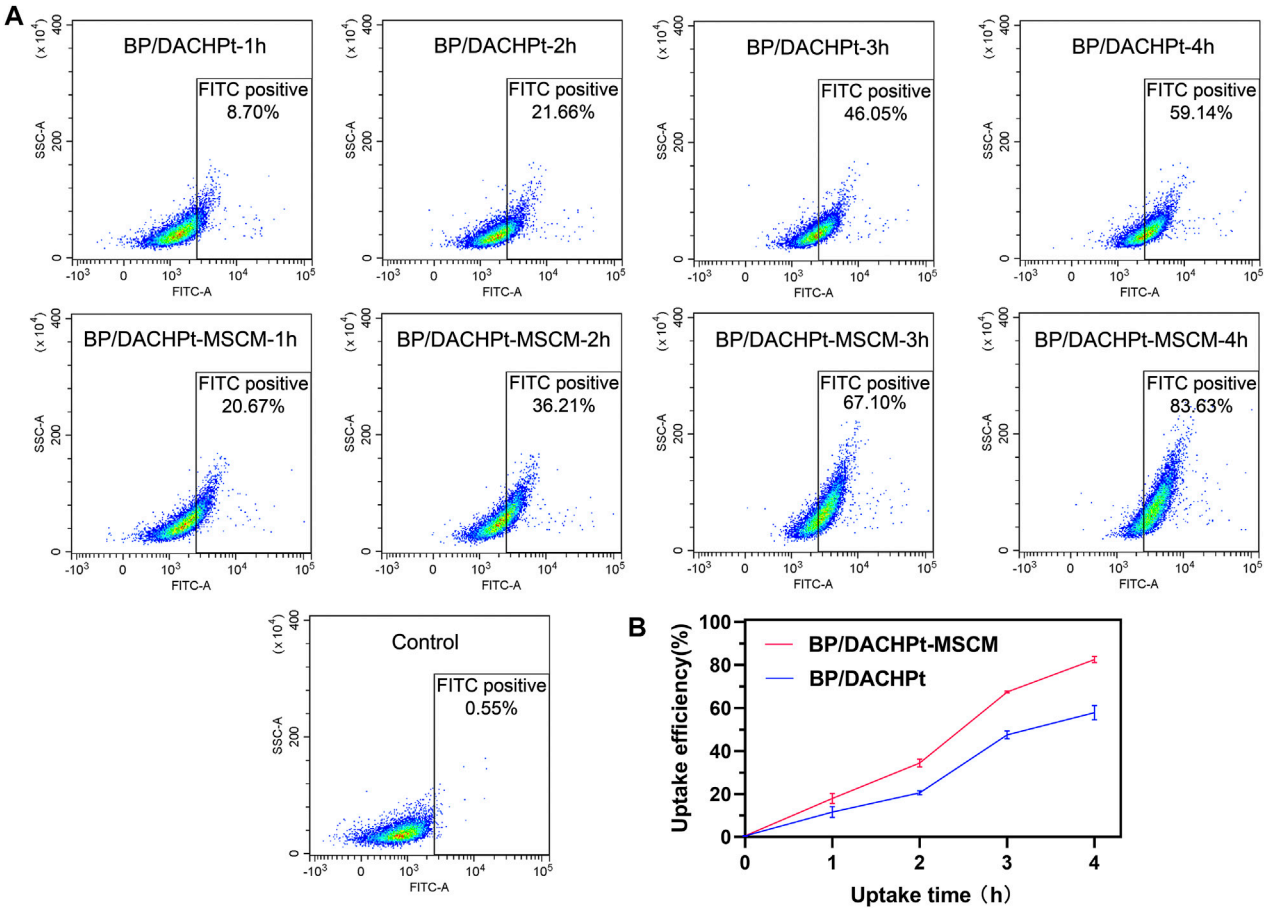

FIGURE 6 | Flow cytometry (FACS) analysis of BP/DACHPt-MSCM nanoparticles for tumor cell targeting. **(A)** Pseudocolor plot of A549 cells cultured with BP/DACHPt or BP/DACHPt-MSCM for 1, 2, 3, and 4 h. The A549 cells incubated with none nanoparticles were used as control. **(B)** Time-course of the mean fluorescence intensity of A549 cell after incubation with different nanoparticles. Data are presented as mean ± s.d. (n = 3).

containing 10% FBS. As shown in **Figures 5K,L**, the three BP formulations (BP NSs, BP/DACHPt, and BP/DACHPt-MSCM) were all well dispersed in DI water within 12 h. Whereas in the salt solution, BP NSs and BP/DACHPt quickly aggregated, BP/DACHPt-MSCM remained homogeneous, which could be attributed to the stabilizing effect of glycans on the hydrophilic surface of biological membranes (Wu, et al., 2021). Moreover, we can see that in a DMEM cell culture medium containing 10% FBS, BP/DACHPt was much more likely to aggregate than BP NSs and the aggregation of BP/DACHPt-MSCM was more slowly than that of BP/DACHPt, indicating that membrane coating can inhibit BP/DACHPt aggregation in a DMEM cell culture medium containing 10% FBS. All these results indicated that the MSC membrane coating could significantly improve the dispersity of BP nanomaterials, which is profitable for its subsequent bio-effects.

Cellular Uptake Assessments of BP/DACHPt-MSCM Nanoparticles

Next, we examined the camouflage effect of MSC membranes on the cellular uptake of BP/DACHPt. For this, the nanoparticles were incubated with the A549 cells, and internalization was analyzed by flow cytometry. As shown in **Figure 6A**, after incubation for the same time (1, 2, 3, or 4 h), the amount of internalized BP/DACHPt-MSCM was higher than that of BP/DACHPt. **Figure 6B** showed the time-course of the mean fluorescence intensity of A549 cell after incubation with different nanoparticles. We can see that, within 4°h, the difference between BP/DACHPt and BP/DACHPt-MSCM became more evident with an increase in incubation time. It indicated that surface coating with MSC membranes greatly increased the cellular uptake of BP/DACHPt. This suggested that MSC membrane-based camouflage significantly improved the transduction efficiency of BP/DACHPt nanoparticles for specific targeting to the cancer cells.

Photothermal-Chemo Antitumor Efficacy of BP/DACHPt-MSCM

To assess the antitumor efficacy of BP/DACHPt-MSCM, we tested the toxic effects of BP NSs, BP/DACHPt, and BP/DACHPt-MSCM (with increasing concentration) against the

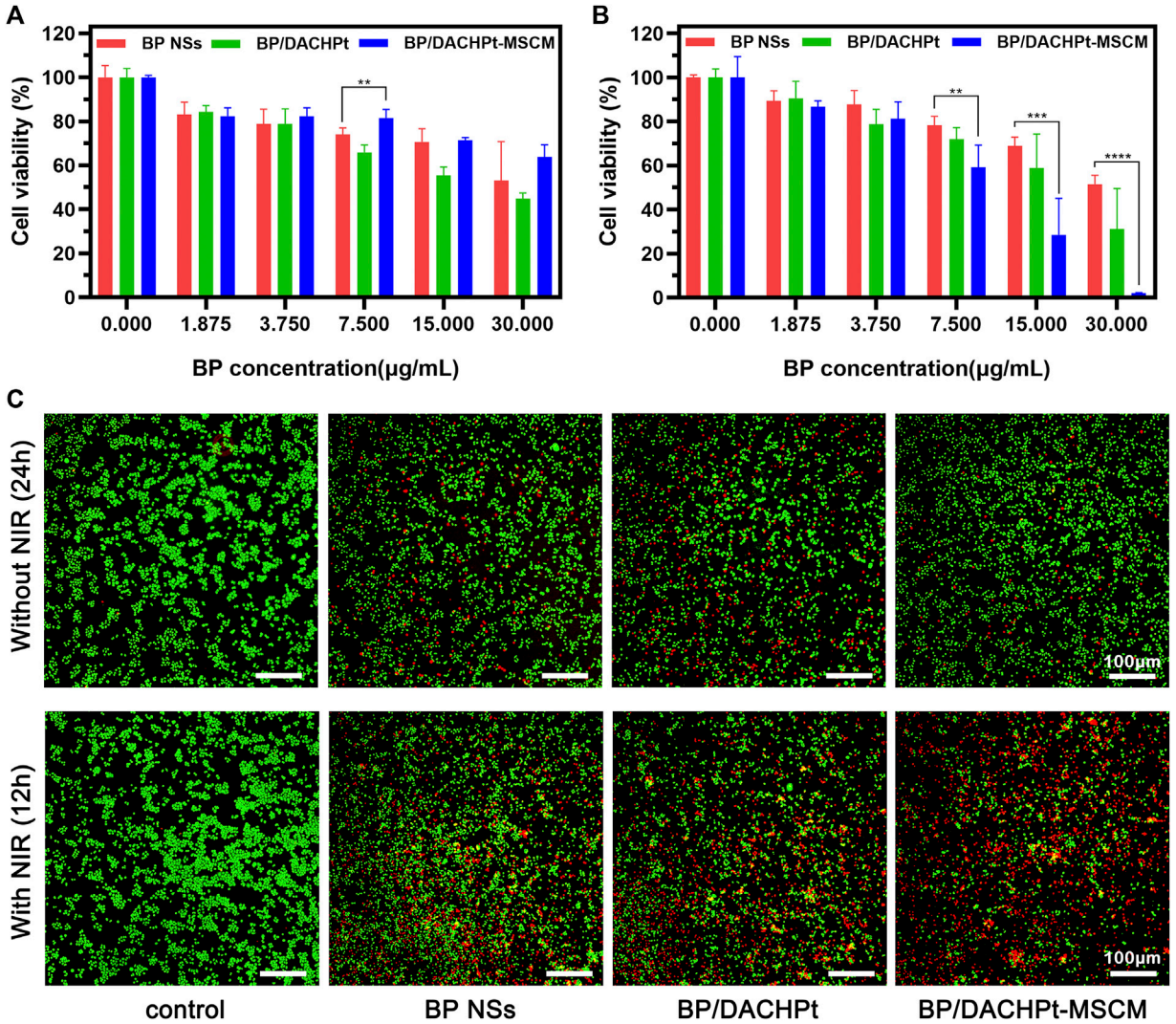

FIGURE 7 | Photothermal and chemotherapeutic effects of BP/DACHPt-MSCM. Cell viability of A549 cells cultured with BP NSs, BP/DACHPt, and BP/DACHPt-MSCM **(A)** for 24 h in the absence or **(B)** for 12 h in the presence of NIR irradiation. **(C)** Fluorescence images of the Calcein-AM (green, live cells) and PI (red, dead cells) co-stained A549 cells in the absence of NIR irradiation, following incubation with BP, BP/DACHPt, or BP/DACHPt-MSCM (having internal BP concentration of 7.5 μg/ml) for 24 h or in the presence of NIR irradiation, following incubation with these three BP formulations (having internal BP concentration of 15.0 μg/ml) for 12 h (data are presented as mean ± s.d., $^{**}p < 0.01$, $^{***}p < 0.001$, $^{****}p < 0.0001$).

A549 cells. The cytotoxicity of the nanoformulations without any NIR irradiation within 24 h was tested by the CCK-8 assay (**Figure 7A**). We found that the nanoparticles showed cytotoxicity against the A549 cells in a concentration manner. Notably, the cytotoxicity of BP/DACHPt was stronger than that of BP NSs at the concentration of 7.500, 15.000, and 30.000 μg/ml, demonstrating that the DACHPt was successfully released and exerted the chemotherapeutic effects. Interestingly, the cytotoxicity of BP/DACHPt-MSCM nanoparticles was the least among the three materials tested. This may be due to the coating of cell membranes interfered certain cytotoxic action of BP NSs.

In addition, the cytotoxicity of these nanoformulations under laser irradiation was studied (**Figure 7B**). As expected, after 12 h of culture, the cell inhibition rate of BP/DACHPt-MSCM was the highest (~98%; at 30.000 μg/ml), next was that of BP/DACHPt (~69%; at 30.000 μg/ml), and that of BP NSs was relatively weak (~48%; at 30.000 μg/ml). The results indicated that both coordination with DACHPt and encapsulation with MSC membranes could enhance the tumor cytotoxicity of BP formulations. To determine the drug interactions, we calculated the combination index (CI) with respect to experimental parameters (IC_{50}). The CI of BP/DACHPt was 0.91, which was less than 1, confirming that the BP and DACHPt in BP/DACHPt have synergistic effects. Doubtlessly, the CI of BP/DACHPt-MSCM was less than 0.91, which was 0.46, showing that encapsulation with MSC could enhance the synergistic effect of BP/DACHPt. Notably, the IC_{50} values calculated from the CCK-8 assay were shown in **Table 1**. The concentration of BP/DACHPt was represented by that of BP in it and the mass ratio of DACHPt to BP in BP/DACHPt was 4:5.

TABLE 1 | IC_{50} (μg/ml) values on A549 cells after incubation with different drugs for 12 h.

BP	DACHPt	BP/DACHPt	BP/DACHPt-MSCM
34.47	32.85	17.07	8.59

Subsequently, the cytotoxicity of all the three nanoformulations was also investigated by the Calcein-AM/PI assay (**Figure 7C**). The results were consistent with prior findings, that is, BP/DACHPt showed a better chemotherapeutic effect without NIR irradiation than BP NSs and its toxicity was lowered after coating with membranes. For the NIR irradiation group, the tumor cell killing effects of BP NSs, BP/DACHPt, and BP/DACHPt-MSCM enhanced in turn. Overall, these results showed the excellent tumor-targeted photothermal-chemo efficacy of BP/DACHPt-MSCM, which could be attributed to the combination of chemotherapy and photothermal therapies, as well as the improved stability and cellular uptake.

CONCLUSION

In summary, we reported a biocompatible and tumor-targeting drug delivery system of MSC membranes coated BP NSs carrying the active species of oxaliplatin DACHPt. This system significantly improved the stability of BP NSs in air-exposed water by the dual protection of DACHPt coordination and MSC membrane coating. Moreover, the surface coating with MSC membranes effectively improved the dispersibility, tumor-targeting property, and photothermal-chemo tumor suppression of BP/DACHPt. We suggested that this strategy of drug-self-stabilization and functionalization with MSC membranes significantly improved the BP NSs applications in targeted photothermal-chemo cancer therapy.

DATA AVAILABILITY STATEMENT

The raw data supporting the conclusions of this article will be made available by the authors, without undue reservation.

AUTHOR CONTRIBUTIONS

GL conceived the idea and experimental project. JC and JQ carried out the synthesis, characterization, data analysis, and interpretation. XL assisted with the synthesis and characterization. YX and FH assisted with data analysis and interpretation. JC wrote the first draft of the manuscript. WD, GL, and JQ contributed to manuscript revision, read, and approved the submitted version.

FUNDING

We are grateful for the financial support from the Shenzhen Science and Technology Program (Grant No. KQTD20190929173853397), Science, Technology & Innovation Commission of Shenzhen Municipality (Grant No. JCYJ20180307154606793), and National Natural Science Foundation of China (Grant Nos. 81772449 and 81971081).

REFERENCES

Abate, Y., Akinwande, D., Gamage, S., Wang, H., Snure, M., Poudel, N., et al. (2018). Recent Progress on Stability and Passivation of Black Phosphorus. *Adv. Mater.* 30, e1704749, 2018 . 1704749. doi:10.1002/adma.201704749

Chou, T.-C. (2010). Drug Combination Studies and Their Synergy Quantification Using the Chou-Talalay Method. *Cancer Res.* 70 (2), 440–446. doi:10.1158/0008-5472.Can-09-1947

Dominici, M., Le Blanc, K., Mueller, I., Slaper-Cortenbach, I., Marini, F. C., Krause, D. S., et al. (2006). Minimal Criteria for Defining Multipotent Mesenchymal Stromal Cells. The International Society for Cellular Therapy Position Statement. *Cytotherapy* 8 (4), 315–317. doi:10.1080/14653240600855905

Fojtů, M., Chia, X., Sofer, Z., Masařík, M., and Pumera, M. (2017). Black Phosphorus Nanoparticles Potentiate the Anticancer Effect of Oxaliplatin in Ovarian Cancer Cell Line. *Adv. Funct. Mater.* 27 (36), 1701955. doi:10.1002/adfm.201770211

Gao, C., Lin, Z., Jurado-Sánchez, B., Lin, X., Wu, Z., and He, Q. (2016a). Stem Cell Membrane-Coated Nanogels for Highly Efficient *In Vivo* Tumor Targeted Drug Delivery. *Small* 12 (30), 4056–4062. doi:10.1002/smll.201600624

Gao, C., Lin, Z., Wu, Z., Lin, X., and He, Q. (2016b). Stem-Cell-Membrane Camouflaging on Near-Infrared Photoactivated Upconversion Nanoarchitectures for *In Vivo* Remote-Controlled Photodynamic Therapy. *ACS Appl. Mater. Inter.* 8 (50), 34252–34260. doi:10.1021/acsami.6b12865

Gao, L., Teng, R., Zhang, S., Zhou, Y., Luo, M., Fang, Y., et al. (2020). Zinc Ion-Stabilized Aptamer-Targeted Black Phosphorus Nanosheets for Enhanced Photothermal/Chemotherapy against Prostate Cancer. *Front. Bioeng. Biotechnol.* 8, 769. doi:10.3389/fbioe.2020.00769

Gao, W., Fang, R. H., Thamphiwatana, S., Luk, B. T., Li, J., Angsantikul, P., et al. (2015). Modulating Antibacterial Immunity via Bacterial Membrane-Coated Nanoparticles. *Nano Lett.* 15 (2), 1403–1409. doi:10.1021/nl504798g

Hu, K., Xie, L., Zhang, Y., Hanyu, M., Yang, Z., Nagatsu, K., et al. (2020). Marriage of Black Phosphorus and Cu2+ as Effective Photothermal Agents for PET-Guided Combination Cancer Therapy. *Nat. Commun.* 11 (1), 2778. doi:10.1038/s41467-020-16513-0

Huang, Y., Qiao, J., He, K., Bliznakov, S., Sutter, E., Chen, X., et al. (2016). Interaction of Black Phosphorus with Oxygen and Water. *Chem. Mater.* 28 (22), 8330–8339. doi:10.1021/acs.chemmater.6b03592

Kusuma, G. D., Menicanin, D., Gronthos, S., Manuelpillai, U., Abumaree, M. H., Pertile, M. D., et al. (2015). Ectopic Bone Formation by Mesenchymal Stem Cells Derived from Human Term Placenta and the Decidua. *PLoS One* 10 (10), e0141246. doi:10.1371/journal.pone.0141246

Liu, G., Tsai, H.-I., Zeng, X., Qi, J., Luo, M., Wang, X., et al. (2019). Black Phosphorus Nanosheets-Based Stable Drug Delivery System via Drug-Self-Stabilization for Combined Photothermal and Chemo Cancer Therapy. *Chem. Eng. J.* 375, 121917. doi:10.1016/j.cej.2019.121917

Luo, M., Cheng, W., Zeng, X., Mei, L., Liu, G., and Deng, W. (2019). Folic Acid-Functionalized Black Phosphorus Quantum Dots for Targeted Chemo-Photothermal Combination Cancer Therapy. *Pharmaceutics* 11 (5), 242. doi:10.3390/pharmaceutics11050242

Luo, M., Zhou, Y., Gao, N., Cheng, W., Wang, X., Cao, J., et al. (2020). Mesenchymal Stem Cells Transporting Black Phosphorus-Based Biocompatible Nanospheres: Active Trojan Horse for Enhanced Photothermal Cancer Therapy. *Chem. Eng. J.* 385, 123942. doi:10.1016/j.cej.2019.123942

Mitchell, M. J., Billingsley, M. M., Haley, R. M., Wechsler, M. E., Peppas, N. A., and Langer, R. (2021). Engineering Precision Nanoparticles for Drug Delivery. *Nat. Rev. Drug Discov.* 20 (2), 101–124. doi:10.1038/s41573-020-0090-8

Momin, E. N., Vela, G., Zaidi, H. A., and Quiñones-Hinojosa, A. (2010). The Oncogenic Potential of Mesenchymal Stem Cells in the Treatment of Cancer: Directions for Future Research. *Curr. Immunol. Rev.* 6 (2), 137–148. doi:10.2174/157339510791111718

Ni, H., Liu, X., and Cheng, Q. (2018). A New Strategy for Air-Stable Black Phosphorus Reinforced PVA Nanocomposites. *J. Mater. Chem. A.* 6 (16), 7142–7147. doi:10.1039/C8TA00113H

Noriega, D. C., Ardura, F., Hernández-Ramajo, R., Martín-Ferrero, M. Á., Sánchez-Lite, I., Toribio, B., et al. (2017). Intervertebral Disc Repair by Allogeneic Mesenchymal Bone Marrow Cells. *Transplantation* 101 (8), 1945–1951. doi:10.1097/tp.0000000000001484

Ou, W., Byeon, J. H., Thapa, R. K., Ku, S. K., Yong, C. S., and Kim, J. O. (2018). Plug-and-Play Nanorization of Coarse Black Phosphorus for Targeted Chemo-Photoimmunotherapy of Colorectal Cancer. *ACS Nano* 12 (10), 10061–10074. doi:10.1021/acsnano.8b04658

Pan, W., Dai, C., Li, Y., Yin, Y., Gong, L., Machuki, J. O. a., et al. (2020). PRP-chitosan Thermoresponsive Hydrogel Combined with Black Phosphorus Nanosheets as Injectable Biomaterial for Biotherapy and Phototherapy Treatment of Rheumatoid Arthritis. *Biomaterials* 239, 119851. doi:10.1016/j.biomaterials.2020.119851

Qi, J., Xiong, Y., Cheng, K., Huang, Q., Cao, J., He, F., et al. (2021). Heterobifunctional PEG-Grafted Black Phosphorus Quantum Dots: "Three-In-One" Nano-Platforms for Mitochondria-Targeted Photothermal Cancer Therapy. *Asian J. Pharm. Sci.* 16, 222–235. doi:10.1016/j.ajps.2020.09.001

Qu, G., Liu, W., Zhao, Y., Gao, J., Xia, T., Shi, J., et al. (2017). Improved Biocompatibility of Black Phosphorus Nanosheets by Chemical Modification. *Angew. Chem. Int. Ed.* 56 (46), 14488–14493. doi:10.1002/anie.201706228

Ray, S. J. (2016). First-principles Study of MoS2, Phosphorene and Graphene Based Single Electron Transistor for Gas Sensing Applications. *Sensors Actuators B: Chem.* 222, 492–498. doi:10.1016/j.snb.2015.08.039

Shao, J., Ruan, C., Xie, H., Li, Z., Wang, H., Chu, P. K., et al. (2018). Black-Phosphorus-Incorporated Hydrogel as a Sprayable and Biodegradable Photothermal Platform for Postsurgical Treatment of Cancer. *Adv. Sci.* 5 (5), 1700848. doi:10.1002/advs.201700848

Tao, W., Zhu, X., Yu, X., Zeng, X., Xiao, Q., Zhang, X., et al. (2017). Black Phosphorus Nanosheets as a Robust Delivery Platform for Cancer Theranostics. *Adv. Mater.* 29 (1), 1603276. doi:10.1002/adma.201603276

Tsumanuma, Y., Iwata, T., Kinoshita, A., Washio, K., Yoshida, T., Yamada, A., et al. (2016). Allogeneic Transplantation of Periodontal Ligament-Derived Multipotent Mesenchymal Stromal Cell Sheets in Canine Critical-Size Supra-alveolar Periodontal Defect Model. *BioResearch Open Access* 5 (1), 22–36. doi:10.1089/biores.2015.0043

Wan, S., Zhang, B., Li, S., He, B., and Pu, Y. (2020). Combination of PEG-Decorated Black Phosphorus Nanosheets and Immunoadjuvant for Photoimmunotherapy of Melanoma. *J. Mater. Chem. B* 8 (14), 2805–2813. doi:10.1039/d0tb00434k

Wang, D., Dong, H., Li, M., Cao, Y., Yang, F., Zhang, K., et al. (2018). Erythrocyte-Cancer Hybrid Membrane Camouflaged Hollow Copper Sulfide Nanoparticles for Prolonged Circulation Life and Homotypic-Targeting Photothermal/Chemotherapy of Melanoma. *ACS Nano* 12 (6), 5241–5252. doi:10.1021/acsnano.7b08355

Wang, J., Zhang, H., Xiao, X., Liang, D., Liang, X., Mi, L., et al. (2020). Gold Nanobipyramid-Loaded Black Phosphorus Nanosheets for Plasmon-Enhanced Photodynamic and Photothermal Therapy of Deep-Seated Orthotopic Lung Tumors. *Acta Biomater.* 107, 260–271. doi:10.1016/j.actbio.2020.03.001

Wu, P., Zhang, B., Ocansey, D. K. W., Xu, W., and Qian, H. (2021). Extracellular Vesicles: A Bright star of Nanomedicine. *Biomaterials* 269, 120467. doi:10.1016/j.biomaterials.2020.120467

Xue, C., Sutrisno, L., Li, M., Zhu, W., Fei, Y., Liu, C., et al. (2021). Implantable Multifunctional Black Phosphorus Nanoformulation-Deposited Biodegradable Scaffold for Combinational Photothermal/Chemotherapy and Wound Healing. *Biomaterials* 269, 120623. doi:10.1016/j.biomaterials.2020.120623

Zhang, T., Wan, Y., Xie, H., Mu, Y., Du, P., Wang, D., et al. (2018). Degradation Chemistry and Stabilization of Exfoliated Few-Layer Black Phosphorus in Water. *J. Am. Chem. Soc.* 140 (24), 7561–7567. doi:10.1021/jacs.8b02156

Zhang, Y., Cai, K., Li, C., Guo, Q., Chen, Q., He, X., et al. (2018). Macrophage-Membrane-Coated Nanoparticles for Tumor-Targeted Chemotherapy. *Nano Lett.* 18 (3), 1908–1915. doi:10.1021/acs.nanolett.7b05263

Conflict of Interest: The authors declare that the research was conducted in the absence of any commercial or financial relationships that could be construed as a potential conflict of interest.

Publisher's Note: All claims expressed in this article are solely those of the authors and do not necessarily represent those of their affiliated organizations, or those of the publisher, the editors and the reviewers. Any product that may be evaluated in this article, or claim that may be made by its manufacturer, is not guaranteed or endorsed by the publisher.

Copyright © 2021 Cao, Qi, Lin, Xiong, He, Deng and Liu. This is an open-access article distributed under the terms of the Creative Commons Attribution License (CC BY). The use, distribution or reproduction in other forums is permitted, provided the original author(s) and the copyright owner(s) are credited and that the original publication in this journal is cited, in accordance with accepted academic practice. No use, distribution or reproduction is permitted which does not comply with these terms.

frontiers in Bioengineering and Biotechnology

ORIGINAL RESEARCH
published: 16 November 2021
doi: 10.3389/fbioe.2021.749910

A Bone-Targeting Enoxacin Delivery System to Eradicate Staphylococcus Aureus-Related Implantation Infections and Bone Loss

Cong Yao [1†], Meisong Zhu [1†], Xiuguo Han [2†], Qiang Xu [1], Min Dai [1], Tao Nie [1] and Xuqiang Liu [1]**

[1]Department of Orthopedics, The First Affiliated Hospital of Nanchang University, Artificial Joints Engineering and Technology Research Center of Jiangxi Province, Nanchang, China, [2]Department of Orthopaedics, Xinhua Hospital Affiliated to Shanghai Jiaotong University School of Medicine, Shanghai, China

OPEN ACCESS

Edited by:
Junqing Wang,
School of Pharmaceutical Sciences (Shenzhen) Sun Yat-sen University, China

Reviewed by:
Chun Xu,
The University of Queensland, Australia
Payam Zarrintaj,
University of Montana, United States
Shuilin Wu,
City University of Hong Kong, Hong Kong SAR, China

***Correspondence:**
Tao Nie
ncnietao@163.com
Xuqiang Liu
shliuxuqiang@163.com

†These authors have contributed equally to this work and share first authorship

Specialty section:
This article was submitted to Biomaterials, a section of the journal Frontiers in Bioengineering and Biotechnology

Received: 30 July 2021
Accepted: 27 October 2021
Published: 16 November 2021

Citation:
Yao C, Zhu M, Han X, Xu Q, Dai M, Nie T and Liu X (2021) A Bone-Targeting Enoxacin Delivery System to Eradicate Staphylococcus Aureus-Related Implantation Infections and Bone Loss. Front. Bioeng. Biotechnol. 9:749910. doi: 10.3389/fbioe.2021.749910

Post-operative infections in orthopaedic implants are severe complications that require urgent solutions. Although conventional antibiotics limit bacterial biofilm formation, they ignore the bone loss caused by osteoclast formation during post-operative orthopaedic implant-related infections. Fortunately, enoxacin exerts both antibacterial and osteoclast inhibitory effects, playing a role in limiting infection and preventing bone loss. However, enoxacin lacks specificity in bone tissue and low bioavailability-related adverse effects, which hinders translational practice. Here, we developed a nanosystem (Eno@MSN-D) based on enoxacin (Eno)-loaded mesoporous silica nanoparticles (MSN), decorated with the eight repeating sequences of aspartate (D-Asp8), and coated with polyethylene glycol The release results suggested that Eno@MSN-D exhibits a high sensitivity to acidic environment. Moreover, this Eno@MSN-D delivery nanosystem exhibited both antibacterial and anti-osteoclast properties *in vitro*. The cytotoxicity assay revealed no cytotoxicity at the low concentration (20 μg/ml) and Eno@MSN-D inhibited RANKL-induced osteoclast differentiation. Importantly, Eno@MSN-D allowed the targeted release of enoxacin in infected bone tissue. Bone morphometric analysis and histopathology assays demonstrated that Eno@MSN-D has antibacterial and antiosteoclastic effects *in vivo*, thereby preventing implant-related infections and bone loss. Overall, our study highlights the significance of novel biomaterials that offer new alternatives to treat and prevent orthopaedic Staphylococcus aureus-related implantation infections and bone loss.

Keywords: implant infection, enoxacin, aspartic acid octapeptide, mesoporous silica nanoparticles, bone-targeting

1 INTRODUCTION

Owing to the beneficial application of orthopaedic implants and improvement in treatments, patients affected by several orthopaedic diseases, including congenital malformations, acquired deformities, and osteoarthritis, as well as fractures can achieve satisfactory therapeutic effects. However, as a "double-edged sword", the widespread use of implants is associated with new medical complications, and post-operative implant-related infections are an issue that needs to be addressed. The incidence of infection in orthopaedic surgery is approximately 5%, with post-operative infection rates of closed fractures making up 3.6–8.1%. In contrast, the incidence of open fracture is as high as 21.2%

(Johnson et al., 2007). Antibiotics are still the primary treatment method for bone and joint infections; however, because of the limited penetration of antibiotics in bone tissues, sufficient blood concentrations cannot be achieved (Noukrati et al., 2016). Additionally, the lack of blood supply around the implant and the formation of bacterial biofilm (Lazzarini et al., 2004; Li et al., 2019), usually result in ineffective anti-infection treatments. This not only increases the duration of hospital stays and the total cost but also reduces the effectiveness of rehabilitation.

The pathogenesis of post-operative infections due to the presence of implants differs from that of general post-operative infections. The gap between the body tissue and the implant is a fibroinflammatory area where host immunity is suppressed, resistance is low, and bacteria can quickly colonise to form infections (Schierholz and Beuth, 2001). Besides, after bacterial invasion of the bone muscle system, due to intra-operative soft tissue injury and destruction of the blood supply, bacteria can colonise the proximities of the implants and form biofilms (Zhou et al., 2020). Bacterial biofilms limit antibiotic diffusion into the infected area, further reducing the concentration of antibiotics that can enter the infected area (Lynch and Abbanat, 2010; Buommino et al., 2014). Therefore, the efficient use of antibiotics is the key to limiting infections and inhibiting biofilm formation. Improving antibiotic treatment efficiency and increasing the concentration of drugs in bony tissues is particularly crucial for treating bone and joint infections. On the contrary, abnormal bone metabolism caused by bacterial erosion and bone destruction can activate a large number of osteoclasts, resulting in bone degradation and absorption (Dapunt et al., 2014; Oliveira et al., 2020). Simple anti-infection treatments of post-operative implant infections cannot eliminate the excessive osteoclast activation due to the inflammatory environment, which results in bone loss and bone destruction. The inhibition of osteoclast formation and bone resorption is an effective strategy to reduce bone loss and maintain long-term implant stability.

Enoxacin, a third-generation fluoroquinolone antibiotic, has a broad-spectrum and robust bactericidal effect. Additionally, enoxacin has an inhibitory effect on osteoclasts (Ostrov et al., 2009; Toro et al., 2012), and we previously reported that its mechanism is to occupy the ATP binding domain of the JNK protein, inhibit the phosphorylation of JNK, and activate the JNK/MAPKs signalling pathway (Liu et al., 2014). In terms of bacterial erosion of post-operative implant infections and the pathological state of a large number of osteoclasts activated in inflammatory environments, enoxacin exerts both antibacterial and anti-osteoclastic activities, making it an ideal drug candidate to prevent and treat post-operative implant-related infections. However, poor bioavailability due to its poor bone-targeting specificity and systemic toxicity (Nielsen and Low, 2020) limits enoxacin clinical applicability in treating orthopaedic implant-related post-operative infections.

In recent years, owing to their high specific surface area and large pore volume, mesoporous silica nanoparticles (MSNs) offer advantages that include excellent loading capability and biocompatibility, making them ideal candidates for drug delivery systems (Ravichandran et al., 2013; Zhou et al., 2015; Martínez-Carmona et al., 2018). Nevertheless, despite the promising applicability of MSNs for patients with post-operative infection related to orthopaedic endophytes, the lack of specific targeting to the infected bone tissue reduces the therapeutic effect of encapsulated antibiotics, simultaneously promoting drug resistance. Reportedly, eight repeating sequences of aspartate (D-Asp8) preferably bound to highly crystalline hydroxyapatite, and D-Asp8 could successfully bind to bone resorption surfaces to target osteoclasts (Liu et al., 2015). Based on these findings, to improve target specificity, we deployed MSNs as a carrier for the transport of enoxacin equipped with the bone-targeting D-Asp8 and coated with polyethylene glycol (PEG) to prevent premature release of enoxacin before reaching the target tissue. A bone-targeted delivery system containing enoxacin (Eno@MSN-D) was prepared for the targeted release of enoxacin in infected bone tissue. We hypothesised that Eno@MSN-D has antibacterial properties and can inhibit osteoclast activation, thereby preventing *Staphylococcus aureus*-related implantation infections and consequent bone loss.

2 MATERIALS AND METHODS

2.1 Materials

Hexadecyl trimethyl ammonium bromide (CTAB), tetraethyl orthosilicate (TEOS), silane-polyethylene glycol-carboxyl (Silane-PEG-COOH), MES buffer, aqueous ammonia, hydrochloric acid, ethanol, ethyl acetate, crystal violet solution, phosphate-buffered saline (PBS), 1-(3-dimethylaminopropyl)-3-ethyl carbodiimide hydrochloride (EDC), and N-hydroxy succinimide (NHS) were obtained from Sinopharm Chemical Reagent Co., China. Enoxacin was obtained from Sigma Aldrich, St. Louis, United States. Dialysis bags were obtained from UC Union Carbide, Danbury, United States. *Staphylococcus aureus* (ATCC25923), *S. epidermidis* (ATCC12228), and methicillin-resistant *S. aureus* (ATCC43300) were obtained from American Type Culture Collection, Manassas, VA, United States. Trypsin soy broth (TSB) and trypsin soybean agar plate was obtained from Shanghai Chengsheng Biotechnology Co., Ltd.

2.2 MSN Synthesis

MSN were synthesised as previously reported, with minor modifications (Lee et al., 2010). NaOH aqueous solution (2 M, 0.35 ml) was mixed with water (50 ml) containing CTAB (100 mg), and the solution was heated to 70°C while stirring. Thereafter, TEOS (0.5 ml) was introduced dropwise to the reaction mixture. After 3 min, ethyl acetate (0.5 ml) was added, and the mixture was stirred for 30 s, followed by an ageing procedure at 70°C for 2 h. The precipitate was collected by centrifugation and washed with ethanol. The collected products were extracted for 6 h using a solution of hydrochloric acid (HCl) in ethanol (10% v/v) at 78°C by refluxing to remove CTAB and obtain the MSNs.

For enoxacin loading, 50 mg of MSN was dispersed in 10 ml of methanol solution mixed with enoxacin (25 mg), and the mixture

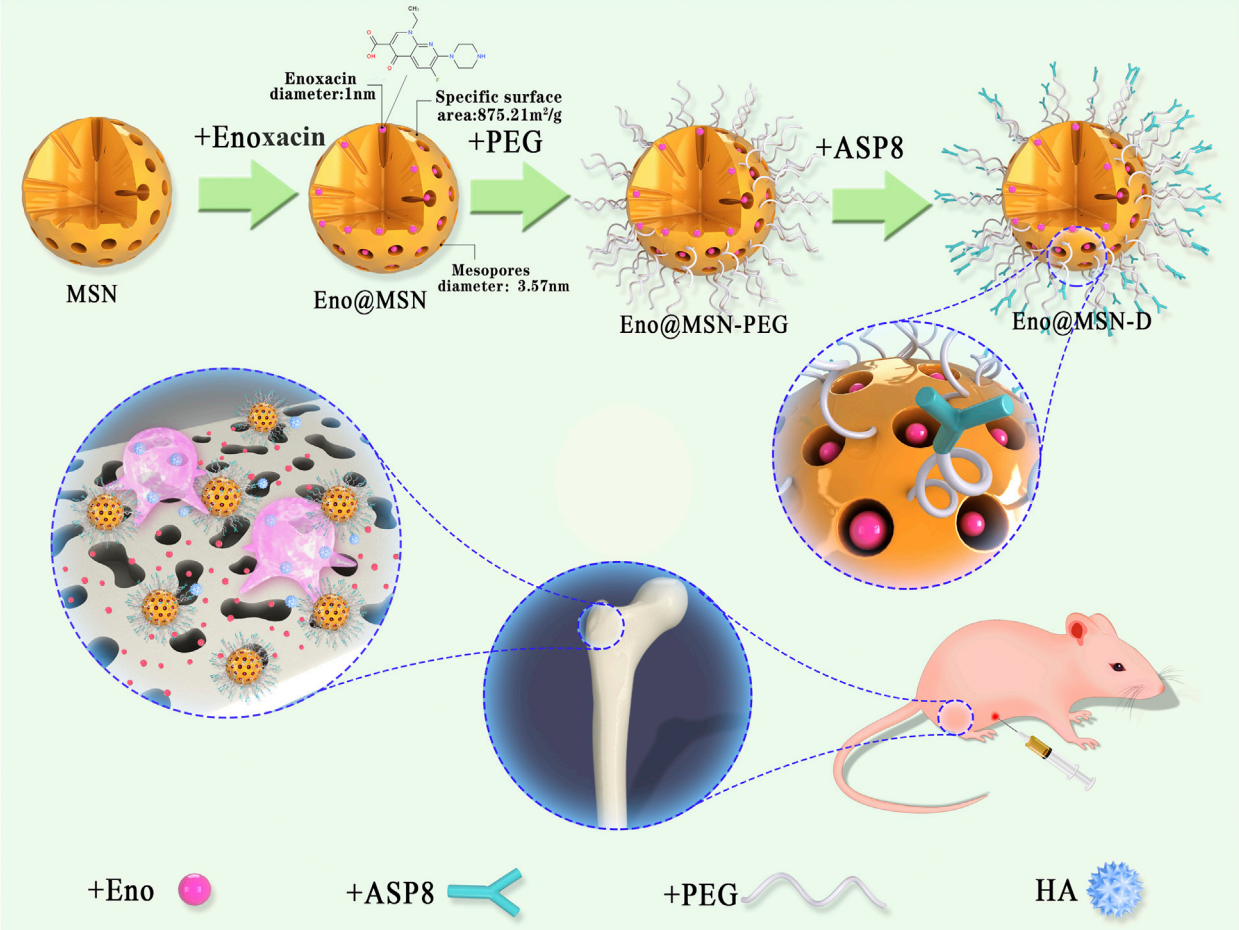

FIGURE 1 | Schematic diagram of the process flow for synthesising Eno@MSN-D nano slow-release particles based on mesoporous silica nanoparticles (MSN) and schematic diagram of the action mechanism of Eno@MSN-D nanoparticles.

was shaken at 25°C for 4 h. The dispersion solution was then centrifuged at 10,000 rpm to collect the enoxacin-loaded MSN (Eno@MSN). Next, the Eno@MSN were washed with distilled water to remove enoxacin from the exterior surface.

2.3 Synthesis of Eno@MSN-D

Briefly, Eno@MSN was dispersed in 10 ml of water mixed with Silane-PEG-COOH (28 mg). Thereafter, 0.2 ml of aqueous ammonia was added to the mixture and stirred for the next 4 h. The dispersion solution was centrifuged at 10,000 rpm, and the nanoparticles were washed with water three times to obtain Eno@MSN-PEG. Next, 30 mg of Eno@MSN-PEG was dispersed in 5 ml of MES buffer, and then 5.0 mg of EDC and 3.8 mg of NHS were added to the solution. After the excitation reaction for 30 min, 5 mg of D-Asp8 moiety was added to the mixture and reacted for 2 h. Subsequently, the solution was then centrifuged at 10,000 rpm and washed with water three times to obtain Eno@MSN-D. Finally, to monitor the cellular uptake of Eno@MSN-D by confocal microscopy, the red fluorescent dye Cy7 was loaded into Eno@MSN-D for tracking and labelling. **Figure 1** shows a scheme of Eno@MSN-D production and its mechanism.

2.4 Characterisation of Nanoparticles

Transmission electron microscopy (TEM) images were obtained using a JEM2010 instrument (JEOL, Tokyo, Japan) with an acceleration voltage of 200 kV to investigate the ultrastructure of drug-free MSN, Eno@MSN, and Eno@MSN-D. Nitrogen adsorption–desorption was measured using a Micromeritics porosity analyser (Micromeritics, Norcross, GA). For the surface area, pore volume was calculated using the Brunauer–Emmett–Teller (BET) and Barrett–Joyner–Halenda (BJH) analyses, respectively. Additionally, the hydrodynamic size of the samples was measured by dynamic light scattering (DLS) using a Zetasizer Nano instrument (Malvern Instruments, Malvern, United Kingdom) at 298 K. Finally, the thermal stability and composition of the solid samples were determined by TGA. TGA was performed on a TG 209F1 thermal analyser (NETZSCH, Germany) at a heating rate of 10°C/min in a continuously moving N_2 atmosphere.

2.5 Drug Release Determination

The *in vitro* pH-sensitive enoxacin release pattern of Eno@MSN-D was evaluated in PBS of pH 7.4 and 6.0. The Eno@MSN-D

dispersion solution was loaded in a dialysis bag with a molecular weight cut-off of 8 kDa. The dialysis bag was placed in 8 ml of PBS and gently shaken at 37°C. One millilitre of the supernatant was collected at predetermined time points, and the amount of drug released was determined using an ultraviolet spectrophotometer at λ = 232 nm. Thereafter, 1 ml of fresh PBS was added to the dialysate to maintain a constant volume.

2.6 Bacterial Strains and Cultures

Staphylococcus aureus (ATCC25923), *S. epidermidis* (ATCC12228), and methicillin-resistant *S. aureus* (ATCC43300) were stored on a TSA plate at −4°C. The three bacterial colonies in a centrifuge tube containing TSB were cultured overnight at 37 °C in an oscillator incubator at 150 rpm. Subsequently, the samples was centrifuged at 5000 rpm for 5 min. After centrifugation, the supernatant was discarded. TSB was used to adjust the bacterial precipitation concentration to 1×10^6 CFU/ml for storage.

2.7 Minimum Inhibitory Concentration

To each well of 96-well plates, 100 μL of ATCC25923, ATCC12228, and ATCC4330 bacteria cells (1×10^6 CFU/ml). Different concentration gradients of TSB (as the blank control), Eno, and Eno@MSN-D were separately added into the 96-well plates. After incubating at 37°C for 24 h, the bottom of the plate was closely inspected for biofilm formation. The lowest concentration without biofilm formation was determined as MIC, and it was determined using a microtiter plate dilution assay.

2.8 Determination of Bacterial Biofilm Formation

A crystal violet assay was performed using 96-well microtiter plates to observe the effects of Eno@MSN-D on bacterial biofilm formation. Briefly, ATCC25923 with a concentration of 1×10^6 CFU/ml were added to 96-well plates at 100 μl/well in triplicate and cultured for 24 h in 37°C. Then, each well of plates was added 100 μl of TSB (10 μg/ml), MSN (10 μg/ml), Eno (10 μg/ml), L-Eno@MSN (5 μg/ml), and H-Eno@MSN-D (10 μg/ml). Next, each well was washed with PBS three times and stained with 0.1% crystal violet solution. The plates were then incubated at room temperature for 15 min and then gently washed with PBS three times to remove excess crystal violet. Afterward, 33% of acetic acid was added to each well and placed in the incubator at 37°C for 30 min. The absorbance at 570 nm was determined using a microplate reader.

2.9 Morphological Characterisation of Bacteria and Bacterial Biofilm

The morphology of bacteria and the formation of biofilm were observed by SEM. ATCC25923 with a concentration of 1×10^6 CFU/ml was added to 12-well plates at 1ml/well in triplicate and cultured for 24 h in 37°C. TSB (10 μg/ml), MSN (10 μg/ml), and Eno@MSN-D (5, 10 μg/ml) were added to 12-well plates at the same time, and cover slides were placed in the wells. Next, the cover slides were gently washed with PBS and fixed in 2.5% glutaraldehyde for 12 h. After washing with PBS, the sample was dehydrated in an ethanol series (50, 60, 70, 80, 90, and 100%). After freeze-drying and gold-sputtering the samples, they were observed by SEM (SU8010, Hitachi, Japan).

2.10 Determination of Antibacterial Properties of Eno@MSN-D *in vitro*

The effects of Eno@MSN-D on bacterial biofilm were observed using a fluorescence inversion microscope system. ATCC25923 was diluted to 1×10^6 CFU/ml by TSB, and 1 ml was placed in a confocal Petri dish with a glass bottom and incubated at 37°C for 24 h. After incubation, the supernatant in the dish was removed, and the biofilm was treated with five or 10 μg/ml Eno@MSN-D. The control group included MSN (10 μg/ml) and TSB (10 μg/ml). The Petri dishes were then washed with aseptic PBS to remove loosely bound bacteria. Bacteria in the biofilm were stained with a LIVE/DEAD® BacLight bacterial viability kit (L7007) at room temperature for 15 min in the dark. The dye was cleaned with aseptic PBS, and the biofilm was observed using a fluorescence inversion microscope. Bacteria with intact and damaged cell membranes were obtained by scanning under excitation using the green (488 nm) and red (543 nm) channels, respectively.

2.11 Cell Viability and Osteoclast Differentiation Assay *in vitro*

To evaluate the cytotoxic effect of Eno@MSN-D, we used Cell Counting Kit-8 (CCK-8, Dojindo Molecular Technologies, Inc, Kumamoto, Japan) according to the manufacturer's instructions. Briefly, bone marrow macrophages (BMMs) were added to 96-well plates at 8×10^3 cells/well in triplicate and cultured for 24 h in alpha modification of Eagle's medium (α-MEM, Gaithersburg, MD, United States) containing 30 ng/ml macrophage colony-stimulating factor (M-CSF; PeproTech, Rocky Hill, NJ, United States), 10% foetal bovine serum (FBS; Gibco-BRL, Sydney, Australia), and 1% penicillin/streptomycin. BMMs were then separately treated with different concentrations of Eno@MSN-D (0, 0.625, 1.25, 2.5, 5, 10, 20, 40, 80 and 160 μg/ml) for 48 or 96 h. Next, 10 μL of CCK-8 substrate was added to each well, and the plate was incubated at 37°C under 5% CO_2 for 2 h. The absorbance of sample in each well was measured at 450 nm using an ELX800 microplate reader (Bio-Tek Instruments Inc, Winooski, VT, United States).

BMMs were seeded in a 96-well plate at a density of 8×10^3 cells/well in α-MEM with 30 ng/ml M-CSF, 50 ng/ml RANKL (PeproTech, Rocky Hill, NJ, United States), and different concentrations of Eno@MSN-D (0, 2.5, 5, and 10 μg/ml). BMMs were supplemented with fresh medium every 2 days until mature osteoclasts were observed. Next, the cells were fixed with 4% paraformaldehyde and stained for tartrate-resistant acid phosphatase (TRAP; Sigma Aldrich, St. Louis, MO, United States) activity. The mature osteoclasts (TRAP-positive cells with ≥3 nuclei) were counted, and their spread area was measured.

2.12 Bone-Targeting Properties of Eno@MSN-D *in vivo*

All animal experiments were performed in the Department of Animal Experimental Sciences of Nanchang University, under the approval and guidance of the Animal Experimental Ethics Committee of the First Affiliated Hospital of Nanchang University. Targeting of common fluorescent MSN and fluorescent Eno@MSN-D was evaluated in Sprague–Dawley (SD) rats [Shanghai SLAC Laboratory Animal Co., Ltd (China)]. Eighteen 3-month-old female SD rats were divided into 3 groups: MSN control group, PEG-MSN group, and Eno@MSN-D experimental group. Six animals from each group were injected in the tail vein with identical doses of nanoparticles (50 mg/kg body weight). After injection, all animals had free access to food and water. The animals were euthanised after 4 and 72 h, and the main organs (heart, liver, spleen, lung, kidney, femur) were removed. A fluorescence imaging system was used to detect the fluorescence of each organ in each group.

2.13 Antibacterial Properties of Eno@MSN-D *in vivo*

Fifty specific pathogen-free grade 12-week-old female SD rats were used and randomly assigned to five independent groups. All animals were housed in clean plastic cages with a 12-h light/dark cycle and free access to fresh food and water. The rats in the five groups were anaesthetised by intraperitoneal injection with 10% chloral hydrate (4 ml/kg). After complete anaesthesia, the rats were placed in the supine position to remove hair from the left knee joint, subsequently sterilised with 75% ethanol. A 15-mm incision was made along the lateral end of the femur. Subcutaneous tissues and muscles of the lateral femoral condyle were incised, the joint capsule and lateral collateral ligaments were retained, and the femoral condyle was fully exposed. The bone marrow cavity of the femur was opened and expanded to a depth of 10 mm using an electric drill of diameter 1 mm. Subsequently, a 1-mm diameter titanium rod of length 10 mm was implanted. The ATCC25923 concentration was set to 1×10^6 CFU/ml, and 100 μl was injected into the bone marrow cavity. The hole in the femoral condyle was blocked with bone wax. A saline solution was used for flushing the wound, and a medical suture was used to close the wound. Berberine was then applied to the wound. In the Sham group, only the condyle of the femur was exposed before closing the incision. After the operation, the rats were resuscitated under a fan heater and put back in their cages. The rats were maintained in separate cages; they had free access to food and water.

In the first week post-operation, body temperature and weight were examined every day. After 1 week of observation, each experimental group was injected with different drugs. Group A: Sham group (normal saline); group B: NS group (normal saline); group C: MSN group (50 mg/kg body weight); group D: Eno group (4 mg/kg body weight); group E: Eno@MSN-D group (50 mg/kg body weight). Body weight and temperature were recorded every 3 days. The drugs were then intraperitoneally injected every day for a total of 4 weeks, and the animals were euthanised 4 weeks later. The femurs were separated from the skin and subcutaneous tissue under aseptic conditions. Soft tissues were removed, and the femurs were prepared for further experiments. All titanium rods were collected and processed for analysis.

Bacteria attached to the titanium rods were detected by SEM, fluorescence staining, plate colony counting method, and plasma coagulase test. After removing the titanium rods from the distal femur and washing with PBS, 5 bars of each group were randomly placed in 2.5% glutaraldehyde for 12 h. Subsequently, they were dehydrated with an ethanol series (50, 60, 70, 80, 90, and 100%). The samples were freeze-dried and gold-sputtered. The surfaces of the titanium rods were then observed by SEM. Five titanium rods were randomly selected and fixed for 12 h as described above. After washing with PBS, the rods were stained using the LIVE/DEAD ®BacLight bacterial viability kit (L7007) at room temperature for 15 min in the dark. They were then observed using a fluorescence inversion microscope. Meanwhile, the titanium rods were washed, placed in 1 ml of TSB, and ultrasonicated for 15 min. After a 10-fold dilution, 100 μl of suspension was evenly applied to a TSA plate and incubated at 37°C for 24 h. The CFU was calculated according to the colony count on the plates. Additionally, a plasma coagulase test was performed to determine whether the bacteria attached to the titanium rods were *S. aureus*. A single colony was picked from the TSA plate and suspended in 50 μl of PBS before adding 50 μl of rabbit plasma. The occurrence of agglutination indicated that the bacteria were *S. aureus*.

2.14 Micro-Computed Tomography

After euthanasia, the femur from the rats of each group was removed completely under sterile conditions. After removing the titanium rod, the femur was fixed with 4% paraformaldehyde for 2 days and washed with tap water for 24 h. The peripheral bone structure of the distal femoral implant was then evaluated 28 days after the injection of different drugs. The femurs were examined using a desktop micro-X-ray computed tomography system (micro-CT Skyscan1076, Aartselaar, Belgium) equipped with a 40 kV X-ray source and 12.60 μm camera pixel size. A reconstructed dataset with an image pixel size of 18.26 μm was generated *via* scanning. To determine the axial trabecular volume of interest, we selected a region of interest (ROI) of length 5.578 mm closest to the growth plate edge. Micro-CT images of the transverse, sagittal, and coronal sections of the area around the implants were obtained. Object volume, total VOI volume, bone evolution fraction, bone mineral density, trabecular thickness, trabecular spacing, and trabecular number were used as indices to measure trabecular bone mass and its distribution.

2.15 Histology and Histomorphometry

Bone histology was used to assess infection and bone structure changes around the distal femoral implants. The femurs of the rats were fixed with 4% paraformaldehyde at room temperature for 24 h. Subsequently, 10% of ethylenediamine tetra-acetic acid was fully decalcified and dehydrated with an ethanol series (50, 75, 80, 85, 90, 95, and 100%). The bone tissue, after transparent treatment in xylene, was embedded in paraffin. The sample was longitudinally cut into 5-μm-thick slices. After slicing, histological sections were

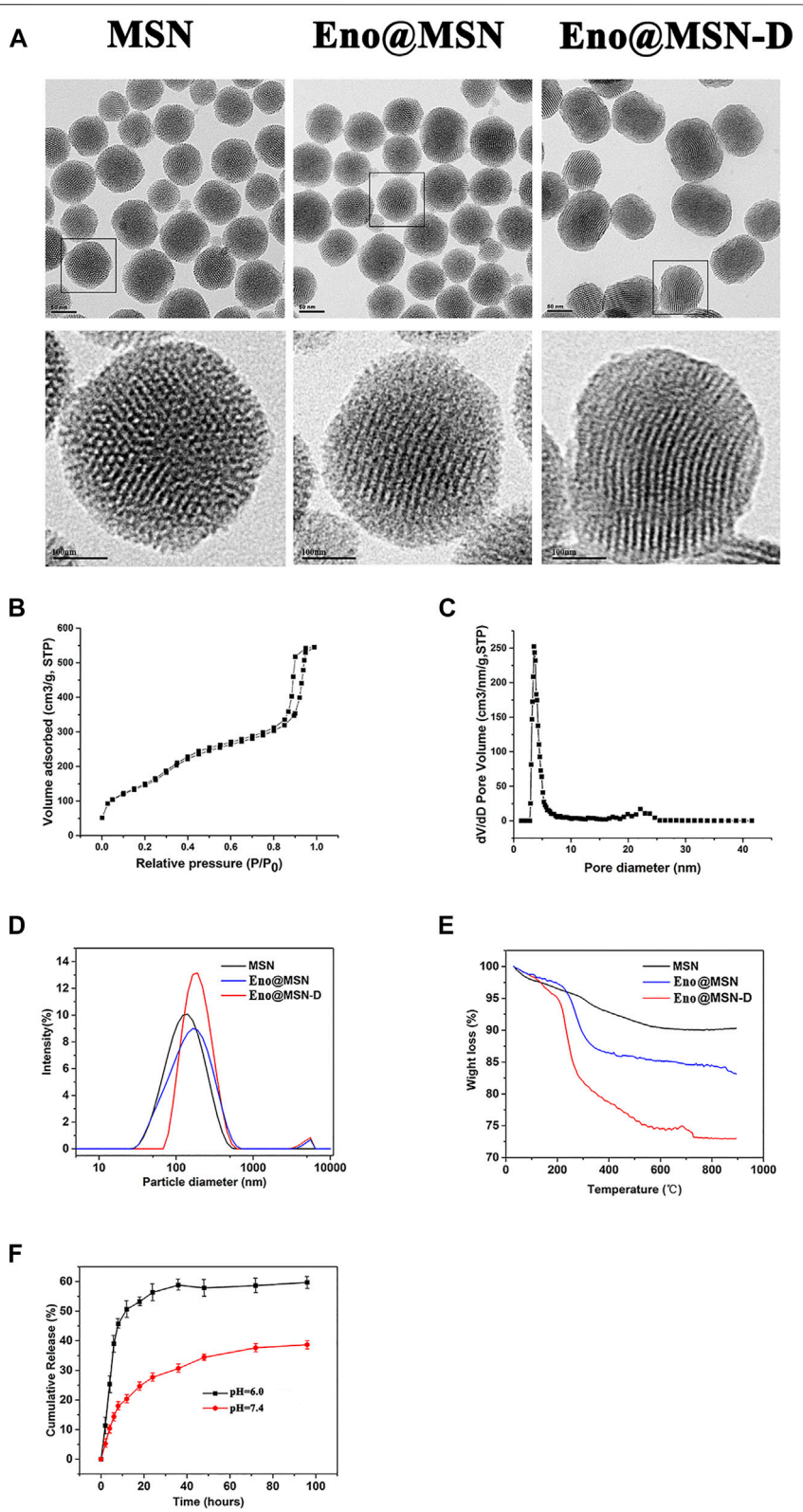

FIGURE 2 | (A) Typical TEM images of MSN, Eno@MSN, and Eno@MSN-D.**(B)**. N_2 adsorption–desorption isotherms curves of the MSN. **(C)** Pore size distribution curves of the MSN. **(D)** The dynamic light scattering (DLS) curves of MSN, Eno@MSN, and Eno@MSN-D. **(E)** TGA curves recorded for MSN, Eno@MSN, and Eno@MSN-D. **(F)** Accumulative release curve of Eno@MSN-D in different pH PBS (*p*H = 7.4, 6.0).

prepared for TRAP and HE staining. The slices were observed with an optical microscope. Representative images were randomly obtained from the distal femur implanted with titanium rods. We used Image-Pro Plus 6.0 software (Media Cybernetics, MD, United States) to process the images of TRAP-stained sections and counted the number and determined the area of osteoclasts per field of view.

2.16 Statistical Analysis

IBM SPSS statistics 22 (SPSS Inc, United States) software was used for statistical analysis. The results are presented as mean ± SD. Experiments were conducted at least three times. One-way analysis of variance (ANOVA) with Bonferroni post hoc test was performed to determine group differences. Results with $p < 0.05$ were considered statistically significant.

3 RESULTS

3.1 Synthesis and Characterisation of Eno@MSN-D

The protocol for the preparation of Eno@MSN-D is shown in **Figure 1**. Nanoparticle mesoporous carriers were prepared using TEOS as a hydrolytic inorganic precursor and the surfactant CTAB as the poreogenic substance. Bare MSN was obtained by solvent extraction of surfactant removal and was then loaded with Eno by free diffusion. Subsequently, PEG was grafted onto silica surfaces and channels to act as a gatekeeper for drug delivery. Finally, Eno@MSN-PEG was constructed by fusing D-Asp8 to Eno@MSN-D.

From the TEM images (**Figure 2A**), we observed the size and morphological characteristics of the three nanoparticle types. MSN maintained a highly ordered mesoporous structure, which disappeared after enoxacin loading and PEG/D-Asp8 immobilisation, and the average particle size of Eno@MSN-D was also larger than that of MSN and Eno@MSN, consistent with the results obtained in the DLS analysis (**Figure 2D**). The average particle diameters of the MSN, Eno@MSN, and Eno@MSN-D were 113.9, 133.8, and 179.7 nm, respectively. Particle dispersion index (PDI) and zeta potential of the nanoparticles were obtained using the DLS analysis. The PDI of MSN, Eno@MSN, and Eno@MSN-D was 0.213, 0.272, and 0.202 nm and their zeta potential was −24.3, −22.4, and −19.3 mV, respectively.

The nitrogen adsorption-desorption isotherm curves further exhibited the classical Langmuir type IV isotherm, indicating the presence of a mesoporous structure in the MSN (**Figure 2B**). Furthermore, the capillar condensation in the range of 0.8–1.0 refers to large pores and the adsorption branch was used for the analysis of the pore size distribution (**Figure 2C**). The specific surface area and pore size of MSN were 875.21 m^2/g and 3.57 nm, respectively. In addition, **Figure 2E** shows the TGA curves of all nanoparticles, indicating that during analysis, the weight loss of MSN, Gen@MSN, and Eno@MSN-D was close to 7.71, 15.62, and 25.65%, respectively.

3.2 Drug Loading and Release *in vitro*

It is well known that controlled release performance is an indispensable key step for the expected nanoparticles. Under simulated physiology conditions (*p*H = 7.4) and acid microenvironment caused by implant infection (*p*H = 6.0), two different pH buffer solutions were simulated for pH-response release pattern. In Eno@MSN-D, burst release was not found after stirring for 150 min at pH 7.4, and approximately 40% of enoxacin was released (**Figure 2F**). Interestingly, when the pH was decreased from 7.4 to 6.0, the cumulative release of enoxacin increased to approximately 60% (**Figure 2F**).

3.3 Antibacterial Properties of Eno@MSN-D *in vitro*

As previously reported, the MIC values of enoxacin against *S. aureus* (ATCC25923), *S. epidermidis* (ATCC12228), and methicillin-resistant *S. aureus* (ATCC43300) were 2, 2, and 4 μg/ml, respectively (Nie et al., 2017). Here, the MIC values of Eno@MSN-D against ATCC25923, ATCC12228, and ATCC43300 were 4, 4, and 8 μg/ml, respectively.

ATCC25923 was co-cultured with different concentrations of Eno@MSN-D for 24 h, and the absorbance of the samples was measured by crystal violet staining to determine the amount of biofilm formation (**Figure 3A**). We established a TSB blank control group, TSB and bacteria (TSB + B) co-culture-positive control group, 10 μg/ml MSN and bacteria (MSN + B) co-culture-positive control group, 10 μg/ml enoxacin and bacteria (Eno + B) co-culture-positive group, low concentration of 5 μg/ml Eno@MSN-D and bacteria (L-Eno@MSN-D + B) co-culture-positive group, and high concentration of 10 μg/ml Eno@MSN-D and bacteria (H-Eno@MSN-D + B) co-culture-positive group. Our results showed that biofilm formation was significantly lower in the TSB groups than in the TSB + B groups. However, both Eno@MSN-D + B and Eno + B groups showed decreased biofilm formation after treatment. Compared to the group treated with L-Eno@MSN-D + B, superior antibacterial effects were observed in the H-Eno@MSN-D + B group. Additionally, the H-Eno@MSN-D + B groups showed superior effects compared with the Eno + B groups, and there was a significant difference between them (**Figure 3C**). This result indicates that the bacterial biofilm formation decreased with Eno@MSN-D concentration, which further proved that the synthesised Eno@MSN-D has an antibacterial effect.

The antibacterial ability of Eno@MSN-D against each strain was verified using the bacterial colony counting plate method. ATCC25923, ATCC12228, and ATCC43300 were co-cultured with TSB, MSN, enoxacin, L-Eno@MSN-D, and H-Eno@MSN-D. **Figures 3B,D–F** shows no colony formation at the H-Eno@MSN-D concentration of 10 μg/ml. At the L-Eno@MSN-D concentration of 5 μg/ml, only a few colonies were formed in ATCC25923 and ATCC12228, while there were relatively more colonies in ATCC43300. However, many colonies were formed in the MSN and TSB groups. Interestingly, compared with the Eno group, the L-Eno@MSN-D group had a higher CFU number, whereas the H-Eno@MSN-D group showed fewer CFUs. In summary, Eno@MSN-D has apparent antibacterial effects.

We observed the surface of treated glass slides by SEM. **Figure 4A** shows that the integrity of some bacterial morphology was disrupted in the L-Eno@MSN-D and H-Eno@MSN-D groups. In the MSN and TSB groups, there was a significant adhesion between the bacteria,

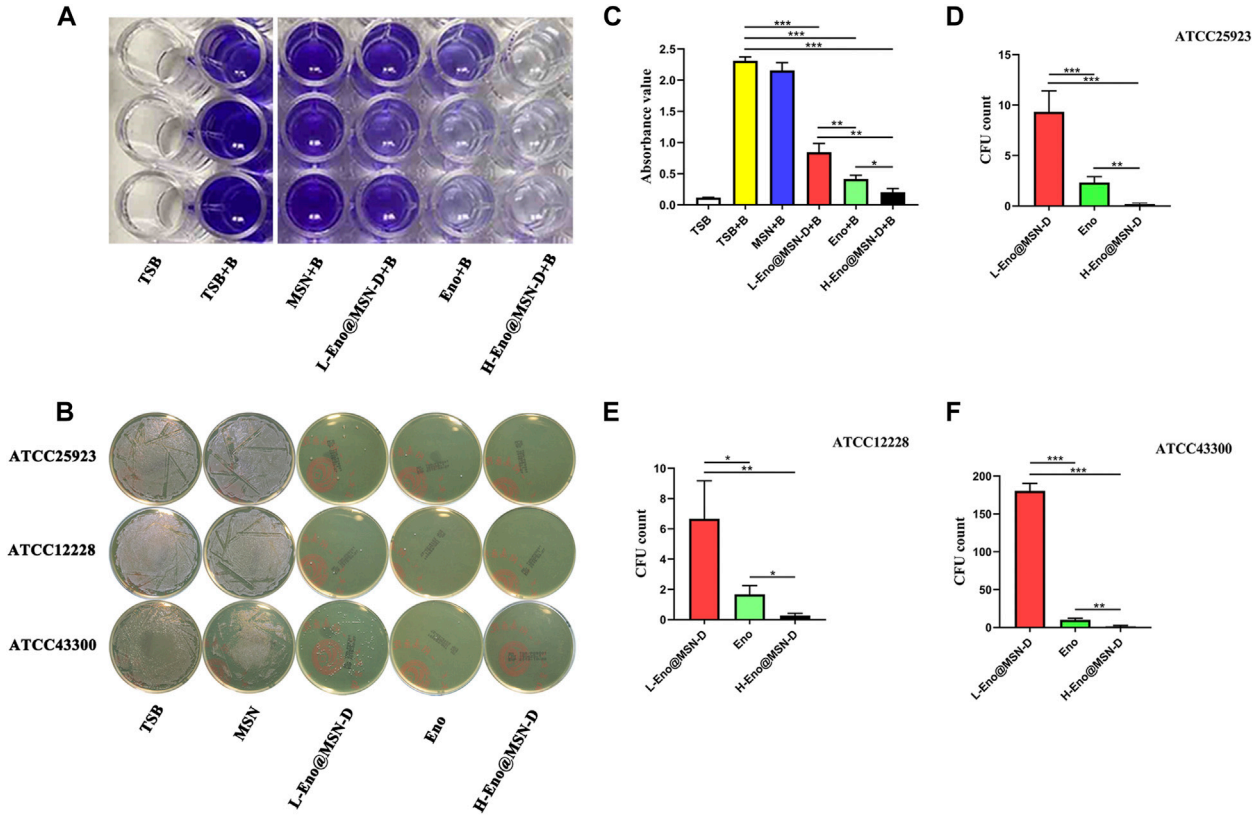

FIGURE 3 | (A–C) TSB (10 μg/ml), MSN (10 μg/ml), Eno (10 μg/ml), L-Eno@MSN (5 μg/ml), and H-Eno@MSN-D (10 μg/ml) were co-cultured with bacteria to form a biofilm, and then the absorbance was measured by crystal violet staining. **(B)** Determination of antimicrobial properties bacterial using the colony counting plate method. **(D)** The number of CFU after co-culture of ATCC25923 with Eno@MSN-D. (E) The number of CFU after co-culture of ATCC12228 with Eno@MSN-D. **(F)** The number of CFU after co-culture of ATCC43300 with Eno@MSN-D.

indicating the formation of biofilm. This observation also shows that Eno@MSN-D could destroy bacterial integrity, playing an antibacterial role, and inhibiting biofilm formation.

Live and dead bacteria were marked by green and red fluorescence, respectively. From the fluorescence inverted microscope pictures (**Figure 4B**), it is evident that with increasing drug concentrations of Eno@MSN-D, the red fluorescence of dead bacteria gradually increased. In contrast, the corresponding green fluorescence gradually weakened.

3.4 Eno@MSN-D Suppressed RANKL-Induced OC Differentiation Without Any Cytotoxicity *in vitro*

Previously, we reported that enoxacin could inhibit osteoclast differentiation and function (Liu et al., 2014). However, the effect of Eno@MSN-D on the formation of osteoclasts needs to be explored. BMMs were stimulated with M-CSF and RANKL in the presence of different concentrations of Eno@MSN-D (0, 2.5, 5, and 10 μg/ml). Interestingly, the BMMs treated with Eno@MSN-D showed a significant concentration-dependent decrease in mature osteoclast formation (**Figures 5C–E**). Additionally, to determine whether the inhibitory effects of Eno@MSN-D were due to cytotoxicity, we used the CCK-8 assay to measure the effect of Eno@MSN-D on BMM proliferation and survival. Our data show that cell viability will not be significantly affected when the concentration is lower than 20 μg/ml Eno@MSN-D (**Figures 5A,B**).

3.5 Bone-Targeting Properties of Eno@MSN-D *in vivo*

As shown in **Figure 6**, after 4 h, the fluorescence signals of the different organs in the MSN, PEG-MSN, and Eno@MSN-D group were almost the same. The MSN group was metabolised cleanly by the liver and kidney. However, the PEG-MSN and Eno@MSN-D group had a strong liver and kidney fluorescence signal after 72 h. More importantly, only the Eno@MSN-D group showed stronger fluorescence signals in the femur after 72 h, indicating that Eno@MSN-D also accumulated in the femur and exhibited bone-targeting abilities *in vivo*.

3.6 Antibacterial Properties of the Eno@MSN-D *in vivo*

We determined the animal model infection by measuring the rats' body temperature and weight over 5 weeks post-operation. As

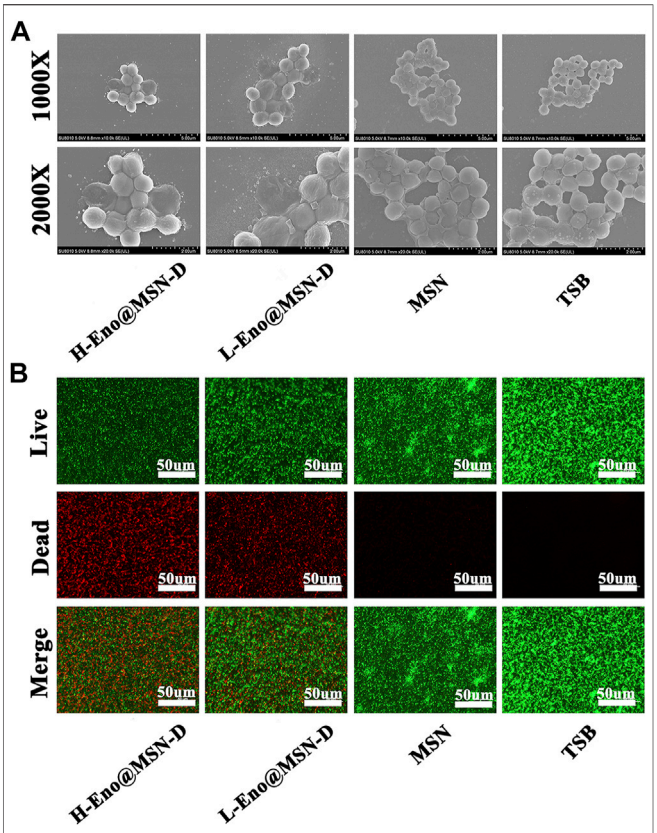

FIGURE 4 | (A) SEM images of TSB (10 μg/ml), MSN (10 μg/ml), Eno (10 μg/ml), L-Eno@MSN (5 μg/ml), H-Eno@MSN-D (10 μg/ml), and bacteria co-cultured on cover slides. **(B)** The fluorescence inverted microscope images of TSB (10 μg/ml), MSN (10 μg/ml), Eno (10 μg/ml), L-Eno@MSN (5 μg/ml), H-Eno@MSN-D (10 μg/ml), and bacteria co-cultured on confocal Petri dishes.

shown in **Figures 7A,B**, the bodyweight of rats in each group gradually decreased within 1 week after the operation, whereas the body temperature gradually increased. One week later, rat bodyweight began to increase in each group, whereas the Sham group body temperature began to decrease. However, the body temperature of the experimental groups did not change. There was no significant difference in body weight between the experimental and Sham groups ($p > 0.05$), but the body temperature differed between the experimental and Sham groups ($p < 0.0001$).

Regarding the plate colony count of titanium rods after the ultrasound treatment, although colony number in the Eno@MSN-D group significantly differed from that in the Eno group, colony numbers between the MSN and NS groups was not significant (**Figures 7C,D**). The titanium rods were fixed with glutaraldehyde, dehydrated with ethanol, gold plated, and observed by SEM. As shown in **Figure 8A**, compared with other groups, including the NS, MSN, and Eno groups, the bacterial biofilm on the surface of the Eno@MSN-D injection titanium rod was loose, with large gaps in the biofilm. Furthermore, in the other groups, the titanium rod surface was not significantly different, and the biofilms on the surface of the other groups were more closely connected than that in the Eno@MSN-D group. We used the living/dead bacterial staining method to observe the bacterial biofilm on the titanium rod surface under an inverted fluorescence microscope. **Figure 8B** shows that the red fluorescence signal in the Eno@MSN-D group was more intense than that in the MSN, NS, and Eno groups. There was no significant difference in red fluorescence among the Eno, MSN, and NS groups, which shows that the Eno@MSN-D group was more substantial than other groups in terms of antibacterial performance *in vivo*.

3.7 Bone Morphometry Assay

We used micro-CT to obtain two- and three-dimensional images from the femur. We also acquired coronal, sagittal, and transverse images of the two-dimensional images and the overall, longitudinal, and transverse three-dimensional images (**Figure 9A**). Compared with those in the Sham control group, the femur morphologies in the four experimental groups changed significantly, and osteolysis of different degrees was observed in all four groups. However, compared with the NS and MSN groups, there was evident bone formation around the titanium rod pores in the Eno@MSN-D and Eno groups. Besides, no significant difference was observed between the NS and MSN groups. By performing parameter analysis on the bone structure of the ROI and using the one-way variance analysis, we obtained some quantitative statistical graphs of the bone parameters (**Figures 9B–E**). The bone volume fraction (BV/TV), trabecular number (Tb.N), and trabecular thickness (Tb.Th) were higher in the Eno@MSN-D and Eno groups than in the NS group, and the Eno@MSN-D group is superior to the Eno group. However, trabecular bone separation (Tb.Sp) was considerably lower in both Eno@MSN-D and Eno groups than in the NS group. Based on the BV/TV, Tb.N, Tb.Th, and Tb. Sp, no noticeable difference was observed between the NS and MSN groups ($p > 0.05$). Overall, these results indicate that both Eno-@MSN-D and Eno groups effectively prevented osteolysis *in vivo*. Of note, the Eno-@MSN-D group was more effective than the Eno group.

3.8 Histopathology

Figures 10A,B shows the longitudinal decalcified sections of different groups. The morphological changes in the left femur were detected by HE staining, and the osteoclasts around the pores of the titanium rod were detected by TRAP staining. **Figure 10A** shows more extensive bone cortex destruction and more abundant bone tissue death in the NS and MSN groups. Although there were signs of intramedullary inflammation in all four experimental groups, these were more severe in the MSN and NS groups. As shown in **Figure 10B**, the number of osteoclasts around the titanium rod pores was less in the Eno@MSN-D and Eno groups that in the NS group. Moreover, the number and area of osteoclasts in each group were measured, and quantitative analysis was performed (**Figure 10C,D**). Noteworthy, compared with the NS group, the number and area of osteoclasts in the Eno@MSN-D group and the ENO group were relatively fewer. Furthermore, the number and area of osteoclasts in the Eno@MSN-D group were lower than those in the ENO group.

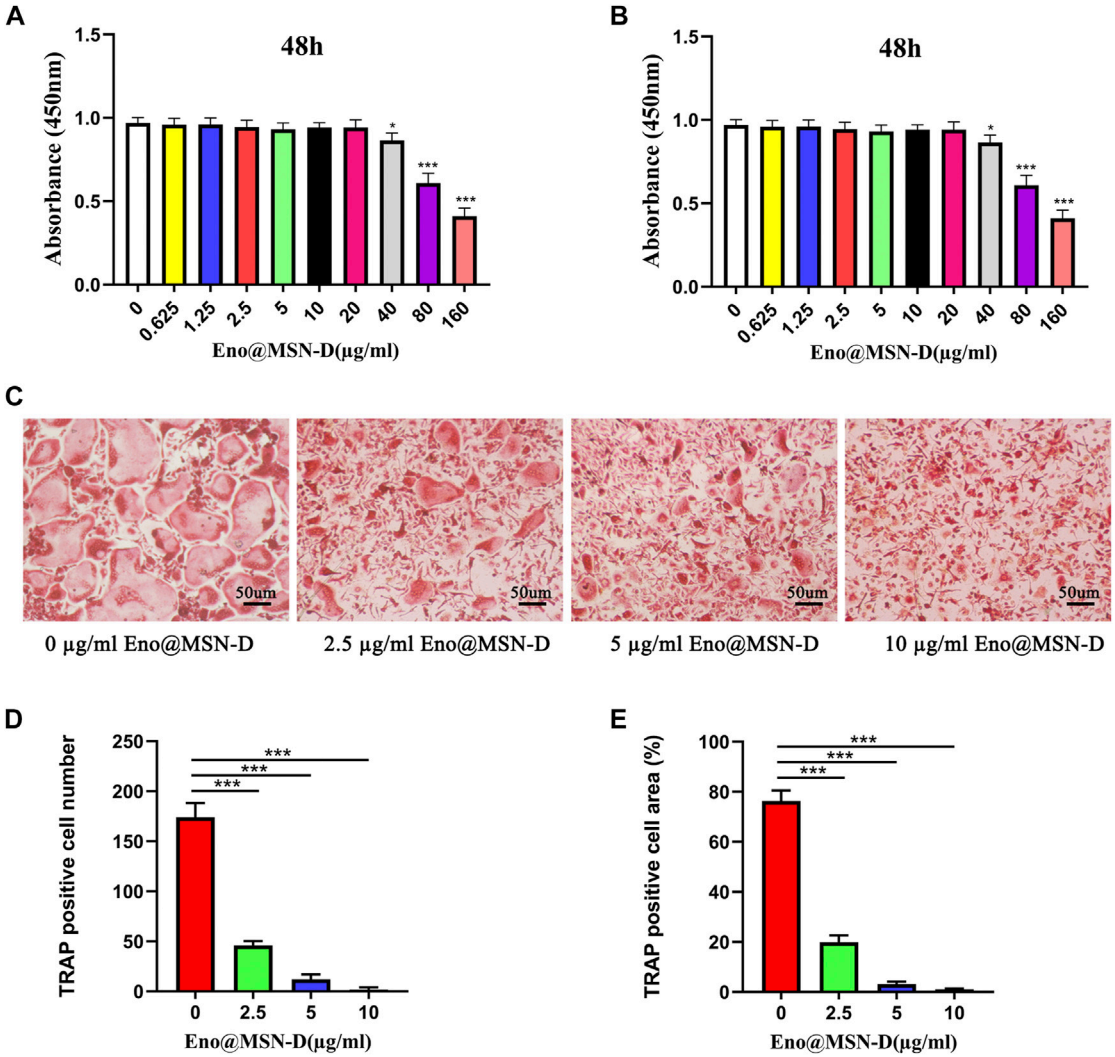

FIGURE 5 | (A,B) BMMs were plated in 96-well plates and stimulated with M-CSF (30 ng/ml) and different concentrations of Eno@MSN-D (0–160 μg/ml) for 48 or 96 h. Cell viability was measured using the CCK-8 assay. **(C)** Bone marrow macrophages (BMMs) were treated with various concentrations of Eno@MSN-D (0, 2.5, 5, and 10 μg/ml) followed by M-CSF and RANKL stimulation for 5 days. The cells were then fixed with 4% paraformaldehyde and subjected to tartrate-resistant acid phosphatase (TRAP) staining. **(D,E)** The number and spread area of TRAP-positive multinuclear cells were determined.

4 DISCUSSION

MSNs have been widely used in nanomedicine because they can be functionalised with chemical groups delivered to specific target sites to alter external organ organisation to accommodate specific target tissues (Chaudhary et al., 2019). However, despite these advances, challenges remain in effectively and sustainably controlling local bone drug release, calibrating the long-term stability and activity of drugs, while minimising cytotoxicity (Campoccia et al., 2010; Bagherifard, 2017). Regarding orthopaedic implant-related infections, nanoparticles are a promising strategy for overcoming biofilm formation and drug resistance (Russo et al., 2017).

In our study, we loaded enoxacin into MSN and coated the nanoparticles with PEG, which is phagocytised by macrophages. Simultaneously, bone-targeting D-Asp8 was connected to the nanoparticles to achieve targeted drug release in the bone tissue (Fu et al., 2014; Chen et al., 2018). Generally, bone adsorption molecules, such as bone-targeting ligands, are coupled to nano-carrier surfaces. The nano-carriers can chelate HA to achieve local drug deposition in bone tissue. After administration, a strong interaction between the bone-targeted ligands and HA leads to rapid retention and accumulation of the nano-carriers in the bone tissue. Therefore, this approach reduces drug leakage in the circulation and ensures highly localised antibiotic concentration (Swami et al., 2014). From the fluorescence signals in rats (**Figure 6**), it is evident that we successfully synthesised Eno@MSN-D nanoparticles that have excellent bone-targeting properties. Our data showed that the present MSNs had ultra-high specific surface areas and suitable pore

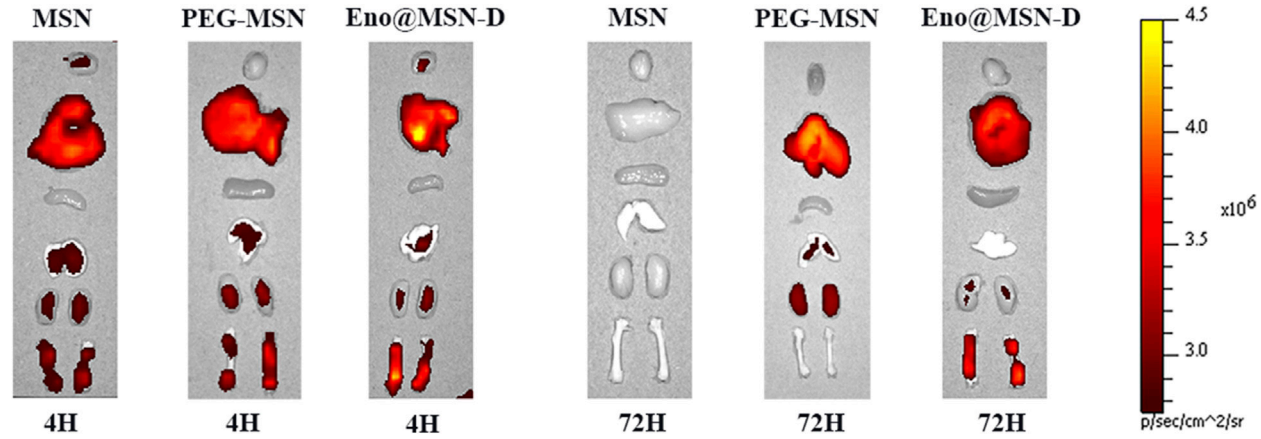

FIGURE 6 | *In vivo* targeted fluorescence experiment: fluorescence diagrams of various organs 4 and 72 h after the injection of MSN, PEG-MSN, and Eno@MSN-D nanoparticles.

sizes for enoxacin loading. During synthesis, the average particle size increased from MSN to Eno@MSN-D. The increase in particle size can be attributed to the loading of drugs inside or outside the pores of the monodisperse silica nanoparticles. The results are in accordance with those of a previous study (Wang et al., 2008), showing that the synthesised carrier size must be larger than that of the pure carrier material when the drugs and polymers are mixed with mesoporous silica nanoparticles.

The PDI reflects particle size uniformity, which is an important index for particle size characterisation. Within a specific distribution range, the smaller the distribution coefficient, the more uniform the particle size (Masarudin et al., 2015). Our data shows that the PDI of the synthesised Eno@MSN-D is the smallest compared with that of MSN and Eno@MSN, and therefore, it has a uniform particle size. The zeta potential of the carrier material can reflect the system's stability, and it has an important influence on the release and circulation of body fluids. The carrier material stability in the surrounding fluid is an important index to overcome aggregate formation in the nano-drug delivery system (Wang et al., 2008). The higher the zeta potential (positive or negative) of the particles, the more stable the system is against aggregation (Yang et al., 2018). Our results show that the zeta potential of the synthesised Eno@MSN-D is −19.3 mVV, which is the smallest value; therefore, it has good dispersion properties. Besides, the TGA curves (**Figure 2E**) showed that the weight loss of Eno@MSN was higher than that of MSN, which indicated that enoxacin was loaded on MSN. In addition, the weight loss of Eno@MSN-D was higher than that of MSN and Eno@MSN; this was due to the loading of the enoxacin and the immobilisation of PEG and D-Asp8 on the surface of the nanoparticles. From the *in vitro* drug release curves of Eno@MSN-D in different pH response release patterns (**Figure 2F**), we determined two main causes of the phenomenon. Firstly, bacterial infections generally feature very low pH values due to their hypoxic nature (Benoit and Koo, 2016). The acidic environment of bacterial infectious sites can be harnessed in the design of pH sensitive drug delivery systems (Gupta et al., 2019). Moreover, *via* protonation at acidic pH, these properties result in greater drug release due to electrostatic repulsion within the nanocarriers (Radovic-Moreno et al., 2012; Zhu and Chen, 2015). These nanoparticles prevent non-specific interaction at physiological pH 7.4, thereby increasing the therapeutic activity with declining pH (Gupta et al., 2019). Secondly, it is due to the enoxacin molecular structure, as studies have reported that enoxacin is least water soluble at neutral pH and highest at acidic pH (Bedard and Bryan, 1989).

From the crystal violet staining, bacterial colony counting plate method unveiled the integrity of some bacterial morphology by SEM and live/dead bacterial staining, and a series of *in vitro* experiments showed that Eno@MSN-D has good antibacterial properties. From the treatment with Eno@MSN-D *in vivo*, it is apparent that the monodisperse silica microspheres were biocompatible with low toxicity, lacked immunogenicity, and degraded into non-toxic compounds (mainly silicic acid) in a short period (Lu et al., 2010). Additionally, our data show that Eno@MSN-D can inhibit osteoclast formation and function when the concentration is lower than the safe concentration of 20 μg/ml Eno@MSN-D.

The successful establishment of a rat infection model is the key to our confirmation that Eno@MSN-D has antibacterial properties *in vivo*. From SEM (**Figure 8A**), live/dead bacterial staining (**Figure 8B**), and bacterial colony plate count on the surface of femoral titanium rods (**Figure 7C**), we observed that Eno@MSN-D has antibacterial effect. In the quantitative bacterial colony plate count graphs (**Figure 7D**), the difference between the Eno@MSN-D and Eno groups as significant, which indirectly indicates that Eno@MSN-D had a better therapeutic effect. Similarly, we observed that, although there was no significant difference between the MSN and NS groups, the colony number in the MSN group was slightly lower; however, this was related to the antibacterial properties of the MSN. The inherent antibacterial activity of the nanoparticles was due to one of the three mechanisms: oxidative stress induction, metal ion release, or non-oxidative stress mechanism (Wang et al., 2017).

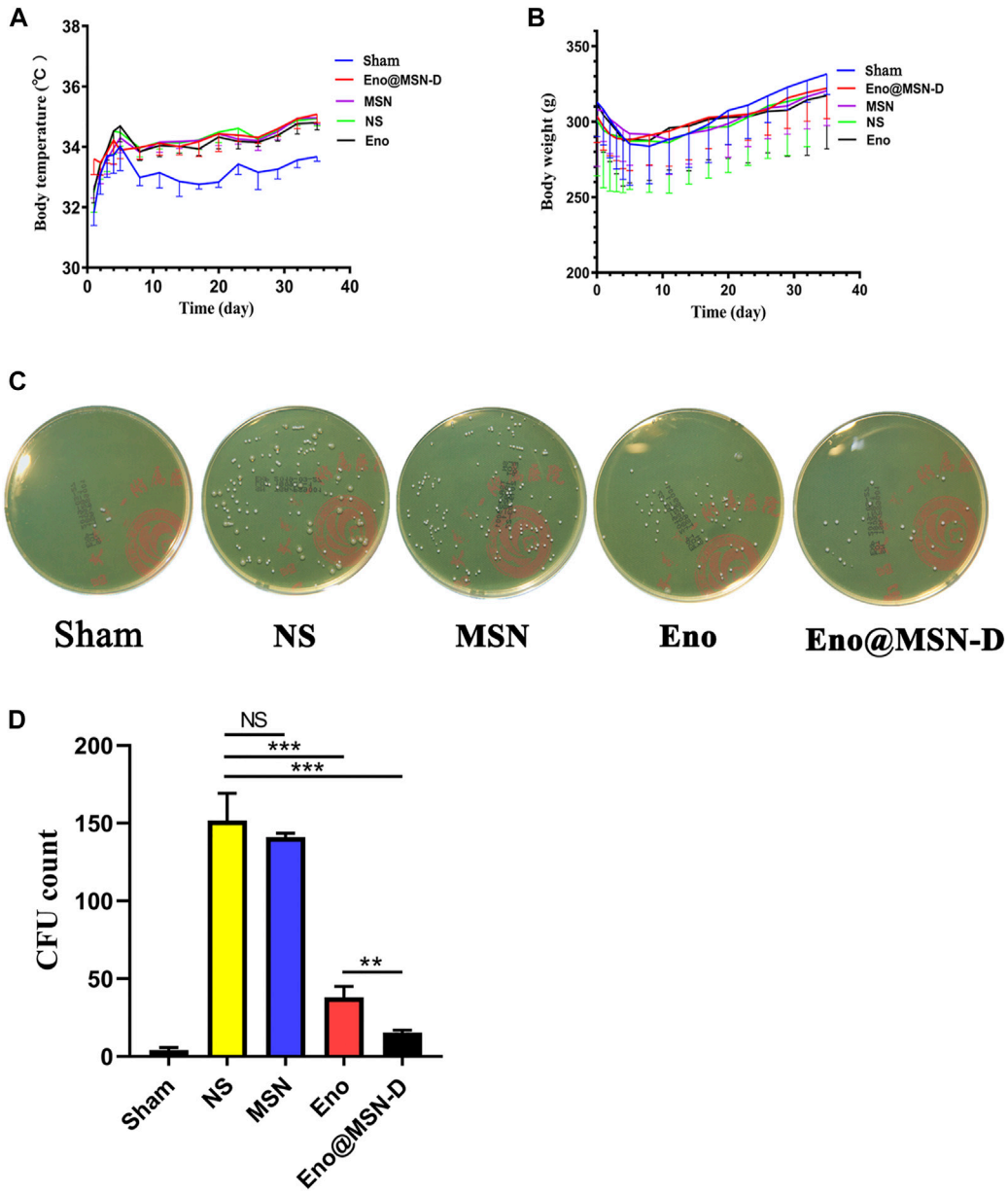

FIGURE 7 | (A) Curve of body temperature change in rats. **(B)** Curve of body weight change in rats. **(C)** Plate colony count after ultrasonic concussion of bacteria on the surface of a titanium rod. **(D)** Statistical chart of plate colony count after the ultrasound treatment.

In the two- and three-dimensional rat femur images (**Figure 9A**), we observed the osteolysis phenomenon in the experimental group, which also confirmed the success of the rat bone infection model. Based on our data (**Figures 9B–D**), we found that the BV/TV, Tb.N, Tb.Th, and Tb. Sp were significantly different between the Eno@MSN-D and Eno groups, which indicated that Eno@MSN-D does play a role in preventing osteolysis *in vivo*. Of note, the Eno-@MSN-D group was more effective than the Eno group.

Bioactive silicon-based nanoparticles reportedly promote the differentiation and mineralisation of osteoblasts (Ha et al., 2014). Additionally, silicon ions released from MSNs have been shown to promote the formation of mineralised nodules, the synthesis of COL1, and the expression of osteogenic genes in osteoblasts (Sun et al., 2009). These observations suggest that MSN plays a role in osteogenesis, and thus may prevent osteolysis. Nevertheless, there was no significant difference in bone parameters between the MSN and NS groups, which indicates that the osteogenic capacity of MSN is still limited, and thus enoxacin still plays a significant role. Besides, the Eno@MSN-D had better osteogenesis abilities to prevent osteolysis, which is consistent with the histomorphological femoral HE (**Figure 10A**). The number and area of osteoclasts (**Figures 10B–D**) in the Eno@MSN-D and Eno groups were smaller than those in the NS groups. Furthermore, the Eno@MSN-D and EN

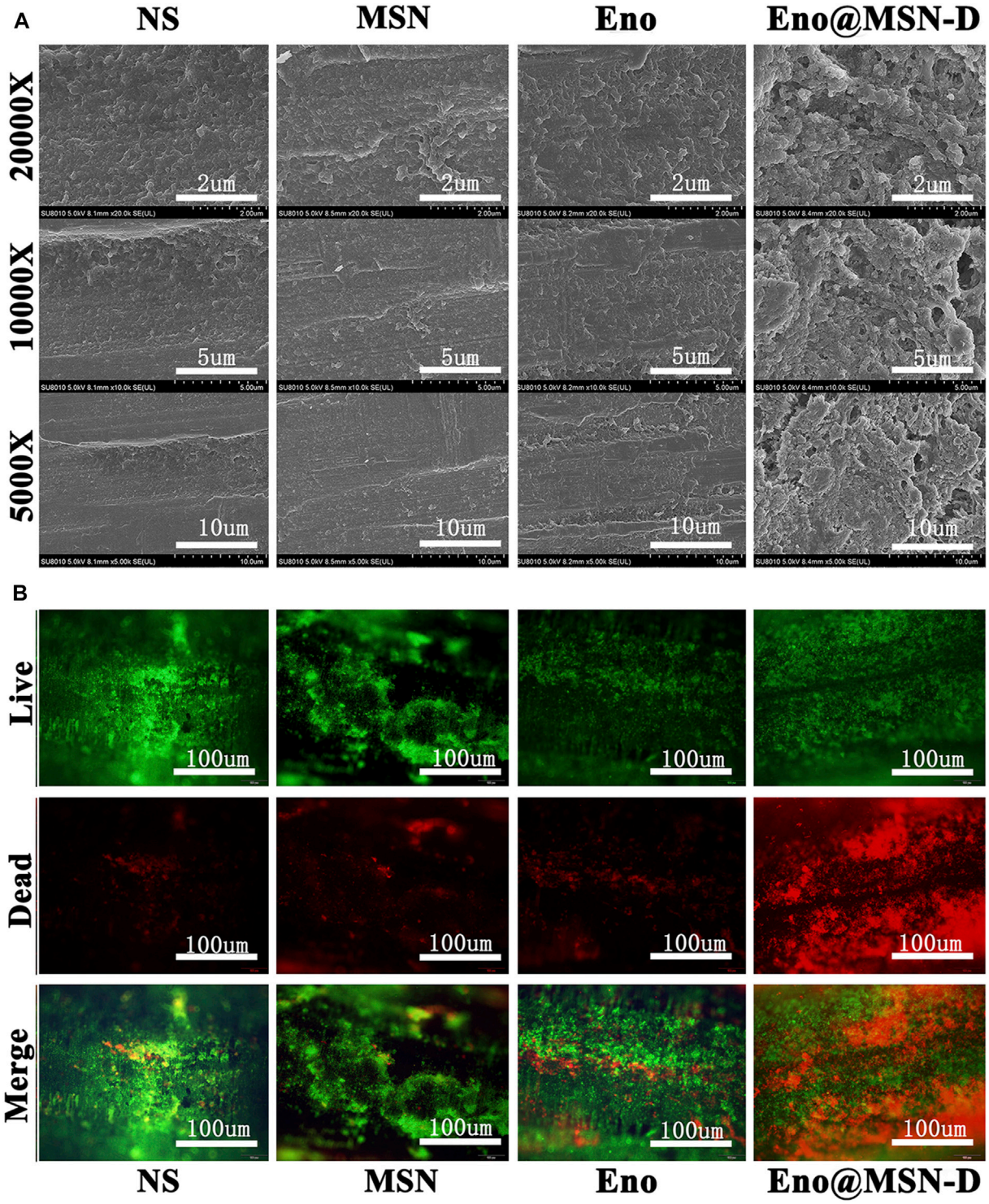

FIGURE 8 | (A) SEM images of biofilm on the surface of the titanium rod. **(B)** The live dead bacterial staining of the biofilm on the surface of the titanium rod was observed under an inverted microscope.

groups significantly differed in terms of osteoclast number and area. Therefore, the Eno@MSN-D group could be more effective than the Eno group to prevent osteolysis.

The *in vitro* and *in vivo* studies of most nanoparticle-based sustained-release systems show that these materials show better antibacterial and antibiofilm activities, which is mainly related to

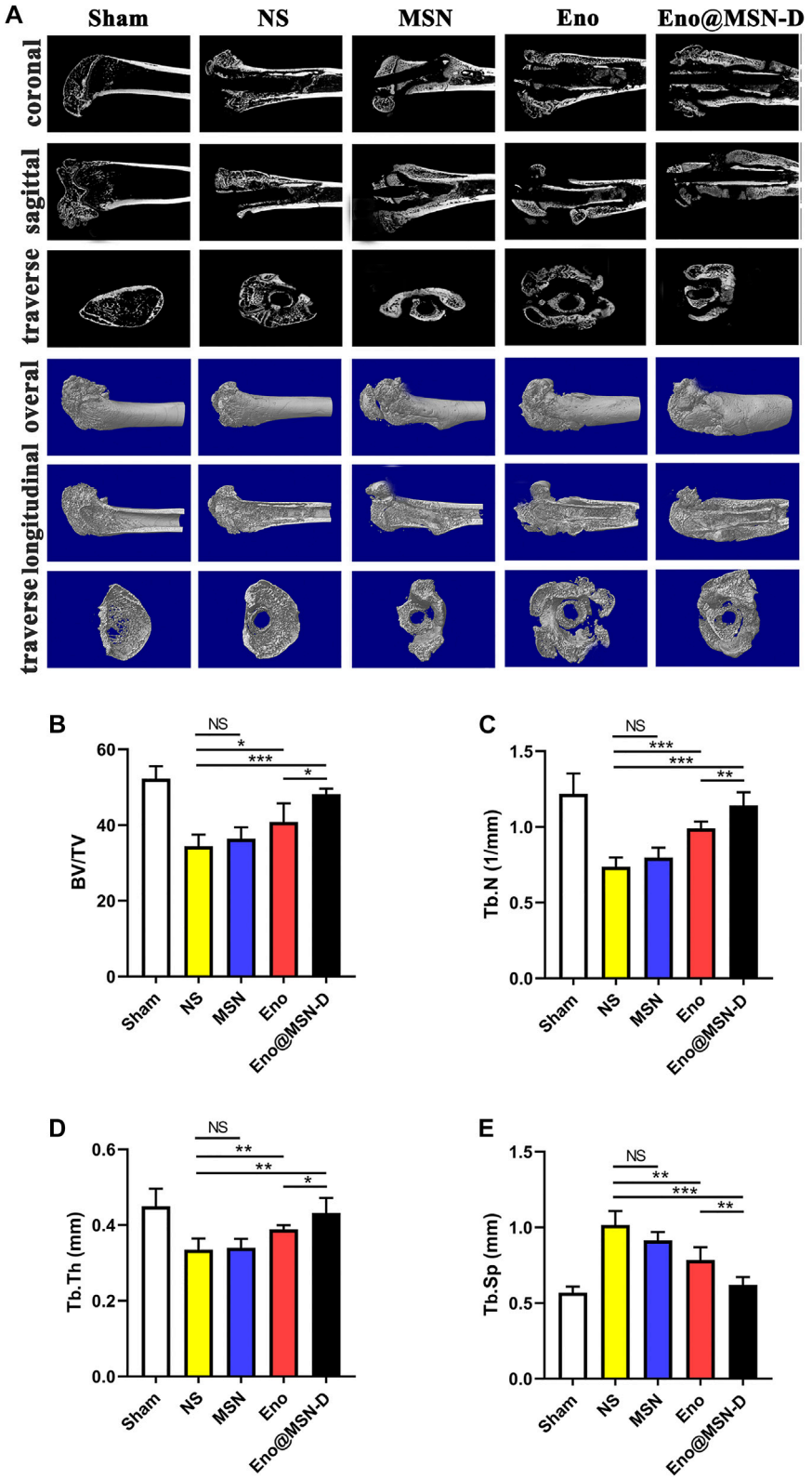

FIGURE 9 | (A) Coronal, sagittal, and transverse two-dimensional micro-CT and integral, longitudinal, transverse three-dimensional micro-CT images of the femur. **(B–E)** Statistic diagram of bone volume fraction, number of bone trabeculae, trabecular bone thickness, and trabecular bone separation.

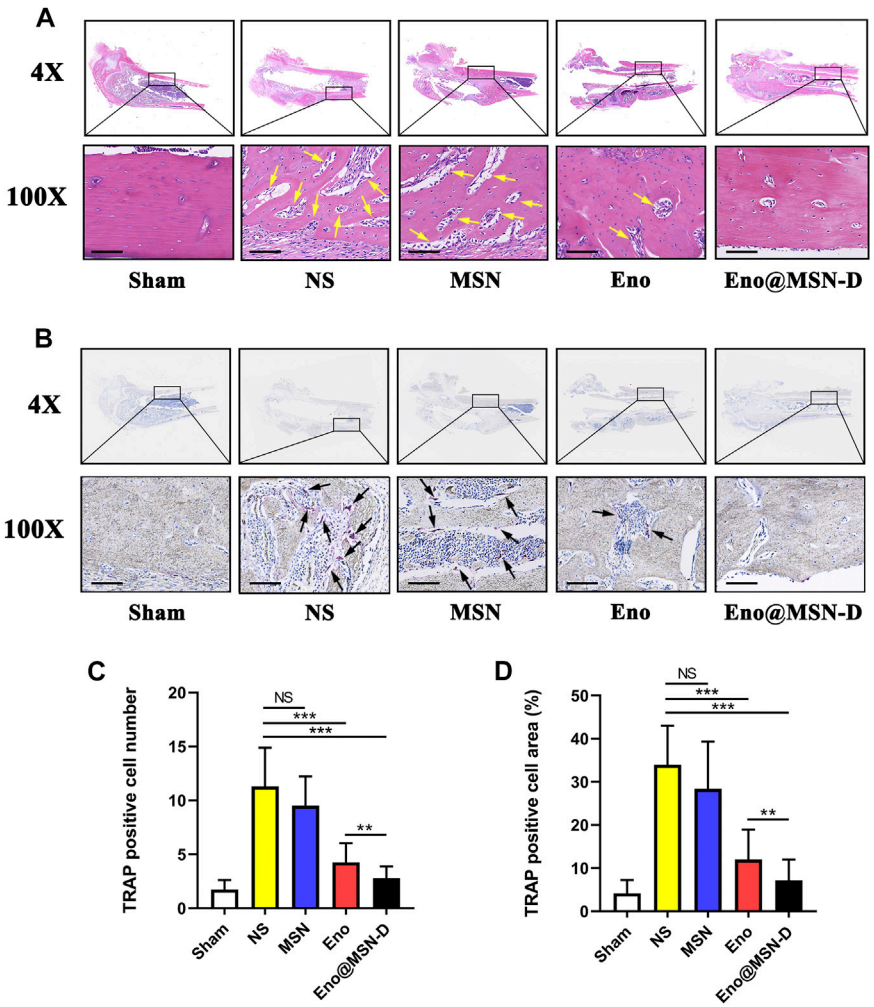

FIGURE 10 | (A) The representative images of HE staining of the middle part of the femur. Yellow arrows indicate dimensional intracortical abscesses or inflammatory cells. **(B)** The representative images of TRAP staining of the middle part of the femur. Black arrows represent osteoclasts. **(C)** Statistical graph of the number of osteoclasts in each field of view. **(D)** Statistical graph of the area of osteoclasts in each field of view. All scale bars = 200 μm.

reducing bacterial adhesion to grafts, higher effectiveness in drug-resistant strains, and/or controlling the antibiotic release. By obtaining sustained-release performance (Zhang et al., 2017; Liu et al., 2018; Zhang et al., 2019), we can achieve better local antibiotic concentrations and prolong the contact time between antibiotics and bacteria, which is essential for removing biofilms. Additionally, carriers offer advantages in terms of therapeutic drug release kinetics, ease of manufacture, biodegradability, chemical binding relative to physical binding, and excellent transport characteristics. Thus, these biomaterials will play a more critical role in medical diagnosis and treatment processes.

5 CONCLUSION

Bacterial colonisation and biofilm formation are issues in post-implantation infections with *S. aureus*. Although conventional antibiotics limit the formation of bacterial biofilms, they ignore the fact that bacterial biofilms restrict the spread of antibiotics to the infected area, further lowering the concentration of antibiotics available to the infected area, as well as bone loss caused by osteoclast formation following orthopaedic implant-associated infections. Despite the dual antibacterial and osteoclast-inhibiting effects of enoxacin, it has limited penetration into bone tissue to achieve adequate blood levels. Fortunately, MSN has been used for the intracellular delivery of antibiotic targets against intracellular infections and bone loss over the last few decades. In this study, we successfully prepared and characterised Eno@MSN-D nanoparticles-based on MSN. Our data show that the synthesised Eno@MSN-D is a safe drug delivery system that enables sustained-release of specific antibiotics to target *S.* aureus-related post-operative implantation infections. Eno@MSN-D not only has excellent antibacterial properties and osteoclast inhibitory properties *in vitro* but also allows the specific targeting of

bone tissues to prevent bone loss *in vivo*. Therefore, this method provides a new way to treat and prevent post-operative, orthopaedic *S. aureus*-related implantation infections and bone loss.

DATA AVAILABILITY STATEMENT

The original contributions presented in the study are included in the article/Supplementary Material, further inquiries can be directed to the corresponding authors.

ETHICS STATEMENT

The animal study was reviewed and approved by The First Affiliated Hospital of Nanchang University.

AUTHOR CONTRIBUTIONS

CY: Methodology, Investigation, Writing—original draft. MZ: Investigation, Writing—original draft. XH: Methodology, Investigation,Validation. QX: Formal analysis. MD: Writing—review and editing, Funding acquisition. TN: Writing—review and editing, Conceptualization, Funding acquisition. XL: Supervision, Writing—review and editing, Funding acquisition.

FUNDING

This work was supported by the National Natural Science Foundation (Grant Nos. 81601912 and 81860404) and Shanghai Sailing Program of Shanghai Science and Technology Innovation Action Plan (Grant No. 20YF1429800).

REFERENCES

Bagherifard, S. (2017). Mediating Bone Regeneration by Means of Drug Eluting Implants: From Passive to Smart Strategies. *Mater. Sci. Eng. C* 71, 1241–1252. doi:10.1016/j.msec.2016.11.011

Bedard, J., and Bryan, L. E. (1989). Interaction of the Fluoroquinolone Antimicrobial Agents Ciprofloxacin and Enoxacin with Liposomes. *Antimicrob. Agents Chemother.* 33 (8), 1379–1382. doi:10.1128/aac.33.8.1379

Benoit, D. S., and Koo, H. (2016). Targeted, Triggered Drug Delivery to Tumor and Biofilm Microenvironments. *Nanomedicine* 11 (8), 873–879. doi:10.2217/nnm-2016-0014

Buommino, E., Scognamiglio, M., Donnarumma, G., Fiorentino, A., and D'Abrosca, B. (2014). Recent Advances in Natural Product-Based Anti-biofilm Approaches to Control Infections. *Mini Rev. Med. Chem.* 14 (14), 1169–1182. doi:10.2174/1389557515666150101095853

Campoccia, D., Montanaro, L., Speziale, P., and Arciola, C. R. (2010). Antibiotic-loaded Biomaterials and the Risks for the Spread of Antibiotic Resistance Following Their Prophylactic and Therapeutic Clinical Use. *Biomaterials* 31 (25), 6363–6377. doi:10.1016/j.biomaterials.2010.05.005

Chaudhary, Z., Subramaniam, S., Khan, G. M., Abeer, M. M., Qu, Z., Janjua, T., et al. (2019). Encapsulation and Controlled Release of Resveratrol within Functionalized Mesoporous Silica Nanoparticles for Prostate Cancer Therapy. *Front. Bioeng. Biotechnol.* 7, 225. doi:10.3389/fbioe.2019.00225

Chen, S., Zheng, L., Zhang, J., Wu, H., Wang, N., Tong, W., et al. (2018). A Novel Bone Targeting Delivery System Carrying Phytomolecule Icaritin for Prevention of Steroid-Associated Osteonecrosis in Rats. *Bone* 106, 52–60. doi:10.1016/j.bone.2017.09.011

Dapunt, U., Maurer, S., Giese, T., Gaida, M. M., and Hänsch, G. M. (2014). The Macrophage Inflammatory Proteins MIP1α (CCL3) and MIP2α (CXCL2) in Implant-Associated Osteomyelitis: Linking Inflammation to Bone Degradation. *Mediators Inflamm.* 2014, 728619. doi:10.1155/2014/728619

Fu, Y.-C., Fu, T.-F., Wang, H.-J., Lin, C.-W., Lee, G.-H., Wu, S.-C., et al. (2014). Aspartic Acid-Based Modified PLGA-PEG Nanoparticles for Bone Targeting: *In Vitro* and *In Vivo* Evaluation. *Acta Biomater.* 10 (11), 4583–4596. doi:10.1016/j.actbio.2014.07.015

Gupta, A., Mumtaz, S., Li, C.-H., Hussain, I., and Rotello, V. M. (2019). Combatting Antibiotic-Resistant Bacteria Using Nanomaterials. *Chem. Soc. Rev.* 48 (2), 415–427. doi:10.1039/c7cs00748e

Ha, S.-W., Weitzmann, M. N., and Beck, G. R., Jr. (2014). Bioactive Silica Nanoparticles Promote Osteoblast Differentiation through Stimulation of Autophagy and Direct Association with LC3 and P62. *ACS Nano* 8 (6), 5898–5910. doi:10.1021/nn5009879

Johnson, E. N., Burns, T. C., Hayda, R. A., Hospenthal, D. R., and Murray, C. K. (2007). Infectious Complications of Open Type III Tibial Fractures Among Combat Casualties. *Clin. Infect. Dis.* 45 (4), 409–415. doi:10.1086/520029

Lazzarini, L., Mader, J. T., and Calhoun, J. H. (2004). Osteomyelitis in Long Bones. *J. Bone Jt. Surg.* 86 (10), 2305–2318. doi:10.2106/00004623-200410000-00028

Lee, J. E., Lee, N., Kim, H., Kim, J., Choi, S. H., Kim, J. H., et al. (2010). Uniform Mesoporous Dye-Doped Silica Nanoparticles Decorated with Multiple Magnetite Nanocrystals for Simultaneous Enhanced Magnetic Resonance Imaging, Fluorescence Imaging, and Drug Delivery. *J. Am. Chem. Soc.* 132 (2), 552–557. doi:10.1021/ja905793q

Li, Y., Liu, G., Zhai, Z., Liu, L., Li, H., Yang, K., et al. (2019). Erratum for Li et al., "Antibacterial Properties of Magnesium *In Vitro* and in an *In Vivo* Model of Implant-Associated Methicillin-Resistant Staphylococcus aureus Infection". *Antimicrob. Agents Chemother.* 63 (4), 7586–7591. doi:10.1128/AAC.00313-19

Liu, J., Dang, L., Li, D., Liang, C., He, X., Wu, H., et al. (2015). A Delivery System Specifically Approaching Bone Resorption Surfaces to Facilitate Therapeutic Modulation of microRNAs in Osteoclasts. *Biomaterials* 52, 148–160. doi:10.1016/j.biomaterials.2015.02.007

Liu, K.-S., Lee, C.-H., Lee, D., Liu, M., Tsai, F.-C., and Tseng, Y.-Y. (2018). Sustained Local Delivery of High-Concentration Vancomycin from a Hybrid Biodegradable, Antibiotic-Eluting, Nanofiber-Loaded Endovascular Prosthesis for Treatment of Mycotic Aortic Aneurysms. *J. Vasc. Surg.* 68 (2), 597–606. doi:10.1016/j.jvs.2017.07.142

Liu, X., Qu, X., Wu, C., Zhai, Z., Tian, B., Li, H., et al. (2014). The Effect of Enoxacin on Osteoclastogenesis and Reduction of Titanium Particle-Induced Osteolysis via Suppression of JNK Signaling Pathway. *Biomaterials* 35 (22), 5721–5730. doi:10.1016/j.biomaterials.2014.04.006

Lu, J., Liong, M., Li, Z., Zink, J. I., and Tamanoi, F. (2010). Biocompatibility, Biodistribution, and Drug-Delivery Efficiency of Mesoporous Silica Nanoparticles for Cancer Therapy in Animals. *Small.* 6 (16), 1794–1805. doi:10.1002/smll.201000538

Lynch, A. S., and Abbanat, D. (2010). New Antibiotic Agents and Approaches to Treat Biofilm-Associated Infections. *Expert Opin. Ther. Patents.* 20 (10), 1373–1387. doi:10.1517/13543776.2010.505923

Martínez-Carmona, M., Lozano, D., Colilla, M., and Vallet-Regí, M. (2018). Lectin-conjugated pH-Responsive Mesoporous Silica Nanoparticles for Targeted Bone Cancer Treatment. *Acta Biomater.* 65, 393–404. doi:10.1016/j.actbio.2017.11.007

Masarudin, M. J., Cutts, S. M., Evison, B. J., Phillips, D. R., and Pigram, P. J. (2015). Factors Determining the Stability, Size Distribution, and Cellular Accumulation of Small, Monodisperse Chitosan Nanoparticles as Candidate Vectors for Anticancer Drug Delivery: Application to the Passive Encapsulation of [14C]-Doxorubicin. *Nsa.* 8, 67–80. doi:10.2147/nsa.s91785

Nie, B., Long, T., Ao, H., Zhou, J., Tang, T., and Yue, B. (2017). Covalent Immobilization of Enoxacin onto Titanium Implant Surfaces for Inhibiting Multiple Bacterial Species Infection and *In Vivo* Methicillin-Resistant Staphylococcus aureus Infection Prophylaxis. *Antimicrob. Agents Chemother.* 61 (1), 01776–1816. doi:10.1128/AAC.01766-16

Nielsen, J. J., and Low, S. A. (2020). Bone-Targeting Systems to Systemically Deliver Therapeutics to Bone Fractures for Accelerated Healing. *Curr. Osteoporos. Rep.* 18 (5), 449–459. doi:10.1007/s11914-020-00604-4

Noukrati, H., Cazalbou, S., Demnati, I., Rey, C., Barroug, A., and Combes, C. (2016). Injectability, Microstructure and Release Properties of Sodium Fusidate-Loaded Apatitic Cement as a Local Drug-Delivery System. *Mater. Sci. Eng. C.* 59, 177–184. doi:10.1016/j.msec.2015.09.070

Oliveira, T. C., Gomes, M. S., and Gomes, A. C. (2020). The Crossroads between Infection and Bone Loss. *Microorganisms.* 8 (11), 1765. doi:10.3390/microorganisms8111765

Ostrov, D. A., Magis, A. T., Wronski, T. J., Chan, E. K. L., Toro, E. J., Donatelli, R. E., et al. (2009). Identification of Enoxacin as an Inhibitor of Osteoclast Formation and Bone Resorption by Structure-Based Virtual Screening. *J. Med. Chem.* 52 (16), 5144–5151. doi:10.1021/jm900277z

Radovic-Moreno, A. F., Lu, T. K., Puscasu, V. A., Yoon, C. J., Langer, R., and Farokhzad, O. C. (2012). Surface Charge-Switching Polymeric Nanoparticles for Bacterial Cell wall-targeted Delivery of Antibiotics. *ACS nano.* 6 (5), 4279–4287. doi:10.1021/nn3008383

Ravichandran, R., Gandhi, S., Sundaramurthi, D., Sethuraman, S., and Krishnan, U. M. (2013). Hierarchical Mesoporous Silica Nanofibers as Multifunctional Scaffolds for Bone Tissue Regeneration. *J. Biomater. Sci. Polym. Edition.* 24 (17), 1988–2005. doi:10.1080/09205063.2013.816930

Russo, T., Gloria, A., De Santis, R., D'Amora, U., Balato, G., Vollaro, A., et al. (2017). Preliminary Focus on the Mechanical and Antibacterial Activity of a PMMA-Based Bone Cement Loaded with Gold Nanoparticles. *Bioactive Mater.* 2 (3), 156–161. doi:10.1016/j.bioactmat.2017.05.002

Schierholz, J. M., and Beuth, J. (2001). Implant Infections: a haven for Opportunistic Bacteria. *J. Hosp. Infect.* 49 (2), 87–93. doi:10.1053/jhin.2001.1052

Sun, J., Wei, L., Liu, X., Li, J., Li, B., Wang, G., et al. (2009). Influences of Ionic Dissolution Products of Dicalcium Silicate Coating on Osteoblastic Proliferation, Differentiation and Gene Expression. *Acta Biomater.* 5 (4), 1284–1293. doi:10.1016/j.actbio.2008.10.011

Swami, A., Reagan, M. R., Basto, P., Mishima, Y., Kamaly, N., Glavey, S., et al. (2014). Engineered Nanomedicine for Myeloma and Bone Microenvironment Targeting. *Proc. Natl. Acad. Sci.* 111 (28), 10287–10292. doi:10.1073/pnas.1401337111

Toro, E. J., Zuo, J., Ostrov, D. A., Catalfamo, D., Bradaschia-Correa, V., Arana-Chavez, V., et al. (2012). Enoxacin Directly Inhibits Osteoclastogenesis without Inducing Apoptosis. *J. Biol. Chem.* 287 (21), 17894–17904. doi:10.1074/jbc.m111.280511

Wang, L., Hu, C., and Shao, L. (2017). The Antimicrobial Activity of Nanoparticles: Present Situation and Prospects for the Future. *Ijn.* Vol. 12, 1227–1249. doi:10.2147/ijn.s121956

Wang, X., Du, Y., and Luo, J. (2008). Biopolymer/montmorillonite Nanocomposite: Preparation, Drug-Controlled Release Property and Cytotoxicity. *Nanotechnology* 19 (6), 065707. doi:10.1088/0957-4484/19/6/065707

Yang, S., Han, X., Yang, Y., Qiao, H., Yu, Z., Liu, Y., et al. (2018). Bacteria-Targeting Nanoparticles with Microenvironment-Responsive Antibiotic Release to Eliminate Intracellular Staphylococcus aureus and Associated Infection. *ACS Appl. Mater. Inter.* 10 (17), 14299–14311. doi:10.1021/acsami.7b15678

Zhang, D., Liu, W., Wu, X.-D., He, X., Lin, X., Wang, H., et al. (2019). Efficacy of Novel Nano-Hydroxyapatite/polyurethane Composite Scaffolds with Silver Phosphate Particles in Chronic Osteomyelitis. *J. Mater. Sci. Mater. Med.* 30 (6), 59. doi:10.1007/s10856-019-6261-7

Zhang, Y., Liang, R.-j., Xu, J.-j., Shen, L.-f., Gao, J.-q., Wang, X.-p., et al. (2017). Efficient Induction of Antimicrobial Activity with Vancomycin Nanoparticle-Loaded Poly(trimethylene Carbonate) Localized Drug Delivery System. *Ijn* Vol. 12, 1201–1214. doi:10.2147/ijn.s127715

Zhou, W., Peng, X., Ma, Y., Hu, Y., Wu, Y., Lan, F., et al. (2020). Two-staged Time-dependent Materials for the Prevention of Implant-Related Infections. *Acta Biomater.* 101, 128–140. doi:10.1016/j.actbio.2019.10.023

Zhou, X., Feng, W., Qiu, K., Chen, L., Wang, W., Nie, W., et al. (2015). BMP-2 Derived Peptide and Dexamethasone Incorporated Mesoporous Silica Nanoparticles for Enhanced Osteogenic Differentiation of Bone Mesenchymal Stem Cells. *ACS Appl. Mater. Inter.* 7 (29), 15777–15789. doi:10.1021/acsami.5b02636

Zhu, Y.-J., and Chen, F. (2015). pH-Responsive Drug-Delivery Systems. *Chem. Asian J.* 10 (2), 284–305. doi:10.1002/asia.201402715

Conflict of Interest: The authors declare that the research was conducted in the absence of any commercial or financial relationships that could be construed as a potential conflict of interest.

Publisher's Note: All claims expressed in this article are solely those of the authors and do not necessarily represent those of their affiliated organizations, or those of the publisher, the editors and the reviewers. Any product that may be evaluated in this article, or claim that may be made by its manufacturer, is not guaranteed or endorsed by the publisher.

Copyright © 2021 Yao, Zhu, Han, Xu, Dai, Nie and Liu. This is an open-access article distributed under the terms of the Creative Commons Attribution License (CC BY). The use, distribution or reproduction in other forums is permitted, provided the original author(s) and the copyright owner(s) are credited and that the original publication in this journal is cited, in accordance with accepted academic practice. No use, distribution or reproduction is permitted which does not comply with these terms.

frontiers in Bioengineering and Biotechnology

ORIGINAL RESEARCH
published: 30 November 2021
doi: 10.3389/fbioe.2021.706423

Improved Osteogenesis by Mineralization Combined With Double-Crosslinked Hydrogel Coating for Proliferation and Differentiation of Mesenchymal Stem Cells

Yiqun Ma[1], Yuwang You[2], Lu Cao[1], Bing Liang[3], Bo Tian[1], Jian Dong[1] and Hong Lin[1]**

[1]Department of Orthopaedic Surgery, Zhongshan Hospital, Fudan University, Shanghai, China, [2]Hospital Infection Management Department, Affiliated Wuxi People's Hospital of Nanjing Medical University, Wuxi, China, [3]Department of Orthopaedic Surgery, Zhongshan Hospital, Fudan University (Xiamen Branch), Xiamen, China

OPEN ACCESS

Edited by:
Jingxiao Chen,
Jiangnan University, China

Reviewed by:
Sanjun Shi,
Chengdu University of Traditional Chinese Medicine, China
Guofeng Luo,
Hebrew University of Jerusalem, Israel

***Correspondence:**
Jian Dong
dong.jian@zs-hospital.sh.cn
Hong Lin
lin.hong1@zs-hospital.sh.cn

Specialty section:
This article was submitted to Biomaterials, a section of the journal Frontiers in Bioengineering and Biotechnology

Received: *07 May 2021*
Accepted: *06 October 2021*
Published: *30 November 2021*

Citation:
Ma Y, You Y, Cao L, Liang B, Tian B, Dong J and Lin H (2021) Improved Osteogenesis by Mineralization Combined With Double-Crosslinked Hydrogel Coating for Proliferation and Differentiation of Mesenchymal Stem Cells. Front. Bioeng. Biotechnol. 9:706423. doi: 10.3389/fbioe.2021.706423

In consideration of improving the interface problems of poly-L-lactic acid (PLLA) that hindered biomedical use, surface coatings have been explored as an appealing strategy in establishing a multi-functional coating for osteogenesis. Though the layer-by-layer (LBL) coating developed, a few studies have applied double-crosslinked hydrogels in this technique. In this research, we established a bilayer coating with double-crosslinked hydrogels [alginate–gelatin methacrylate (GelMA)] containing bone morphogenic protein (BMP)-2 [alginate-GelMA/hydroxyapatite (HA)/BMP-2], which displayed great biocompatibility and osteogenesis. The characterization of the coating showed improved properties and enhanced wettability of the native PLLA. To evaluate the biosafety and inductive ability of osteogenesis, the behavior (viability, adherence, and proliferation) and morphology of human bone mesenchymal stem cells (hBMSCs) on the bilayer coatings were tested by multiple exams. The satisfactory function of osteogenesis was verified in bilayer coatings. We found the best ratios between GelMA and alginate for biological applications. The Alg70-Gel30 and Alg50-Gel50 groups facilitated the osteogenic transformation of hBMSCs. In brief, alginate-GelMA/HA/BMP-2 could increase the hBMSCs' early transformation of osteoblast lineage and promote the osteogenesis of bone defect, especially the outer hydrogel layer such as Alg70-Gel30 and Alg50-Gel50.

Keywords: hydrogel coating, gelatin methacrylate (GelMA), alginate, double crosslink, mesenchymal stem cells

INTRODUCTION

The treatment of bone defects still needs further exploration because of the unsatisfactory clinical outcome. With the increased understanding of tissue engineering and degeneration, polymeric material grafts have been tailored highly biocompatible and widely available so as to reduce rehabilitation time (Rai et al., 2016; Sobolev et al., 2019). Among them, poly-L-lactic acid (PLLA), one of the most applied bioresorbable polymers, opens up a great deal of possibilities in bone substitutes. However, the acidic degradation products released from PLLA may cause an aseptic inflammatory response in bone repair microenvironment and impede bone healing (Kaito et al.,

2005). Kandziora et al. (2004) used a fusion cage made of PLLA to treat cervical and lumbar spine diseases. During follow-up, osteolysis occurred around the fusion cage, which is predictive of bone non-union. In order to overcome the shortcoming, several strategies have been designed to modify PLLA, especially the interface between PLLA and adjacent tissues. Based on the potential application in bone engineering, PLLA is usually combined with apatite ceramics, such as hydroxyapatite or tricalcium phosphate, to improve this polymer's property. The strengthened osteoconductivity and better bone-binding ability provide the conditions for bone regeneration. *In vitro* experiments showed that the hydrophilicity of the PLLA increased and the cell attachment and proliferation enhanced as well (Szustakiewicz et al., 2021; Tan et al., 2021). All this is possible thanks to the component and microstructural similarity between the apatite ceramics and native bone.

Apatite ceramics can also be doped onto the interface of PLLA, which is called biomineralization. It means inorganic crystal, such as hydroxyapatite (HA), is induced to wrap the organic materials. Simulated body fluid (SBF) is widely applied to develop hydroxyapatite coating over PLLA. However, the interface bonding force between HA and PLLA is relatively poor and may last for several weeks. In order to form a negative charge to bind constituents of HA, the surface of PLLA is always pretreated for hydrolysis of carboxyl group. Therefore, polydopamine coating inspired by mussels' adhesive mechanism has been introduced as the medium to "fix" HA (Lee, Dellatore, Miller, & Messersmith, 2007). The polydopamine coating is tightly bound to the material surface by the exhaustively repeated 3,4-dihydroxy-L-phenylalanine-lysine motif and is easy to administer in alkaline solutions of dopamine. On the other hand, nanoclusters of HA can be secondarily "grown" on polydopamine films (Tsai et al., 2011), and subsequent studies have further increased the generation rate of HA (Tas and Bhaduri, 2004). Chen et al. (2019) used polydopamine (PDA) to biomineralize electrospinning PLLA fibrous membrane, which was excellent for bone tissue repair. A previous study revealed that an organic–inorganic hybrid coating is able to reduce cytotoxicity and improve cell viability, thus prolonging the time of osteogenesis (Li et al., 2016). Hsu et al. (2020) reported that the composition of chlorine-substituted hydroxyapatite/polydopamine on a titanium-64 surface strengthened the osteointegration *in vivo*. Nevertheless, even loose inorganic structures are still unsatisfactory for controlled release of growth factors that induce bone formation.

Except for good biocompatibility and mimicking natural extracellular matrices, hydrogel was found to be the superior carrier for growth factors (Liang et al., 2020). Alginate, a natural polymer, includes (1-4)-linked b-D-mannuronic acid and a-L-guluronic acid with good biocompatibility (Drury et al., 2004; Ahn et al., 2021). With the participation of divalent cations (e.g., Ca^{2+}), rapid ionic crosslinking can be achieved in sodium alginate (Ahn et al., 2021). Sodium alginate has been approved by the U.S. Food and Drug Administration (FDA) for medical use, because there is no toxic medium in the sodium alginate gel preparation process (Wang et al., 2020). However, the lack of stem cell adhesion and the uncontrolled degradative kinetics must be addressed (Nair et al., 2020). These defects hampered the proliferation and functionality of the encapsulated cells. Many binding motifs and polymers have been studied, such as matrix metalloproteinase (MMP)-sensitive degradation sequences and collagen, to adjust the compliance with the extracellular matrix (ECM) (Kraehenbuehl et al., 2008; Gregurec et al., 2016). Additionally, a layer-by-layer assembly of chitosan and alginate was applied to modify surface chemistry and expedite the adhesion of human umbilical vein endothelial cells (Silva, Garcia, Reis, Garcia, & Mano, 2017).

Studies have illustrated that modified alginate hydrogels can act as a desired "soil" for the target cells to proliferate and differentiate to the expected phenotypes (Silva et al., 2017; Simo, Fernandez-Fernandez, Vila-Crespo, Ruiperez, & Rodriguez-Nogales, 2017). The gelatin–alginate coating is capable to withstand cyclic compression and even retain proteins entrapped in hydrogel (Pacelli, Basu, Berkland, Wang, & Paul, 2018). Gelatin methacrylate (GelMA), a newly developed photo-crosslinkable hydrogel, has been applied in wound healing and controlled drug release and as a cell culture substrate. For example, Chen et al. (2021) grafted GelMA hydrogel on the surface of expanded nanofiber scaffolds and photo-crosslinked the hydrogel to fit invasive surgery such as laparoscopy and thoracoscopy. Ashwin et al. (2020) made PLLA scaffolds coated with GelMA that were loaded with mucic acid and demonstrated the controlled release of mucic acid and potential capability of osteoblast differentiation. In order to combine gel strength with drug loading performance; achieve better simulation of the biomechanical properties of natural ECM; and improve stem cell adhesion, encapsulation, and differentiation to target phenotypes, a hydrogel coating that is double crosslinked with GelMA and alginate may be a good choice for promoting high-quality bone tissue regeneration.

In consideration of a layer-by-layer (LBL) assembly technique as a successful measurement, it has been explored as an appealing strategy in establishing the multi-functional coating for osteogenesis (Blatchley et al., 2021; Piluso et al., 2021). It could not only regulate local and extended drug release on the surface of PLLA acting as seal barrier but it could also orient the osteogenic differentiation of bone mesenchymal stem cells (BMSCs) and bone formation (Lin, Hsieh, Tseng, & Hsu, 2016; Tsai et al., 2015). Therefore, the aim of this research was to establish a coating to induce osteogenesis of bone mesenchymal stem cells by a combination of alginate and GelMA DN structure for controllable bone morphogenic protein (BMP)-2 release and to check the behavior (adhesion, proliferation, and differentiation) of human bone mesenchymal stem cells (hBMSCs) in the hydrogel platform and its underlying mechanism.

MATERIALS AND METHODS

Materials

PLLA were purchased from Jufukai Biotechnology Co. (Shangdong, China). Sodium alginate, gelatin, dopamine, and Igracure 2959 were purchased from Sigma-Aldrich (St. Louis, MO, United States). Yuanxiang Medical Instrument Co. (Shanghai, China) provided CCK-8 assay kit, alkaline

TABLE 1 | Labels for functional composition of different ratios and concentration.

Weight ratios (%)		Final concentration (*w*/*v*%)		Labels for composition
Alginate	Gelma	Alginate	Gelma	
90	10	4.5	0.5	Alg90-Gel10
70	30	3.5	1.5	Alg70-Gel30
50	50	2.5	2.5	Alg50-Gel50
30	70	1.5	3.5	Alg30-Gel70
10	90	0.5	4.5	Alg10-Gel90

phosphatase (ALP) assay kit, and Dulbecco's Modified Eagle Medium (DMEM). PCR primers were supplied by Sangon Biotech Co. (Shanghai, China). Total RNA Kit, rhodamine phalloidin, and 4,6-diamidino-2-phenylindole (DAPI) solution were bought from Yeason Biotechnology Co. (Shangdong, China).

Substrate Preparation and Polydopamine/ HA Modification

PLLA composite substrate was synthesized according to our previous report (Cao et al., 2012). Substrate films were dried at −30°C for 24 h after being cast in custom-made Teflon molds. Then, these films were divided into small squares (10 mm in length and 1 mm in thickness) and were stored at room temperature. For biomedical use, the substrate was washed in distilled water ultrasonically and then sterilized with gamma irradiation at 25 kGy.

The prepared substrates were dipped into 2 mg/ ml dopamine alkaline solution in which the pH value was adjusted to 8.5 with 10 mmol Tris-HCl buffer. The solution was stirred carefully to ensure sufficient contact with the PLLA substrate for 24 h. Then, these sheets were washed by distilled water three times to get rid of the free dopamine. The polydopamine-modified PLLA membranes were then dried at 40°C before further use.

Biomineralization was performed largely according to a previous study (Zhang, Zhang, Bao, & Chen, 2014). For rapid synthesis of the HA on polydopamine, first, a simulated body fluid solution, which was used to form HA coating, was prepared according to the work of Tas & Bhaduri (2004) and the pH adjusted to 4.0–4.5 prior to the coating procedure. Second, the polydopamine-modified PLLA membranes were dipped in the above solution with a pH value 6.5 for a certain period; finally, these membranes were denoted as PLLA-PDA-HA, respectively.

Preparation of Double-Crosslinked Hydrogel Coatings

Sodium alginate was dissolved in phosphate-buffered saline (PBS) at a certain concentration according to **Table 1**. GelMA was synthesized according to a previous study (Nichol et al., 2010). Next, freeze-dried GelMA and the photoinitiator (Irgacure 2959, Sigma-Aldrich) were dissolved in the prepared sodium alginate solution in a given proportion. The concentration of GelMA solution was set at 0.5%, 1.5%, 2.5%, 3.57, and 4.5% *w*/*v*, respectively. Consequently, BMP-2 (10 μg/ml) was dissolved in the alginate-GelMA solution at 37°C before gel formation. The PLLA-PDA-HA films were dipped into the alginate-GelMA solution for 60 s and withdrawn at a speed of 3,000 rpm for 30 s. The prepared films were dried at room temperature and ionically crosslinked in 100 mM $CaCl_2$ solution for 5 min, following irradiation by UV for 15 s with an OmniCure S2000 UV lamp. Finally, the formed double-crosslinked platform was ultrasonically cleaned and sterilized by ultraviolet irradiation for 30 min before cell experiment. According to various component ratios of hydrogel, the samples were denoted as Alg90-Gel10, Alg70-Gel30, Alg50-Gel50, Alg30-Gel70, and Alg10-Gel90 (**Table 1**). All of them were kept at 4 C overnight.

Sample Characterization

The morphology of the prepared samples with predetermined LBL coating was observed by field emission scanning electron microscopy (FE-TEM, HT7700, Japan). Atomic force microscopy (AFM, MFP-3D-BIO, Asylum Research, United States) was applied to observe the microstructure and surface roughness. The chemical structures of the double-crosslinked hydrogel were measured by Fourier transform infrared (FTIR) spectroscopy (PerkinElmer Spectrum Two) in the 400–4,000 cm^{-1} range. Energy-dispersive spectrometry was performed by EDS (Oxford Instruments, United Kingdom). Surface hydrophilicity is another factor affecting cell attachment, and it was measured by surface water contact angles by a surface roughness meter (Perthometer M1, Mahr, Germany).

Cell Culture and BMP-2 Release

hBMSC line was purchased from the Chinese Academy of Sciences (Shanghai, China). The hBMSCs were maintained in culture with Dulbecco's Modified Eagle's Medium with low glucose (Low/DMEM) (HyClone, Tauranga, New Zealand) containing 10% fetal bovine serum (FBS, Gibco, United States). It was supplemented with antibiotics (100 U ml^{-1} penicillin and 100 μg ml^{-1} streptomycin) (Gibco BRL) in a humidified incubator with a 5% CO_2 atmosphere at 37°C. The medium was changed every 2 days. When the cell density exceeded 85%, the cells were digested with trypsin and passed to the cultured cells in a ratio of 1:3.

The cumulative of BMP-2 release was a representative study on the release of growth factor in this double-crosslinked hydrogel (Niu et al., 2009). Five groups of hydrogels (Alg90-Gel10, Alg70-Gel30, Alg50-Gel50, Alg30-Gel70, and Alg10-Gel90) carrying BMP-2 (10 μg per sample) were put in a 2-ml PBS system (pH = 7.4). The solution stayed in a sustained shaking condition at 120 rpm and 37°C for 14 days. At specified time points, 1 ml of solution was sucked out and an equal volume of PBS was added. The measurement of released BMP-2 from each hydrogel samples was carried out by BCA method. The final cumulative release of BMP-2 (%) was calculated as follows: BMP-2 (%) = (total release of BMP2 / total load of BMP2 in the sample) × 100%).

Cell Viability

Cell adhesion is the first step in facilitating osteogenesis in the scaffold. To check the adhesive effect, the GelMA-alginate hydrogel coating films were put into 24-well plates after

TABLE 2 | Primer sequences of osteogenic genes expressed by hBMSCs.

Gene target	Primers sequence (5′-3′)
OCN	Forward primer: 5′ CGTGGCAACTCCATCTT 3′
	Reverse primer: 5′ AGGGTTTCTTGTCCGTGT 3′
BMP-2	Forward primer: 5′ TGAGGATTAGCAGGTCTTT 3′
	Reverse primer: 5′ TGGATTTGAGGCGTTT 3′
OPN	Forward primer: 5′ TACCTTCTGATTGGGACA 3′
	Reverse primer: 5′ CGAAATTCACGGCTCT 3′
RUNX-2	Forward primer: 5′ GACCACCCAGCCGAACT 3′
	Reverse primer: 5′ CAGCACCGAGCACAGGA 3′

sterilization by UV. Then, the hBMSCs were seeded in each hole at a density of 5×10^4/hole for 4 h. Cell viability was determined using Cell Counting Kit-8 (CCK-8) assay. The suspension was transferred into 96-well plates to detect absorbance value.

Cell Morphology

To verify the morphology of the hBMSCs attached on the coating, the GelMA-alginate hydrogel coating films were co-cultured with hBMSCs for 4 h. The films were gently washed to get rid of impurities and were fixed with 4% paraformaldehyde. Then, the samples were successively stained with 50 mg/ml rhodamine phalloidin for 60 min and with DAPI for 5 min at 4°C. Images were captured by confocal microscopy (Olympus, LX81-ZDC, Japan).

For transmission electron microscopy (TEM) detection, hBMSCs were incubated with GelMA-alginate hydrogel coating films for 4 h at 37°C. Subsequently, after fixing with 4% glutaraldehyde, the fixed samples were dehydrated with a gradient concentration of alcohol (from 30% to 99.5%). The films were dried and sputtered with platinum to test by TEM (HT7700, Hitachi, Japan), respectively.

Cell Proliferation

The hBMSCs were seeded on different surfaces of the films at a density of 5×10^4 cells/hole in 24-well plates. The samples were cleaned by PBS and stained with live and dead cells for 5 min at 3 days, respectively. The images were captured with a fluorescence microscope. Quantitation of cell proliferation was performed by the CCK-8 test, and optical density (OD) was measured at 450 nm on a microplate reader.

Real-Time PCR

After seeding hBMSCs for 7 days, the Total RNA Kit was used to extract total RNA of the cells according to the manufacturer's protocol. Then, the first strand cDNA kits were applied to reverse-transcribe the collected total RNA. Real-time PCR (qPCR) with the Bio-Rad CFX Manager system was performed according to the standard procedure. Amplification was realized by two-step cycling. Melting curves were recorded at a temperature range from 65°C to 95°C. The primers in this study are presented in **Table 2**.

Alkaline Phosphatase Activity Assay

The hBMSCs were seeded on different surfaces of the films at a density of 5×10^4 cells/hole in 24-well plates until the hBMSCs in each group adhered to the films. Subsequently, the osteogenic medium was prepared consisting of 0.2 mmol/ l ascorbic acid, 100 nmol/ l dexamethasone, and 10 mmol/ l β-glycerol phosphate and applied to the hBMSCs. The medium was changed every 2 days. ALP activity was measured at 4 and 7 days after the use of osteogenic medium by a BCIP/NBT ALP Color Development Kit (Beyotime, China).

Alizarin Red Staining

The samples were incubated for 28 days with osteogenic medium and fixed with 4% paraformaldehyde for 10 min at 4°C. Alizarin red (pH = 4.2) staining was carried out at 25°C. Images were captured by microscopy.

Statistical Analysis

Data were recorded as mean ± standard deviation (SD). Student's *t*-test was used for assessing the difference between two groups, while one-way analysis of variance (ANOVA) was used for evaluating the significance among multiple groups. All the statistical analyses were applied with SPSS 13.0 software (SPSS Inc., United States). Differences were regarded significant if $p < 0.05$.

RESULTS AND DISCUSSION

Characterization

In our research, polydopamine coating is firstly formed on PLLA films in alkaline and weak oxidation environment, which has an affinity for hydroxyapatite (Wu, Zhang, Zhang, & Chen, 2021). Relevant research found that hydroxyapatite grown on the surface of dopamine in simulated body fluid is more uniform and more consistent with the extracellular environment of bone tissues than hydroxyapatite mixed in hydrogel (Li et al., 2016; Z.; Wang, Chen, Wang, Chen, & Zhang, 2016). Meanwhile, the outer-

TABLE 3 | Distribution of elements in composition of different ratios (%)

Elements	Alg90-Gel10	Alg70-Gel30	Alg50-Gel50	Alg30-Gel70	Alg10-Gel90
O	40.87	46.97	45.55	53.82	65.99
Na	0.71	0.75	0.73	0.70	4.26
P	1.88	1.57	0.99	1.37	1.51
Cl	29.99	27.30	27.08	22.52	13.25
Ca	26.54	23.42	22.44	21.59	14.99

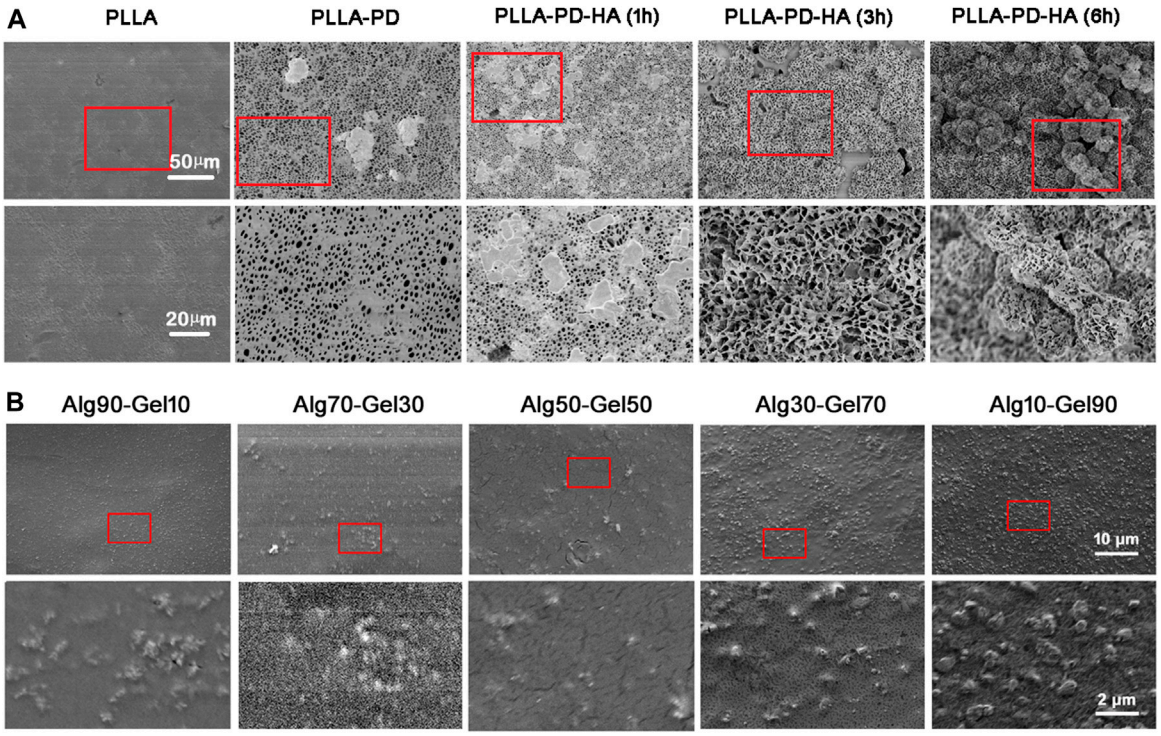

FIGURE 1 | SEM images of **(A)** synthesis of composite coatings: PLLA, PLLA-PD, PLLA-PD-HA (1 h), PLLA-PD-HA (3 h), and PLLA-PD-HA (6 h) and **(B)** different ratios of alginate and GelMA. SEM, scanning electron microscopy; PLLA, poly-L-lactic acid; PD, polydopamine; HA, hydroxyapatite; GelMA, gelatin methacrylate.

layer alginate/GelMA pairs provide enough strength to contain growth factors. The design has obvious advantages: firstly, the microstructure of hydroxyapatite is helpful for achieving the three-dimension-stimulating bone environment for osteogenic-associated cells to grow in. Secondly, the covering alginate/GelMA DN, acting as a barrier, would be beneficial for sustained release of BMP-2, resulting in extending its biofunction toward hBMSCs in a relatively long term (Hu et al., 2012).

Scanning electron microscopy (SEM) and AFM were used to observe the surface morphology of PLLA substrates. As shown in **Figure 1A**, the native PLLA displayed a relatively flat surface feature. The synthesis of polydopamine on the PLLA surface formed an eruptive microporous structure. With the assistance of strengthened simulated body fluid, well-aligned and highly ordered HA clusters were gradually constructed onto the PLLA films. The piles of HA cluster increased with the prolonged time of simulated body fluid on the PLLA. The pore diameter of the HA was approximately 1–5 μm and was distributed at regular intervals. After covering the alginate/GelMA DN outer layer in different proportions, the sample surfaces were scattered with various degrees of projections (**Figure 1B**). As sodium alginate is more viscous than GelMA at the same concentration, the protuberance on substrate surface becomes more obvious as the proportion of sodium alginate in the outer coating decreases.

To measure the distribution of element of the coatings, SEM-EDS was performed for hydrogel analysis. As presented in **Figure 2A**, the hydrogel coatings displayed largely characteristic C, O, H, and Ca elements. The Ca element was derived from hydroxyapatite. In each group, the amount of Ca was presented ~3%. Meanwhile, with the increase of GelMA in the outer layer, the peak of C and O element content gradually accumulated, attributing to the substitution of the methacrylic anhydride for the amino groups of GelMA molecules (**Table 3**). The result of SEM-EDS indirectly manifested the successful coverage of multilayer coating on the PLLA films.

To further verify the double-crosslinked hydrogel, FTIR spectra (**Figure 2B**) showed a similar trend in the hybrid hydrogel composed of GelMA and alginate. The characteristic band peaks of the alginate range of 1,460–1,649 cm^{-1} correspond to carboxylate ions and those of 935–1,107 cm^{-1} relate to C–O of the pyranose ring (Golafshan, Kharaziha, & Fathi, 2017; Craciun, Barhalescu, Agop, Ochiuz, & Medicine, 2019). In addition, the spectrum of GelMA consisted of the peak of C=O at 1,630, 1,548, and 1,240 cm^{-1}. The C–N–H at 1,500–1,570 cm^{-1} could also be recognized. These characters illustrated the reaction of anhydride methacrylate with free amine groups of gelatin (Rahali et al., 2017). The spectrum of Alg90-Gel10, Alg70-Gel30, Alg50-Gel50, Alg30-Gel70, and Alg10-Gel90 presents broad band peaks at 1,621 and 1,557 cm^{-1} probably because of overlapping with the functional groups of the GelMA and alginate composition, implying the successful introduction of the double-crosslinked hydrogel on the surface of PLLA sheets. Moreover, it semi-quantitatively analyzes specific reference bands of functional

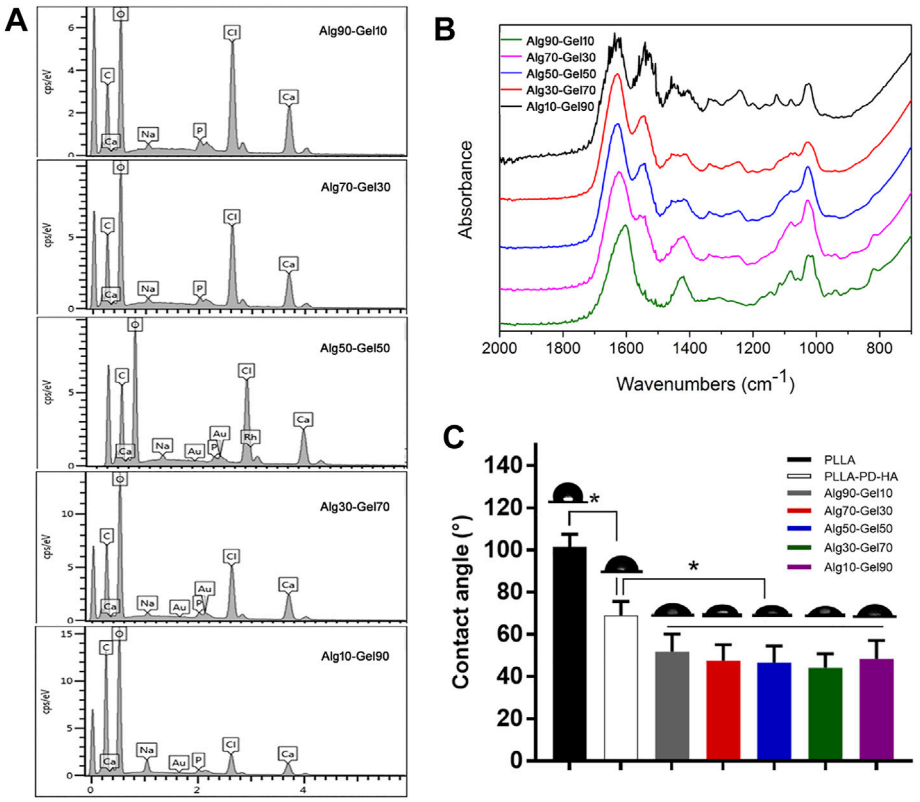

FIGURE 2 | (A) SEM-EDS and **(B)** FTIR spectra for Alg90-Gel10, Alg70-Gel30, Alg50-Gel50, Alg30-Gel70, and Alg10-Gel90. **(C)** Contact angle measurement of water on the surface of different samples. FTIR, Fourier transform infrared.

groups according to the two components of the coatings, which were less affected by the chemical reaction.

Hydrophilicity is another necessary requirement for the osteoblast-related cells to access bone tissue implants (Oliveira et al., 2021). **Figure 2C** displays the water contact angles on the surfaces of the substrate and customized coatings, of which, native PLLA showed a contact angle of 101.40°, while mineralization showed an obviously hydrophilic contact angle of 68.12°. After incorporation of hydrogel, there was a further decrease of contact angle to 51.86°–44.24°. In addition, various proportions of hydrogel components did not affect the change of the contact angle. The result may reflect the corresponding deposition of alginate-GelMA/HA bilayers. The hierarchical microstructure may promote hydrophilicity in a progressive behavior, which has a capillary function to facilitate the drop spreading and coincides with a previous report (Xing et al., 2020). These results demonstrate the successful construction of alginate-GelMA/HA bilayer coating on the PLLA films.

Cell Viability, Attachment, and Proliferation

Cell adhesion, growth, and differentiation are dependent on the degree of biocompatibility. To evaluate the cytotoxicity of the coated samples, the survival rate of cells on the coating surface of each group was determined at the same magnification by staining with dead cells on the third day (green dot: live cells; red dot: dead cells) (**Figure 3A**). Cell viability was assessed by fluorescence microscopy. Although the proportion of dead cells increased slightly in the PLLA group, there were no significant dead cells in each group, indicating that the bilayer coatings in each group had good biosafety and provided an appropriate growth environment for hBMSCs (**Figure 3B**). It is remarkable, however, that there were fewer viable cells in the native PLLA films than in the coatings, which may result in short-term cell adhesion and relative long-term cell proliferation.

After seeding the cells on the samples for 2 h, quantification was performed to measure the cell attachment according to a previous study (Zhang et al., 2018) (**Figure 3C**). Notably, the bilayer coatings facilitated the cells adhering on the substrate rather than the bare PLLA film. The OD values of CCK-8 had nearly identical results in the Alg90-Gel10, Alg70-Gel30, Alg50-Gel50, Alg30-Gel70, and Alg10-Gel90 groups, but were higher than those in the PLLA group. To further evaluate the proliferation of cells in each samples, the number of live hBMSCs was measured by CCK-8 test on days 1, 3, and 7 (**Figure 3D**). Cell numbers increased in all groups, indicating that not only all the bilayer coatings but also the native PLLA provided a suitable microenvironment for cell growth. There were no differences in hBMSCs among the groups on the first day. The proliferative rate in the bilayer groups began to present higher than that in the PLLA alone on day 3. Finally, on day 7, the

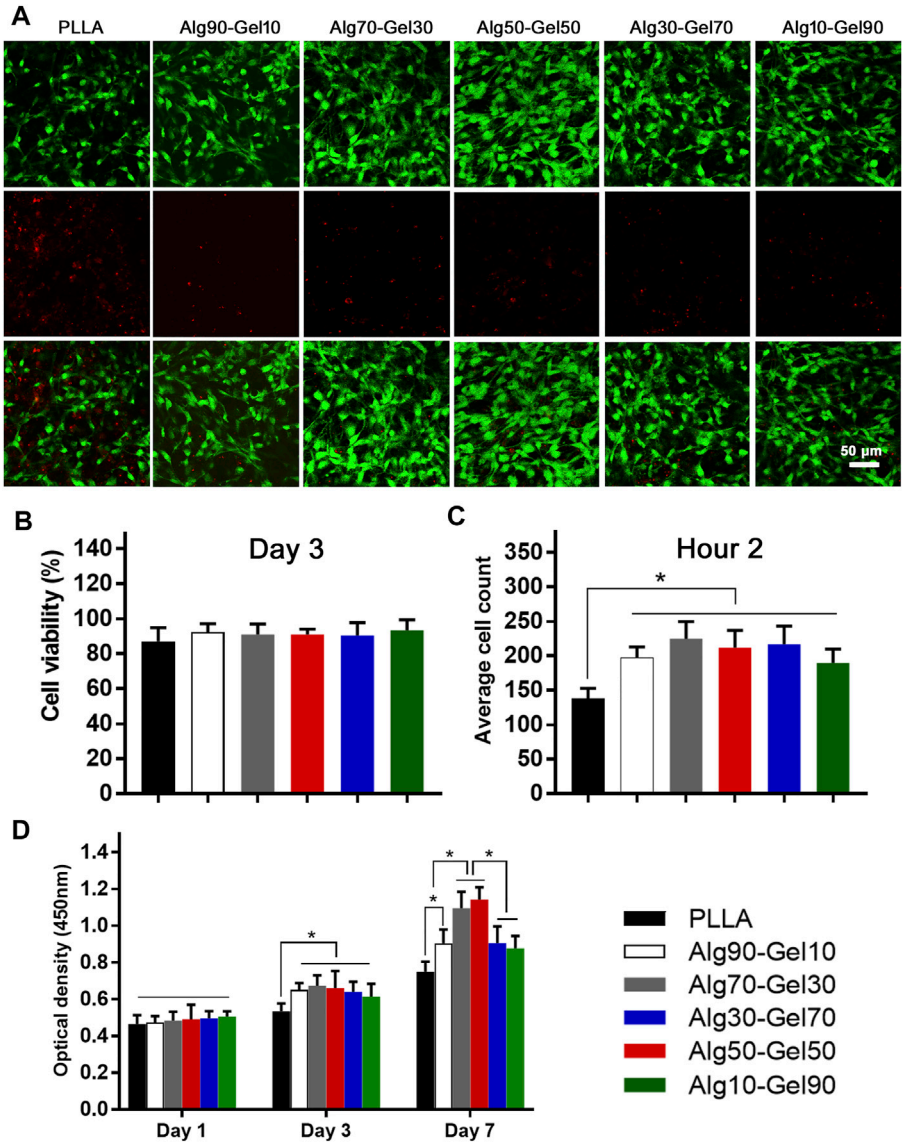

FIGURE 3 | (A) Cell viability of human bone mesenchymal stem cells (hBMSCs) on the different samples (scale: 50 μm) and **(B)** statistical analysis. **(C)** The short-term cell adhesion at hour 2 and **(D)** cell proliferation at days 1, 3, and 7 on the PLLA and bilayer coatings (*$p < 0.05$ compared with the control).

cell proliferation in the Alg70-Gel30 and Alg50-Gel50 groups did an outstanding performance than that in the other five groups, among which the cell growth of the Alg90-Gel10, Alg30-Gel70, and Alg10-Gel90 groups was far superior to that of the PLLA group. These results illustrated that the double-crosslinked hydrogel combined with HA has the advantage to attract osteoblast-related cells more rapidly to adhere to the surface of the substrate.

Cell Morphology

Additionally, the function of hBMSCs corresponds with a well-ordered morphology. Immunofluorescence detection at hour two showed the intracellular microstructure on the surface of the PLLA sheet and bilayer coatings in different proportions. The cytoskeleton was stained with rhodamine-labeled phalloidin, and nuclei were stained with DAPI by confocal microscopy (**Figure 4A**). Most of the hBMSCs that adhered to the PLLA film seemed spherical, while the cells on the bilayer coatings had many obvious cytoskeleton/microfilaments, as well as clear intercellular connections. Particularly, a better directional rearrangement of the cell cytoskeleton was displayed in the Alg70-Gel30 and Alg50-Gel50 groups.

To avoid the interference of fluorescence on cell microstructure, SEM was applied to observe the activity of cells on the coating after 3 days of seeding on the samples (**Figure 4B**). At higher magnification, there were a few hBMSCs on the surface of the native PLLA, and their morphology tended to be elongated. Intercellular connections

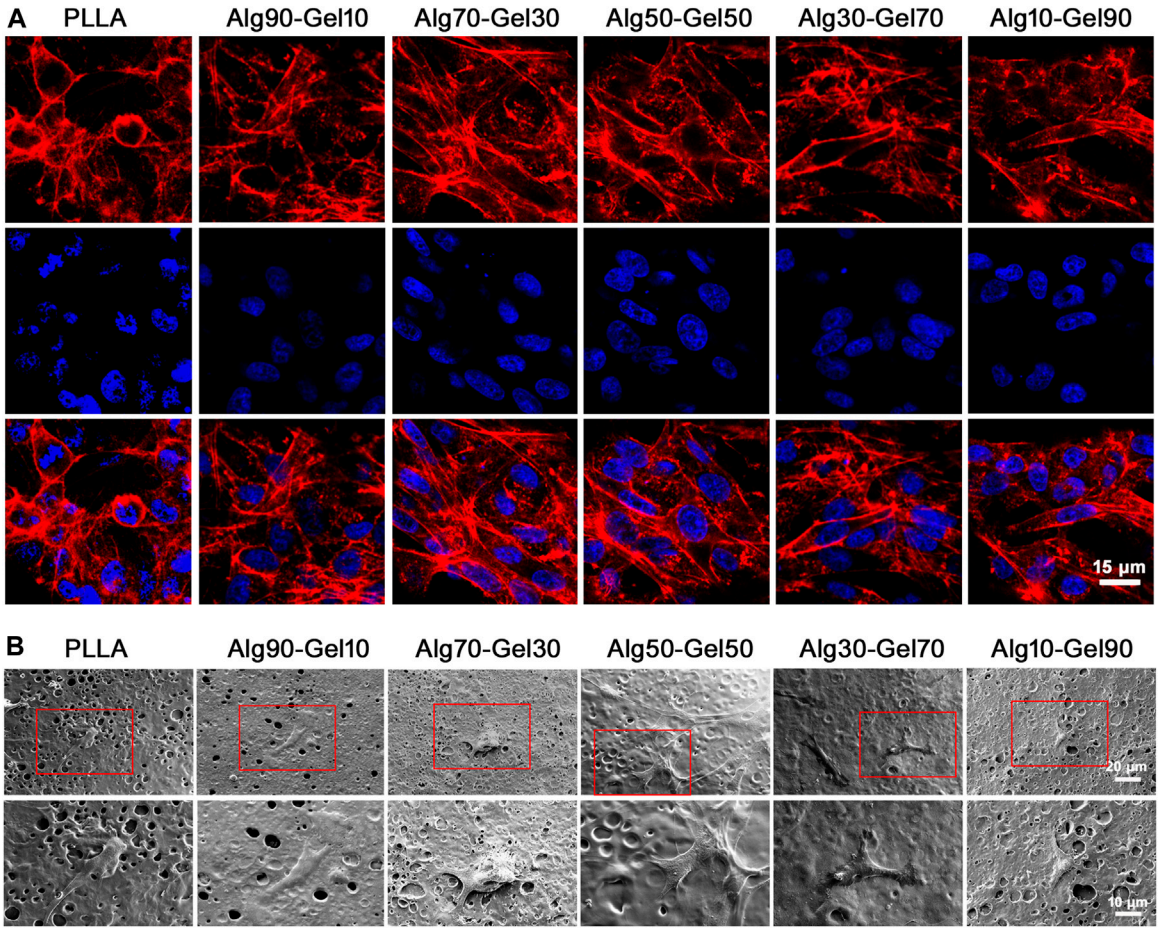

FIGURE 4 | (A) Confocal microscopy images of hBMSCs on different groups at 2 h (red, rhodamine phalloidin; blue, DAPI for nucleus) (scale: 15 μm). **(B)** SEM images of hBMSCs in different groups at 3 days.

between cells were not detected. Cells in the Alg90-Gel10 and Alg10-Gel90 groups began to develop a typical fusiform shape and clearly extend their pseudopods, but the cell size was smaller and the intercellular filaments were still not as clear. In the Alg70-Gel30, Alg50-Gel50, and Alg30-Gel70 groups, we found a longer irregular fusiform structure; the pseudopods were normal size, and the number of cells on the surface of the material increased significantly. For the Alg70-Gel30 and Alg50-Gel50 groups, the extended microstructure with some cell–cell interactions was easy to observe, and the pseudopods tended to extend to the microspores in multiple directions. These results showed that the adhesion and migration of hBMSCs in the Alg70-Gel30 and Alg50-Gel50 groups were significantly better than those in other double-crosslinked coatings, especially in the PLLA group.

Sustained Release of BMP-2 and Expression of Gene

Figure 5A shows an *in vitro* BMP-2 release curve from different ratios of double-crosslinked hydrogels. All the hydrogel systems displayed a sustained release for 2 weeks. In the first 2 days, the release curve of each group showed a relatively steep but not a burst release. The next 5 days, all the groups exhibited a "plateau" release curves and then entered a process of steady and moderate release. The total BMP-2 release of Alg90-Gel10, Alg70-Gel30, Alg50-Gel50, Alg30-Gel70, and Alg10-Gel90 reached 74.08%, 57.12%, 52.84%, 67.81%, and 71.64%, respectively. Then, the additional release of BMP-2 was less than 10%. Since the BMP-2 was kept inside the hydrogel, it is helpful for hBMSCs and osteoblasts attached or grown into the coatings to proliferate, differentiate, and induce bone formation. Moreover, the results seemed to show the higher crosslinking hydrogel as a barrier against growth factor release. On 2 weeks, the BMP-2 loading capacity of five samples was 18.44%, 29.65%, 38.64%, 27.55%, and 22.70%, respectively, and the drug encapsulation efficiency of Alg50-Gel50 hydrogels was 20.20% and 16.94% higher than that of the Alg90-Gel10 and Alg10-Gel90 groups.

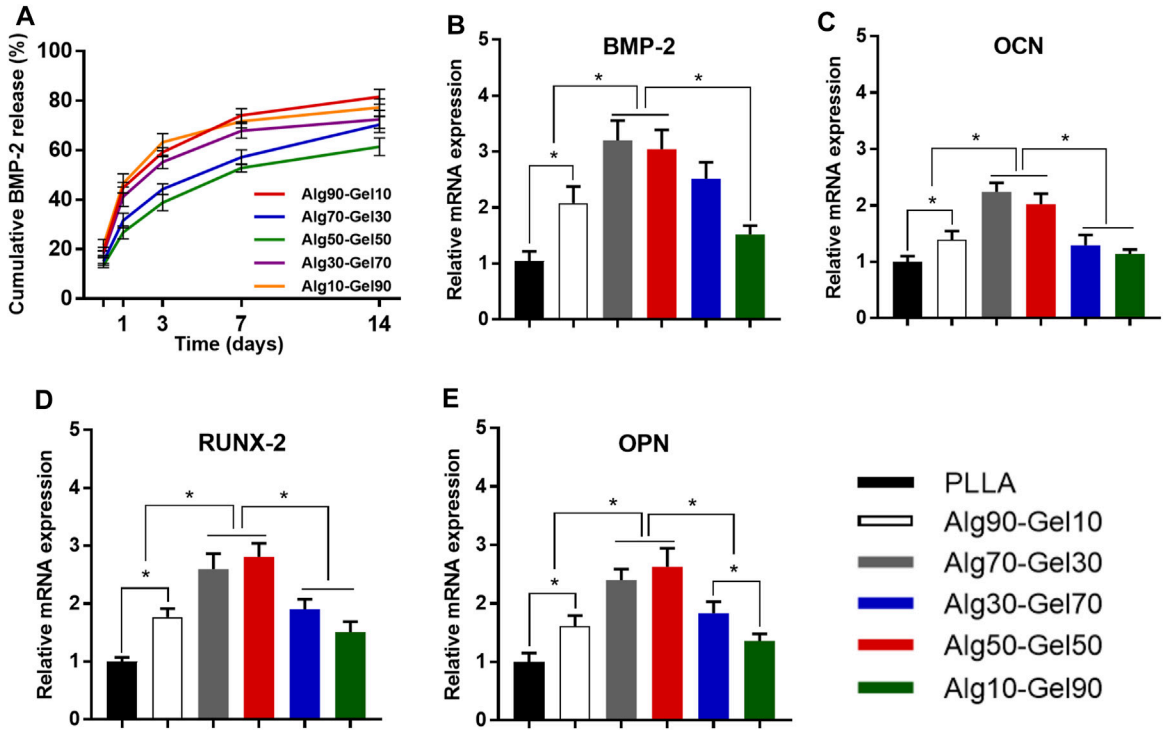

FIGURE 5 | (A) Release curves of BMP-2 from different double-crosslinked hydrogels. The mRNA levels of **(B)** BMP-2, **(C)** OCN, **(D)** RUNX-2, and **(E)** OPN were quantified from hBMSCs cultured in various substrates (*$p < 0.05$ compared with the control).

The differentiation of hBMSCs toward osteoblast lineage could be valued by specific osteoblast mRNA expression. The expression of the four osteogenic-related genes (RUNX-2, BMP-2, OCN, and OPN) was detected by RT-PCR experiments on day 14 (**Table 3**). The cells cultured on PLLA films in DMEM were set as negative control for each experiment, which failed to extract osteogenic-specific genes. In the positive control group, an osteogenic medium, which replaced DMEM, was used to culture hBMSCs on PLLA films. We detected osteogenic-specific gene expression in the positive control group that we treated as reference for other groups. By the 14th day, the expression levels of RUNX-2 and BMP-2, which are the markers of early osteoblast differentiation and bone formation, was higher in the Alg70-Gel30 and Alg50-Gel50 groups than in other bilayer coatings. Meanwhile, the expression of OCN and OPN, which represents late osteogenic formation, showed a similar trend (**Figure 5**).

Osteogenic Differentiation

To reveal the sustained promotion of osteogenesis of hBMSCs on the coatings, alkaline phosphatase staining was applied to detect ALP expression. After hBMSCs were seeded on the surface of different double-crosslinked coatings and constantly induced with osteogenic medium, the staining was carried out on day 4 and day 7 (**Figure 6A**). From the perspective of density, the samples in the Alg70-Gel30 and Alg50-Gel50 groups are more deeply stained compared with the other coating groups and the PLLA group. It indicates that early-stage differentiation could occur in Alg70-Gel30 and Alg50-Gel50 bilayer coatings. To accurately depict the early osteogenesis in these groups, the ALP activity was used in quantification. The ALP expression activity in each group enhanced as the time went on. Among them, the highest was in the Alg70-Gel30 and Alg50-Gel50 groups, which coincided with the result of staining (**Figure 6C**).

At the end stage of osteoblast differentiation, the formation of mineralized nodules is a crucial phenomenon that indicates the maturation of osteoblasts. To evaluate this, Alizarin red staining was used to quantify the degree of mineralization by measuring the number of calcium nodules (stained red spots). Alizarin red staining was conducted on day 28 (**Figure 6B**). The Alg70-Gel30 and Alg50-Gel50 groups had significantly more nodules compared to every other groups (**Figure 6D**). The poor performance of mineral nodules in the PLLA group may result from the lack of BMP-2 release "barrier layer." In consideration of the controlled release of BMP-2 in the hydrogel layer, long-term osteogenic differentiation of hBMSCs can be sustained, which probably has a key role in the formation of mineralized nodules (Feng et al., 2019). In addition, the crosslinked layer of hydrogels provides suitable biological strength for cell adhesion, infiltration, and proliferation (Zhang et al., 2018). In brief, double-crosslinked coating/HA could promote the greatest amount of osteogenesis, especially the outer hydrogel layer such as Alg70-Gel30 and Alg50-Gel50.

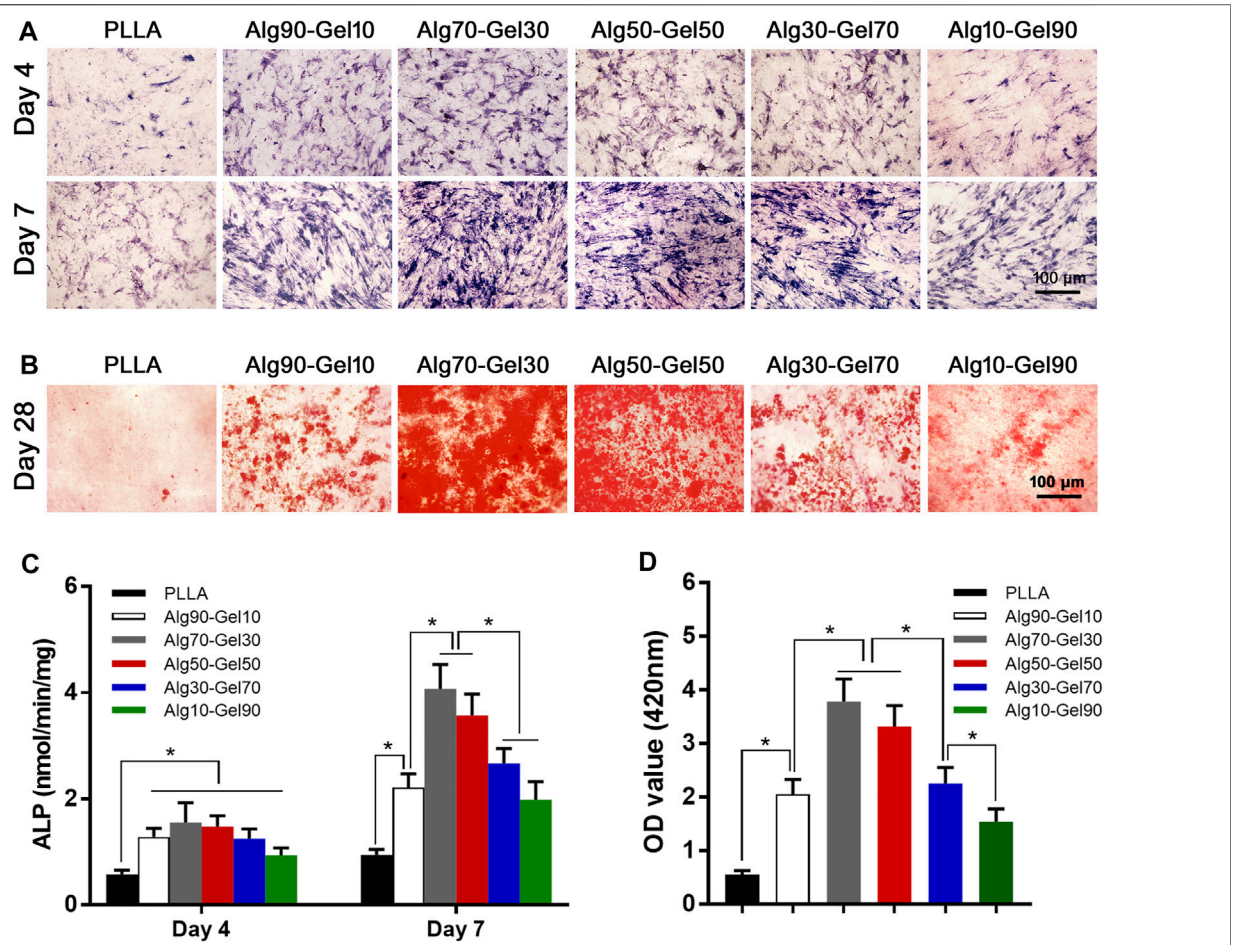

FIGURE 6 | (A) ALP staining at 4 and 7 days (scale: 100 μm). **(B)** Alizarin red staining images at 28 days (scale: 100 μm). Quantitative results of **(C)** ALP activity and **(D)** Alizarin red staining (*$p < 0.05$). ALP, alkaline phosphatase.

CONCLUSION

In this research, we established a bilayer coating with double-crosslinked hydrogels (alginate-GelMA) containing BMP-2 proteins (alginate-GelMA/HA/BMP-2), which displayed great biocompatibility and osteogenesis. The characterization of the coating improved the properties and enhanced the wettability of the native PLLA. To evaluate the biosafety and inductive ability of osteogenesis, the behavior (viability, adherence, and proliferation) and morphology of hBMSCs on the bilayer coatings were tested by multiple exams. The satisfactory function of osteogenesis was verified in bilayer coatings, especially in the specific ratio of alginate to GelMA. We found the best ratios between GelMA and alginate for biological applications. The Alg70-Gel30 and Alg50-Gel50 groups facilitated the osteogenic transformation of hBMSCs. In brief, alginate-GelMA/HA/BMP-2 could increase the hBMSCs' early transformation of osteoblast lineage and promote the osteogenesis of bone defect, especially the outer hydrogel layer such as Alg70-Gel30 and Alg50-Gel50.

DATA AVAILABILITY STATEMENT

The original contributions presented in the study are included in the article/Supplementary Material, and further inquiries can be directed to the corresponding authors.

AUTHOR CONTRIBUTIONS

YM and YY made the same contribution to this work. All authors contributed to the article and approved the submitted version.

FUNDING

This study was funded by the Shanghai "Rising Stars of Medical Talent" Youth Development Program (Shanghai Municipal Health Commission 2019–72) and the Shanghai Sailing Program (No. 18YF1404400).

REFERENCES

Ahn, S. H., Rath, M., Tsao, C.-Y., Bentley, W. E., and Raghavan, S. R. (2021). Single-Step Synthesis of Alginate Microgels Enveloped with a Covalent Polymeric Shell: A Simple Way to Protect Encapsulated Cells. *ACS Appl. Mater. Inter.* 13 (16), 18432–18442. doi:10.1021/acsami.0c20613

Ashwin, B., Abinaya, B., Prasith, T. P., Chandran, S. V., Yadav, L. R., Vairamani, M., et al. (2020). 3D-poly (Lactic Acid) Scaffolds Coated with Gelatin and Mucic Acid for Bone Tissue Engineering. *Int. J. Biol. Macromolecules* 162, 523–532. doi:10.1016/j.ijbiomac.2020.06.157

Blatchley, M. R., Hall, F., Ntekoumes, D., Cho, H., Kailash, V., Vazquez-Duhalt, R., et al. (2021). Discretizing Three-Dimensional Oxygen Gradients to Modulate and Investigate Cellular Processes. *Adv. Sci.* 8 (14), 2100190. doi:10.1002/advs.202100190

Cao, L., Duan, P. G., Wang, H. R., Li, X. L., Yuan, F. L., Fan, Z. Y., et al. (2012). Degradation and Osteogenic Potential of a Novel Poly(lactic Acid)/nano-Sized β-tricalcium Phosphate Scaffold. *Ijn* 7, 5881–5888. doi:10.2147/IJN.S38127

Chen, S., Carlson, M. A., Li, X., Siddique, A., Zhu, W., and Xie, J. (2021). Minimally Invasive Delivery of 3D Shape Recoverable Constructs with Ordered Structures for Tissue Repair. *ACS Biomater. Sci. Eng.* 7, 2204–2211. doi:10.1021/acsbiomaterials.1c00344

Chen, X., Zhu, L., Liu, H., Wen, W., Li, H., Zhou, C., et al. (2019). Biomineralization Guided by Polydopamine-Modifed poly(L-Lactide) Fibrous Membrane for Promoted Osteoconductive Activity. *Biomed. Mater.* 14 (5), 055005. doi:10.1088/1748-605X/ab2f2d

Craciun, A.-M., Barhalescu, M. L., Agop, M., Ochiuz, L., and Medicine, M. M. I. (2019). Theoretical Modeling of Long-Time Drug Release from Nitrosalicyl-Imine-Chitosan Hydrogels through Multifractal Logistic Type Laws. *Comput. Math. Methods Med.* 2019 (2), 1–10. doi:10.1155/2019/4091464

Drury, J. L., Dennis, R. G., and Mooney, D. J. (2004). The Tensile Properties of Alginate Hydrogels. *Biomaterials* 25 (16), 3187–3199. doi:10.1016/j.biomaterials.2003.10.002

Feng, Q., Xu, J., Zhang, K., Yao, H., Zheng, N., Zheng, L., et al. (2019). Dynamic and Cell-Infiltratable Hydrogels as Injectable Carrier of Therapeutic Cells and Drugs for Treating Challenging Bone Defects. *ACS Cent. Sci.* 5 (3), 440–450. doi:10.1021/acscentsci.8b00764

Golafshan, N., Kharaziha, M., and Fathi, M. (2017). Tough and Conductive Hybrid Graphene-PVA: Alginate Fibrous Scaffolds for Engineering Neural Construct. *Carbon* 111, 752–763. doi:10.1016/j.carbon.2016.10.042

Gregurec, D., Wang, G., Pires, R. H., Kosutic, M., Lüdtke, T., Delcea, M., et al. (2016). Bioinspired Titanium Coatings: Self-Assembly of Collagen-Alginate Films for Enhanced Osseointegration. *J. Mater. Chem. B* 4 (11), 1978–1986. doi:10.1039/c6tb00204h

Hsu, C.-S., Haag, S. L., Bernards, M. T., and Li, Q. (2020). Evaluation of Chlorine Substituted Hydroxyapatite (ClHAP)/polydopamine Composite Coatings on Ti64. *Colloids Surf. B: Biointerfaces* 189, 110799. doi:10.1016/j.colsurfb.2020.110799

Hu, Y., Cai, K., Luo, Z., Xu, D., Xie, D., Huang, Y., et al. (2012). TiO2 Nanotubes as Drug Nanoreservoirs for the Regulation of Mobility and Differentiation of Mesenchymal Stem Cells. *Acta Biomater.* 8 (1), 439–448. doi:10.1016/j.actbio.2011.10.021

Kaito, T., Myoui, A., Takaoka, K., Saito, N., Nishikawa, M., Tamai, N., et al. (2005). Potentiation of the Activity of Bone Morphogenetic Protein-2 in Bone Regeneration by a PLA-PEG/hydroxyapatite Composite. *Biomaterials* 26 (1), 73–79. doi:10.1016/j.biomaterials.2004.02.010

Kandziora, F., Pflugmacher, R., Scholz, M., Eindorf, T., Schnake, K. J., and Haas, N. P. (2004). Bioabsorbable Interbody Cages in a Sheep Cervical Spine Fusion Model. *Spine* 29 (17), 1845–1855. discussion 1856. doi:10.1097/01.brs.0000137060.79732.78

Kraehenbuehl, T. P., Zammaretti, P., Van der Vlies, A. J., Schoenmakers, R. G., Lutolf, M. P., Jaconi, M. E., et al. (2008). Three-dimensional Extracellular Matrix-Directed Cardioprogenitor Differentiation: Systematic Modulation of a Synthetic Cell-Responsive PEG-Hydrogel. *Biomaterials* 29 (18), 2757–2766. doi:10.1016/j.biomaterials.2008.03.016

Lee, H., Dellatore, S. M., Miller, W. M., and Messersmith, P. B. (2007). Mussel-inspired Surface Chemistry for Multifunctional Coatings. *Science* 318 (5849), 426–430. doi:10.1126/science.1147241

Li, M., Liu, X., Xu, Z., Yeung, K. W. K., and Wu, S. (2016). Dopamine Modified Organic-Inorganic Hybrid Coating for Antimicrobial and Osteogenesis. *ACS Appl. Mater. Inter.* 8 (49), 33972–33981. doi:10.1021/acsami.6b09457

Liang, Y., Chen, B., Li, M., He, J., Yin, Z., and Guo, B. (2020). Injectable Antimicrobial Conductive Hydrogels for Wound Disinfection and Infectious Wound Healing. *Biomacromolecules* 21 (5), 1841–1852. doi:10.1021/acs.biomac.9b01732

Lin, H.-H., Hsieh, F.-Y., Tseng, C.-S., and Hsu, S.-h. (2016). Preparation and Characterization of a Biodegradable Polyurethane Hydrogel and the Hybrid Gel with Soy Protein for 3D Cell-Laden Bioprinting. *J. Mater. Chem. B* 4 (41), 6694–6705. doi:10.1039/c6tb01501h

Nair, M. S., Tomar, M., Punia, S., Kukula-Koch, W., and Kumar, M. (2020). Enhancing the Functionality of Chitosan- and Alginate-Based Active Edible Coatings/films for the Preservation of Fruits and Vegetables: A Review. *Int. J. Biol. Macromolecules* 164, 304–320. doi:10.1016/j.ijbiomac.2020.07.083

Nichol, J. W., Koshy, S. T., Bae, H., Hwang, C. M., Yamanlar, S., and Khademhosseini, A. (2010). Cell-laden Microengineered Gelatin Methacrylate Hydrogels. *Biomaterials* 31 (21), 5536–5544. doi:10.1016/j.biomaterials.2010.03.064

Niu, X., Feng, Q., Wang, M., Guo, X., and Zheng, Q. (2009). Porous Nano-HA/collagen/PLLA Scaffold Containing Chitosan Microspheres for Controlled Delivery of Synthetic Peptide Derived from BMP-2. *J. Controlled Release* 134 (2), 111–117. doi:10.1016/j.jconrel.2008.11.020

Oliveira, F. C., Carvalho, J. O., Magalhães, L. S. S. M., da Silva, J. M., Pereira, S. R., Gomes Júnior, A. L., et al. (2021). Biomineralization Inspired Engineering of Nanobiomaterials Promoting Bone Repair. *Mater. Sci. Eng. C* 120, 111776. doi:10.1016/j.msec.2020.111776

Pacelli, S., Basu, S., Berkland, C., Wang, J., and Paul, A. (2018). Design of a Cytocompatible Hydrogel Coating to Modulate Properties of Ceramic-Based Scaffolds for Bone Repair. *Cel. Mol. Bioeng.* 11 (3), 211–217. doi:10.1007/s12195-018-0521-3

Piluso, S., Skvortsov, G. A., Altunbek, M., Afghah, F., Khani, N., Koç, B., et al. (2021). 3D Bioprinting of Molecularly Engineered PEG-Based Hydrogels Utilizing Gelatin Fragments. *Biofabrication* 13 (4), 045008. doi:10.1088/1758-5090/ac0ff0

Rahali, K., Ben Messaoud, G., Kahn, C., Sanchez-Gonzalez, L., Kaci, M., Cleymand, F., et al. (2017). Arab-tehrany, E. (Synthesis and Characterization of Nanofunctionalized Gelatin Methacrylate Hydrogels. *Ijms* 18 (12), 2675. doi:10.3390/ijms18122675

Rai, A., Pinto, S., Evangelista, M. B., Gil, H., Kallip, S., Ferreira, M. G. S., et al. (2016). High-density Antimicrobial Peptide Coating with Broad Activity and Low Cytotoxicity against Human Cells. *Acta Biomater.* 33, 64–77. doi:10.1016/j.actbio.2016.01.035

Silva, J. M., García, J. R., Reis, R. L., García, A. J., and Mano, J. F. (2017). Tuning Cell Adhesive Properties via Layer-By-Layer Assembly of Chitosan and Alginate. *Acta Biomater.* 51, 279–293. doi:10.1016/j.actbio.2017.01.058

Simó, G., Fernández-Fernández, E., Vila-Crespo, J., Ruipérez, V., and Rodríguez-Nogales, J. M. (2017). Research Progress in Coating Techniques of Alginate Gel Polymer for Cell Encapsulation. *Carbohydr. Polym.* 170, 1–14. doi:10.1016/j.carbpol.2017.04.013

Sobolev, A., Valkov, A., Kossenko, A., Wolicki, I., Zinigrad, M., and Borodianskiy, K. (2019). Bioactive Coating on Ti Alloy with High Osseointegration and Antibacterial Ag Nanoparticles. *ACS Appl. Mater. Inter.* 11 (43), 39534–39544. doi:10.1021/acsami.9b13849

Szustakiewicz, K., Włodarczyk, M., Gazińska, M., Rudnicka, K., Płociński, P., Szymczyk-Ziółkowska, P., et al. (2021). The Effect of Pore Size Distribution and L-Lysine Modified Apatite Whiskers (HAP) on Osteoblasts Response in PLLA/HAP Foam Scaffolds Obtained in the Thermally Induced Phase Separation Process. *Ijms* 22 (7), 3607. doi:10.3390/ijms22073607

Tan, W., Gao, C., Feng, P., Liu, Q., Liu, C., Wang, Z., et al. (2021). Dual-functional Scaffolds of poly(L-Lactic Acid)/nanohydroxyapatite Encapsulated with Metformin: Simultaneous Enhancement of Bone Repair and Bone Tumor Inhibition. *Mater. Sci. Eng. C* 120, 111592. doi:10.1016/j.msec.2020.111592

Tas, A. C., and Bhaduri, S. B. (2004). Rapid Coating of Ti6Al4V at Room Temperature with a Calcium Phosphate Solution Similar to 10× Simulated Body Fluid. *J. Mater. Res.* 19 (9), 2742–2749. doi:10.1557/JMR.2004.0349

Tsai, W.-B., Chien, C.-Y., Thissen, H., and Lai, J.-Y. (2011). Dopamine-assisted Immobilization of Poly(ethylene Imine) Based Polymers for Control of Cell-

Surface Interactions. *Acta Biomater.* 7 (6), 2518–2525. doi:10.1016/j.actbio.2011.03.010

Tsai, Y.-C., Li, S., Hu, S.-G., Chang, W.-C., Jeng, U.-S., and Hsu, S.-h. (2015). Synthesis of Thermoresponsive Amphiphilic Polyurethane Gel as a New Cell Printing Material Near Body Temperature. *ACS Appl. Mater. Inter.* 7 (50), 27613–27623. doi:10.1021/acsami.5b10697

Wang, X., Guan, S., Zhang, K., and Li, J. (2020). Benlysta-Loaded Sodium Alginate Hydrogel and its Selective Functions in Promoting Skin Cell Growth and Inhibiting Inflammation. *ACS Omega* 5 (18), 10395–10400. doi:10.1021/acsomega.0c00283

Wang, Z., Chen, L., Wang, Y., Chen, X., and Zhang, P. (2016). Improved Cell Adhesion and Osteogenesis of Op-HA/PLGA Composite by Poly(dopamine)-Assisted Immobilization of Collagen Mimetic Peptide and Osteogenic Growth Peptide. *ACS Appl. Mater. Inter.* 8 (40), 26559–26569. doi:10.1021/acsami.6b08733

Wu, Y., Zhang, Y., Zhang, R., and Chen, S. (2021). Preparation and Properties of Antibacterial Polydopamine and Nano-Hydroxyapatite Modified Polyethylene Terephthalate Artificial Ligament. *Front. Bioeng. Biotechnol.* 9, 630745. doi:10.3389/fbioe.2021.630745

Xing, H., Li, R., Wei, Y., Ying, B., Li, D., and Qin, Y. (2020). Improved Osteogenesis of Selective-Laser-Melted Titanium Alloy by Coating Strontium-Doped Phosphate with High-Efficiency Air-Plasma Treatment. *Front. Bioeng. Biotechnol.* 8 (367). doi:10.3389/fbioe.2020.00367

Zhang, J., Zhang, W., Bao, T., and Chen, Z. (2014). Mussel-inspired Polydopamine-Assisted Hydroxyapatite as the Stationary Phase for Capillary Electrochromatography. *Analyst* 139 (1), 242–250. doi:10.1039/c3an01668d

Zhang, K., Jia, Z., Yang, B., Feng, Q., Xu, X., Yuan, W., et al. (2018). Adaptable Hydrogels Mediate Cofactor-Assisted Activation of Biomarker-Responsive Drug Delivery via Positive Feedback for Enhanced Tissue Regeneration. *Adv. Sci.* 5 (12), 1800875. doi:10.1002/advs.201800875

Zhang, Y., Li, R., Wu, W., Qing, Y. a., Tang, X., Ye, W., et al. (2018). Adhesion and Proliferation of Osteoblast-like Cells on Porous Polyetherimide Scaffolds. *Biomed. Res. Int.* 2018, 1–7. doi:10.1155/2018/1491028

Conflict of Interest: The authors declare that the research was conducted in the absence of any commercial or financial relationships that could be construed as a potential conflict of interest.

Publisher's Note: All claims expressed in this article are solely those of the authors and do not necessarily represent those of their affiliated organizations or those of the publisher, the editors and the reviewers. Any product that may be evaluated in this article, or claim that may be made by its manufacturer, is not guaranteed or endorsed by the publisher.

Copyright © 2021 Ma, You, Cao, Liang, Tian, Dong and Lin. This is an open-access article distributed under the terms of the Creative Commons Attribution License (CC BY). The use, distribution or reproduction in other forums is permitted, provided the original author(s) and the copyright owner(s) are credited and that the original publication in this journal is cited, in accordance with accepted academic practice. No use, distribution or reproduction is permitted which does not comply with these terms.

frontiers in Bioengineering and Biotechnology

ORIGINAL RESEARCH
published: 02 December 2021
doi: 10.3389/fbioe.2021.794769

A Sequential Therapeutic Hydrogel With Injectability and Antibacterial Activity for Deep Burn Wounds' Cleaning and Healing

Sizhen Wang[1†], Jie Li[2†], Zhiqiang Ma[3†], Linhong Sun[3], Lei Hou[3], Ying Huang[3], Yunchang Zhang[3], Beibei Guo[3*] and Feng Yang[3*]*

[1]College of Pharmacy, Fujian University of Traditional Chinese Medicine, Fuzhou, China, [2]Department of Dermatology, 967 Hospital of the Joint Logistics Support Force of PLA, Dalian, China, [3]Department of Inorganic Chemistry, School of Pharmacy, Second Military Medical University, Shanghai, China

OPEN ACCESS

Edited by:
Junqing Wang,
Sun Yat-sen University, China

Reviewed by:
Xiaowei Zeng,
Sun Yat-sen University, China
Huaping Tan,
Nanjing University of Science and Technology, China

***Correspondence:**
Zhiqiang Ma
briskbreeze@126.com
Beibei Guo
bbguo@smmu.edu.cn
Feng Yang
yangfeng1008@126.com

[†]These authors have contributed equally to this work and share first authorship

Specialty section:
This article was submitted to Biomaterials, a section of the journal Frontiers in Bioengineering and Biotechnology

Received: 14 October 2021
Accepted: 11 November 2021
Published: 02 December 2021

Citation:
Wang S, Li J, Ma Z, Sun L, Hou L, Huang Y, Zhang Y, Guo B and Yang F (2021) A Sequential Therapeutic Hydrogel With Injectability and Antibacterial Activity for Deep Burn Wounds' Cleaning and Healing. Front. Bioeng. Biotechnol. 9:794769. doi: 10.3389/fbioe.2021.794769

As a severe clinical challenge, escharotomy and infection are always the core concerns of deep burn injuries. However, a usual dressing without multifunctionality leads to intractable treatment on deep burn wounds. Herein, we fabricated a sequential therapeutic hydrogel to solve this problem. Cross-linked by modified polyvinyl alcohol (PVA-SH/ε-PL) and benzaldehyde-terminated F127 triblock copolymers (PF127-CHO), the hydrogel demonstrated excellent mechanical properties, injectability, tissue adhesiveness, antibacterial activity, biocompatibility, and satisfactory wound cleaning through both *in vitro* and *in vivo* assays. Additionally, based on the conception of "sequential therapy," we proposed for the first time to load bromelain and EGF into the same hydrogel in stages for wound cleaning and healing. This work provides a strategy to fabricate a promising wound dressing for the treatment of deep burn wounds with injectability and improved patients' compliance as it simplified the process of treatment due to its "three in one" characteristic (antibacterial activity, wound cleaning, and healing effects); therefore, it has great potential in wound dressing development and clinical application.

Keywords: hydrogel, sequential therapy, deep burn wounds, eschar cleaning, antibiosis, injectability

INTRODUCTION

Burn injury is a major cause of trauma in both civilian and military environments (Yaacobi et al., 2021). Each year, there are more than 11 million burn patients with severe necrosis, and about 180,000 people died (Najath et al., 2021; Kaddoura et al., 2017; Dong et al., 2020). Also, the complex wound environment leads to a series of complications that occur during the long and slow repair processes. The necrosis and complication gravely threaten to burn patients' lives. Traditional treatment for burn injuries includes debridement, skin grafting for large-scale burn, and medical care to prevent infection and promote wound healing. Hence, it always takes a long period to heal the burn wound, especially for the debridement surgery in which parts of healthy tissue are inevitably discarded, generating a more complicated and aggravated situation. Besides, in a medically deprived environment, deficiency of medical care makes debridement surgery unavailable and a lower compliance of burned patients. In short, the above situations urgently call a simple and effective treatment for burn injuries.

A number of products have been utilized to dress the burn wounds with simpler and more efficient strategies. For example, NexoBrid® from Israel is a selective enzymatic wound cleaning product (Rosenberg et al., 2014; Shoham et al., 2020). It can clean eschar based on bromelain without surgery in clinical research, which has been included in the European Consensus Guidelines since 2017 (Hirche et al., 2020). Unfortunately, without injectability, insufficient coating may occur on the irregular shaped wounds with NexoBrid®. Besides, gauze (Fang et al., 2021; Chen et al., 2021a; Said et al., 2021), electrospun nanofiber (Lutfi et al., 2021; Shahrousvand et al., 2021; Zhu et al., 2021), porous foam (Wang et al., 2008; Staruch et al., 2017), biocompatible membrane (Huang et al., 2021), microfibers (Zhao et al., 2015; Yu et al., 2017), and hydrogels (Soriano et al., 2020; Yuan et al., 2021; Kopecki, 2021) can be used as burn wound dressings today. However, most of them cannot display critical properties such as exudates which are absorbing and moisture-maintaining at the same time compared with hydrogel dressings (Gou and Ma, 2018; Zhao et al., 2018; Gobhril and Grinstaff, 2015). Last but not least, burn injury is always intractable as a result of infection, so dressings with antimicrobial activity are requisite (Chen et al., 2021b). Therefore, injectable dressing with exudates absorbing, moisture-maintaining, and antibacterial effect is urgently demanded for deep burn wound.

Herein, we fabricated a novel multifunctional hydrogel with a triple-network structure for wound cleaning and accelerating burn wound healing. Briefly, precursor solutions such as PF127-CHO and PVA-SH/ε-PL were mixed and stirred to make PVA-SH/ε-PL-az-PF127-CHO hydrogel (PLC). In this system, PVA-SH was designed to prevent bromelain oxidation by the sulfhydryl groups. Moreover, amino groups on PVA-SH and ε-PL activated Schiff-base reaction with PF127-CHO to provide a double-network structure; at the same time, PF127-CHO was self-assembled into micelles through physical cross-linking, leading to the preparation of triple-network PLC hydrogel. Meanwhile, partial sulfhydryl groups on PVA-SH could be oxidized to form disulfide bonds to enhance cross-linking. The novel Schiff-base hydrogel we designed had the inherent ability of an antibacterial, which was credited to Schiff-base compounds (Huijun et al., 2020; Suo et al., 2021). What is more, the weak acid environment of the wound promotes the release of ε-PL from PLC, improving the antibacterial efficiency of PLC because of its fantastic antimicrobial property (Huang et al., 2020). The anti-infective effect against methicillin-resistant *Staphylococcus aureus* (MRSA) and *Escherichia coli* (*E. coli*) was verified by antibacterial assays *in vitro*, and the tissue adhesiveness was confirmed by the adhesive strength test. Based on a concept of "sequential therapy" first proposed here, which means different treatments are adopted at certain times in a course of treatment, we loaded bromelain (BM) and EGF in stages to prepare (BM/EGF)@PLC at a certain time for wound cleaning and healing. As a result, with its injectability, (BM/EGF)@PLC is geared for irregular shaped wounds; with the combination of "sequential therapy," (BM/EGF)@PLC shows great potential in dressing development and clinical treatment for deep burn wounds while improving patients' compliance.

MATERIALS AND METHODS

Materials

Polyvinyl alcohol (PVA) and Pluronic F127 (PF127, Mn = 12,600) were purchased from Sinopharm Chemical Reagents Co. Ltd. (China) and BASF(Germany), respectively. Glutathione (GSH), L-Cysteine (L-Cys), ethyl sulfonyl chloride, triethylamine, p-hydroxy benzaldehyde, and bromelain were supplied by damas-beta (China). ε-poly-L-lysine (ε-PL) and human recombinant epidermal growth factor (EGF) were provided by Alladin (China) and Shanghai Huidun Biotechnology Co., Ltd (China), respectively.

Preparation of PLC Hydrogels and Drug-Loaded Hydrogels

Methods on the preparation of hydrogel precursors were described in the Supplementary Material. PLC hydrogels and drug-loaded hydrogels were prepared as below: PF127-CHO was dissolved in phosphate buffer saline (PBS) (10 mM, pH 7.4) to a final concentration of 25% (w/v). PVA-SH/ε-PL solution was prepared according to the molar ratio of carboxyl groups on ε-PL and hydroxy groups on PVA, which were 75:1, 50:1, 100:1, and 200:1, respectively. Then, PF127-CHO and PVA-SH/ε-PL solution was mixed homogenously with the molar ratio of aldehyde groups on PF127-CHO and amino groups on PVA-SH/ε-PL being 3:1, and was stirred for complete hydrogel formation. The obtained hydrogels were named according to the molar ratio of the precursor solutions. Briefly, the hydrogel prepared with PF127-CHO and PVA-SH/ε-PL (75:1, 50:1, 100:1, and 200:1) was named PLC3, PLC3-1, PLC3-2, and PLC3-3, respectively. To encapsulate bromelain and EGF into the hydrogel in stages, bromelain and EGF aqueous solution containing the pre-set amounts of drugs were mixed with PF127-CHO solution and then hydrogel was formed with PVA-SH/ε-PL, respectively. The final drug-loaded hydrogel system was simplified as (BM/EGF)@PLC.

Characterization

Polymers were verified by ^{1}H NMR, and the special functional groups were recorded by FT-IR. SEM (Tescan Mira 3 XH, Czech Republic) was utilized to investigate the morphology of PLC after freeze-drying. Rheological properties of PLC were studied by a rheometer (HAAKE MARS, thermo scientific). The properties of swelling, degradation, and moisturizing were assessed as below.

For the swelling test, the freeze-dried hydrogel samples were weighed accurately and immersed in PBS (pH 7.4) solution at 37°C. Then, the samples were taken out and weighed immediately after drying the surface. The swelling ratio (SR) was calculated by the following equation:

$$SR(\%) = \frac{(W_t - W_0)}{W_0} \times 100\%,$$

where W_t is the weight of PLC at predetermined time intervals and W_0 is the weight of the initial dried sample.

For the degradation kinetics, hydrogel bulks were immersed into PBS (pH7.4) and incubated at 37°C. At predetermined time intervals, the hydrogel samples were taken out and freeze-dried before the determination of dry weight. The biodegradation rate (BR) was calculated according to the following equation:

$$BR(\%) = \frac{(W_0 - W_t)}{W_0} \times 100\%,$$

where W_0 and W_t are the weights of original hydrogels and remanent hydrogels, respectively.

For the moisture retention assay, PLCs were weighed before being put into the dryer and then taken out to be weighed at the predetermined time. The moisture rate (MR) was calculated by the following equation:

$$MR(\%) = \frac{(W_t - W_0)}{W_0} \times 100\%,$$

where W_t is the weight of PLC at predetermined time intervals and W_0 is the weight of the initial sample. The experiments were conducted in triplicate.

In Vitro Drug Release Assay

1 ml PLC hydrogel loaded with bromelain (10 mg) were immersed into 5 ml PBS (pH = 7.4) and placed into a shaking incubator of 37°C, 100 rpm. At pre-set intervals, 60 μL release medium was withdrawn and 60 μL fresh buffer was supplemented. The absorbance of the release medium at 562 nm was measured. The release amount of bromelain was calculated using a predetermined standard profile. The *in vitro* release of EGF (3 mg) from the hydrogel was conducted in PBS using the aforementioned method. The release amounts of both drugs were quantified with a BCA Protein Assay Kit (P0012, Beyotime).

Adhesive Strength Test

Adhesive strength of PLC was tested by a lap shear testing (Li et al., 2018). Briefly, 0.3 ml hydrogel precursor solution of PLC (PLC1, PLC3, PLC3-1, PLC3-2, and PLC3-3) was applied onto a piece of gelatin-coated glass to form a hydrogel layer (PLC1 was synthesized with a similar method as PLC3, except for the use of PF127 instead of PF127-CHO in preparation). After that, the sample was pasted by another piece of gelatin-coated glass with a contacting area of 25 mm × 25 mm and tested by a tensile machine (TH-8203A). All measurements were conducted in triplicate.

Antimicrobial Test

The antibacterial activity of PLC was tested by the inhibitor zone test and agar plate colony counting test against MRSA and *E. coli*. First, the inhibitor zone test was performed with bacteria suspension applied on the culture medium. Second, hydrogel samples were cut into about 10 mm in diameter and put on the surface of the culture medium to cover the bacteria, and then cultured at 37°C for 24 h. The antibacterial effect was assessed by measuring the diameter of the inhibitor zone. For the agar plate colony counting test, the hydrogel extract was added into bacteria suspension and the mixture was applied on the culture medium evenly, and then cultured at 37°C for 24 h. The number of colonies was counted to evaluate the antibacterial activity of PLC. All measurements were conducted in triplicate.

Cytocompatibility Evaluation

The cytocompatibility of PLC was evaluated by the following tests. Briefly, L929 cells were seeded into 96-well microplates at a density of 1×10^4 cells per well. After incubation for 12 h, 100 μL culture medium containing different concentrations (10, 5, 2.5, 1, and 0.5 mg/ml) of the hydrogel extracts (PLC3, PLC3-1, PLC3-2, and PLC3-3) was added into per well and incubated for 24 h, respectively. After washing with PBS, CCK-8 dye solution was used to evaluate the cell viability.

The Live/Dead assay and CCK-8 assay were further conducted to assess the cytocompatibility of (BM/EGF)@PLC including BM@PLC3 and EGF@PLC3. CCK-8 assay was conducted in the same way as the method above, except the concentrations (10, 5, 2.5, 1.25, and 0.625 mg/ml) of hydrogel samples (PLC3, BM@PLC3, and EGF@PLC3). The Live/Dead staining assay was carried out with L929 cells seeded into 24 well microplates at a density of 5×10^4 cells per well. After incubation for 12 h, the 300 μL culture medium containing EGF@PLC3 (10 μg/ml of EGF), EGF (10 μg/ml), BM@PLC3 (20 μg/ml of bromelain), and bromelain (20 μg/ml) was added into per well, respectively, and incubated for 24 h. The fluorescent images were taken by a fluorescence microscope, on which live cells were stained as green and dead cells were stained as red. All measurements were conducted in triplicate.

Hemolytic Test

Briefly, the hydrogel extract (PLC3, PLC3-1, PLC3-2, PLC3-3, BM@PLC3, and EGF@PLC3) and the red blood cell suspension were mixed with equal volumes and incubated at 37°C for 1 h. The samples were centrifugated and the supernatants were collected to determine the absorbance value under 540 nm. Besides, the sodium chloride injection (0.9%) and the red blood cell suspension that mixed with equal volume served as the negative group, while using ultra-pure water instead of sodium chloride injection (0.9%) served as the positive group. The hemolysis ratio (HR) was calculated by the following equation:

$$HR(\%) = \frac{(A_i - A_n)}{(A_p - A_n)} \times 100\%,$$

where A_i is the absorbance value of hydrogel samples, and A_n and A_p are the absorbance values of negative and positive groups, respectively. The experiment was conducted in triplicate.

Cell Scratch Experiment

L929 cells were seeded into 6-well microplates at a density of 4×10^5 cells per well. After incubation for 48 h, 2 ml culture

medium containing EGF@PLC3, EGF, and PLC3 was added into per well, respectively. The result in each group was investigated by a microscope, and photos were taken at 0, 24, and 48 h, respectively. The scratch area in each group was measured by ImageJ. The migration rate (MR) was calculated by the following equation:

$$MR(\%) = \frac{(S_0 - S_i)}{S_0} \times 100\%,$$

where S_i is the scratch area of the hydrogel at predetermined time intervals and S_0 is the area of 0 h. The experiment was conducted in triplicate.

Deep Partial-Thickness Skin Burns' Wound Healing Effect *In Vivo*

Male Sprague Dawley rats (SD), weighing 200–250 g, were divided into 4 groups randomly, with 6 rats in each group. A deep partial-thickness skin burn wound on the dorsum was made using a scald apparatus (ZH-YLS-5Q, Huaibei Zhenghua Biological Instrument Co., Ltd) with a copper rod (11 mm, 100°C, 10 s) after anesthetizing by intraperitoneal injection of 10% chloral hydrate at a dose of 0.3 ml/100 g. Then, the (BM/EGF)@PLC3 group was covered with (BM/EGF)@PLC3 hydrogels in stages according to the "sequential therapy." Therein, BM@PLC3 was used on the first day, while EGF@PLC3 was adopted in the following treatment. The PLC3 group was treated with PLC3 dressing, the positive group was covered with sulfadiazine silver cream (25 g, China Resources Kunming Shenghuo Pharmaceutical Co., Ltd.), and the control group with no further treatment. The dressings were renewed every day, and the burn wounds were photographed on days 0, 2, 8, 15, and 21 with a digital camera before treatment. Besides, the wound closure rate (WR) was described by the following equation:

$$WR(\%) = \frac{(W_0 - W_i)}{W_0} \times 100\%,$$

where W_0 is the initial wound area, and W_i is the residual wound area on days 2, 8, 15, and 21 before treatment.

Histological Analysis

The wound tissue samples were collected on days 0, 8, 15, and 21 before treatment and fixed in 4% formaldehyde solution before being embedded in paraffin, following by cutting into 3 mm sections. Afterward, samples were tested with H&E, Masson's trichrome, and immunohistochemical staining (CD31, VEGF).

The Effect of Removing Eschar on a Full-Thickness Skin Burn Model

16 rats were divided into 4 groups randomly, including BM@PLC3 group, PLC3 group, positive group, and control group. Then, a full-thickness skin burn wound was made by the scald instrument with 100°C for 20 s. The wound was treated with different dressings as above, and photos were taken on days 0, 3, 5, and 12. The wound tissues were collected on days 0, 5, and 12 before treatment and fixed in 4% formaldehyde solution to carry out H&E.

Statistical Analysis

The statistical significance was analyzed by statistical computation using SPSS (Version 23.0). Briefly, one-way ANOVA was used for three or more groups. Data were presented as mean ± SD. The significant level was set as $p < 0.05$.

RESULTS AND DISCUSSIONS

Structural Characterization and Rheological Properties

The preparation routes of PF127-CHO/ε-PL, PVA-SH, and PLC hydrogel are shown in **Supplementary Figure S1**, and the morphology of hydrogel is shown in **Supplementary Figure S2**. The results of ^{1}H NMR are shown in **Supplementary Figure S3**; therein, the chemical shifts (δ = 9.87 and 9.77, δ = 8.67) belonged to aldehyde groups and amino groups, respectively, indicating the successful synthesis of PF127-CHO and PVA-SH. For FT-IR, the wavenumbers of 1,692.29 and 843.56 cm^{-1} belonged to the vibration of aldehyde groups on PF127-CHO; the wavenumbers of 3,069.14, 2,930.60, 1,671.43, and 1,319.79 cm^{-1} were affiliated to the vibration of carboxyl groups on PVA-SH/ε-PL; and the wavenumbers of 1,679.60 and 1,510.87 cm^{-1} belonged to amido groups on PLC, demonstrating the successful synthesis of PLC (**Supplementary Figure S4**). Above all, it could be confirmed that PLC was cross-linked through amido bonds to provide a double-network structure by dynamic Schiff-base reaction among PVA-SH, ε-PL, and PF127-CHO. At the same time, PF127-CHO could self-assemble to make a triple-network hydrogel, while partial sulfhydryl groups on PVA-SH could be oxidized to form disulfide bonds to enhance cross-linking.

SEM investigation showed the porous structures clearly, and the pore sizes of PLC hydrogels were decreased with the addition of ε-PL (**Figure 1A**). It obstructed the Schiff-base reaction between PF127-CHO and PVA-SH on the one hand; on the other hand, it could form a Schiff-base bond with PF127-CHO to promote cross-linking of hydrogel. Under the influence of both, the pore size of PLC was decreased.

According to the frequency sweep test (**Figure 1B**), the elastic modulus (G′) of these four hydrogel samples was in the range from 1,000 Pa to 10,000 Pa with a frequency from 0.01 to 10 Hz, which were reached to the modulus of natural skin tissue, suggesting their suitability of treatment for human skin (Li et al., 2018). Strain sweep test (**Figure 1C**) showed that the strain curves of G' and G" in each group had similar intersection points. With the further increase of strain to 100.0%, G' of these hydrogels decreased dramatically, due to the collapse of the hydrogel networks. Among these four samples, PLC3 had the least loss modulus, indicating that it had the most stable structure among these four samples.

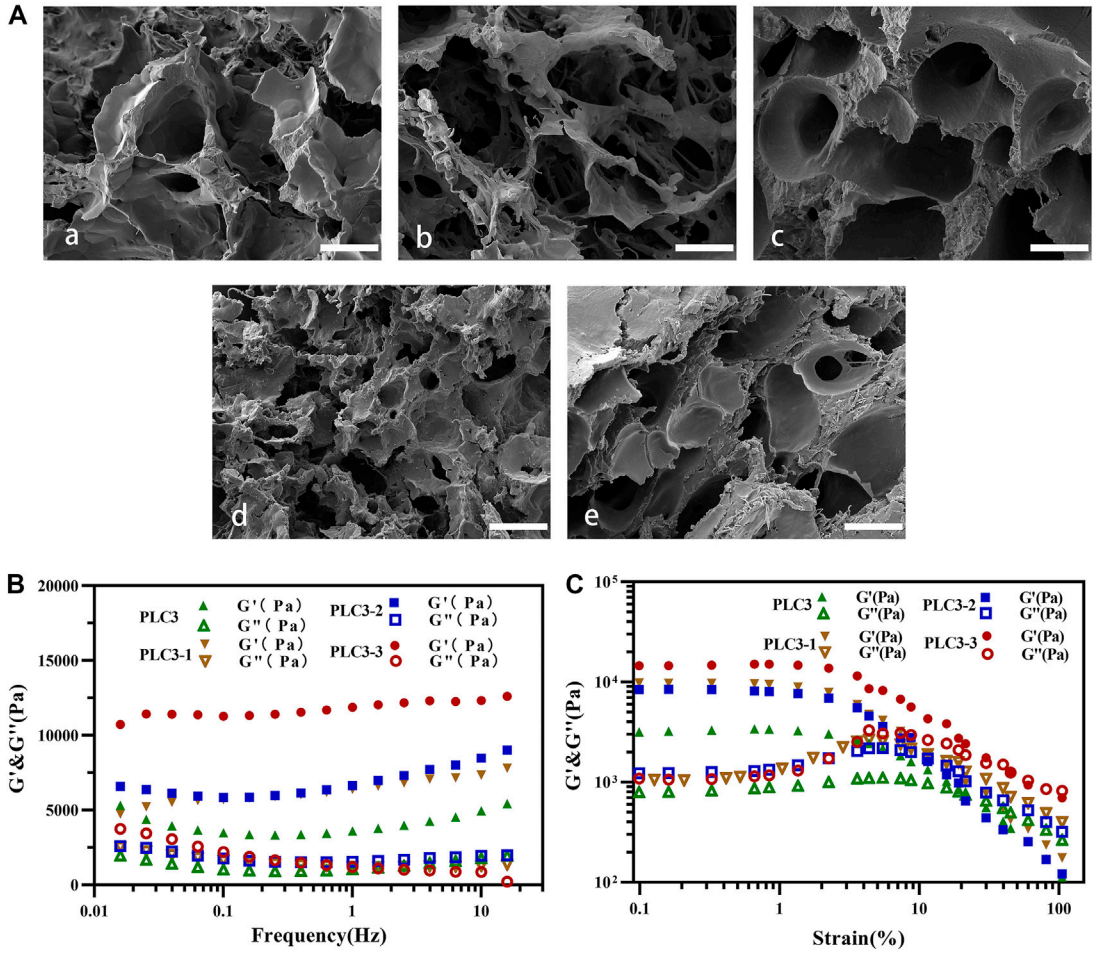

FIGURE 1 | SEM investigation for **(A)** a) blank hydrogel (without ε-PL), b) PLC3-3, c) PLC3-2, d) PLC3, and e) PLC3-1; scale bar: 20 μm. Rheological results of PLC3, PLC3-1, PLC3-2, and PLC3-3 for **(B)** frequency sweep tests and **(C)** strain sweep tests.

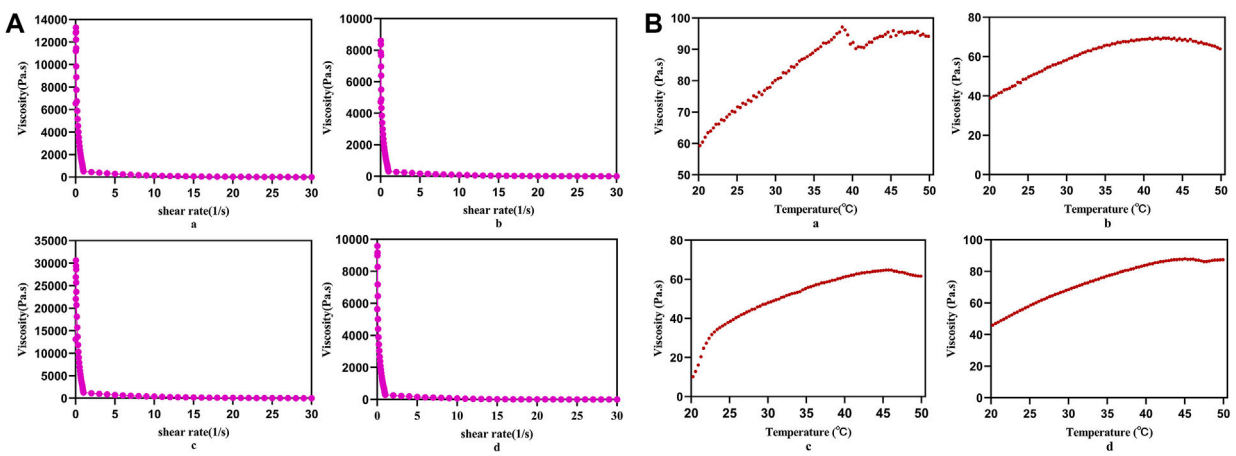

FIGURE 2 | (A) Static shear rate sweep test and **(B)** temperature sweep test of a) PLC3, b) PLC3-1, c) PLC3-2, and d) PLC3-3.

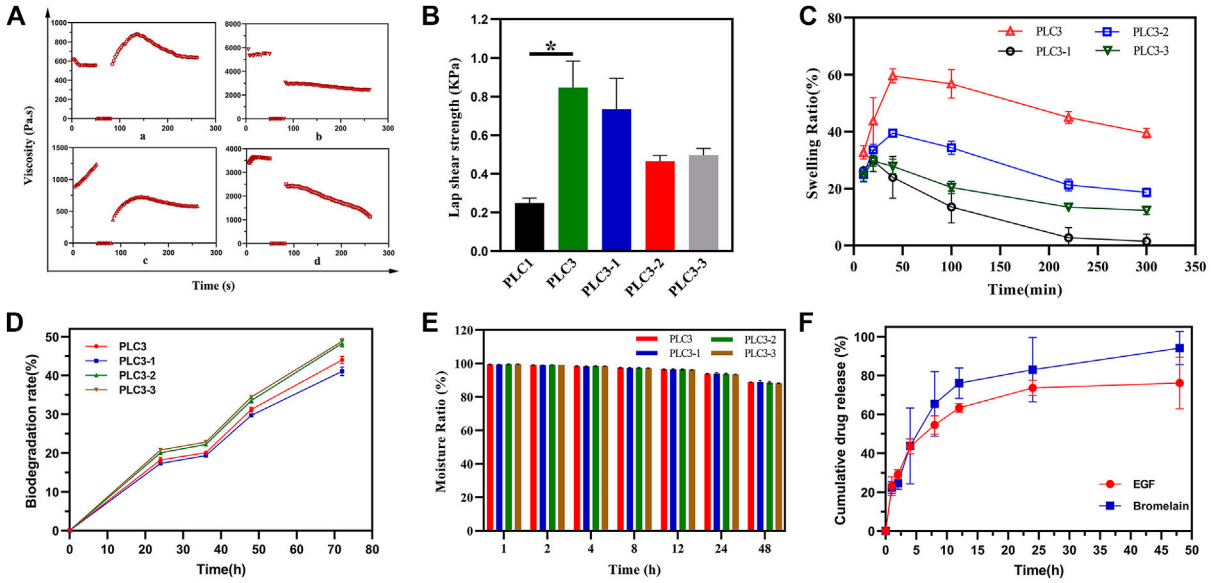

FIGURE 3 | (A) Thixotropy test of a) PLC3, b) PLC3-1, c) PLC3-2, and d) PLC3-3. **(B)** The lap shear strength for hydrogels adhering to gelatin film. **(C)** Swelling tests, **(D)** biodegradation evaluation, and **(E)** moisture retention assay of PLC3, PLC3-1, PLC3-2 and PLC3-3. **(F)** Drugs release curve in 48 h. With the data shown as means ± SD (n = 3, $^*p < 0.05$).

Injectable and Thermal-Responsive Performances of PLC

With the increase of the shear rate, the viscosities of PLC3, PLC3-1, PLC3-2, and PLC3-3 decreased sharply (**Figure 2A**), showing that PLC had the shear thinning property. When the shearing rate increased to 20 s^{-1}, the viscosities of the samples were all bellow 100 Pa s, implying they were quite injectable. When the temperature went up from 20 to 50°C, the viscosity increased gradually and became stable finally (**Figure 2B**), demonstrating that PLC had the characteristic of thermal-responsiveness. Besides, the macroscopic phenomenon showed that PLC was in the liquid form at room temperature, but when it was injected by a syringe on a heating plate under a temperature of 37°C, the hydrogel precursor solution transferred to hydrogel immediately (**Supplementary Figure S4C**), further indicating the injectability and thermal responsiveness of PLC. Therein, the injectable property was obtained owing to the disassociation of self-assembly PF127 micelles in the gel network.

Self-Healing and Enhanced Adhesiveness Properties of PLC

The thixotropy test was conducted to assess the self-healing property of PLC after external damage (**Figure 3A**). In the first stage, the shear rate was kept at 0.1 s^{-1} for 50 s. In the second stage, it was at 100 s^{-1} for 30 s, and then at 0.1 s^{-1} for 180 s in the end. After 40 s in the response stage (the third stage), the viscosities of PLC3, PLC3-1, PLC3-2, and PLC3-3 were restored to 151.48, 54.14, 55.73, and 64.94%, respectively. In addition, compared to the initial state, the viscosities of PLC3-1, PLC3-2, and PLC3-3 decreased by 3,019 Pa s, 651.1 Pa s, and 2,460 Pa s respectively, while that of PLC3 increased by 80.98 Pa s. The result indicated the excellent self-healing property of PLC3.

As the result of shear adhesive strength (**Figure 3B**), the lap shear strength of PLC3 was the strongest among these four hydrogels, and there was a significant difference between PLC1 and PLC3 ($p < 0.05$), indicating that the adhesion of PLC3 with skin tissue was promoted remarkably. The reason was that the modification of aldehyde functional groups in hydrogel system contributed to chemical cross-linking with skin tissue based on the Schiff-base reaction, leading to enhanced tissue-adhesiveness.

Liquid Absorption, Biodegradation, and Moisturizing Performance of PLC

Liquid absorption property, one of the most important indexes for wound dressing, was evaluated by the swelling test. As shown in **Figure 3C**, PLC3, PLC3-1, PLC3-2, and PLC3-3 achieved the maximum swelling ratio in 50 min and then gradually descended. Among these hydrogels, PLC3 possessed the best liquid absorption performance (59.62%). This result may be owed to the components. Briefly, the molar ratio of hydroxy groups on PVA and carboxyl groups on ε-PL were 75:1, 50:1, 100:1, and 200:1 to make up PLC3, PLC3-1, PLC3-2, and PLC3-3, respectively. So, with the increase of ε-PL, the pore of these hydrogels had changed from large to small because ε-PL led to a gel block between PVA-SH and PF127-CHO; at the same time, ε-PL could gel with PF127-CHO based on the Schiff-base reaction, leading to the increased number of pores that promoted swelling. Under the double actions, PLC3 had the better swelling ratio among these

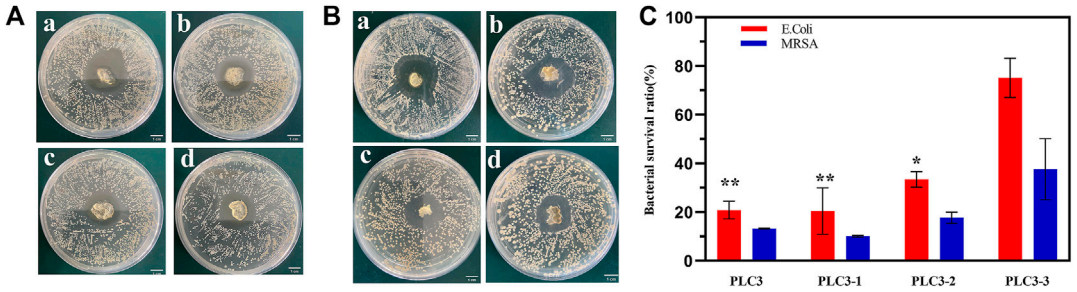

FIGURE 4 | The inhibitor zone test against **(A)** *E. Coli* and **(B)** MRSA on a) PLC3-1, b) PLC3, c) PLC3-2, and d) PLC3-3; scale bar: 1 cm. **(C)** Agar plate colony counting test against *E. Coli* and MRSA on PLC3, PLC3-1, PLC3-2 and PLC3-3, with the data shown as means ± SD (n = 3, $^{**}p < 0.01$, $^{*}p < 0.05$).

samples. Biodegradability is noticeable for biosafety materials. For PLCs, the degradation performance was eligible. As shown in **Figure 3D**, the biodegradation rates of PLCs were all more than 40% after 72 h, indicating that PLCs possessed excellent biodegradability and there was little harm to skin. However, PLC3-2 and PLC3-3 possessed stronger biodegradability than PLC3 and PLC3-1. This was mainly because of the different cross-linking strength of PLCs. SEM showed that the pores of PLC3 and PLC3-1 were smaller than those of PLC3-2 and PLC3-3, suggesting that the cross-linking strength of PLC3 and PLC3-1 was stronger than that of PLC3-2 and PLC3-3, resulting in their lower degradation rates. Moreover, hydrogels possessed a water conservation function, which could make a hydrated environment around the wound and further facilitate the wound healing. According to **Figure 3E**, the moisturizing ratios of PLCs were up to 88%, revealing their excellent moisturizing performance to maintain the hydrated environment for the wound.

Drugs Release *In Vitro*

Subsequently, the drug release behavior *in vitro* was studied. Bromelain and EGF in PLC hydrogel showed slight sudden release of 22.38 and 23.07% at 1 h, respectively. After 24 h, the cumulative release of bromelain was 82.97% and it was still releasing at a certain rate. At 48 h, the cumulative release was up to 94.14%. Different from bromelain, the cumulative release of EGF was 73.65% at 24 h, and it maintained a slow release to 48 h (76.16%) (**Figure 3F**). The release of the therapeutic drug was mainly mediated by the diffusion and degradation of hydrogel skeleton. However, EGF had significantly slower and longer release kinetics than bromelain, which may be due to the dynamic involvement of free amino groups in the EGF structure by the Schiff-base reaction, resulting in covalent binding of EGF to hydrogel network, thus prolonging the EGF release process. Sequential release of bromelain and EGF was very beneficial to burn wound healing. Briefly, the early release of bromelain could remove the wound eschar in time, while the long-term release of EGF effectively supported the migration and proliferation of cells, and the formation of extracellular matrix in the later stage, thus promoting wound healing.

Antimicrobial Activity *In Vitro*

The inhibitor zone test was utilized for qualitative analysis of the antibacterial property of PLC. The result (**Figures 4A,B**) showed that the diameters of the antibacterial zone against *E. coli* were 2.45 ± 1.06 cm (PLC3), 2.6 ± 0.42 cm (PLC3-1), 2.05 ± 1.06 cm (PLC3-2), and 2.05 ± 0.78 cm (PLC3-3), respectively, while those against MRSA were 2.5 ± 0.71 cm (PLC3), 2.6 ± 0.85 cm (PLC3-1), 2.1 ± 0.56 cm (PLC3-2), and 1.95 ± 0.64 cm (PLC3-3). The results revealed that PLC possessed antibacterial activity against *E. coli* and MRSA that depended on concentration. The agar plate colony counting test was further exploited for quantitative analysis. As shown in **Figure 4C**, for *E. coli*, there was significant difference among PLC3, PLC3-1, and PLC3-3 ($p < 0.01$). For MRSA, there was no significant difference between the groups, but the antibacterial activity of PLC was improved with the increased content of ε-PL. The antibacterial property was acquired on the basis of Schiff bases and further improved with the introduction of ε-PL. Briefly, PVA-SH and ε-PL were made to react with PF127-CHO based on the Schiff-base reaction; when this dressing coated on infectious wound where the environment was weak acid, the Schiff-base bonds cracked and ε-PL would release from PLC, promoting the antibacterial activity of PLC. More importantly, this hydrogel did not contain any antibiotics, and thus it had great potential for the treatment of multidrug-resistant bacterial infections according to the antibacterial test against MRSA, and it would not have any problems about microbial resistance.

In Vitro Biocompatibility and Cell Proliferation Ability

Live/Dead staining showed that live cells (green) in each group were in the majority, and red cells were rare, even none (**Figure 5A**), indicating the benign biocompatibility of PLC. Besides, the result of CCK-8 for PLC suggested that the relative cell viabilities cultured with blank hydrogels were all higher than 88% (**Figure 5B**), revealing that PLC hardly had cytotoxicity, and were quite safe for humans. In addition, the relative cell viability of BM@PLC3 and EGF@PLC3 (**Figure 5C**) was higher than 88 and 100%, respectively, suggesting that (BM/EGF)@PLC not only had satisfied

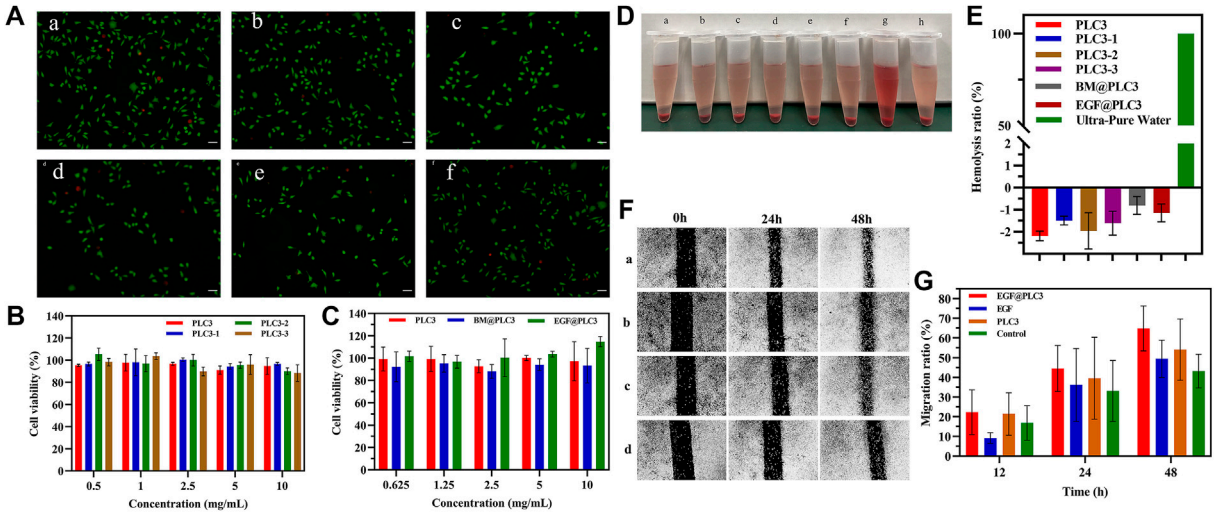

FIGURE 5 | *In vitro* biocompatibility and cell-proliferation tests. **(A)** Live/Dead staining of a) EGF@PLC3, b) BM@PLC3, c) PLC3, d) EGF, e) BM, and f) control; scale bar: 100 μm. **(B)** CCK-8 for blank hydrogels. **(C)** CCK-8 for hydrogels loaded with drugs. **(D)** Hemolysis test on a) PLC3, b) PLC3-1, c) PLC3-2, d) PLC3-3, e) BM@PLC3, f) EGF@PLC3, g) Ultra-pure water, and h) saline. **(E)** The quantitative result of hemolysis test. **(F)** Cell scratch test on a) EGF@PLC3, b) EGF, c) PLC3, and d) control groups. **(G)** Measuring analysis on cell scratch test. With the data shown as means ± SD (n = 3).

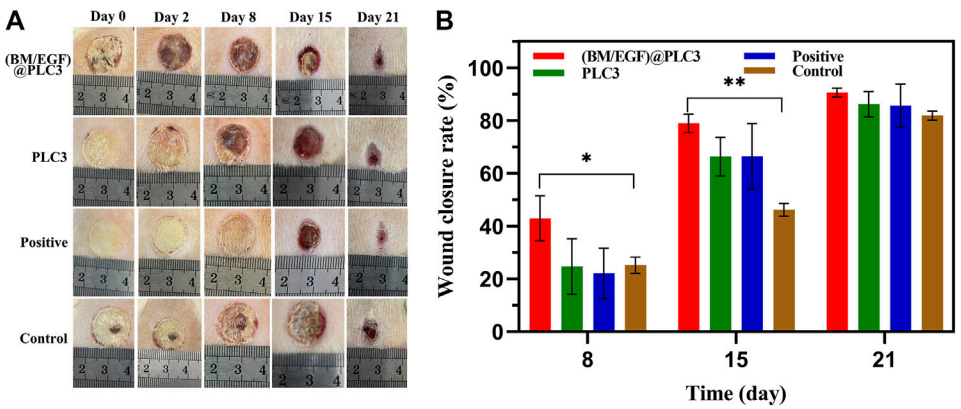

FIGURE 6 | *In vivo* treatment of the burning rat model. **(A)** Assessment of the effect of treatment on days 0, 2, 8, 15, and 21. **(B)** Wound closure rates on days 8, 15, and 21 before treatment. With the data shown as means ± SD (n = 3, *p < 0.05, **p < 0.01).

biocompatibility but also had a cell proliferation–promoting ability because EGF had the ability to promote L929 transport and proliferation.

The result of hemocompatibility clearly exhibited that the supernatant color of hydrogel groups had significant differences when compared with ultrapure water (positive group), while they were the same as saline groups (**Figure 5D**). From **Figure 5E**, the hemolysis ratio of each hydrogel group was lower than 5%, and the hemoglobin absorbance value was similar to the saline group or even a little lower than that, and it was demonstrated that PLC possessed excellent hemocompatibility, which could be applied in the biomedicine field. The reason that the hemoglobin absorbance value of each hydrogel group was a little lower than the saline group may be due to the addition of ε-PL. As we know, ε-PL was rich in cations and had good penetration into biofilms as a drug carrier, which could avoid something to damage cells. Besides, it was found that the cell membrane adsorption of ε-PL will reduce the critical voltage of breakage. Therefore, we could infer that with the addition of ε-PL, the relative hemolysis ratios of hydrogel groups were similar to those of the saline group or even a little lower than that, exhibiting the excellent biocompatibility of PLC.

Cell scratch experiment was carried out to evaluate the cell proliferation–promoting ability of PLC. The result (**Figures 5F,G**) showed that the area of cell scratch was decreased gradually on each group. At 48 h, the migration rates of

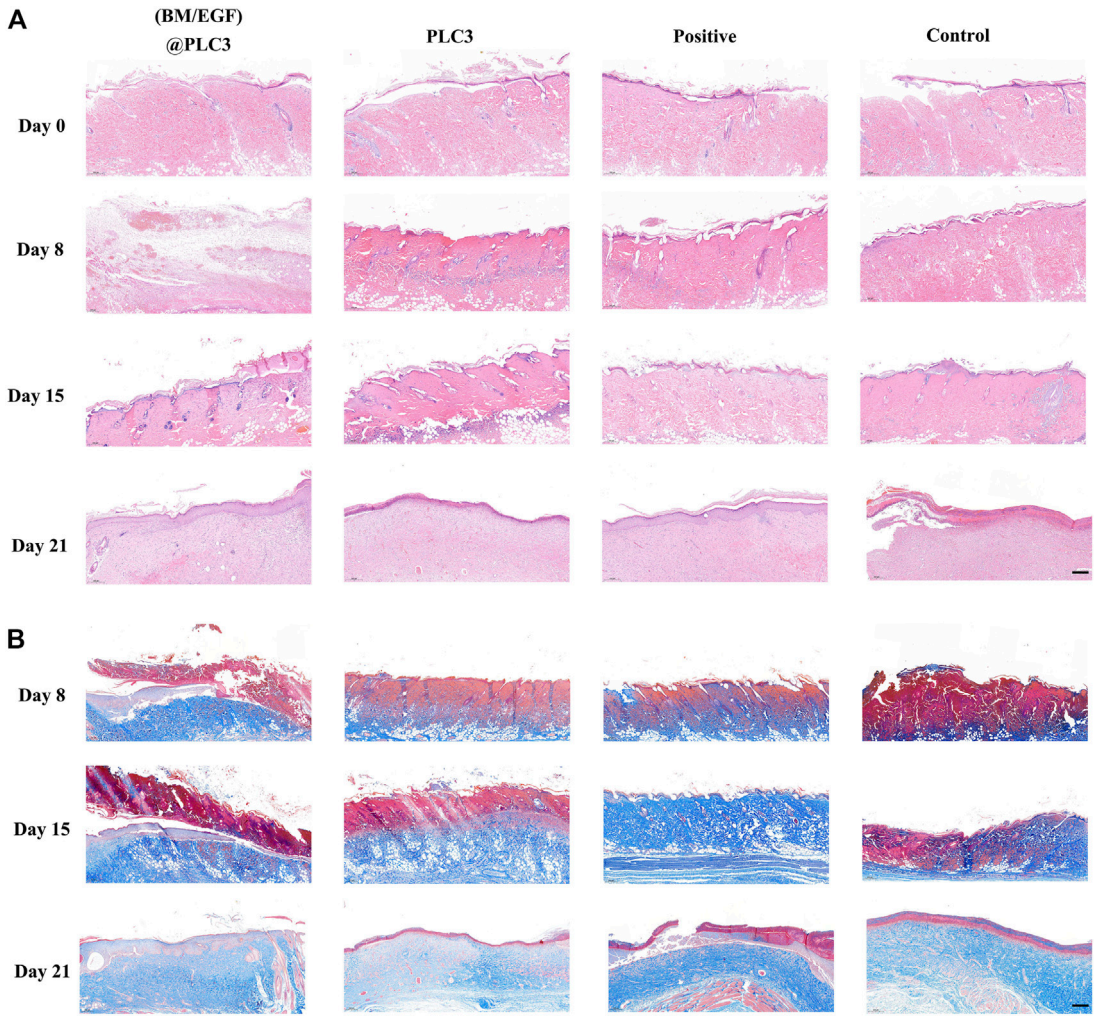

FIGURE 7 | The result of histopathological examination. **(A)** H&E staining of sampled tissue on days 0, 8, 15, and 21. **(B)** Masson's trichrome staining of samples on days 8, 15, and 21; scale bar: 200 μm.

EGF@PLC3, EGF, PLC3, and EGF@PLC3 groups were 70.2, 54.2, 62.7, and 48%, respectively, indicating that EGF@PLC3 had more excellent promotion of cell proliferation ability among these groups.

Wound Healing Enhancement by (BM/EGF)@PLC *In Vivo*

During the treatment for 21 days, the deep-partial thickness skin burn wounds were healing gradually. The wound status of all groups declared that with the treatment of (BM/EGF)@PLC3, the necrotic tissue was eliminated and the remnant dermis was disclosed on day 2, while the necrotic tissues treated with PLC3 and sulfadiazine silver cream were shed gradually on day 8 and day 15, respectively. As for the control group, the necrotic tissue was cleaned up inapparently after 15 days (**Figure 6A**). Besides, wound closure rates of the (BM/EGF)@PLC3 group were achieved as 90.60% (**Figure 6B**), exhibiting the marvelous effect of healing on burn wound. Hence, the result demonstrated comparing the "sequential therapy," the (BM/EGF)@PLC3 hydrogel was proven to fulfill the demands of deep burn injuries in wound cleaning and healing.

Histopathological Analysis

The result of the H&E staining showed that the epidermis of wound tissue in four groups were thinner or even disappeared with skin appendages damaged partially after being scalded on day 0, indicating the successful construction of deep partial-thickness skin burn models. On day 21, the thickness of the epidermis in the (BM/EGF)@PLC3 group and positive group was thicker than that of the PLC3 group and control group (**Figure 7A**). The result of Masson's trichrome staining showed that the array of collagen fiber in the (BM/EGF)

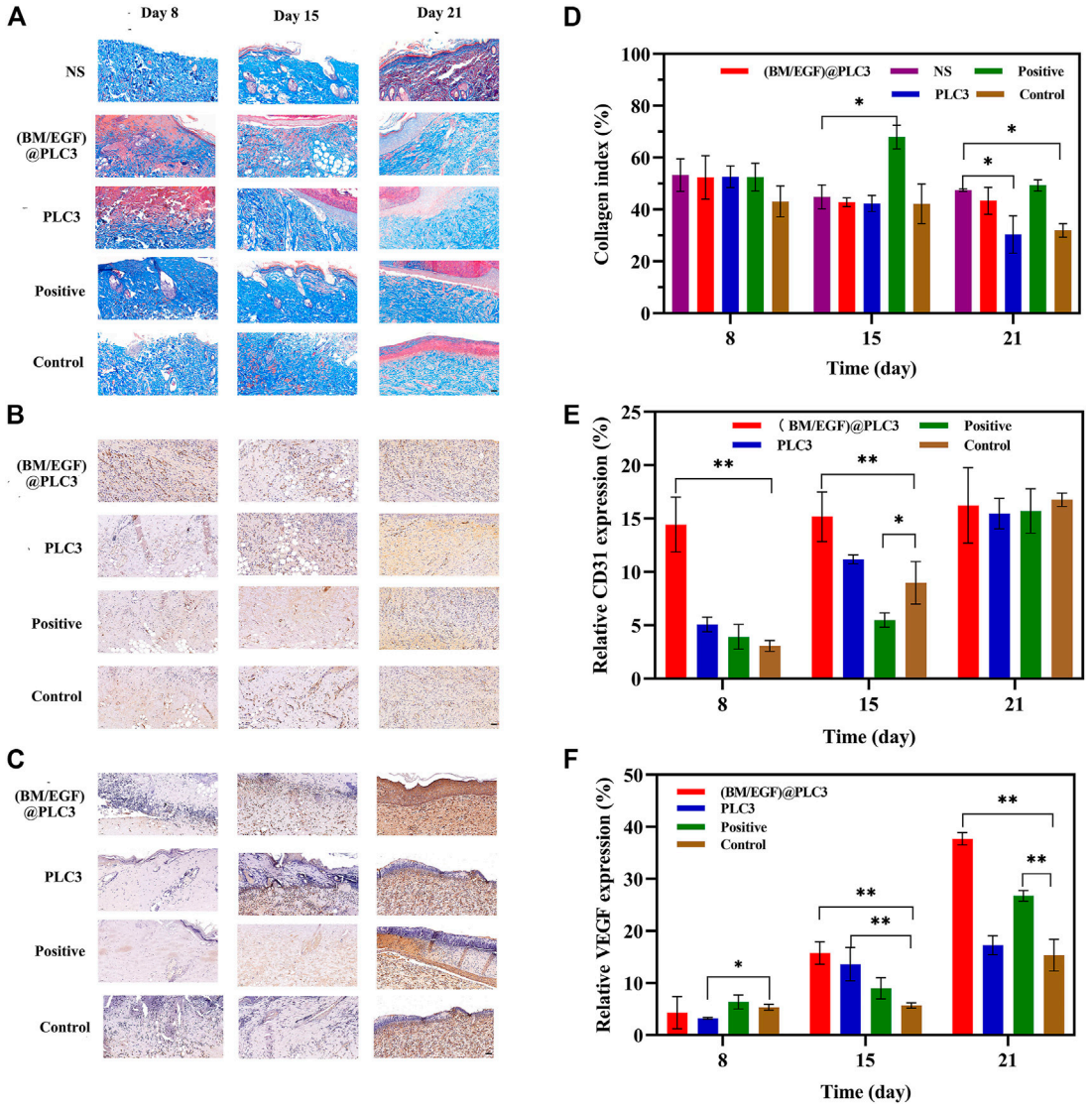

FIGURE 8 | The result of quantitative detection. **(A)** Masson's trichrome staining, **(B)** CD31 Staining, and **(C)** VEGF staining of sampled tissue on days 8, 15, and 21 before treatment. Quantitative detection for **(D)** collagen, **(E)** CD31, and **(F)** VEGF of sampled tissue. With the data shown as means ± SD ($n = 3$, $^{*}p < 0.05$, $^{**}p < 0.01$), scale bar: 50 μm.

@PLC3 group was orderly, and it was hard to find any cellulous on the epidermal, while there were cellulous stained red in other groups on day 21 (**Figure 7B**).

Quantitative detection of collagen, CD31, and VEGF were also adopted to confirm the effect of (BM/EGF)@PLC3. The collagen index of (BM/EGF)@PLC3 group had a similar trend as the normal skin tissue (NS), while PLC3 and control groups had significant differences with NS ($p < 0.05$) on day 21 (**Figures 8A,D**). What is more, the proportion of CD31 in the (BM/EGF)@PLC3 group (14.44%) was nearly 5 times higher than that of the control group (3.06%) on day 8 and about double on day 15 (15.17 vs. 8.97%) (**Figures 8B,E**). As for the proportion of VEGF (**Figures 8C,F**), significant differences between the (BM/EGF)@PLC3 group and the control group were shown clearly ($p < 0.01$). The results further confirmed that (BM/EGF)@PLC3 could promote burn wound healing effectively.

The Effect of Debridement With Bromelain

After treatment for 2 days, the eschar of full-thickness skin burn wounds could be easily cleaned by tweezers only in the BM@PLC3 group (**Figure 9A**), revealing that bromelain had the marvelous effect to ease the eschar removing and it did not affect normal skin tissues at the same time. The H&E staining was adopted to observe the pathological changes of wounds on days 0, 5, and 12. From the result (**Figure 9B**), the epidermis of sample tissues became thinner and even disappeared compared with normal skin tissue (NS), and the

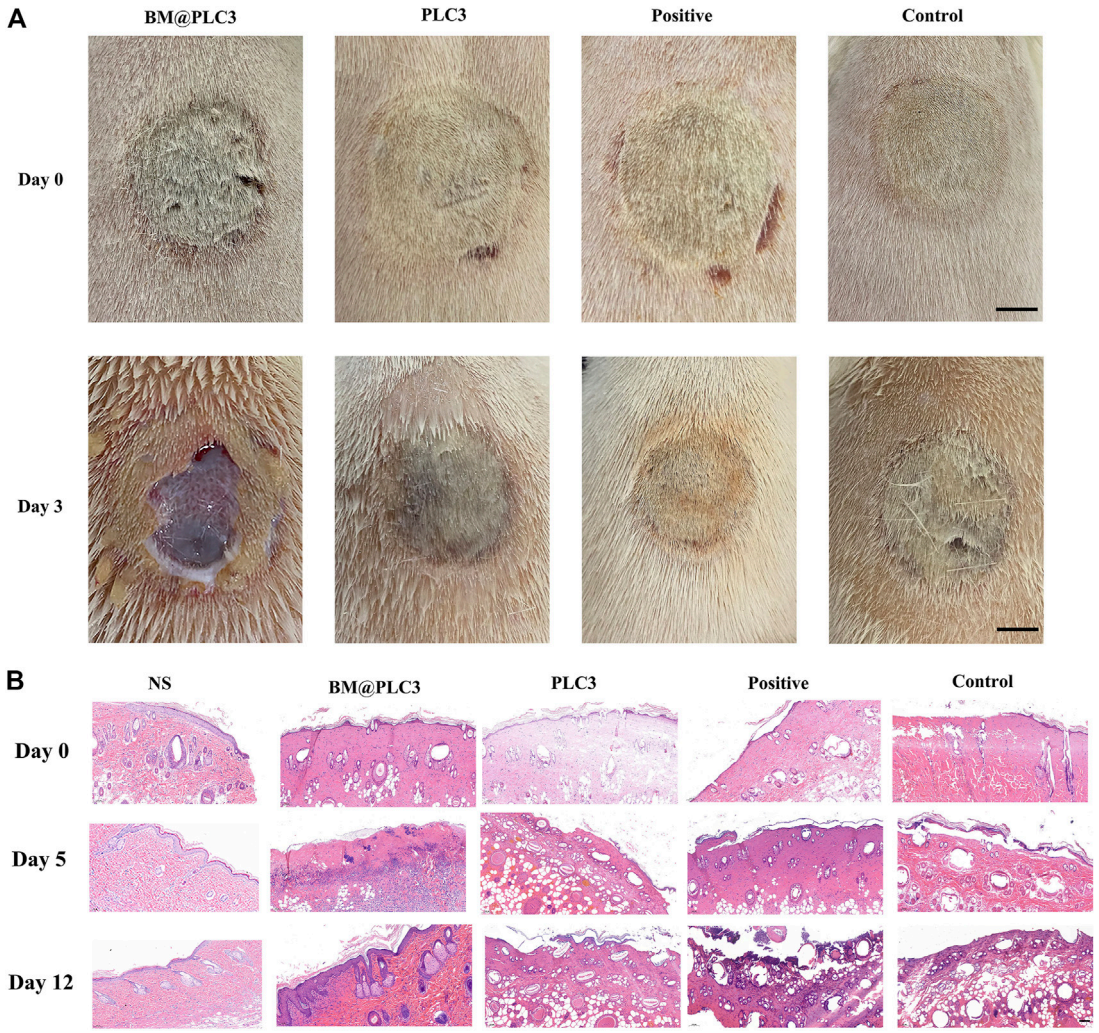

FIGURE 9 | The result of burn magnification test. **(A)** The image of burn wound before treatment on days 0 and 3, scale bar: 1 cm. **(B)** H&E staining on the normal skin group (NS), BM@PLC3 group, PLC3 group, positive group, and control group on days 0, 5, and 12; scale bar: 100 μm.

skin appendages such as hair follicles were damaged seriously on day 0, indicating that the full-thickness skin burn wound model was successfully manufactured. On day 5, partial necrotic tissue in the BM@PLC3 group started to fall off naturally, and there were almost no eschar remaining on day 12. Moreover, the newborn epidermis was in good condition, and the skin appendages returned to normal. In contrast, the other three groups still showed inapparent wound cleaning on day 12, blocking the growth of new epidermis.

CONCLUSION

In this study, a novel PLC hydrogel has been developed as a multifunctional dressing for deep burn injuries. This triple-network structure endows PLC benign mechanical property, self-healing ability, tissue-adhesiveness, antibacterial activity, biosafety, and marvelous wound cleaning and healing efficiency. In short, the (BM/EGF)@PLC hydrogel we designed has a great potential in treating deep burn injuries, and it is especially geared for irregular shaped deep burn wounds in poor medical conditions. Thus, it makes great sense in developing new-generation dressing and treatment for burn injuries in clinics.

DATA AVAILABILITY STATEMENT

The original contributions presented in the study are included in the article/**Supplementary Material**; further inquiries can be directed to the corresponding authors.

ETHICS STATEMENT

The animal study was reviewed and approved by the Institutional Animal Care and Use Committee of the Second Military Medical University.

AUTHOR CONTRIBUTIONS

FY conceived the idea. SW and FY designed the project. SW, JL, and ZM performed the experiments and analyzed the data. LH, YH, LS, and YZ interpreted the data. SW wrote the manuscript. ZM and BG revised the manuscript. All authors contributed to the article and approved the submitted version.

FUNDING

This research was funded by the Shanghai Sailing Program (Grant Nos. 21YF1457700 and 20YF1458000) and the Ministry of Science and Technology (Grant No. 20SWAQK24).

SUPPLEMENTARY MATERIAL

The Supplementary Material for this article can be found online at: https://www.frontiersin.org/articles/10.3389/fbioe.2021.794769/full#supplementary-material

REFERENCES

Chen, L., Ai, J., Cai, H., Chen, X., Liu, Z., Li, Z., et al. (2021a). Antibacterial Gauze Based on the Synergistic Antibacterial Mechanism of Antimicrobial Peptides and Silver Nanoparticles. *J. Polym. Res.* 28 (2), 32. doi:10.1007/S10965-020-02363-3

Chen, Y., Wang, Q., Li, D., Mensah, A., Qiu, Y., Ke, H., et al. (2021b). Mussel-inspired Double Cross-Linked Hydrogels with Desirable Mechanical Properties, strong Tissue-Adhesiveness, Self-Healing Properties and Antibacterial Properties. *Mater. Sci. Eng. C* 120, 111690. doi:10.1016/J.MSEC.2020.111690

Dong, Y., Cui, M., Qu, J., Wang, X., Kwon, S. H., Barrera, J., et al. (2020). Conformable Hyaluronic Acid Hydrogel Delivers Adipose-Derived Stem Cells and Promotes Regeneration of Burn Injury. *Acta Biomater.* 108, 56–66. doi:10.1016/j.actbio.2020.03.040

Fang, H., Li, D., Xu, L., Wang, Y., Fei, X., Tian, J., et al. (2021). A Reusable Ionic Liquid-Grafted Antibacterial Cotton Gauze Wound Dressing. *J. Mater. Sci.* 56 (12), 7598–7612. doi:10.1007/S10853-020-05751-8

Ghobril, C., and Grinstaff, M. W. (2015). The Chemistry and Engineering of Polymeric Hydrogel Adhesives for Wound Closure: a Tutorial. *Chem. Soc. Rev.* 44 (7), 1820–1835. doi:10.1039/c4cs00332b

Guo, B., and Ma, P. X. (2018). Conducting Polymers for Tissue Engineering. *Biomacromolecules* 19 (6), 1764–1782. doi:10.1021/acs.biomac.8b00276

Hirche, C., Kreken Almeland, S., Dheansa, B., Fuchs, P., Governa, M., Hoeksema, H., et al. (2020). Eschar Removal by Bromelain Based Enzymatic Debridement (Nexobrid) in burns: European Consensus Guidelines Update. *Burns* 46 (4), 782–796. doi:10.1016/j.burns.2020.03.002

Huang, J., Fan, Q., Guo, M., Wu, M., Wu, S., Shen, S., et al. (2021). Octenidine Dihydrochloride Treatment of a Meticillin-Resistant *Staphylococcus aureus* Biofilm-Infected Mouse Wound. *J. Wound Care* 30 (2), 106–114. doi:10.12968/JOWC.2021.30.2.106

Huang, X., Wang, L., Zhang, J., Du, X., Wu, S., Wang, H., et al. (2020). A Novel ε-polylysine-modified Microcrystalline Cellulose Based Antibacterial Hydrogel for Removal of Heavy Metal. *Int. J. Biol. macromolecules* 163, 1915–1925. doi:10.1016/j.ijbiomac.2020.09.047

Huijun, X., Chao, N., Zeyang, C., Nuramina, M., and Haji, A. A. (2020). Synthesis and Activity of New Schiff Bases of Furocoumarin. *Heterocyclic Commun.* 26 (1), 176–184. doi:10.1515/hc-2020-0115

Kaddoura, I., Abu-Sittah, G., Ibrahim, A., Karamanoukian, R., and Papazian, N. (2017). Burn Injury: Review of Pathophysiology and Therapeutic Modalities in Major burns. *Ann. Burns Fire Disasters* 30 (2), 95–102.

Kopecki, Z. (2021). Development of Next-Generation Antimicrobial Hydrogel Dressing to Combat Burn Wound Infection. *Biosci. Rep.* 41 (2), BSR20203404. doi:10.1042/BSR20203404

Li, Z., Zhou, F., Li, Z., Lin, S., Chen, L., Liu, L., et al. (2018). Hydrogel Cross-Linked with Dynamic Covalent Bonding and Micellization for Promoting Burn Wound Healing. *ACS Appl. Mater. Inter.* 10 (30), 25194–25202. doi:10.1021/acsami.8b08165

Lutfi, E. S., Prastuti, O. P., Machmudah, S., Winardi, S., Wahyudiono, K. H., Kanda, H., et al. (2021). Phenolic Compound, Antioxidant and Antibacterial Properties of Electrospun PVP Nanofiber Loaded with Bassela Rubra linn Extract and Alginate from Sargassum Sp. *IOP Conf. Ser. Mater. Sci. Eng.* 1143 (1), 012015. doi:10.1088/1757-899X/1143/1/012015

Najath, A. K., Ayesha, A., and Jeschke, M. G. (2021). Stem Cell Therapy for Burns: Story so Far. *Biol.: Targets Ther.* 15, 379–397. doi:10.2147/BTT.S259124

Rosenberg, L., Krieger, Y., Bogdanov-Berezovski, A., Silberstein, E., Shoham, Y., and Singer, A. J. (2014). A Novel Rapid and Selective Enzymatic Debridement Agent for Burn Wound Management: a Multi-center RCT. *Burns* 40 (3), 466–474. doi:10.1016/j.burns.2013.08.013

Said, M. M., Rehan, M., El-Sheikh, S. M., Zahran, M. K., Abdel-Aziz, M. S., Bechelany, M., et al. (2021). Multifunctional Hydroxyapatite/Silver Nanoparticles/Cotton Gauze for Antimicrobial and Biomedical Applications. *Nanomaterials* 11 (2), 429. doi:10.3390/NANO11020429

Schanuel, F. S., Raggio Santos, K. S., Monte-Alto-Costa, A., and de Oliveira, M. G. (2015). Combined Nitric Oxide-Releasing Poly(vinyl Alcohol) film/F127 Hydrogel for Accelerating Wound Healing. *Colloids Surf. B: Biointerfaces.* 130, 182–191. doi:10.1016/j.colsurfb.2015.04.007

Shahrousvand, M., Haddadi-Asl, V., and Mohsen, S. (2021). Step-by-step Design of Poly (ε-Caprolactone)/chitosan/Melilotus Officinalis Extract Electrospun Nanofibers for Wound Dressing Applications. *Int. J. Biol. Macromolecules* 180, 36–50. doi:10.1016/J.IJBIOMAC.2021.03.046

Shoham, Y., Krieger, Y., Rubin, G., Koenigs, I., Hartmann, B., Sander, F., et al. (2020). Rapid Enzymatic Burn Debridement: A Review of the Paediatric Clinical Trial Experience. *Int. Wound J.* 17, 1337–1345. doi:10.1111/iwj.13405

Soriano, J. L., Calpena, A. C., Rodríguez-Lagunas, M. J., Domènech, Ò., Bozal-de Febrer, N., Garduño-Ramírez, M. L., et al. (2020). Endogenous Antioxidant Cocktail Loaded Hydrogel for Topical Wound Healing of Burns. *Pharmaceutics* 13 (1), 8. doi:10.3390/PHARMACEUTICS13010008

Staruch, R. M. T., Glass, G. E., Rickard, R., Hettiaratchy, S. P., and Butler, P. E. M. (2017). Injectable Pore-Forming Hydrogel Scaffolds for Complex Wound Tissue Engineering: Designing and Controlling Their Porosity and Mechanical Properties. *Tissue Eng. B: Rev.* 23 (2), 183–198. doi:10.1089/ten.TEB.2016.0305

Suo, H., Hussain, M., Wang, H., Zhou, N., Tao, J., Jiang, H., et al. (2021). Injectable and pH-Sensitive Hyaluronic Acid-Based Hydrogels with On-Demand Release of Antimicrobial Peptides for Infected Wound Healing. *Biomacromolecules* 22, 3049–3059. doi:10.1021/acs.biomac.1c00502

Wang, G., Wang, Y., Liu, W., and Zhan, Y. (2008). The Experimental Study of Repairing Cutaneous Deficiency by Transplanting the Compound of Mesenchymal Stem Cells and PLGA Porous Foam Scaffolds. *Cell Res* 18 (Suppl. 1), S66. doi:10.1038/cr.2008.156

Yaacobi, D., Lvovsky, A., Ad-El, N., Levi, D., Yaacobi, E., Olshinka, A., et al. (2021). Burns in the Military Setting-Analyzing 12,799 Routine and Combat Cases. *J. burn Care researchofficial Publ. Am. Burn Assoc.* 42 (1), 67–70. doi:10.1093/JBCR/IRAA107

Yu, Y., Fu, F., Shang, L., Cheng, Y., Gu, Z., and Zhao, Y. (2017). Bioinspired Helical Microfibers from Microfluidics. *Adv. Mater.* 29 (18), 1605765. doi:10.1002/adma.201605765

Yuan, Y., Shen, S., and Fan, D. (2021). A Physicochemical Double Cross-Linked Multifunctional Hydrogel for Dynamic Burn Wound Healing: Shape Adaptability, Injectable Self-Healing Property and Enhanced Adhesion. *Biomaterials* 276, 120838. doi:10.1016/J.BIOMATERIALS.2021.120838

Zhao, S., Li, L., Wang, H., Zhang, Y., Cheng, X., Zhou, N., et al. (2015). Wound Dressings Composed of Copper-Doped Borate Bioactive Glass Microfibers Stimulate Angiogenesis and Heal Full-Thickness Skin Defects in a Rodent Model. *Biomaterials* 53, 379–391. doi:10.1016/j.biomaterials.2015.02.112

Zhao, X., Guo, B., Wu, H., Liang, Y., and Ma, P. X. (2018). Injectable Antibacterial Conductive Nanocomposite Cryogels with Rapid Shape Recovery for Noncompressible Hemorrhage and Wound Healing. *Nat. Commun.* 9 (1), 21–25. doi:10.1038/s41467-018-04998-9

Zhu, P., Zhang, X., Wang, Y., Li, C., Wang, X., Tie, J., et al. (2021). Electrospun Polylactic Acid Nanofiber Membranes Containing Capparis Spinosa L . Extracts for Potential Wound Dressing Applications. *J. Appl. Polym. Sci.* 138 (32), 50800. doi:10.1002/APP.50800

Conflict of Interest: The authors declare that the research was conducted in the absence of any commercial or financial relationships that could be construed as a potential conflict of interest.

Publisher's Note: All claims expressed in this article are solely those of the authors and do not necessarily represent those of their affiliated organizations, or those of the publisher, the editors, and the reviewers. Any product that may be evaluated in this article, or claim that may be made by its manufacturer, is not guaranteed or endorsed by the publisher.

Copyright © 2021 Wang, Li, Ma, Sun, Hou, Huang, Zhang, Guo and Yang. This is an open-access article distributed under the terms of the Creative Commons Attribution License (CC BY). The use, distribution or reproduction in other forums is permitted, provided the original author(s) and the copyright owner(s) are credited and that the original publication in this journal is cited, in accordance with accepted academic practice. No use, distribution or reproduction is permitted which does not comply with these terms.

frontiers in Bioengineering and Biotechnology

ORIGINAL RESEARCH
published: 17 February 2022
doi: 10.3389/fbioe.2022.847901

Dacarbazine-Loaded Targeted Polymeric Nanoparticles for Enhancing Malignant Melanoma Therapy

Wei Xiong[1], Zhengdong Guo[1], Baoyan Zeng[1], Teng Wang[2], Xiaowei Zeng[2], Wei Cao[2] and Daizheng Lian[3]*

[1]Department of Plastic and Burn Surgery, Huazhong University of Science and Technology Union Shenzhen Hospital, Shenzhen, China, [2]Graduate School at Shenzhen, Tsinghua University, Shenzhen, China, [3]Department of Radiation Oncology, Shenzhen People's Hospital The Second Clinical Medical College, Jinan University, The First Affiliated Hospital, Southern University of Science and Technology, Shenzhen, China

Dacarbazine (DTIC) dominates chemotherapy for malignant melanoma (MM). However, the hydrophobicity, photosensitivity, instability, and toxicity to normal cells of DTIC limit its efficacy in treating MM. In the present study, we constructed star-shaped block polymers nanoparticles (NPs) based on Cholic acid -poly (lactide-*co*-glycolide)-*b*-polyethylene glycol (CA-PLGA-*b*-PEG) for DTIC encapsulation and MM targeted therapy. DTIC-loaded CA-PLGA-*b*-PEG NPs (DTIC-NPs) were employed to increase the drug loading and achieve control release of DTIC, followed by further modification with nucleic acid aptamer AS1411 (DTIC-NPs-Apt), which played an important role for active targeted therapy of MM. *In vitro*, DTIC-NPs-Apt showed good pH-responsive release and the strongest cytotoxicity to A875 cells compared with DTIC-NPs and free DTIC. *In vivo* results demonstrated that the versatile DTIC-NPs-Apt can actively target the site of MM and exhibited excellent anti-tumor effects with no obvious side effects. Overall, this research provided multi-functional NPs, which endow a new option for the treatment of MM.

Keywords: cancer nanocarriers, targeted drug delivery, controlled release, copolymer, malignant melanoma

OPEN ACCESS

Edited by:
Junqing Wang,
Sun Yat-sen University, China

Reviewed by:
Tongkai Chen,
Guangzhou University of Chinese Medicine, China
Guoqing Pan,
Jiangsu University, China

****Correspondence:***
Wei Xiong
wxiong68@email.szu.edu.cn

Specialty section:
This article was submitted to Biomaterials, a section of the journal Frontiers in Bioengineering and Biotechnology

Received: *03 January 2022*
Accepted: *24 January 2022*
Published: *17 February 2022*

Citation:
Xiong W, Guo Z, Zeng B, Wang T, Zeng X, Cao W and Lian D (2022) Dacarbazine-Loaded Targeted Polymeric Nanoparticles for Enhancing Malignant Melanoma Therapy. Front. Bioeng. Biotechnol. 10:847901. doi: 10.3389/fbioe.2022.847901

INTRODUCTION

Malignant melanoma (MM) is one of the most life-threatening malignancies (Li et al., 2015; Liu et al., 2017). Although melanoma rarely occurs, accounting for only 5% of skin cancers, the survival rate of patients is low due to its rapid recurrence, high multidrug resistance, and easy metastasis. Specifically, the average survival time of patients with MM is about 8–9 months, and overall survival rate is less than 15% with 3 years (Balch et al., 2009). Although many studies have explored treatment of MM (Tagne et al., 2008; Li and Han, 2020), few have obtained satisfactory results. Surgery, chemotherapy, and immunotherapy are the most common methods for treatment (Chapman et al., 2011; Hamid et al., 2013; Koyama et al., 2016). Among them, chemotherapy occupies an important position in the comprehensive treatment of tumor (Hafeez and Kazmi, 2017; Yuan et al., 2017). Dacarbazine (DTIC) is the only US Food and Drug Administration (FDA)-approved chemotherapeutic agent for melanoma, it is also the first-line drug for MM (Chapman et al., 1999; Tarhini and Agarwala, 2006; Bei et al., 2009). DTIC is an alkylating agent that kills tumor cells by destroying DNA (Eigentler et al., 2011; Demetri et al., 2017). However, DTIC has limited efficacy in treating melanoma due to its

hydrophobicity and short half-life (Tagne et al., 2008; Koyama et al., 2016) In addition, DTIC has photosensitivity and instability, which increase the difficulty of drug storage and transportation. Moreover, DTIC has non-specific toxicity to normal cells, which is a common defect of chemotherapy drugs (Almousallam et al., 2015). Therefore, it is very necessary to develop an effective platform to reduce toxic side effects and improve the cytotoxicity to MM cells, thereby inhibiting further metastasis and recurrence of metastatic MM.

Targeted therapy of tumors opened up a new world for chemotherapy. It is considered to be the most promising method in cancer treatment. In recent years, new tumor-targeted strategies have emerged, such as tumor-targeted drug therapy (Jin et al., 2021; Kerns et al., 2021; Li et al., 2021; Li et al., 2021), immunotherapy (Chen et al., 2021; Lu et al., 2021; Pei et al., 2021), gene therapy (Chada et al., 2015; Wang et al., 2021; Wang et al., 2021), virus therapy (Kemler et al., 2021; Wan et al., 2021; Zhang et al., 2021), and cell-based targeted therapy (Collet et al., 2016). Among them, tumor active targeted drug therapy based on nanoparticles (NPs) drug delivery systems achieved the most success. The targeted NPs utilize specific interaction between receptors expression on the surface of target cells and ligands conjugated with the NPs, specifically to deliver drug to tumor cells and organs, significantly improve drug concentration in the target area and effectively reduce side effects to normal tissues (Ashley et al., 2011; Bao et al., 2012; Dahlberg et al., 2015; Li et al., 2021). Moreover, versatile NPs could improve the stability of drugs and control release of cargos (Berger et al., 2015; Gong et al., 2019). Nucleolin is a protein widely present in the nucleus, cytoplasm, and cell membrane of many kinds of cells (Kabirian-Dehkordi et al., 2019). Interestingly, nucleolin is more abundantly expressed on the surface of tumor cell membranes than normal cells, which means that nucleolin can be a potential therapeutic target for anti-tumor (Koutsioumpa and Papadimitriou, 2014; Palmieri et al., 2015; Romano et al., 2018). Increasing interest in nucleolin anti-tumor research has led to the development of several small molecule antagonists (Kabirian-Dehkordi et al., 2019). Aptamer has attracted the most interest in the field of tumor targeted treatment due to its high affinity, strong specificity, no significant immunogenicity, small molecular size, and easy modification. Nucleic acid aptamer AS1411, the first aptamer approved by the FDA, was used in various cancer clinical treatment trials. AS1411 can specifically bind to nucleolin, which was highly expressed on the surface of tumor cells, to achieve the purpose of targeted therapy (Destouches et al., 2011; Ding et al., 2011). However, AS1411 was observed to be effective on partial tumors in clinical trials and suffer from its rapid clearance from the blood (Kabirian-Dehkordi et al., 2019). Therefore, the AS1411 conjugated to the NPs surface would improve its stability in the blood and endow NPs the ability to target tumor cells, maximizing anti-tumor effect.

With the development of nano-targeting technology, a variety of targeted NPs have been reported for the delivery of DTIC (Bei et al., 2009; Ding et al., 2011; Ding et al., 2011; Kakumanu et al., 2011). Yet, there are extremely rare drug carriers with targeted functions *in vivo* that have been successfully used in clinical practice because of following obstacles. First, the capacity of ligands which bind to these drug carriers is not enough to effectively recognize the target. Second, the binding stability between ligands and drug carriers is not strong enough to achieve systemic circulation, and is unable to reach the target site. Third, the speed and strength of ligands to bind to the target are insufficient after delivery to the destination. Obviously, there is an urgent need to design a carrier with multiple active sites, which can combine multiple ligands and drugs at the same time, to realize the synergy of targeted multivalency and drugs. Star-shaped block polymers based on Poly (lactide-*co*-glycolide) (PLGA) is a simple example of highly specific targeting carrier material. They are branched polymer with all branches extending from a single core, which endow them a higher drug loading capacity and encapsulation efficiency than linear polymers with the same molar mass (Nguyen-Van et al., 2011; Ma et al., 2013; Tao et al., 2014; Peng et al., 2018; Liu et al., 2019). Thus, they can flexibly guide target molecules to a destination in the complex environment of the body. Polyethylene glycol (PEG), a water-soluble polymer, was often introduced to PLGA in order to improve hydrophilicity of PLGA, to further meet the needs of drug delivery carriers (Yildiz and Kacar, 2021). In the process of PLGA star-shaped block polymers synthesis, the most commonly used core is cholic acid (CA). CA is composed of a steroid unit with three hydroxyl groups and one carboxyl group, which can be selected as the poly-hydroxy initiator. Furthermore, CA is the main bile acid in the body. This biological source can synthesize copolymers based on CA due to its good biocompatibility (Janvier et al., 2013; Su et al., 2017).

In the present study, CA-PLGA-*b*-PEG nanocarriers were constructed to encapsulate DTIC, and then modified with aptamer for targeted therapy of MM. The star-shaped block copolymer CA-PLGA-*b*-PEG was prepared by the core-first method, and NPs were fabricated by an improved nanoprecipitation method. Morphology and drug loading of the NPs were characterized and the antitumor effect of the NPs was evaluated both *in vitro* and *in vivo*. The results show the NPs exhibited an excellent anti-tumor effect, providing a new option for MM patients.

RESULTS AND DISCUSSIONS

Synthesis and Characterization of Star-Shaped Copolymer CA-PLGA-b-PEG-COOH

The chemical reaction scheme for synthesis of star-shaped polymer CA-PLGA-*b*-PEG-COOH was shown in **Figure 1** The CA-PLGA-*b*-PEG-COOH with a well-defined three-branched structure were prepared successfully. The gel permeation chromatography (GPC) molecular weight M_n of CA-PLGA and CA-PLGA-*b*-PEG-COOH are 13,265 and 20,872, respectively. The results of GPC molecular weight could prove the CA-PLGA-*b*-PEG-COOH was synthesized successfully by the coupling reaction between CA-PLGA-COOH and NH_2-PEG_{2k}-COOH.

For star-shaped copolymer CA-PLGA-*b*-PEG-COOH, the typical ^{1}H NMR signals from PEG and monomers lactide (LA) and glycolide (GA) repeating units can be observed. As

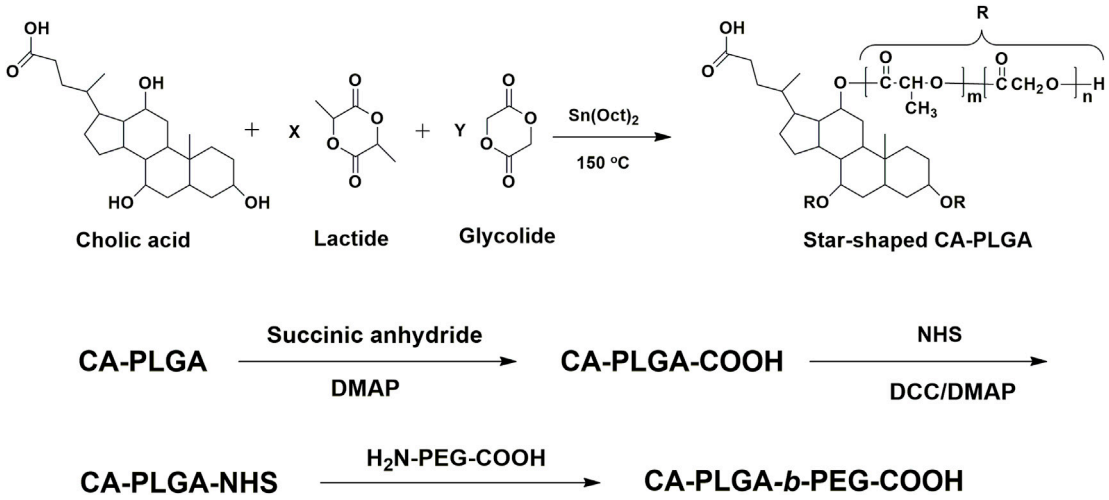

FIGURE 1 | Schematic representation of synthesis of amphiphilic block copolymer CA-PLGA-*b*-PEG-COOH.

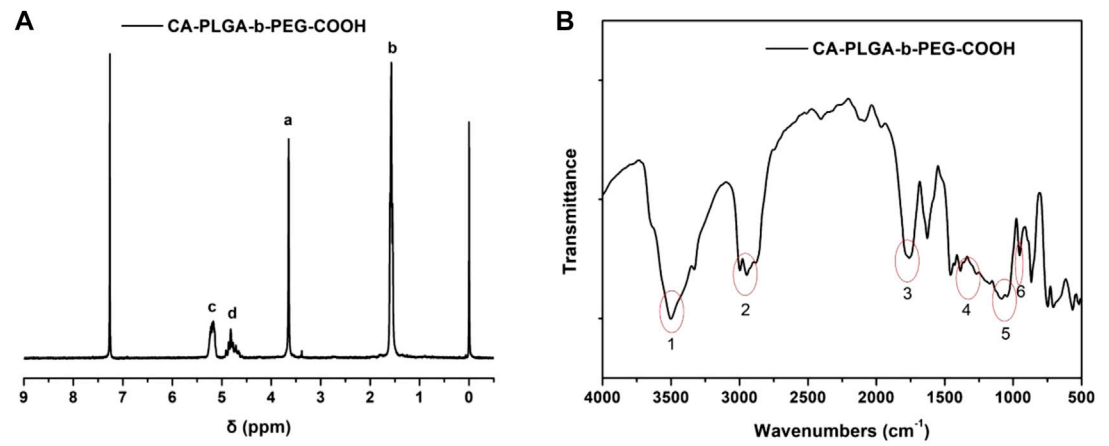

FIGURE 2 | Typical characterization of copolymer CA-PLGA-*b*-PEG-COOH **(A)** ^{1}H NMR spectra; **(B)** FT-IR spectra.

shown in **Figure 2A** of ^{1}H NMR ($CDCl_3$), four characteristic signals can be observed: peak a (δ = 3.63 ppm, PEG repeating unit: -C**H**$_2$C**H**$_2$O-), b (δ = 1.60 ppm, LA repeating unit: -CHC**H**$_3$), c (δ = 5.19 ppm, LA repeating unit: -C**H**CH$_3$), and d (δ = 4.81 ppm, GA repeating unit: -C**H**$_2$-). As shown in spectra, we can further demonstrate that the successful coupling of star-shaped CA-PLGA-COOH and NH_2-PEG_{2k}-COOH, and the star-shaped copolymer CA-PLGA-*b*-PEG-COOH was prepared successfully.

FT-IR spectroscopy was adopted for further confirming the structure and successfully synthesizing CA-PLGA-*b*-PEG-COOH. As shown in **Figure 2B**, the obvious characteristic peak at 1750 cm^{-1} (peak 3) could be ascribed to the presence of a carbonyl group in CA-PLGA. The stretching vibrations peak at 1,115–1,025 cm^{-1} (peak 5) could be ascribed to the presence of a C-O-C in PEG. The broad absorbance between 3,010 and 2,850 cm^{-1} (peak 2) corresponded to the stretching vibrations of C-H. The characteristic peak at 1, 2, 4, and 6 could be ascribed to the presence of a carboxy group (COOH) in the copolymer of CA-PLGA-*b*-PEG-COOH.

Preparation and Characterization of Nanoparticles

DTIC-NPs was prepared by a modified nanoprecipitation method, and the synthesis process is shown in **Figure 3A**. Specifically, DTIC and copolymer are dissolved in a mixed solvent of acetone and methanol to form an organic solution. Then, the mixed solvent was added dropwise to the aqueous solution which contained emulsifier D-a-tocopheryl polyethylene glycol 1,000 succinate (TPGS). During this process, PLGA in the copolymer precipitates due to its hydrophobicity, resulting in the formation of drug loaded CA-PLGA-*b*-PEG NPs spontaneously. Finally, the organic solvent was evaporated by stirring overnight, and then, CA-PLGA-*b*-PEG NPs were centrifuged, washed, and

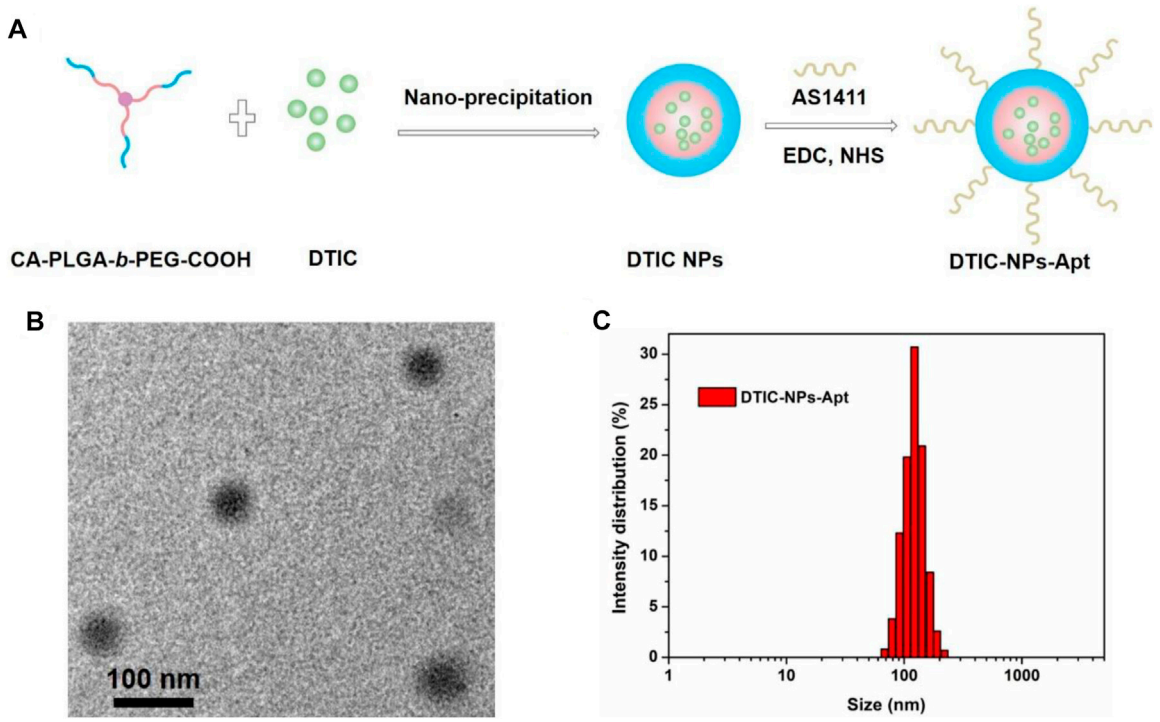

FIGURE 3 | (A) Schematic illustration of the preparation technics for the targeted DTIC-NPs-Apt; **(B)** TEM image of DTIC-NPs-Apt; **(C)** DLS size distribution of DTIC-NPs-Apt.

TABLE 1 | Characterization of DTIC-NPs and DTIC-NPs-Apt (Mean ± SD, *n* = 3).

Samples	Size (nm)	PDI	ZP (mV)	LC (%)	EE (%)
DTIC-NPs	116.3 ± 5.2	0.128	−26.4 ± 3.9	8.72	88.53
DTIC-NPs-Apt	125.9 ± 4.1	0.115	−15.7 ± 2.6	7.64	N/A

PDI, polydispersity index; ZP, zeta potential; LC, loading content; EE, encapsulation efficiency; N/A, not applicable.

lyophilized. For DTIC-NPs-Apt, EDC and NHS were utilized as catalysts to couple aptamer AS1411 to DTIC-NPs.

Stability, cumulative release of drug, cellular uptake, and *in vivo* biodistribution of NPs were mainly affected by its particle size and surface properties. The particle sizes and size distributions of the DTIC NPs and DTIC-NPs-Apt were studied by dynamic light scattering (DLS) method, and the results are shown in **Table 1**. The average diameter of DTIC NPs and DTIC-NPs-Apt was 116.3 ± 5.2 nm and 125.9 ± 4.1 nm, respectively. The average diameter of DTIC-NPs-Apt was slightly larger than DTIC NPs, which is because aptamer AS1411 was introduced into the surface of DTIC NPs. The nanoparticles used as drug delivery system possess high cellular uptake, more desirable biodistribution, and preferentially accumulate at the tumor site because of the enhanced permeability and retention (EPR) effect. Furthermore, nanoparticles can reduce tumor resistance to a certain extent. The hydrated particle size of both NPs is in a range that is suitable for cell uptake, which would boost the NPs to be passively targeted to the tumor tissue through the EPR effect, and more accumulated in the tumor tissue. **Figure 3B** exhibited the result of DTIC-NPs-Apt transmission electron microscopy (TEM), and the DTIC-NPs-Apt were spherical shaped. The average diameter of DTIC-NPs-Apt presented in TEM was about 70 nm, which was significantly reduced compared to the average diameter measured by DLS. This difference may be attributed to a shrinkage while the DTIC-NPs-Apt are in dry state during the TEM characterization. **Figure 3C** shows the size distribution of the DTIC-NPs-Apt. Polydispersity index of both NPs was less than 0.2, indicated the particle size is uniform, which was beneficial to deliver the cargos. The drug loading of DTIC NPs and DTIC-NPs-Apt was 8.72 and 7.64%, respectively. It was noted that the aptamer AS1411 functionalization dose not influence the drug loading content of NPs. These results suggested that the successful construction of DTIC-NPs-Apt with suitable average diameter, uniform particle size, and high drug loading.

Stability of DTIC-NPs and DTIC-NPs-Apt

Zeta potential can detect the mutual repulsion between NPs, which plays an important role in maintaining the physical stability of NPs. The zeta potential of DTIC NPs and DTIC-NPs-Apt are presented in **Table 1**, which were -26.4 ± 3.9 mV and -15.7 ± 2.6 mV, respectively. Both NPs behaved negatively charged, which is due to the ionized carboxyl groups of polylactic acid and polyglycolic acid segments. The absolute value of modified DTIC-NPs-Apt zeta potential was reduced, which indicated that modified aptamer AS1411 on the NPs surface has a surface charge shielding effect. To further assess

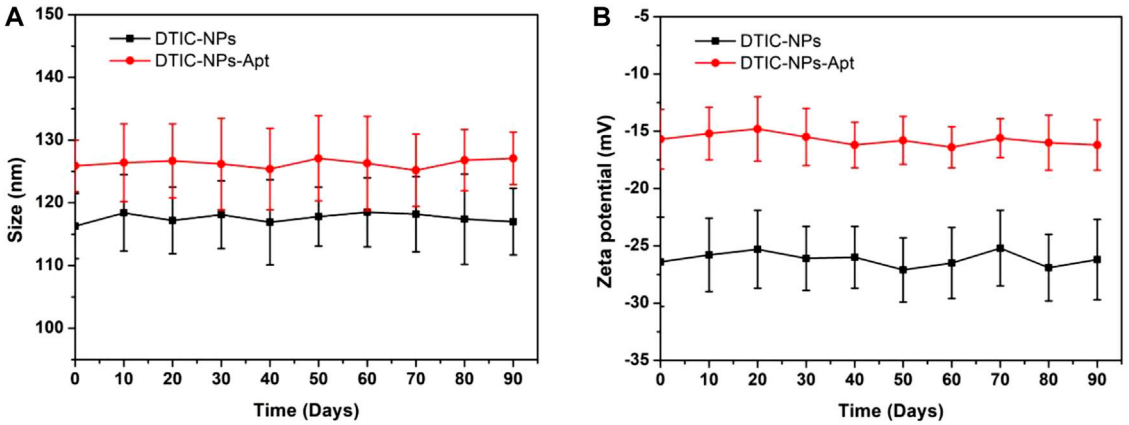

FIGURE 4 | *In vitro* stability of DTIC-NPs and DTIC-NPs-Apt. **(A)** Particle size and **(B)** zeta potential during 90 days of storage, respectively.

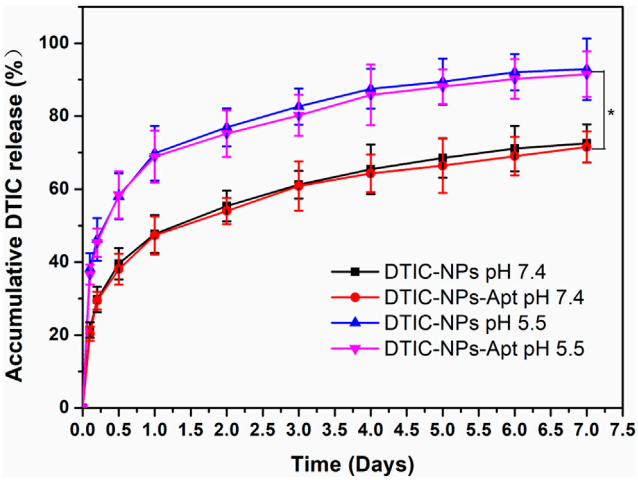

FIGURE 5 | *In vitro* drug release profiles of the DTIC-NPs and DTIC-NPs-Apt at pH 5.5 and 7.4, respectively. $* p < 0.05$.

the stability of two kinds of NPs, we monitored the changes in the size and zeta potential of the DTIC NPs and DTIC-NPs-Apt during storage. The results are shown in **Figure 4**; no obvious change was observed in particle size and zeta potential during 3 months. These data show NPs exhibit excellent stability, which was important to achieve clinical translation.

In Vitro Drug Release Profiles

Figure 5 displayed the cumulative drug release profiles of the DTIC-NPs and DTIC-NPs-Apt in PBS (pH 7.4) for 7 days. During the first day, the initial burst release of DTIC-NPs and DTIC-NPs-Apt was found to be 47.7 and 47.3%, respectively. However, both NPs exhibited continuous, steady release patterns in the following few days. After 1 week, the accumulative drug releases of DTIC-NPs and DTIC-NPs-Apt reached 72.5 and 71.6%, respectively. These data indicated that both the NPs exhibited a typically biphasic pattern release with an initial burst. Because DTIC was absorbed on the surface or entrapped weakly by NPs, DTIC was quickly released in the initial day. Subsequently, DTIC was released with a sustained behavior dominantly attributed to the diffusion of the cargo from the rigid core or hydrophobic inner shell. *In vitro* cumulative drug release profiles of DTIC-NPs and DTIC-NPs-Apt at pH 5.5 PBS were also carried out. The release behavior of both NPs at pH 5.5 was similar to that at pH 7.4, but the release rate is faster. The initial burst release of DTIC-NPs and DTIC-NPs-Apt at pH 5.5 was found to be 69.8 and 69.0%, respectively. The cumulative release of DTIC after 7 days was 92.9 and 91.5%, respectively. The reason may be because the structure of the NPs is destroyed in the acidic environment of pH 5.5. Based on the characteristics of acid response, the DTIC loaded in NPs can be better released in the acidic environment of tumors, promoting anti-tumor effect.

In vitro Cell Viability of NPs

Human melanoma A875 cells were cultured to evaluate cytotoxicity of the NPs *in vitro*. Free DTIC, DTIC-NPs, and DTIC-NPs-Apt with same drug concentrations ranging from 0.1 to 100 μg/ml were tested. Drug free NPs-Apt with equivalent NPs dosage were used as well. As shown in **Figure 6**, blank NPs-Apt at different concentrations seem not to have exhibited significant cytotoxicity at a different time, which suggested NPs possess nontoxic and excellent biocompatibility. The cytotoxicity of free DTIC and DITC-loaded NPs showed dose-dependent and time-dependent behavior. In addition, DTIC-NPs-Apt exhibited the strongest cytotoxicity. After incubation with NPs for 24 h with DTIC concentration of 100 μg/ml, viability of A875 cells was 60.6% for free DTIC, 40.1% for DTIC-NPs, and 32.8% for DTIC-NPs-Apt. However, after incubating A875 cells with NPs for 48 h, the cytotoxicity of DTIC-NPs-Apt was 11.8%, significantly lower than DTIC-NPs, which was 20.7%. This result was attributed to the modification of aptamer AS1411 on the DTIC-NPs-Apt, which could target to nucleolin. Nucleolin was highly expressed on the surface of A875 cells, DTIC-NPs-Apt with active targeting function could enhance cellular uptake of NPs, therefore improving cytotoxicity to A875 cells.

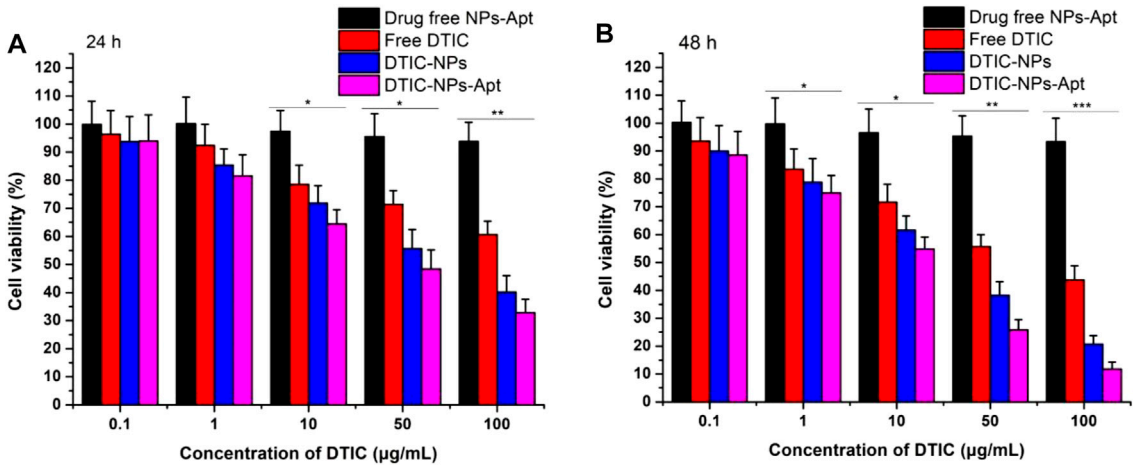

FIGURE 6 | Viability of human melanoma A875 cells cultured with drug free NPs-Apt, free DTIC, DTIC-NPs, and DTIC-NPs-Apt at equivalent drug concentrations ranging from 0.1 to 100 μg/ml. The amount of drug free NPs-Apt was the same as that of the NPs, $n = 3$. **(A)** 24 h; **(B)** 48 h $* p < 0.05$; $** p < 0.01$; $*** p < 0.001$ indicate significant difference compared with drug free NPs-Apt.

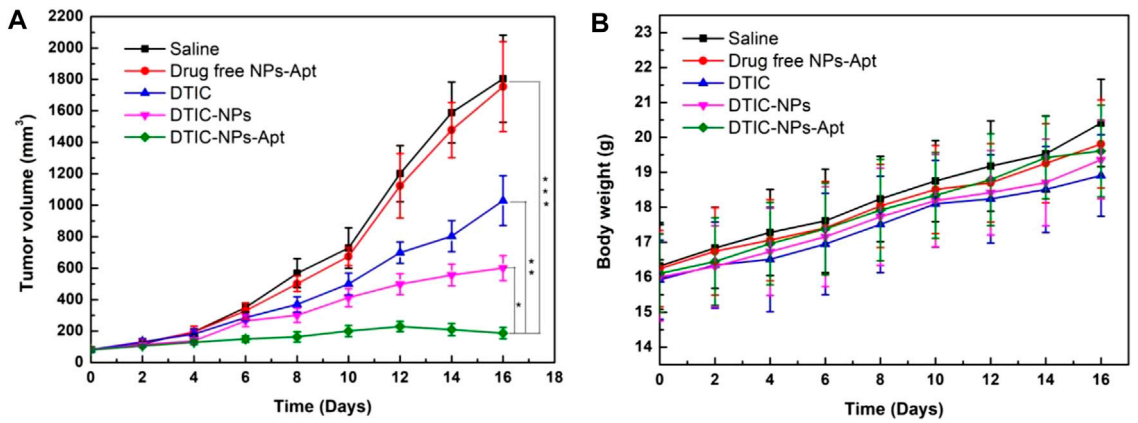

FIGURE 7 | Antitumor efficacy of targeted DTIC-NPs-Apt in comparison with saline, drug free NPs-Apt, free DTIC, and DTIC-NPs ($n = 5$). **(A)** Tumor growth curve of the SCID nude mice bearing human melanoma A875 cells xenograft. **(B)** Animal body weight of the nude mice in different groups after treatment at different time intervals. $* p < 0.05$; $** p < 0.01$. $*** p < 0.001$ indicate significant difference compared with DTIC-NPs-Apt.

The IC_{50} values of free DTIC, DTIC-NPs, and DTIC-NPs-Apt against A875 cells were also quantified. IC_{50} values of A875 cells treated with three DTIC formulations for 24 and 48 h are summarized in **Supplementary Table S1**. Compared with free DTIC, DTIC NPs can significantly reduce the value of IC_{50}, which benefits from the continuous release effect of nanocarrier on DTIC. Especially the IC_{50} of DTIC-NPs-Apt group was less than half of DTIC-NPs group, demonstrating that after active targeting group-aptamer AS1411 modified, DTIC-NPs-Apt showing strongest cytotoxicity of A875 cells.

In Vivo Antitumor Efficacy

Due to the excellent cytotoxicity to A875 cells *in vitro*, DTIC-NPs-Apt bring a potential hope to the treatment of MM. In this study, the antitumor effect of DTIC-NPs-Apt was also evaluated *in vivo*. Twenty-five tumor-bearing nude mice were employed and divided into five groups randomly. Then, five groups were injected with saline (control), blank NPs-Apt, free DTIC, DTIC-NPs, and DTIC-NPs-Apt through the tail vein, respectively. Every other day, we recorded the tumor volume and weight of the mouse until the end of the treatment. Tumor growth curve of tumor-bearing mice was shown in **Figure 7A**. Compared with control group, three DTIC formulation groups significantly reduced tumor growth. Furthermore, DTIC-NPs-Apt group displayed the strongest ability to inhibit tumor growth over the free DTIC and DTIC-NPs groups. In general, when various formulations were injected into the tail vein, the surface modification of aptamer AS1411 (DTIC-NPs-Apt group) can actively target to MM cells to achieve high concentration aggregation of tumor sites, and release DTIC in response to the acidic environment of the tumor, resulting in the strongest anti-tumor effect. In the development of novel carriers, the side effects of carriers have received extensive attention. The body weight of the mice during

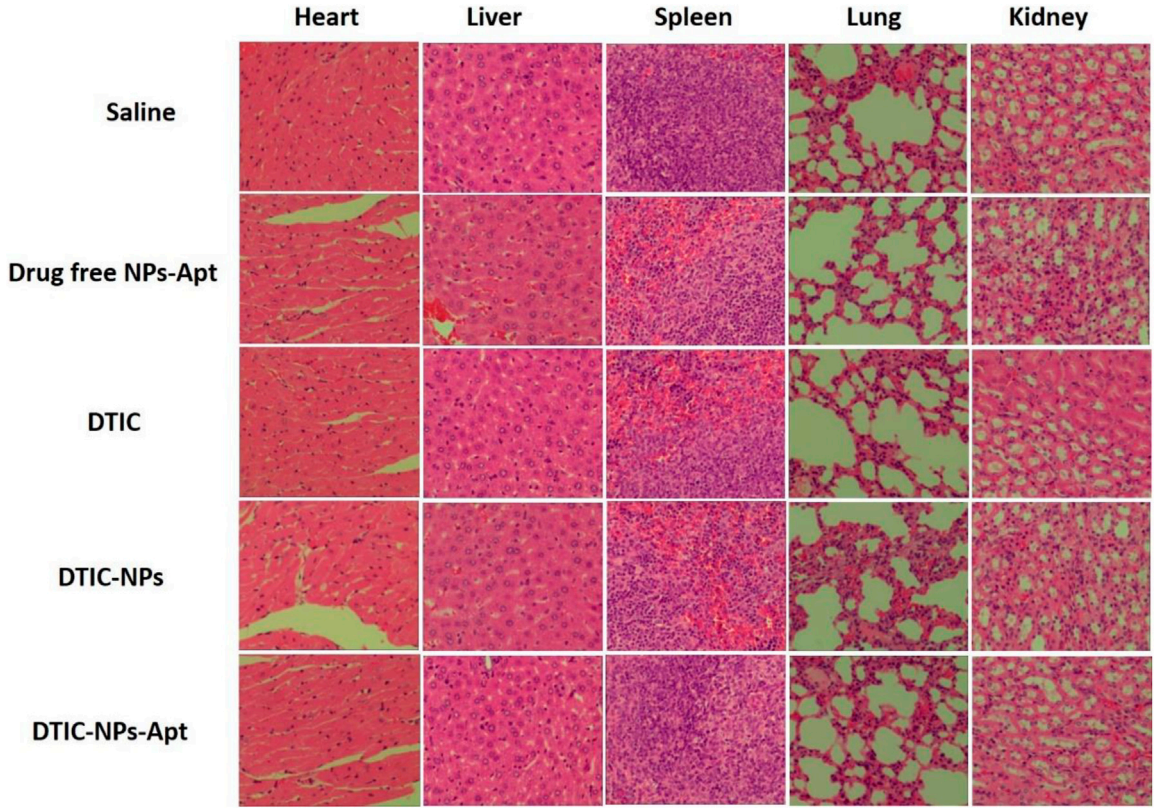

FIGURE 8 | Representative tissue sections of mice stained with hematoxylin and eosin (H&E) after 16 days of treatment. For all the groups, no apparent tissue injury was observed in the tissues of heart, liver, spleen, lung, and kidney.

the treatment was also recorded to evaluate the systemic toxicity of star-shaped nanocarriers constructed in this study. Body weights of all nude mice was presented in **Figure 7B**. All groups gained weight, which indicated the nanocarriers show no obviously systemic side effects on mice.

In order to further explore the toxic and side effects of the constructed nanocarriers, we used hematoxylin and eosin (H&E) staining to observe the changes in the heart, liver, spleen, lung, and kidney of mice after treatment. The results are shown in **Figure 8**. For all the groups, no apparent tissue injury was observed in the tissues of heart, liver, spleen, lung, and kidney. Therefore, all the results indicated that DTIC-NPs-Apt own excellent effects to treat MM with almost no toxic side effects. DTIC-NPs-Apt have the potential to provide a new treatment method for MM patients.

CONCLUSION

In short, we have successfully constructed DTIC-NPs-Apt based on star-shaped block polymers and modified nucleic acid aptamer to realize active targeted therapy of MM. The appearance of DTIC-NPs-Apt was nearly spherical, and they had a suitable particle size range with a narrow size distribution and exhibited good stability. Moreover, DTIC-NPs-Apt displayed high drug loading of DTIC, showing controlled release and pH-response release behavior. Compared with DTIC-NPs or free DTIC, the modification of AS1411 and the controlled release effect of DTIC make the DTIC-NPs-Apt possess the best anti-tumor effect *in vivo* and *in vitro* without showing toxic side effects. In conclusion, DTIC-NPs-Apt have a potential for MM targeting therapy.

DATA AVAILABILITY STATEMENT

The original contributions presented in the study are included in the article/**Supplementary Material**, further inquiries can be directed to the corresponding author.

ETHICS STATEMENT

The animal study was reviewed and approved by Shenzhen Nanshan People's Hospital (Huazhong University of Science and Technology Union Shenzhen Hospital).

AUTHOR CONTRIBUTIONS

WX designed the research project; WX, ZG, TW, WC, and DL had full controlled the experiments, data analysis, and preparation of article; BZ, XZ, WX, and DL were involved in planning the analysis and drafting the article. The final draft article was approved by all the authors.

ACKNOWLEDGMENTS

We are grateful for the financial support from the Science, Technology & Innovation Commission of Shenzhen Municipality (JCYJ20160429182415013).

SUPPLEMENTARY MATERIAL

The Supplementary Material for this article can be found online at: https://www.frontiersin.org/articles/10.3389/fbioe.2022.847901/full#supplementary-material

REFERENCES

Almousallam, M., Moia, C., and Zhu, H. (2015). Development of Nanostructured Lipid Carrier for Dacarbazine Delivery. *Int. Nano Lett.* 5 (4), 241–248. doi:10.1007/s40089-015-0161-8

Ashley, C. E., Carnes, E. C., Phillips, G. K., Padilla, D., Durfee, P. N., Brown, P. A., et al. (2011). Erratum: The Targeted Delivery of Multicomponent Cargos to Cancer Cells by Nanoporous Particle-Supported Lipid Bilayers. *Nat. Mater* 10 (6), 476. doi:10.1038/nmat3042

Balch, C. M., Gershenwald, J. E., Soong, S.-j., Thompson, J. F., Atkins, M. B., Byrd, D. R., et al. (2009). Final Version of 2009 AJCC Melanoma Staging and Classification. *Jco* 27 (36), 6199–6206. doi:10.1200/jco.2009.23.4799

Bao, Q., Zhao, Y., Niess, H., Conrad, C., Schwarz, B., Jauch, K.-W., et al. (2012). Mesenchymal Stem Cell-Based Tumor-Targeted Gene Therapy in Gastrointestinal Cancer. *Stem Cell Dev.* 21 (13), 2355–2363. doi:10.1089/scd.2012.0060

Bei, D., Marszalek, J., and Youan, B.-B. C. (2009). Formulation of Dacarbazine-Loaded Cubosomes-Part I: Influence of Formulation Variables. *Aaps Pharmscitech* 10 (3), 1032–1039. doi:10.1208/s12249-009-9293-3

Berger, C. M., Gaume, X., and Bouvet, P. (2015). The Roles of Nucleolin Subcellular Localization in Cancer. *Biochimie* 113, 78–85. doi:10.1016/j.biochi.2015.03.023

Chada, S., Wiederhold, D., Menander, K. B., Sellman, B., Talbott, M., Nemunaitis, J. J., et al. (2015). Tumor Suppressor Immune Gene Therapy to Reverse Immunotherapy Resistance. *Cancer Gene Ther* doi:10.1038/s41417-021-00369-7

Chapman, P. B., Einhorn, L. H., Meyers, M. L., Saxman, S., Destro, A. N., Panageas, K. S., et al. (1999). Phase III Multicenter Randomized Trial of the Dartmouth Regimen versus Dacarbazine in Patients with Metastatic Melanoma. *Jco* 17 (9), 2745. doi:10.1200/jco.1999.17.9.2745

Chapman, P. B., Hauschild, A., Robert, C., Haanen, J. B., Ascierto, P., Larkin, J., et al. (2011). Improved Survival with Vemurafenib in Melanoma with BRAF V600E Mutation. *N. Engl. J. Med.* 364 (26), 2507–2516. doi:10.1056/NEJMoa1103782

Chen, M. Y., Zhang, Y. L., Cui, L. F., Cao, Z. Q., Wang, Y. W., Zhang, W., et al. (2021). Protonated 2D Carbon Nitride Sensitized with Ce6 as a Smart Metal-free Nanoplatform for Boosted Acute Multimodal Photo-Sono Tumor Inactivation and Long-Term Cancer Immunotherapy. *Chem. Eng. J.* 422. doi:10.1016/j.cej.2021.130089

Collet, G., Szade, K., Nowak, W., Klimkiewicz, K., El Hafny-Rahbi, B., Szczepanek, K., et al. (2016). Endothelial Precursor Cell-Based Therapy to Target the Pathologic Angiogenesis and Compensate Tumor Hypoxia. *Cancer Lett.* 370 (2), 345–357. doi:10.1016/j.canlet.2015.11.008

Dahlberg, C. I. M., Sarhan, D., Chrobok, M., Duru, A. D., and Alici, E. (2015). Natural Killer Cell-Based Therapies Targeting Cancer: Possible Strategies to Gain and Sustain Anti-tumor Activity. *Front. Immunol.* 6. doi:10.3389/fimmu.2015.00605

Demetri, G. D., Schöffski, P., Grignani, G., Blay, J. Y., Maki, R. G., Van Tine, B. A., et al. (2017). Activity of Eribulin in Patients with Advanced Liposarcoma Demonstrated in a Subgroup Analysis from a Randomized Phase III Study of Eribulin versus Dacarbazine. *J. Clin. Oncol.* 35 (30), 3433–3439. doi:10.1200/jco.2016.71.6605

Destouches, D., Page, N., Hamma-Kourbali, Y., Machi, V., Chaloin, O., Frechault, S., et al. (2011). A Simple Approach to Cancer Therapy Afforded by Multivalent Pseudopeptides that Target Cell-Surface Nucleoproteins. *Cancer Res.* 71 (9), 3296–3305. doi:10.1158/0008-5472.Can-10-3459

Ding, B., Wu, X., Fan, W., Wu, Z., Gao, J., Zhang, W., et al. (2011). Anti-DR5 Monoclonal Antibody-Mediated DTIC-Loaded Nanoparticles Combining Chemotherapy and Immunotherapy for Malignant Melanoma: Target Formulation Development and *In Vitro* Anticancer Activity. *Int. J. Nanomedicine* 6, 1991–2005. doi:10.2147/ijn.S24094

Ding, B.-y., Zhang, W., Wu, X., Wang, X., Fan, W., Gao, S., et al. (2011). Biodegradable Methoxy Poly (Ethylene Glycol)-Poly (Lactide) Nanoparticles for Controlled Delivery of Dacarbazine: Preparation, Characterization and Anticancer Activity Evaluation. *Afr. J. Pharm. Pharmacol.* 5 (11), 1369–1377. doi:10.5897/ajpp11.236

Eigentler, T. K., Weide, B., de Braud, F., Spitaleri, G., Romanini, A., Pflugfelder, A., et al. (2011). A Dose-Escalation and Signal-Generating Study of the Immunocytokine L19-IL2 in Combination with Dacarbazine for the Therapy of Patients with Metastatic Melanoma. *Clin. Cancer Res.* 17 (24), 7732–7742. doi:10.1158/1078-0432.Ccr-11-1203

Gong, X., Zheng, Y., He, G., Chen, K., Zeng, X., and Chen, Z. (2019). Multifunctional Nanoplatform Based on star-shaped Copolymer for Liver Cancer Targeting Therapy. *Drug Deliv.* 26 (1), 595–603. doi:10.1080/10717544.2019.1625467

Hafeez, A., and Kazmi, I. (2017). Dacarbazine Nanoparticle Topical Delivery System for the Treatment of Melanoma. *Scientific Rep.* 7. doi:10.1038/s41598-017-16878-1

Hamid, O., Robert, C., Daud, A., Hodi, F. S., Hwu, W.-J., Kefford, R., et al. (2013). Safety and Tumor Responses with Lambrolizumab (Anti-PD-1) in Melanoma. *N. Engl. J. Med.* 369 (2), 134–144. doi:10.1056/NEJMoa1305133

Janvier, F., Zhu, J. X. X., Armstrong, J., Meiselman, H. J., and Cloutier, G. (2013). Effects of Amphiphilic star-shaped Poly(ethylene Glycol) Polymers with a Cholic Acid Core on Human Red Blood Cell Aggregation. *J. Mech. Behav. Biomed. Mater.* 18, 100–107. doi:10.1016/j.jmbbm.2012.11.008

Jin, R. R., Wang, J. X., Gao, M. X., and Zhang, X. M. (2021). Pollen-like Silica Nanoparticles as a Nanocarrier for Tumor Targeted and pH-Responsive Drug Delivery. *Talanta*, 231. doi:10.1016/j.talanta.2021.122402

Kabirian-Dehkordi, S., Chalabi-Dchar, M., Mertani, H. C., Le Guellec, D., Verrier, B., Diaz, J. J., et al. (2019). AS1411-conjugated Gold Nanoparticles Affect Cell Proliferation through a Mechanism that Seems Independent of Nucleolin. *Nanomedicine-Nanotechnology Biol. Med.* 21. doi:10.1016/j.nano.2019.102060

Kakumanu, S., Tagne, J. B., Wilson, T. A., and Nicolosi, R. J. (2011). A Nanoemulsion Formulation of Dacarbazine Reduces Tumor Size in a Xenograft Mouse Epidermoid Carcinoma Model Compared to Dacarbazine Suspension. *Nanomedicine: Nanotechnology, Biol. Med.* 7 (3), 277–283. doi:10.1016/j.nano.2010.12.002

Kemler, I., Karamched, B., Neuhauser, C., and Dingli, D. (2021). Quantitative Imaging and Dynamics of Tumor Therapy with Viruses. *Febs J.* 288 (21), 6273–6285. doi:10.1111/febs.16102

Kerns, S. J., Belgur, C., Petropolis, D., Kanellias, M., Barrile, R., Sam, J., et al. (2021). "Human Immunocompetent Organ-On-Chip Platforms Allow Safety Profiling of Tumor-Targeted T-Cell Bispecific Antibodies. *Elife*, 10. doi:10.7554/eLife.67106

Koutsioumpa, M., and Papadimitriou, E. (2014). "Cell Surface Nucleolin as a Target for Anti-cancer Therapies. *Recent Patents Anti-Cancer Drug Discov.* 9(2). doi:10.2174/1574892808666131119095953

Koyama, S., Akbay, E. A., Li, Y. Y., Herter-Sprie, G. S., Buczkowski, K. A., Richards, W. G., et al. (2016). Adaptive Resistance to Therapeutic PD-1 Blockade Is Associated with Upregulation of Alternative Immune Checkpoints. *Nat. Commun.* 7. doi:10.1038/ncomms10501

Li, C. Y., and Han, X. P. (2020). Co-delivery of Dacarbazine and All-Trans Retinoic Acid (ATRA) Using Lipid Nanoformulations for Synergistic Antitumor Efficacy against Malignant Melanoma. *Nanoscale Res. Lett.* 15 (1). doi:10.1186/s11671-020-3293-3

Li, J., Wang, Y., Liang, R., An, X., Wang, K., Shen, G., et al. (2015). Recent Advances in Targeted Nanoparticles Drug Delivery to Melanoma. *Nanomedicine: Nanotechnology, Biol. Med.* 11 (3), 769–794. doi:10.1016/j.nano.2014.11.006

Li, Y. M., Chen, X. L., Ji, J. B., Li, L. B., and Zhai, G. X. (2021). "Redox-responsive Nanoparticles Based on Chondroitin Sulfate and Docetaxel Prodrug for Tumor Targeted Delivery of Docetaxel. *Carbohydr. Polym.* 255. doi:10.1016/j.carbpol.2020.117393

Li, Z. M., Shan, X. T., Chen, Z. D., Gao, N. S., Zeng, W. F., Zeng, X. W., et al. (2021). Applications of Surface Modification Technologies in Nanomedicine for Deep Tumor Penetration. *Adv. Sci.* 8 (1). doi:10.1002/advs.202002589

Li, Z., Yang, Y., Wei, H., Shan, X., Wang, X., Ou, M., et al. (2021). Charge-reversal Biodegradable MSNs for Tumor Synergetic Chemo/photothermal and Visualized Therapy. *J. Controlled Release* 338, 719–730. doi:10.1016/j.jconrel.2021.09.005

Liu, G., Gao, N. S., Zhou, Y., Nie, J. P., Cheng, W., Luo, M. M., et al. (2019). "Polydopamine-Based "Four-In-One" Versatile Nanoplatforms for Targeted Dual Chemo and Photothermal Synergistic Cancer Therapy. *Pharmaceutics* 11 (10). doi:10.3390/pharmaceutics11100507

Liu, Q., Xu, N., Liu, L., Li, J., Zhang, Y., Shen, C., et al. (2017). Dacarbazine-Loaded Hollow Mesoporous Silica Nanoparticles Grafted with Folic Acid for Enhancing Antimetastatic Melanoma Response. *ACS Appl. Mater. Inter.* 9 (26), 21673–21687. doi:10.1021/acsami.7b05278

Lu, J., Jiao, Y. P., Cao, G. C., and Liu, Z. H. (2021). Multimode CaCO3/pneumolysin Antigen Delivery Systems for Inducing Efficient Cellular Immunity for Anti-tumor Immunotherapy. *Chem. Eng. J.*, 420. doi:10.1016/j.cej.2021.129746

Ma, D., Liu, Z.-H., Zheng, Q.-Q., Zhou, X.-Y., Zhang, Y., Shi, Y.-F., et al. (2013). Star-shaped Polymer Consisting of a Porphyrin Core and Poly(L-Lysine) Dendron Arms: Synthesis, Drug Delivery, and *In Vitro* Chemo/Photodynamic Therapy. *Macromol. Rapid Commun.* 34 (6), 548–552. doi:10.1002/marc.201200742

Nguyen-Van, C., Hsieh, M.-F., Chen, Y.-T., and Liau, I. (2011). "Doxorubicin-Loaded Nanosized Micelles of a Star-Shaped Poly(epsilon-Caprolactone)-Polyphosphoester Block Co-polymer for Treatment of Human Breast Cancer.". *J. Biomater. Science-Polymer Edition* 22 (11), 1409–1426. doi:10.1163/092050610x510533

Palmieri, D., Richmond, T., Piovan, C., Sheetz, T., Zanesi, N., Troise, F., et al. (2015). Human Anti-nucleolin Recombinant Immunoagent for Cancer Therapy. *Proc. Natl. Acad. Sci. USA* 112 (30), 9418–9423. doi:10.1073/pnas.1507087112

Pei, X., Zhang, X. J., Zhang, L., Yuan, M. M., Sun, L., Yu, F., et al. (2021). Targeted Exosomes for Co-delivery of siFGL1 and siTGF-Beta 1 Trigger Combined Cancer Immunotherapy by Remodeling Immunosuppressive Tumor Microenvironment. *Chem. Eng. J.* 421. doi:10.1016/j.cej.2021.129774

Peng, Y., Nie, J., Cheng, W., Liu, G., Zhu, D., Zhang, L., et al. (2018). A Multifunctional Nanoplatform for Cancer Chemo-Photothermal Synergistic Therapy and Overcoming Multidrug Resistance. *Biomater. Sci.* 6 (5), 1084–1098. doi:10.1039/c7bm01206c

Romano, S., Moura, V., Simoes, S., Moreira, J. N., and Goncalves, J. (2018). Anticancer Activity and Antibody-dependent Cell-Mediated Cytotoxicity of Novel Anti-nucleolin Antibodies. *Scientific Rep.* 8. doi:10.1038/s41598-018-25816-8

Su, Y., Hu, J., Huang, Z., Huang, Y., Peng, B., Xie, N., et al. (2017). Paclitaxel-loaded star-shaped Copolymer Nanoparticles for Enhanced Malignant Melanoma Chemotherapy against Multidrug Resistance. *Dddt* 11, 659–668. doi:10.2147/dddt.S127328

Tagne, J.-B., Kakumanu, S., and Nicolosi, R. J. (2008). Nanoemulsion Preparations of the Anticancer Drug Dacarbazine Significantly Increase its Efficacy in a Xenograft Mouse Melanoma Model. *Mol. Pharmaceutics* 5 (6), 1055–1063. doi:10.1021/mp8000556

Tao, W., Zeng, X., Zhang, J., Zhu, H., Chang, D., Zhang, X., et al. (2014). Synthesis of Cholic Acid-Core Poly(ε-Caprolactone-Ran-Lactide)-B-Poly(ethylene Glycol) 1000 Random Copolymer as a Chemotherapeutic Nanocarrier for Liver Cancer Treatment. *Biomater. Sci.* 2 (9), 1262–1274. doi:10.1039/c4bm00134f

Tarhini, A. A., and Agarwala, S. S. (2006). Cutaneous Melanoma: Available Therapy for Metastatic Disease. *Dermatol. Ther.* 19 (1), 19–25. doi:10.1111/j.1529-8019.2005.00052.x

Wan, P. K.-T., Ryan, A. J., and Seymour, L. W. (2021). Beyond Cancer Cells: Targeting the Tumor Microenvironment with Gene Therapy and Armed Oncolytic Virus. *Mol. Ther.* 29 (5), 1668–1682. doi:10.1016/j.ymthe.2021.04.015

Wang, C.-S., Chang, C.-H., Tzeng, T.-Y., Lin, A. M.-Y., and Lo, Y.-L. (2021). Gene-editing by CRISPR-Cas9 in Combination with Anthracycline Therapy via Tumor Microenvironment-Switchable, EGFR-Targeted, and Nucleus-Directed Nanoparticles for Head and Neck Cancer Suppression. *Nanoscale Horiz.* 6 (9), 729–743. doi:10.1039/d1nh00254f

Wang, J., Chen, P., Dong, Y., Xie, H., Wang, Y. C., Soto, F., et al. (2021). Designer Exosomes Enabling Tumor Targeted Efficient Chemo/gene/ Photothermal Therapy. *Biomaterials* 276. doi:10.1016/j.biomaterials.2021.121056

Yildiz, M., and Kacar, G. (2021). Investigation of Ibuprofen Loading in PEG-PLGA-PEG Micelles by Coarse-Grained DPD Simulations. *Mrs Adv.* 6. doi:10.1557/s43580-021-00073-6

Yuan, G., Wu, L., Li, B., and An, J. (2017). Primary Malignant Melanoma of the Cervix: Report of 14 Cases and Review of Literature. *Oncotarget* 8 (42), 73162–73167. doi:10.18632/oncotarget.17183

Zhang, L., Yang, J. R., Xia, L., Chen, H. Q., Chen, X. L., Qian, X. J., et al. (2021). Study on the Prognostic Value of Preoperative Anti Hepatitis B Virus Therapy in Patients with Hepatocellular Carcinoma Complicated with Microvascular Tumor Thrombus and Establishment of Survival Prediction Model. *Zhonghua yi xue za zhi* 101 (28), 2203–2209. doi:10.3760/cma.j.cn112137-20210107-00039

Conflict of Interest: The authors declare that the research was conducted in the absence of any commercial or financial relationships that could be construed as a potential conflict of interest.

Publisher's Note: All claims expressed in this article are solely those of the authors and do not necessarily represent those of their affiliated organizations, or those of the publisher, the editors and the reviewers. Any product that may be evaluated in this article, orclaim that may be made by its manufacturer, is not guaranteed or endorsed by the publisher.

Copyright © 2022 Xiong, Guo, Zeng, Wang, Zeng, Cao and Lian. This is an open-access article distributed under the terms of the Creative Commons Attribution License (CC BY). The use, distribution or reproduction in other forums is permitted, provided the original author(s) and the copyright owner(s) are credited and that the original publication in this journal is cited, in accordance with accepted academic practice. No use, distribution or reproduction is permitted which does not comply with these terms.

Advantages of publishing in Frontiers

OPEN ACCESS
Articles are free to read for greatest visibility and readership

FAST PUBLICATION
Around 90 days from submission to decision

HIGH QUALITY PEER-REVIEW
Rigorous, collaborative, and constructive peer-review

TRANSPARENT PEER-REVIEW
Editors and reviewers acknowledged by name on published articles

Frontiers
Avenue du Tribunal-Fédéral 34
1005 Lausanne | Switzerland

Visit us: www.frontiersin.org
Contact us: frontiersin.org/about/contact

REPRODUCIBILITY OF RESEARCH
Support open data and methods to enhance research reproducibility

DIGITAL PUBLISHING
Articles designed for optimal readership across devices

FOLLOW US
@frontiersin

IMPACT METRICS
Advanced article metrics track visibility across digital media

EXTENSIVE PROMOTION
Marketing and promotion of impactful research

LOOP RESEARCH NETWORK
Our network increases your article's readership